predictive mineral discovery
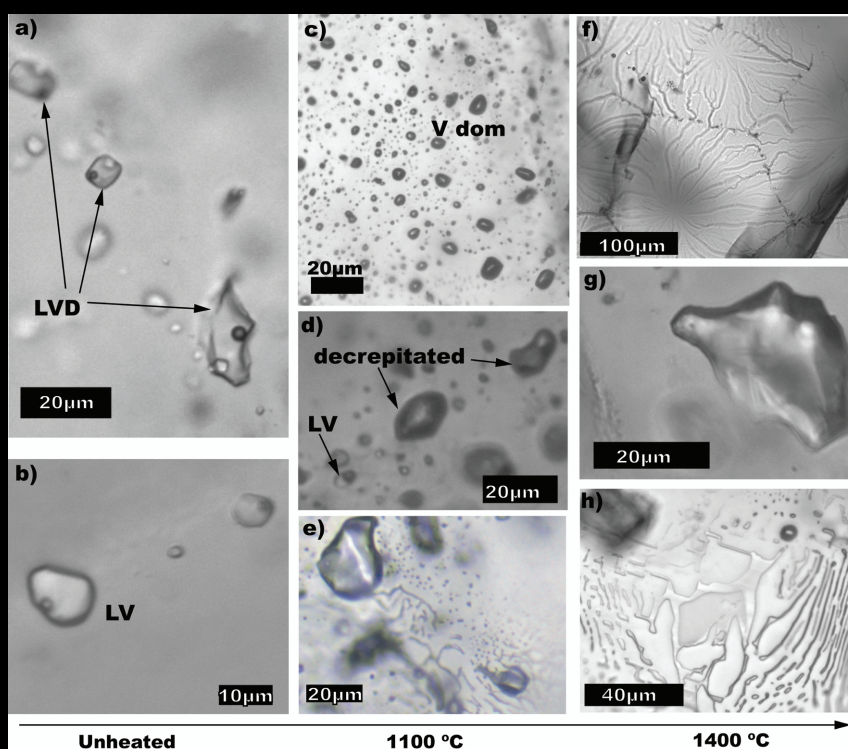COOPERATIVE RESEARCH CENTRE

pmd*CRC

Final Report

^{40}Ar/^{39}Ar dating of mineralisation metamorphism and deformation

Project H4

David Phillips (editor)

Photomicrographs of a fluid inclusion sample from Osborne mine - (a & b) before heating, (c, d & e) after heating to 1100°C in the UHV resistance furnace, (f, g & h) after heating to 1400°C in the UHV resistance furnace.

CSIRO

AMIRA INTERNATIONAL

Australian Government
Geoscience Australia

MONASH University

THE UNIVERSITY OF MELBOURNE

JCU JAMES COOK UNIVERSITY

THE UNIVERSITY OF WESTERN AUSTRALIA

H4: $^{40}Ar/^{39}Ar$ dating of mineralisation, metamorphism and deformation.

Final Report (2002 – 2005)

The *pmd*CRC* H4 project commenced in 2002 with the aim of evaluating existing $^{40}Ar/^{39}Ar$ methods and developing new enabling technologies for the geochronology and geochemistry of ore systems. This report also encompasses development work on halogen/noble gas geochemistry of mineralising systems.

The *pmd*CRC* project team for the H4 project is as follows:

Role	Name	Affiliation
Program Coordinator	Prof Andy Gleadow	The University of Melbourne
	Dr Bruce Schaefer	Monash University
Project Leader	Dr David Phillips	The University of Melbourne
Team Members	Dr John Miller	The University of Melbourne
	Dr Mark Kendrick	The University of Melbourne
	Mr Stan Szczepanski	The University of Melbourne
Academic Contributors	Dr Tim Baker	James Cook University
	Dr Pat Williams	James Cook University
	Dr Roger Mustard	James Cook University
	Dr Geordie Mark	James Cook University / Monash University
	Dr Andy Wilde	Monash University
	Dr Terry Mernagh	GeoScience Australia
Industry Contributors	Mr Jon Dugdale	Leviathan Resources (MPI)
	Mr Greg Hall	Placer Dome Asia Pacific
	Dr Glen Masterman	Placer Dome Asia Pacific/The University of Melbourne
Honours Students	Mr Jarrod MacCulloch	The University of Melbourne

Table of Contents

H4: ^{40}Ar/^{39}Ar dating of mineralisation, metamorphism and deformation.

Executive Summary

D. Phillips

Introduction

The principal objective of the History Program (Program 3) was to evaluate existing techniques and develop new enabling technologies in geochronology and isotope geoscience to significantly improve our ability to constrain the timing of ore formation and, therefore, expand predictive capabilities. The ^{40}Ar/^{39}Ar dating method is one of the most widely utilised geochronology techniques, because of the abundance of potassium-bearing minerals in the Earth's crust, a high precision age capability, the use of micro-analytical sampling methods (e.g. lasers) and the usefulness of argon isotopes for constraining ore fluid sources. The ^{40}Ar/^{39}Ar dating method has been widely applied to ore systems, but with varying degrees of success, due to a susceptibility to resetting and, in low grade metamorphic terranes, recoil loss/redistribution of ^{39}Ar, caused by neutron bombardment in the nuclear reactor. In general, the technique is considered to be inferior to the U-Pb dating method, despite the fact that minerals suitable for U-Pb dating (e.g. zircon, titanite) are rarely associated with mineral deposits – in many instances, mineralisation timing is constrained by U-Pb dating of cross-cutting igneous intrusions that contain suitable U-bearing phases such as zircon. This is not always satisfactory, as cross-cutting intrusions may be uncommon, unrelated in age, and/or contain abundant inherited zircons that complicate precise age determinations. One of the fundamental goals of the H4 project was to evaluate existing dating methods and interpretations, particularly with respect to gold deposits in low grade terranes, and to investigate potential new dating methods such as ^{40}Ar/^{39}Ar laser probe analyses of mica-bearing pyrite linked to gold mineralisation.

An additional application linked to the ^{40}Ar/^{39}Ar technique is the use of argon isotopes to constrain the origin of mineralising fluids. Extension of the technique to the heavier noble gases, Kr and Xe, also allows for measurement of the halogens Cl, Br and I in small samples. In combination, noble gas and halogen geochemistry provides a powerful tool for investigating the origin of ore fluids as well as the processes involved in fluid evolution (e.g. mixing, boiling, etc.). Therefore, a second major goal of the H4 project was to initiate development of halogen/noble gas geochemistry technology and expertise within the pmd*CRC to enable this unique geochemical method to be applied to ore deposits in the flagship terranes in the second stage of the CRC.

Project goals and deliverables

The H4 project was established as on the History Program' enabling technology projects within the predictive mineral discovery Cooperative Research Centre (pmd*CRC). The project was based at The University of Melbourne, but developed linkages with other programs and projects such as the Fluids Program (James Cook University, The University of Western Australia) and the T1 Project (Prof. Chris Wilson, MPI mines). The specific goals of the H4 project evolved over the period of the project, with the main objectives as follows:

i)   To Evaluate $^{40}Ar/^{39}Ar$ techniques for dating fine-grained white micas associated with gold deposits in low-grade terranes, with emphasis on the western Victoria and Yilgarn terranes.

ii)   To Develop and evaluate $^{40}Ar/^{39}Ar$ methods for dating single mica-bearing pyrite grains associated with gold deposits in the western Victoria and Yilgarn terranes.

iii) To develop technologies, techniques and procedures for combined analyses of halogens (Cl, Br, I) and noble gases (He, Ne, Ar, Kr, Xe) in fluid inclusion-bearing quartz samples, with initial emphasis on the Mt Isa terrane.

iv)   To evaluate $^{40}Ar/^{39}Ar$ methods for dating fluid inclusion-bearing quartz samples from selected Mt Isa Terrane localities.

In relation to the above project goals, the key deliverables of the H4 project were as follows:

1)   Establishment of a geological framework for gold deposits in western Victoria, based on new $^{40}Ar/^{39}Ar$ dating analyses, combined with existing geochronological data.

2)   Enhanced analytical and interpretative methods for $^{40}Ar/^{39}Ar$ dating of fine-grained white micas associated with gold deposits in low-grade terranes (western Victoria and Yilgarn terranes).

3)   Development and evaluation of $^{40}Ar/^{39}Ar$ laser probe methods for dating single mica-bearing pyrite grains from well-constrained gold deposits in the western Victoria and Yilgarn terranes.

4)   Establishment of analytical facilities and expertise for noble gas (Ar, Kr, Xe) and halogen (Cl, Br, I) analyses of quartz samples containing fluid inclusions. Development of analytical protocols for halogen/noble gas analyses of quartz samples and provision of test results on selected samples from the Mt Isa terrane.

5)   Development of $^{40}Ar/^{39}Ar$ analytical and interpretative methods for dating fluid inclusion-bearing quartz samples from selected Mt Isa Terrane localities.

6)   Education of industry sponsors on the theory and applicability of new $^{40}Ar/^{39}Ar$ dating and halogen/noble gas geochemical methodologies.

Relationship of the project to the pmd*CRC vision

The H4 project focussed on evaluating existing techniques and developing new technologies with respect to $^{40}Ar/^{39}Ar$ dating and halogen/noble gas geochemical methods. In addressing the goals of the pmd*CRC, the H4 project focussed on the Flagship Terranes, which became 'natural testing laboratories'. Consequently the results obtained are directly relevant to the Terrane projects and contribute to developing the 3D architecture of the terranes as well as providing key data for the development of 4D predictive models for mineral exploration.

Project achievements

The H4 project operated for three and a half years, during which time the main project team grew to include John Miller (September, 2002) and Mark Kendrick (February, 2004). Although the H4 project enjoyed a number of successes, the key achievements were the establishment of $^{40}Ar/^{39}Ar$ methods to reliably date mica-bearing pyrite grains and the development of instrumentation, expertise and analytical methods for halogen/noble gas analyses of minerals related to mineralisation systems.

Chapter one of this report documents $^{40}Ar/^{39}Ar$ age data from the boundary between the Delamerian and Lachlan Orogens. This study showed that the Stawell Zone in western Victoria is a reworked orogenic zone between the Lachlan and Delamerian Fold Belts that contains the eastern section of the Cambrian Delamerian Orogen and the western limit of orogenesis associated with the formation of an Ordovician to Silurian accretionary wedge (Lachlan Fold Belt). This metamorphic zonation is consistent with a westerly-dipping subduction zone and reflects deformation processes associated with a Cambrian subduction zone that dipped towards the Gondwana super-continent. The revised orogenic boundary has implications for the location of 440 Ma orogenic gold deposits in south and southeast Australia, as it implies that 440 Ma gold mineralisation may not be restricted to the Lachlan fold-belt. The structural complexity of the 440 Ma Stawell gold deposit reflects its location within a reworked part of the Cambrian Delamerian Fold Belt, while the structurally simpler 440 Ma Bendigo deposit is hosted by younger Ordovician turbidites solely deformed by Lachlan orogenesis.

Chapter 2 discusses the causes behind the discordance associated with $^{40}Ar/^{39}Ar$ dating of fine-grained mica. In this study, the $^{40}Ar/^{39}Ar$ technique was applied to alteration within samples from various phases of alteration and gold mineralisation that are structurally well constrained within the Stawell gold deposit in western Victoria. The majority of the samples yielded ages within previously constrained age brackets (from $^{40}Ar/^{39}Ar$ dating and U-Pb dating of intrusives). One sericite sample from a 440 Ma gold lode (age confirmed by pyrite dating presented in Chapter 3) gave a ca. 400 Ma age, which reflects overprinting from hydrothermal fluids linked to the 400 Ma Stawell intrusion. This highlights the danger in relying too much on $^{40}Ar/^{39}Ar$ ages from wall rock sericite adjacent to gold lodes, even within structurally well-constrained systems such as Stawell. The majority of age spectra are complicated by a combination of ^{39}Ar recoil, inherited detrital and metamorphic mica and multiple phases of alteration. It is concluded that the way forward in dating fine-grained micas is via the mica-in-pyrite method discussed in chapter 3.

In chapter 3, we test the hypothesis that pyrite is capable of armouring potassium-bearing mineral inclusions from alteration-induced argon loss, thus providing improved $^{40}Ar/^{39}Ar$ age results. In this study, matrix muscovite and pyrite crystals hosting muscovite inclusions were selected from three variably overprinted orogenic gold deposits and analysed by combined single crystal $^{40}Ar/^{39}Ar$ laser-probe and *in vacuo* crushing methods. Pyrite grains from the ~2.60 Ga Mt

Charlotte gold deposit yielded concordant ages averaging 2594 ± 8 Ma (2σ), indistinguishable from previous age estimates. Matrix mica from the ~2.63 Ga Kanowna Belle gold deposit yielded a discordant age spectrum with all ages younger than 2.5 Ga, indicating substantial $^{40}Ar*$ loss related to mid-Proterozoic thermal overprinting. Analyses of pyrite crystals from Kanowna Belle produced anomalously old apparent ages (up to 7.0 Ga) from low temperature steps – however, in contrast to the matrix mica, total-gas pyrite ages generally approach or overlap the inferred time of gold mineralization. This behaviour is attributed to diffusion of $^{40}Ar*$ to internal muscovite/pyrite grain boundaries in response to the mid-Proterozoic thermal event, with limited external loss of argon. Matrix mica from the ~440 Ma Stawell gold deposit, hydrothermally overprinted at ~400 Ma, exhibits a discordant age spectrum attributed to recoil loss/redistribution of $^{39}Ar_K$. High temperature steps from most Stawell pyrite grains give ages averaging 436 ± 4 Ma, within error of the inferred time of gold mineralisation. It is concluded that pyrite acts as a partially closed system for argon, but that the $^{40}Ar/^{39}Ar$ 'pyrite' dating method has the potential to 'see through' later thermal/alteration events and resolve controversial aspects of ore deposit geochronology.

Chapter 4 describes the noble gas and halogen degassing behaviour of quartz. In this study, samples were selected from the Eloise and Osborne, Iron Oxide Copper Gold (IOCG) ore deposits, and the Railway Fault, 13 km south of the Mt Isa Mine, in the Mt Isa Inlier. Quartz was found to exhibit a bimodal degassing profile with mechanical decrepitation of fluid inclusions accounting for the release of gas at temperatures of <700 °C. Changes in the Br/Cl, I/Cl, Ar/Cl and $^{40}Ar/^{36}Ar$ composition of gas released at different temperatures up to 700 °C can be related to the decrepitation of different types of fluid inclusion. This approach is advantageous for the IOCG samples that are characterized by complex fluid inclusion assemblages. Three of the IOCG samples have interpreted primary MS and LVD fluid inclusions characterized by molar Br/Cl values of between $0.25×10^{-3}$ and $0.66×10^{-3}$, I/Cl between $0.37×10^{-6}$ and $5.0×10^{-6}$ and $^{40}Ar/^{36}Ar$ of <1000. These values are most easily explained by the involvement of halite dissolution water in IOCG genesis. One of the IOCG samples has Br/Cl of $1.3-2.0×10^{-3}$ and I/Cl of $10×10^{-6}$, similar to juvenile magmatic fluids in Phanerozoic Porphyry Copper Deposits. This sample also has a slightly elevated $^{40}Ar/^{36}Ar$ of 2236. The Railway Fault samples have mean values of $8.1×10^{-3}$ for Br/Cl; $9.4-12×10^{-6}$ for I/Cl; <2000 for $^{40}Ar/^{36}Ar$; and $4.7-4.8×10^{-6}$ $cm^3cm^{-3}H_2O$ for ^{36}Ar concentration. The Br/Cl values are similar to those previously reported for basinal brines present in silicic alteration at the Mt Isa Mine and the additional data can be explained by interaction of such a bittern brine with fine-grained sedimentary rocks in the subsurface. The second mode of quartz degassing occurs between 1200 and 1450 °C and releases a greater volume of gas than the first mode. Several lines of evidence indicate that the gas released at high temperature is also from the fluid inclusion reservoir. However, its release may be triggered by a metastable phase transition of quartz (~1200 ºC) and caution is required in interpretation of the fluid compositions obtained at these temperatures.

Chapter 5 involves a study of the argon isotope systematics of quartz vein samples related to the Mt Isa copper mineralization, and the Osborne plus Eloise iron-oxide-copper-gold (IOCG) deposits. The goal of this study was to ascertain the potential for $^{40}Ar/^{39}Ar$ dating of fluid inclusions in quartz. Results obtained demonstrate that, when fluid inclusions contain captive-mica impurities, excess $^{40}Ar_E$ is strongly correlated with fluid inclusion Cl while radiogenic $^{40}Ar_R$ is strongly correlated with K. The data define a plane in 3D ^{40}Ar-K-Cl-^{36}Ar space, which enables the determination of a robust 3D isochron. However, we conclude that in this case the ~1027 Ma age obtained for Mt Isa is related to thermal cooling and in these circumstances quartz ages do not always represent the age of quartz formation. In contrast, fluid inclusions from Osborne and Eloise are K-rich but do not contain captive-mica. In these cases multiple stepped heating

experiments constrained the maximum formation ages to a precision of 5% for Osborne and 15% for Eloise. The data support models in which the Osborne deposit formed during an early syn-D_2 1595 Ma event and are compatible with the Eloise deposit forming during a later 1514-1530 Ma mineralisation event.   Where captive mica impurities are absent, the correction for post mineralization radiogenic ^{40}Ar production is small and, the measured ^{40}Ar/^{36}Ar value is close to the initial value. The data indicate that quartz is retentive to Ar over billions of years. However, where captive mica is present ^{40}Ar-loss can occur from within the sub-reservoir into the surrounding fluid inclusion. The presence of mica impurities can be identified from sample degassing profiles and mean K/Cl values of >1.

Chapter 1: Definition of the timing of deformation and metamorphism in the western Victorian gold fields - a new tectonic model

J.McL. Miller, D. Phillips, C.J.L. Wilson and L.J. Dugdale

Summary

$^{40}Ar/^{39}Ar$ age data from the boundary between the Delamerian and Lachlan Orogens identify the Moornambool Metamorphic Complex as a Cambrian metamorphic belt within the western Stawell Zone of the Palaeozoic Tasmanide System of southeastern Australia. A reworked orogenic zone exists between the Lachlan and Delamerian Fold Belts that contains the eastern section of the Cambrian Delamerian Orogen and the western limit of orogenesis associated with the formation of an Ordovician to Silurian accretionary wedge (Lachlan Fold Belt). Delamerian thrusting is craton-verging and occurred at the same time as the final consolidation of Gondwana. $^{40}Ar/^{39}Ar$ age data indicate rapid cooling of the Moornambool Metamorphic Complex at about 500 Ma at a rate of 20 to 30°C per million years, temporally associated with calc-alkaline volcanism followed by clastic sedimentation. Extension in the over-riding plate of a subduction zone is interpreted to have exhumed the metamorphic rocks within the Moornambool Metamorphic Complex. The Delamerian system varies from a high geothermal gradient with syn-tectonic plutonism in the west to lower geothermal gradients in the east (no syn-tectonic plutonism). This metamorphic zonation is consistent with a westerly-dipping subduction zone. Contrary to some previous models involving a reversal in subduction polarity, the Ross and Delamerian systems of Antarctica and Australia are inferred to reflect deformation processes associated with a Cambrian subduction zone that dipped towards the Gondwana supercontinent. Western Lachlan Fold Belt orogenesis occurred about 40 million years after the Delamerian Orogeny and deformed older, colder, and denser oceanic crust, with metamorphism indicative of a low geothermal gradient. This orogenesis closed a marginal ocean basin by west-directed under-thrusting of oceanic crust that produced an accretionary wedge with west-dipping faults that verge away from the major craton. The western Lachlan Fold Belt was not associated with arc-related volcanism and plutonism occurred 40 to 60 million years after initial deformation. The revised orogenic boundaries have implications for the location of world-class 440 Ma orogenic gold deposits. The structural complexity of the 440 Ma Stawell gold deposit reflects its location within a reworked part of the Cambrian Delamerian Fold Belt, while the structurally simpler 440 Ma Bendigo deposit is hosted by younger Ordovician turbidites solely deformed by Lachlan orogenesis.

1.1 Introduction

Accretion of geological terranes to the western margin of the Gondwana supercontinent during the Palaeozoic converted extensive oceanic turbidites into new continental crust (Foster & Gray 2000a). In Australia this accretion is defined by the New England, Lachlan, Tyennan and Delamerian Fold Belts that have a strike length of about 3000 km and a width in excess of 1500 kilometres: together these fold belts define the Tasmanides (Fig 1.1). Areally, the Lachlan Fold Belt represents about half of the exposed Tasmanides and understanding its

evolution is one of the keys to unravelling Palaeozoic crustal growth processes. However, the geodynamic mechanisms that forged the Lachlan Fold Belt have invoked considerable controversy in recent years (O'Halloran *et al.* 1998; Taylor & Cayley 2000; Gray & Foster 2000; Foster & Gray 2000b; VandenBerg 2000; Lister 2001; Gray & Foster 2001; Bierlein *et al.* 2002; Taylor & Cayley 2002). In particular, divergent tectonic models have evolved for the western and central sub-provinces of the Lachlan Fold Belt (Figures 1.1b, 1.2). These range from intra-plate deformation models driven by outboard processes with fault geometries equated with the classic craton-verging fault systems of North America (Fig 1.2a), to subduction-accretion models that require under-thrusting of oceanic crust to produce the observed fault geometries (Fig 1.2b). Correctly ascertaining the manner in which deformation propagated through the Cambro-Ordovician turbidite sequences is one way to resolve the controversies surrounding these contrasting models.

The Delamerian system is an extension of the Cambrian Ross Orogen preserved in the Trans-Antarctic Mountains (Fig 1.1a). The rocks defining the orogenic boundary between the Delamerian and Lachlan Fold Belts in Australia have been directly correlated with the terranes in northern Victoria Land, Antarctica (Fig 1.1a; Flöttman & Kleinschmidt 1993). In spite of similar structural associations and lithologies, these systems are inferred to have had the opposite subduction polarity. The Ross Orogen is considered to represent deformation processes within the over-riding plate of a subduction zone that dipped towards the Gondwana supercontinent (e.g. Gibson & Wright 1985; Dallmeyer & Wright 1992; Goodge & Dallmeyer 1996; Goodge 1997). In contrast the Delamerian and Tyennan systems are generally thought to have been associated with an easterly dipping subduction zone (Flöttman *et al.* 1998; Münker & Crawford 2000; VandenBerg *et al.* 2000). A transform fault or intra-continental tear is inferred to have separated the two opposing subduction systems (Flöttman *et al.* 1998; Münker & Crawford 2000), although west-dipping models for some or all of the Cambrian evolution of mainland Australia have also been proposed recently (Spaggiari *et al.* 2003; Boger & Miller 2004; Foden *et al.* 2004; Foster *et al.* 2005).
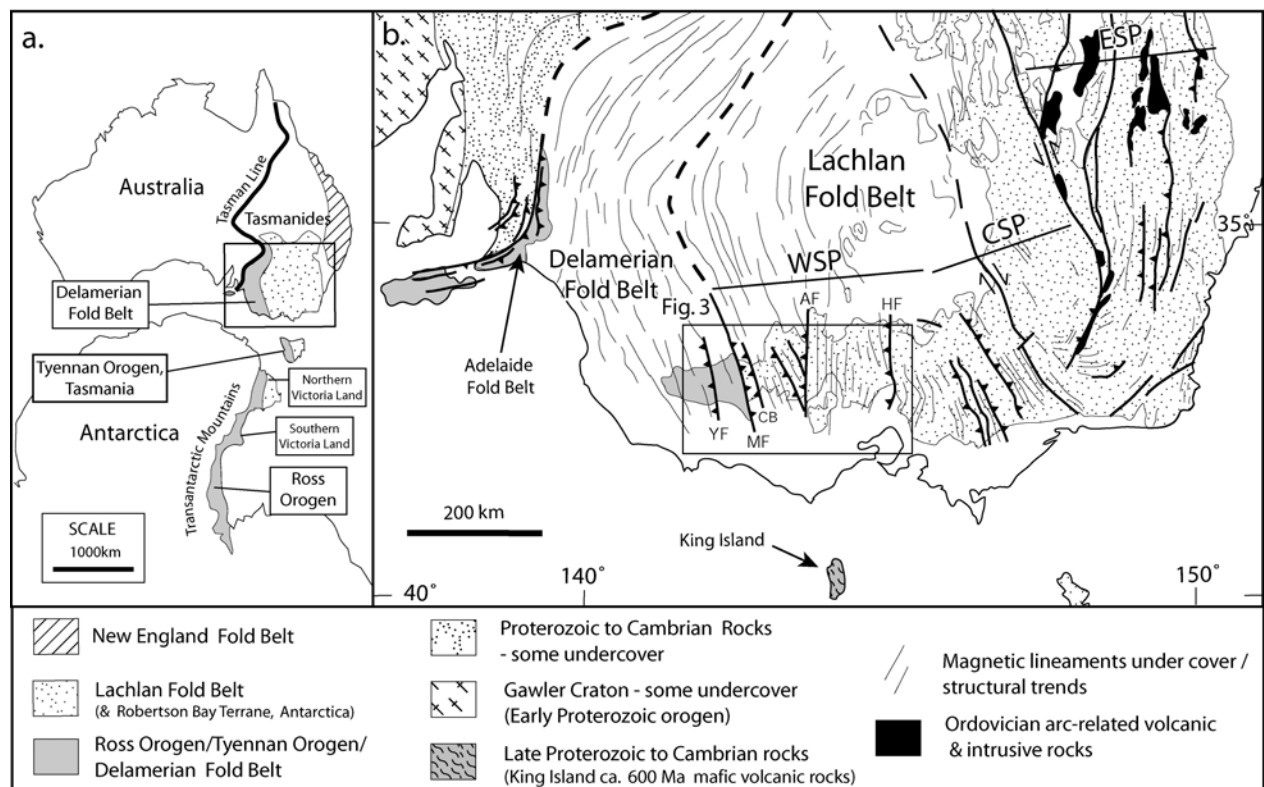
Fig 1.1. Map of the Tasmanides (modified from Gray & Foster 1998) and relationship to the Ross Orogen, Antarctica (locations of Antarctica and Australia reflect relative positions at about 110 Ma prior to the break up of eastern Gondwana). Abbreviations; WSP – Western sub-province, CSP – Central sub-province, ESP – Eastern sub-province, YF – Yarramjylup, MF – Moyston Fault, AF – Avoca Fault, HF – Heathcote Fault, CB – Coongee Break.
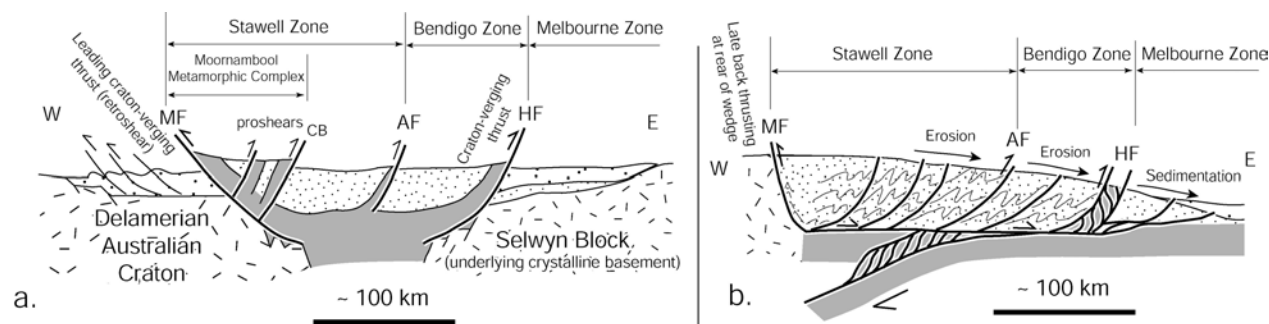
Fig 1.2. Current tectonic models for the western Lachlan Orogen. (a) Intraplate model (modified from Cayley *et al.* 2002). The east-dipping Moyston Fault (MF) is the leading fault of the Lachlan Orogen. West-dipping faults to the east of the Moyston Fault, such as the Coongee Break (CB) and the Avoca Fault (AF), define proshears that have propagated from the main craton-verging fault. Deformation within the Stawell and Bendigo Zones is inferred to reflect intra-plate deformation of a weak zone deformed in a "vice" scenario between two converging continental blocks. This produced a doubly-vergent thrust belt with two main craton-verging faults, the Moyston Fault (MF) and the Heathcote Fault (HF). (b) Under thrusting of oceanic crust in an analogous situation to an accretionary wedge above a subduction zone (modified from Gray & Foster 1998). The Moyston Fault (MF) represents a late back thrust. The dominant west dip of the faults, and the low geothermal gradient, is caused by the under-thrusting of oceanic crust.

This chapter presents new ^{40}Ar/^{39}Ar geochronology for key localities along the boundary of the Lachlan and Delamerian Fold Belts in an effort to resolve the deformation mechanics at this critical orogenic junction. These data reveal the boundary between the two fold belts to be a complex reworked tectonic zone, thus requiring a redefinition of the orogenic boundary between these two fold belts. The current study delineates a newly identified Cambrian metamorphic belt with a similar configuration to the Ross Orogen, highlights the marked contrast in the orogenic style of the Lachlan and Delamerian Fold Belts, and permits a reassessment of the geodynamic evolution for this region of Eastern Gondwana.

1.2. Geological framework

1.2.1 Adelaide Fold Belt

The Adelaide Fold Belt (Fig 1.1b) is the western-most expression of Delamerian Fold Belt and has three main stratigraphic components: Proterozoic crystalline basement, Proterozoic shallow water meta-sedimentary successions, and an Early Cambrian deep marine turbidite succession (Jenkins & Sandiford 1992; Foden *et al.* 1999, 2002a, 2002b; Preiss 2000). Geochronological constraints indicate that the Adelaide Fold Belt evolved rapidly from a sedimentary basin to a fold belt marked by craton-verging thrusting that initiated between 514 to 510 Ma (Haines & Flöttman 1998; Foden *et al.* 1999; Preiss 2000). The west-vergent fold belt appears to have reactivated older east-dipping normal faults associated with basin

formation (Flöttman *et al.* 1994, 1995). The substrate to the Delamerian orogenesis within the Adelaide Fold Belt is believed to be solely continental (Jenkins & Sandiford 1992).

Deformation is associated with high temperature-low pressure metamorphism that in many areas coincided with the intrusion of syn-tectonic I- and S-type plutons (Foden *et al.* 2002a). There is also a patchy and diachronous development of late stage folding associated with plutonism that may reflect thermal weakening (Jenkins & Sandiford 1992). U-Pb and Pb-Pb dating of syn- and post-tectonic intrusions has constrained the last of the Delamerian deformation to 492±2 Ma (Haines & Flöttman 1998; Foden *et al.* 2002a). $^{40}Ar/^{39}Ar$ cooling ages on post-tectonic A-type plutons range from 490 to 485 Ma (Turner *et al.* 1996).

1.2.2 Glenelg and Grampians-Stavely Zones

The Glenelg Zone (Fig 1.3) contains Early Cambrian turbidites, carbonates and Proterozoic (?) volcanics. The volcanics have compositions ranging from intra-plate basalts and rift tholeiites to rocks transitional to MORBs (VandenBerg *et al.* 2000; Gray *et al.* 2002; Crawford *et al.* 2003a). Slivers of fault-bounded serpentinite with boninitic affinities, also occur within the Glenelg Zone and are interpreted to be Early Cambrian in age (Fig 1.3; VandenBerg *et al.* 2000; Crawford *et al.* 2003a). The metamorphic grade varies from lower greenschist facies in the west to amphibolite facies in the east (VandenBerg *et al.* 2000). The style of deformation and magmatism within the Glenelg Zone is almost identical to that of the Adelaide Fold Belt and includes syn-tectonic plutonism e.g., Gibson & Nihill (1992), VandenBerg *et al.* (2000), Gray *et al.* (2002). The eastern margin of the Glenelg Zone is defined by the Yarramyljup Fault (Fig 1.3; Gibson & Nihill 1992). This fault separates sillimanite-bearing schists in the west from the less strongly deformed and lower grade metamorphic rocks of the Grampians-Stavely Zone in the east (Gibson & Nihill 1992).
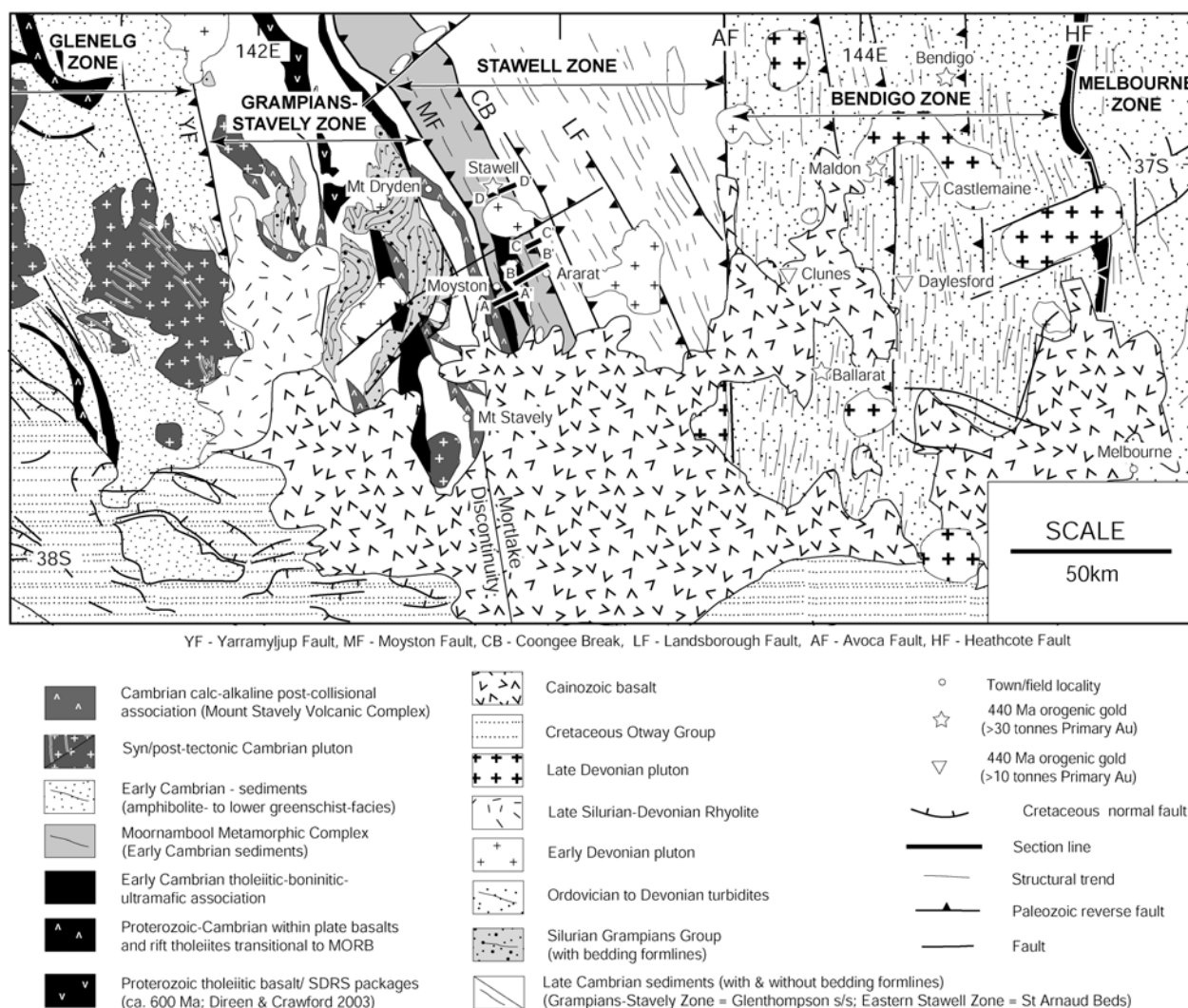
Fig 1.3. Geologic map of the western sub-province of the Lachlan Orogen (modified from Miller *et al.* 2002 and references therein, rock types for Grampians-Stavely Zone and Glenelg Zone summarised from VandenBerg *et al.* 2000 and Crawford *et al.* 2003a, 2003b). Section lines for Figures 1.4, 1.5, 1.6 are marked. Map is compiled from a large number of sources and some distortion will exist. Abbreviation for Proterozoic units, SDRS – seaward-dipping reflector sequences (Direen & Crawford 2003).

The Grampians-Stavely Zone contains fault-bounded packages of tholeiites, boninites, calc-alkaline volcanics, slate and sandstone. Some of the volcanic rocks have been related to *ca.* 600 Ma continental break-up of Rodinia and the development of a seaward-dipping reflector sequences (SDRS) along a volcanic passive margin (Direen & Crawford 2003; note SDRS unit on Fig 1.3). The boninites in this zone are part of an Early Cambrian tholeiitic-bonintic-ultramafic association that occurs throughout much of the Lachlan Fold Belt (Fig 3) and in the Tyennan Orogen of Tasamania (Crawford *et al.* 2003a). Younger Late Cambrian calc-alkaline volcanics (Mount Stavely Volcanic Complex) are considered to represent a post-collisional suite that may have developed on thinned continental crust (Fig 1.3; Münker & Crawford 2000; VandenBerg *et al.* 2000). An ^{40}Ar/^{39}Ar age of 500 Ma ± 2 Ma (2σ) has been obtained from primary hornblende separated from a dacite unit of this volcanic complex (Foster *et al.* 1998). A tuffaceous unit from the upper part of the Mount Stavely Volcanic Complex has a U-Pb SHRIMP zircon age of 495 ± 5 Ma (Stuart-Smith & Black 1999).

Late Cambrian sandstone and mudstone units within the Grampians-Stavely Zone (Fig 1.3) overlie, and are interlayered with, the Mount Stavely Volcanic Complex. These units are deformed by open to tight folds and faults (Gibson & Nihill 1992; VandenBerg *et al.* 2000). Late Cambrian post-tectonic I-type plutons intrude the folded sequences (Foster *et al.* 1998; VandenBerg *et al.* 2000). The Cambrian successions are unconformably overlain by the Ordovician(?) to Silurian fluvial to shallow marine sediments of the Grampians Group and Devonian rhyolites (Cayley & Taylor 2001). All units are intruded by Early Devonian plutons (Fig 3).

1.2.3 The Moyston Fault – a major lithospheric boundary

The Moyston Fault (Figures 1.1, 1.3) is currently inferred to be the orogenic boundary between the Lachlan and Delamerian Fold Belts (VandenBerg *et al.* 2000; Cayley *et al.* 2002). Seismic profiling and tomography studies have imaged a major lithospheric boundary with an easterly dip beneath the surficial expression of the Moyston Fault to depths of ~100 km (Korsch *et al.* 2002; Graeber *et al.* 2002). The Cambrian sedimentary and volcanic rocks in the footwall (west) exhibit low metamorphic grades and limited deformation. In contrast, the rocks in the hangingwall of the fault (east) have been isoclinally folded and poly-deformed with metamorphic grades locally attaining amphibolite facies (Cayley & Taylor 2001; Phillips *et al.* 2002). Thermobarometry of the amphibolites indicates that 15 to 20 km of vertical exhumation occurred prior to the intrusion of shallow level Early Devonian plutons (Cayley & Taylor 2001; Phillips *et al.* 2002).

Existing geochemical (Chappell *et al.* 1988; Price *et al.* 1997; Handler & Bennett 2001) and geophysical data (Graeber *et al.* 2002; Korsch *et al.* 2002) highlight that the lithosphere beneath the Grampians-Stavely Zone (i.e. directly west of the Moyston Fault) is different to that of the Stawell Zone. This has been inferred to represent a change from Proterozoic (west) to Phanerozoic (east) sub-continental lithospheric mantle (Handler & Bennett 2001).

Recent modelling of the geophysical responses across the Grampians-Stavely zone indicate that the observed magnetic intensities are inconsistent with a rock package comprised solely of Cambrian arc-related volcanism and sedimentation (Direen & Crawford, 2003). Instead the observed response is interpreted to reflect the presence of substantial amounts of Proterozoic mafic volcanics possibly related to *ca.* 600 Ma continental break up (SDRS units; Fig 1.3). These volcanic rocks are inferred to have erupted onto continental crust (Direen & Crawford 2003), suggesting that the substrate beneath the Grampians-Stavely Zone is not oceanic. These inferred SDRS units in the Grampians-Stavely Zone are correlated with Proterozoic basalts occurring on King Island and in western Tasmania (Fig 1; Direen & Crawford 2003).

1.2.4 Western Lachlan Fold Belt

The western sub-province of the Lachlan Fold Belt is dominated by turbidite sequences and is divided into three structural zones - the Stawell, Bendigo and Melbourne Zones (Gray & Foster 1998; VandenBerg *et al.* 2000; Fig 1.3). All structural zones are bounded by steep reverse faults and comprise turbidite sequences that are folded into tight to isoclinal upright folds (Fergusson *et al.* 1986; Cox *et al.* 1991; Wilson *et al.* 1992; Gray & Foster 1998). Most deformation in the Stawell and Bendigo Zones appears to have occurred between 455 and 440 Ma with possible sinistral reactivation of existing faults at ~426-420 Ma (Foster *et al.* 1998,

1999).   All structural zones are intruded by extensive high-level Devonian granitoids (Chappell *et al.* 1988).

The nature of the substrate to the turbidites in the Stawell, Bendigo-Ballarat and Melbourne Zones is controversial with some authors arguing for a solely oceanic substrate (e.g., Gray & Foster 1998). In contrast, Cayley *et al.* (2002) suggest that the correlation of field and aeromagnetic data between mainland Australia and Tasmania support the existence of a Proterozoic/Palaeozoic basement block, termed the Selwyn Block, beneath the eastern half of the Bendigo-Ballarat Zone and the Melbourne Zone. The turbidites in the western Stawell Zone are considered to be underlain by tholeiitic basalt (VandenBerg *et al.* 2000; Crawford *et al.* 2003a).

1.2.5 The Stawell Zone

The Stawell Zone (Fig 1.3) is subdivided into two structural regions by the steep west-dipping Coongee Break (Figures 1.3, 1.4). Detrital zircons from sandstones to the west of the Coongee Break have Proterozoic and older U-Pb ages, and have been correlated with the deformed Early Cambrian turbidite succession in the Adelaide Fold Belt and Glenelg Zone (part of the Kanmantoo Group; Squire *et al.* 2003). The sandstones to the east of the Coongee Break have detrital zircons with younger age populations (~500 Ma; Williams *et al.* 1991; Veevers 2000); these sediments have an inferred Late Cambrian age (VandenBerg *et al.* 2000).

Rocks to the east of the Coongee Break consist of simply folded turbidites that have been metamorphosed to sub-greenschist grade (Offler *et al.* 1998). The region west of the Coongee Break is characterised by greater structural complexity and is subdivided into a higher grade amphibolite facies western zone (Figures 1.4, 1.5a, 1.5b) and a lower greenschist facies eastern zone (Figures 4, 6a-h; Wilson *et al.* 1992; Miller & Wilson 2002; Phillips *et al.* 2002). Together these two zones define the Moornambool Metamorphic Complex (Cayley & Taylor 2001; Fig 1.4). The Stawell Gold Mine lies within the eastern zone of the Moornambool Metamorphic Complex (Fig 1.3).

Ductile deformation west of the Coongee Break is characterised by early bedding-parallel cleavages (Fig 1.6a), tight to isoclinal D_2 folds with S_2 crenulation cleavages (Fig 1.6d), S_3 crenulation cleavages and localised S_4 fabrics. Peak metamorphism is pre- to syn-D_2. The age of ductile deformation in the Moornambool Metamorphic Complex is poorly constrained with most previous $^{40}Ar/^{39}Ar$ analyses yielding difficult to interpret discordant age spectra with apparent ages ranging from 400 to 535 Ma (Foster *et al.* 1998, 1999). Foster *et al.* (1999) argued that discordant spectra from the eastern zone of the metamorphic complex recorded a component of Delamerian metamorphism and not a detrital component (e.g. Fig 8b of Foster *et al.* 1999).
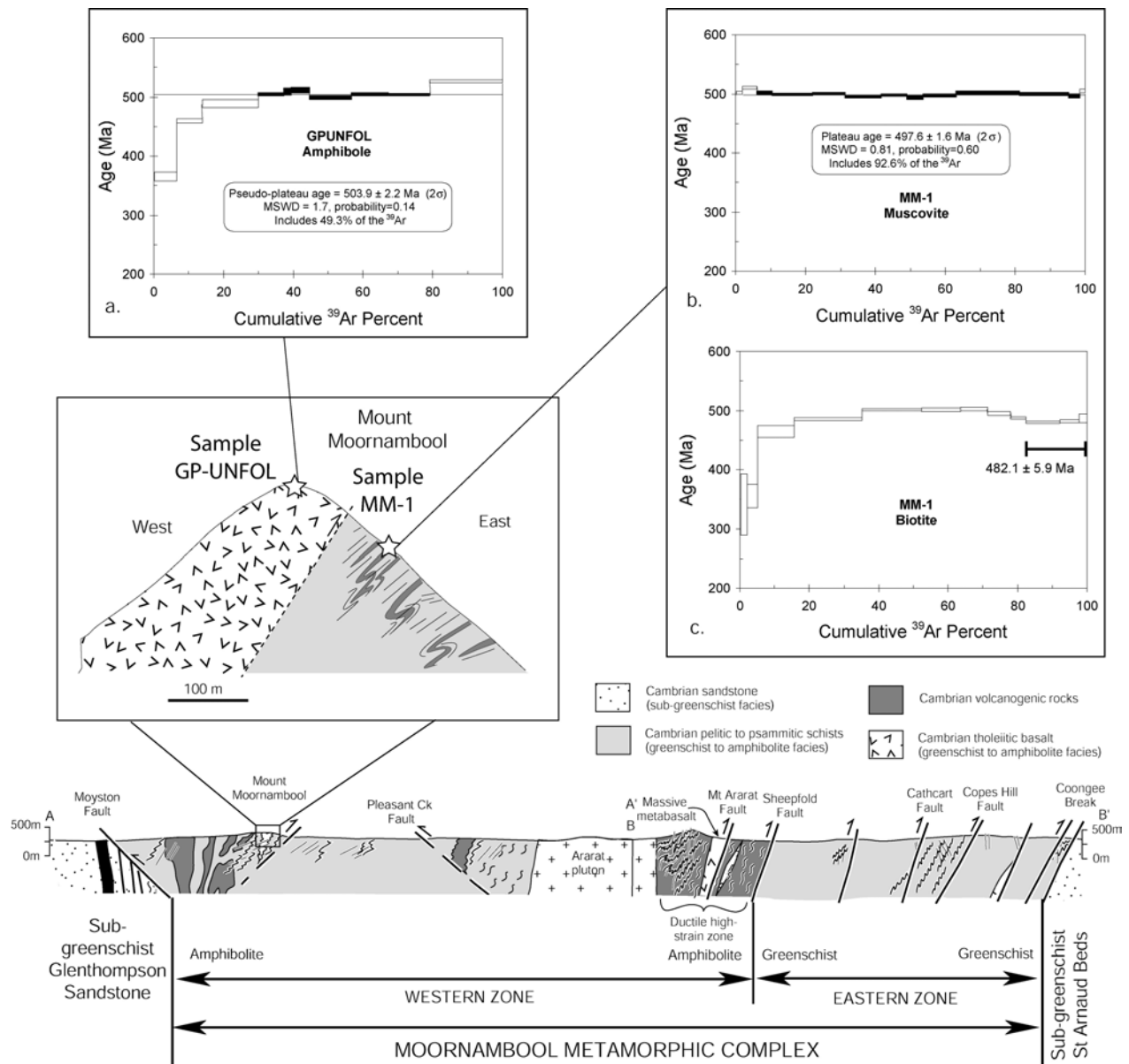
Fig 1.4. ^{40}Ar/^{39}Ar data with structural profile through the Ararat-Mount Moornambool transect (modified from Miller & Wilson 2002 and references therein). Vertical scale equals horizontal scale. Detail of Mount Moornambool highlights sample localities. Errors on age steps are 1σ. Stratigraphic units same as Fig 1.3.

The transition to brittle deformation in the Stawell zone is defined by the development of east- and west-dipping reverse faults. Gold mineralisation is related to brittle deformation and high fluid pressures (Miller & Wilson 2002). At the Stawell Gold Mine (Fig 1.7), sericite associated with mineralisation has been dated at 439 ± 2 Ma (2σ) using the ^{40}Ar/^{39}Ar dating method (Foster *et al.* 1998). This *ca.* 440 Ma age is the same as mica ages obtained from the Avoca Fault (Fig 1.2) and several intra-zone faults within the Bendigo Zone (Foster *et al.* 1998, 1999). These ages are interpreted to represent a component of the compressional deformation in the western Lachlan Fold Belt (Foster *et al.* 1998, 1999). The majority of fault transport along ductile and brittle structures occurred prior to the intrusion of the Early Devonian plutons, such as the Ararat granodiorite (Fig 1.4), which has been dated at 401 ± 4 Ma (SHRIMP U-Pb on zircon; Arne *et al.* 1998).

1.3. Sample localities and description of $^{40}Ar/^{39}Ar$ data

In this study the $^{40}Ar/^{39}Ar$ geochronology focussed on three key regions of the Moornambool Metamorphic Complex. The first region in the western zone of the Moornambool Metamorphic Complex was selected to ascertain the cooling history of the amphibolite facies rocks in the hangingwall of the Moyston Fault (Mount Moornambool amphibolite, samples **GP-UNFOL** and **MM-1**; Figures 1.3, 1.4, 1.5a, 1.5b). This locality was also used to assess if these rocks, which have metamorphic assemblages that imply 15 to 20 km of vertical offset across the Moyston fault (Cayley & Taylor 2001; Phillips *et al.* 2002), are indeed part of the Lachlan Fold Belt. The second sample locality was the Stawell Gold Mine in the eastern zone of Moornambool Metamorphic Complex (samples **SD-534** and **JM-8a**; Figures 1.3, 1.5c, 1.6a-e, 1.7). This site was selected to date mica growth away from major intra-zone faults in the Stawell Zone and to characterise hydrothermal alteration and resetting of metamorphic mica during orogenic gold lode formation. The third sample locality was selected to characterise the age of fabrics in the hangingwall and footwall of the Coongee Break that defines the eastern limit of the Moornambool Metamorphic Complex. This locality marks the boundary defining a change in structural complexity and detrital zircon provenance (Samples **ARA-23a** and **ARA-23g**; Figures 1.3, 1.6f-h, 1.8).
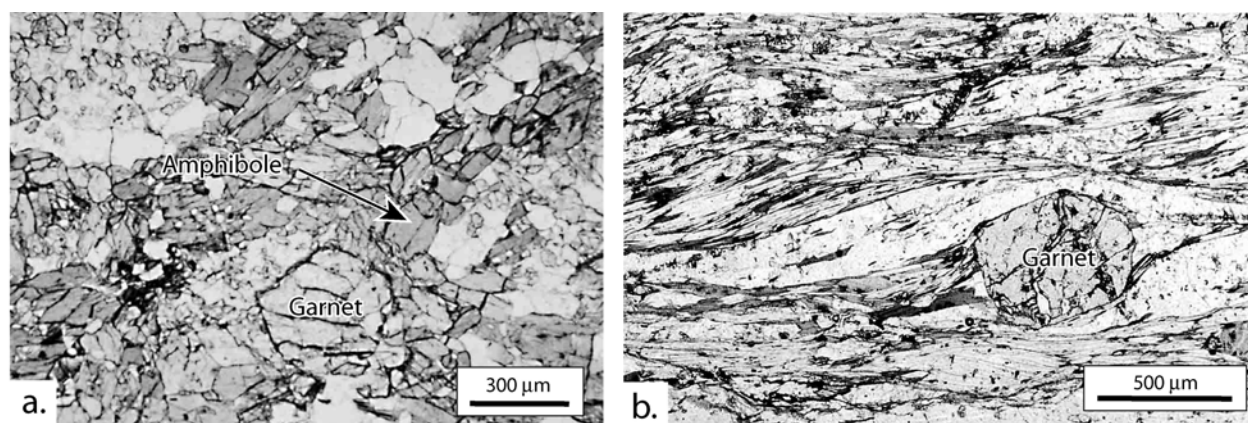
Fig 1.5. Photomicrographs of rocks from the western zone of the Moornambool Metamorphic Complex. (a) Garnet-bearing amphibolite schist from Mount Moornambool. Sample **GP-UNFOL**. Plane polarised light. Sample located in Fig 1.4. (b) Garnet-bearing muscovite, biotite schist from Mount Moornambool. Sample **MM-1**. Plane polarised light. Sample located in Fig 1.4.

1.3.1 Analytical procedures

Mineral separates were prepared from samples **GP-UNFOL** (amphibole) and **MM-1** (biotite + muscovite) using standard crushing, sieving and magnetic separation methods. The separates were hand-picked to greater than 99% purity. Samples **ARA-23a**, **ARA-23g JM-8A**, and **SD-534** contained white mica with a grain size <30µm. 75-125µm concentrates were prepared using magnetic separation and hand picking. This size fraction was found to be effective in removing most coarse-grained detrital muscovite grains. The purity of these samples was estimated to be >80%, with quartz being the main contaminant. All samples were washed in dilute nitric acid, deionised water and acetone prior to being shipped for irradiation.

The mineral separates were wrapped in aluminium packets and placed into an aluminium irradiation canister together with aliquots of the flux monitor GA1550 biotite (Age = 98.8 ± 0.5 Ma; Renne *et al.* 1998). Packets containing K_2SO_4 were placed at either end of the canister to monitor ^{40}Ar production from potassium. Samples were irradiated in two separate batches. Samples **MM-1**, **GPUNFOL**, **ARA-23a, ARA-23g**, and **JM-8A** were irradiated for 504 hours in position X34 of the HIFAR reactor, Lucas Heights, New South Wales, Australia. The canister was lined with 0.2 mm Cd to absorb thermal neutrons and was inverted three times during the irradiation, which reduced neutron flux gradients to <2% along the length of the canister (see Tetley *et al.* 1980). Correction factors for interfering reactions are as follows: $(^{36}Ar/^{37}Ar)_{Ca}$ = 3.50 (± 0.14) x 10^{-4}; $(^{39}Ar/^{37}Ar)_{Ca}$ = 7.86 (± 0.01) x 10^{-4}; (McDougall & Harrison 1999); $(^{40}Ar/^{39}Ar)_K$ = 0.03 (± 0.01). K/Ca = 1.9 x $^{37}Ar/^{39}Ar$.

Sample **SD-534** was placed in a cadmium-lined irradiation canister and irradiated for 40 hours in position 5C of the McMaster University reactor, Hamilton, Ontario. Correction factors for interfering reactions are as follows: $(^{36}Ar/^{37}Ar)_{Ca}$ = 2.54 (± 0.09) x 10^{-4}; $(^{39}Ar/^{37}Ar)_{Ca}$ = 6.51 (± 0.31) x 10^{-4}; (Bottomley & York 1976); $(^{40}Ar/^{39}Ar)_K$ = 0.001 (± 0.001). K/Ca = 1.9 x $^{37}Ar/^{39}Ar$.

After irradiation, the samples were removed from their aluminium irradiation packets, loaded into tin-foil packets, and step-heated in a tantalum resistance furnace. $^{40}Ar/^{39}Ar$ analyses were carried out on a VG3600 mass spectrometer using a Daly photomultiplier detector. Mass discrimination was monitored by analyses of standard air volumes, referenced to a $^{40}Ar/^{36}Ar$ ratio of 295.5.

The reported data have been corrected for system backgrounds, mass discrimination, fluence gradients and atmospheric contamination. The errors on individual age steps for each spectrum are one sigma. Unless otherwise stated, errors associated with the age determinations are two sigma and exclude errors in the J-value, the age of the fluence monitor GA1550 and the uncertainties in the decay constants. Inclusion of all external errors increases the uncertainties to between 0.6 and 0.8% (1σ). Decay constants are those of Steiger & Jager (1977). Data tables for all spectra are provided in the appendix.

1.3.2 Western zone

Sample **GP-UNFOL** was collected from a massive unfoliated amphibolite from Mount Moornambool in the western zone of the Moornambool Metamorphic Complex (Figures 1.3, 1.4). The sample contains the assemblage garnet-amphibole-plagioclase-quartz (Fig 1.5a). Amphibole-plagioclase thermometry (Phillips *et al.* 2002) returned average results of 563˚C (at 6 kbar) and 583˚C (at 8 kbar). Average pressure estimates calculated using THERMOCALC v. 3.0 (Powell & Holland 1994) returned estimates ranging from 7.8 to 8.5 kbar (for a temperature range of 540-580˚C).

Sample **MM-1** is a garnet-mica-quartz schist from Mount Moornambool in the western zone of the Moornambool Metamorphic Complex (Figures 1.3, 1.4, 1.5b). The sample contains the assemblage garnet-biotite-muscovite-plagioclase-quartz. There is minor alteration on the rims of mica grains − this is most pronounced for the biotite. Garnet-biotite thermometry (Phillips *et al.* 2002) yielded average results of 540˚C (at 6 kbar) and 548˚C (at 8 kbar). Average pressure estimates (Phillips *et al.* 2002) calculated using THERMOCALC v. 3.0 (Powell & Holland 1994) range from 7.3 to 8.5 kbar (for a temperature range of 540-580˚C).

Furnace analyses of the amphibole separate **GP-UNFOL** (Fig 1.4a) yielded apparent ages that increase with increasing temperature from ~360 to ~530 Ma. The intermediate temperature steps are concordant and almost fulfil the requirements for an age plateau as defined by McDougall & Harrison (1999). This pseudo-plateau region has a weighted mean age of 503.9 ± 2.2 Ma (49.3% of gas released), which is inferred to approximate the time when the garnet-bearing amphibolites cooled below ~500°C (± 50°C) (McDougall & Harrison 1999). Younger apparent ages obtained from the lowest temperature steps are attributed to alteration-induced argon loss. The older highest temperature result of 527 Ma could reflect minor contamination by excess argon or more retentive diffusion domains possibly coupled with a slower cooling rate.

Furnace analyses of a muscovite separate from sample **MM-1** produced a flat age spectrum (Fig 1.4b) with a weighted mean plateau age of 497.6 ± 1.6 Ma (92.6% of gas released). The concordance of the age spectrum suggests that this is a reliable age for defining when the meta-sedimentary garnet-bearing amphibolite facies rocks cooled below ~350°C ("nominal" closure temperature for muscovite; McDougall & Harrison 1999).

Step heating of a biotite separate from **MM-1** produced a more discordant, 'hump-shaped' age spectrum (Fig 1.4c) with apparent ages ranging from ~340 Ma to ~500 Ma. Similar 'hump-shaped' age spectra have been reported from a number of localities previously, and are usually attributed to the presence of chlorite inter-layers and $^{39}Ar_K$ recoil redistribution during sample irradiation (e.g. Lo & Onstott 1989; Di Vincenzo *et al.* 2003). Di Vincenzo *et al.* (2003) showed that elevated $^{40}Ar/^{39}Ar$ ages associated with intermediate temperature steps from chloritised Antarctic biotite samples are anomalously old. In contrast, higher temperature steps record argon release from larger biotite domains that are less affected by recoil processes and give ages approaching the time of biotite crystallisation (Di Vincenzo *et al.* 2003). Given that the MM-1 biotite sample exhibits minor chlorite alteration, the discordance of the current age spectrum may relate to recoil effects. If correct, then the 'hump' ages of ~500 Ma may be anomalously old, with the highest temperature ages (Mean age = 482.1 ± 5.9 Ma; 95% confidence level; MSWD = 2.1) more closely approximating the time of biotite cooling. Therefore, it is suggested that the MM-1 biotite may have cooled below ~300°C (± 50°C) (McDougall & Harrison 1999) in the interval 480 – 490 Ma. This interpretation is consistent with the hornblende and muscovite results, given expected differences in closure temperatures, and implies regional cooling at ~480-510 Ma.

1.3.3 Eastern zone

SD–534 is a strongly foliated pelite sampled from the hangingwall of the Stawell Fault adjacent to the Stawell Gold Mine (~250 m southwest of the fault; Figures 1.6a, b, 1.7a, b). The sample has a strong composite S_1/S_2 cleavage (the fabrics are sub-parallel) defined by white mica and occasional chlorite grains. A later S_3 crenulation cleavage (note F_3 axis marked on Figures 6a, c) is associated with minor pressure solution (no mica growth). Occasional coarse grained (>100 μm) detrital mica grains were observed in thin section (Fig 6b).

JM-8a is a strongly foliated pelite sampled from the direct footwall of Central Lode in the Stawell Gold Mine (Figures 1.6d, e, 1.7c). The sample contains a strong early mica fabric (S_1) folded into tight F_2 folds associated with an S_2 cleavage (minor mica growth). Only very occasional detrital mica grains were observed in thin section.

ARA-23a is a strongly foliated pelite located in the eastern zone of the Moornambool Metamorphic Complex, southwest of the Stawell pluton (Figures 1.3, 1.6f, 1.8). The sample is located ~ 50 m west of the Coongee Break and occurs in a package of sediments hosting several gold lodes (note Au marked on the drill hole in Fig 1.8). The sample contains a strong mica fabric (S_1) folded into isoclinal F_2 folds associated with an S_2 cleavage (some mica growth) with later S_3 crenulation cleavages associated with minor pressure solution (no mica growth). Only minor detrital mica was observed. The sample also contains D_4 quartz-biotite-chlorite veins that cross-cut the earlier cleavages (Fig 1.6g) with evidence for a pervasive hydrothermal/thermal over print defined by biotite over growing the earlier S_1 and S_2 cleavages (Fig 1.6h). Note that most of the larger late-stage biotite grains were removed during mineral separation (via magnetic separation), but some finer grained biotite would have remained.
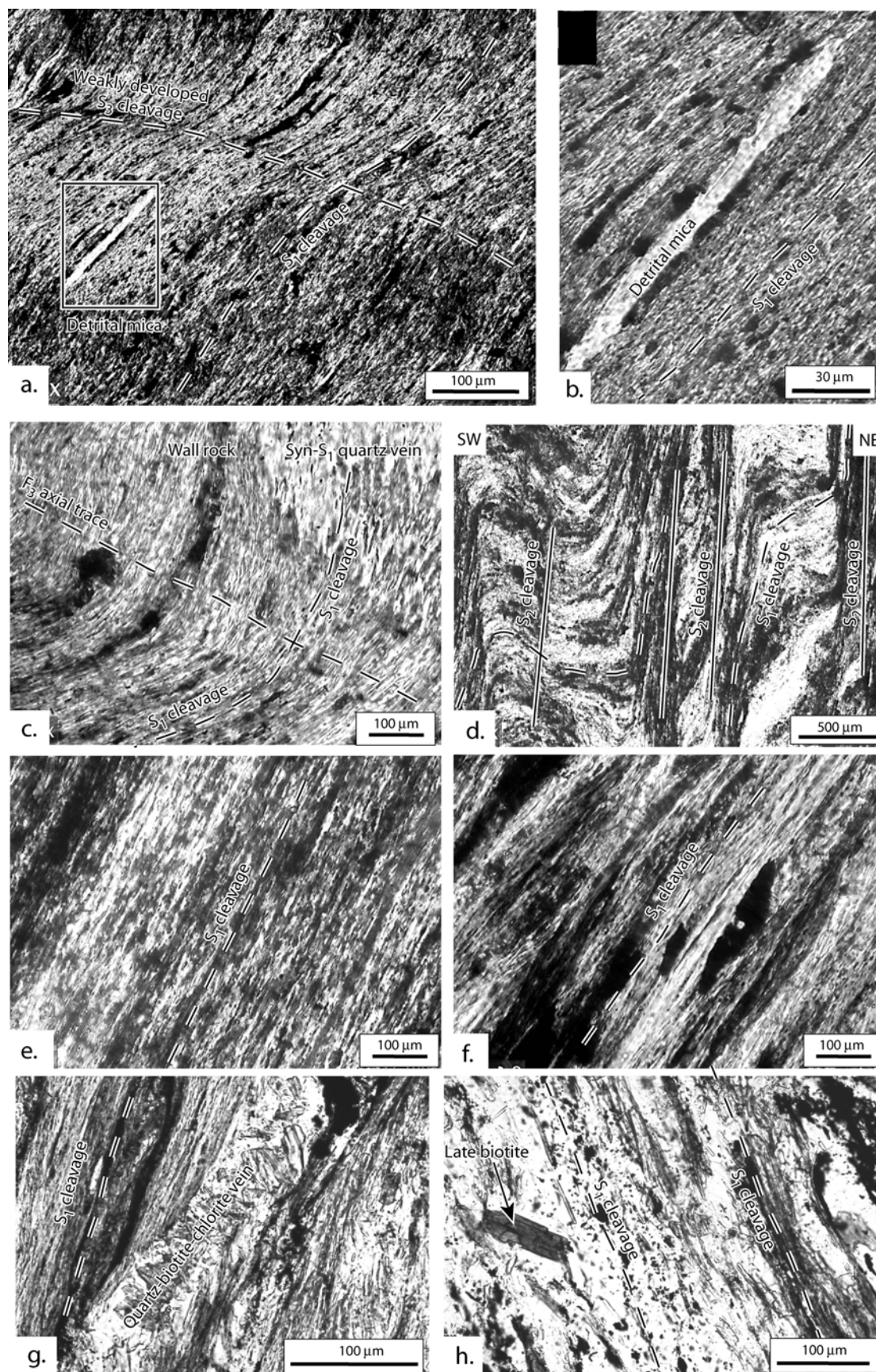
Fig 1.6 (previous page). Photomicrographs of rocks from the eastern zone of the Moornambool Metamorphic Complex. (a) Lower greenschist rock from Stawell with an S_1 cleavage and weak S_3 cleavage. Sample **SD-534**, Cross polarised light. Box marks location of Fig 1.6b. Sample located in Fig 1.7. (b) Detrital mica in lower greenschist rock from Stawell. **Sample SD-534**. Plane polarised light. Sample located in Fig 1.7. (c) Lower

greenschist rock from Stawell with an S_1 cleavage, V_1 vein (containing mica aligned parallel to S_1) and a weak S_3 cleavage. **Sample SD-534**. Plane polarised light. Sample located in Fig 1.7. (d) Lower greenschist rock from Stawell with a strong S_2 crenulation cleavage. Sample **JM-8a**. Plane polarised light. Sample located in Fig 1.7. (e) S_1 cleavage in lower greenschist rock from Stawell. Sample **JM-8a**. Plane polarised light. Sample located in Fig 1.7. (f) S_1 cleavage in lower greenschist facies rock from the direct hangingwall of the Coongee Break. Sample **ARA-23a**. Plane polarised light. Sample located in Fig 1.8. (g) Late (D_4) quartz vein containing biotite, and chlorite overprinting an S_1 cleavage in a lower greenschist facies rock from the direct hangingwall of the Coongee Break. Sample **ARA-23a**. Plane polarised light. Sample located in Fig 1.8. (h) Late biotite overgrowing S_1 cleavage in lower greenschist facies rock from the direct hangingwall of the Coongee Break. Sample **ARA-23a**. Plane polarised light. Sample located in Fig 1.8.
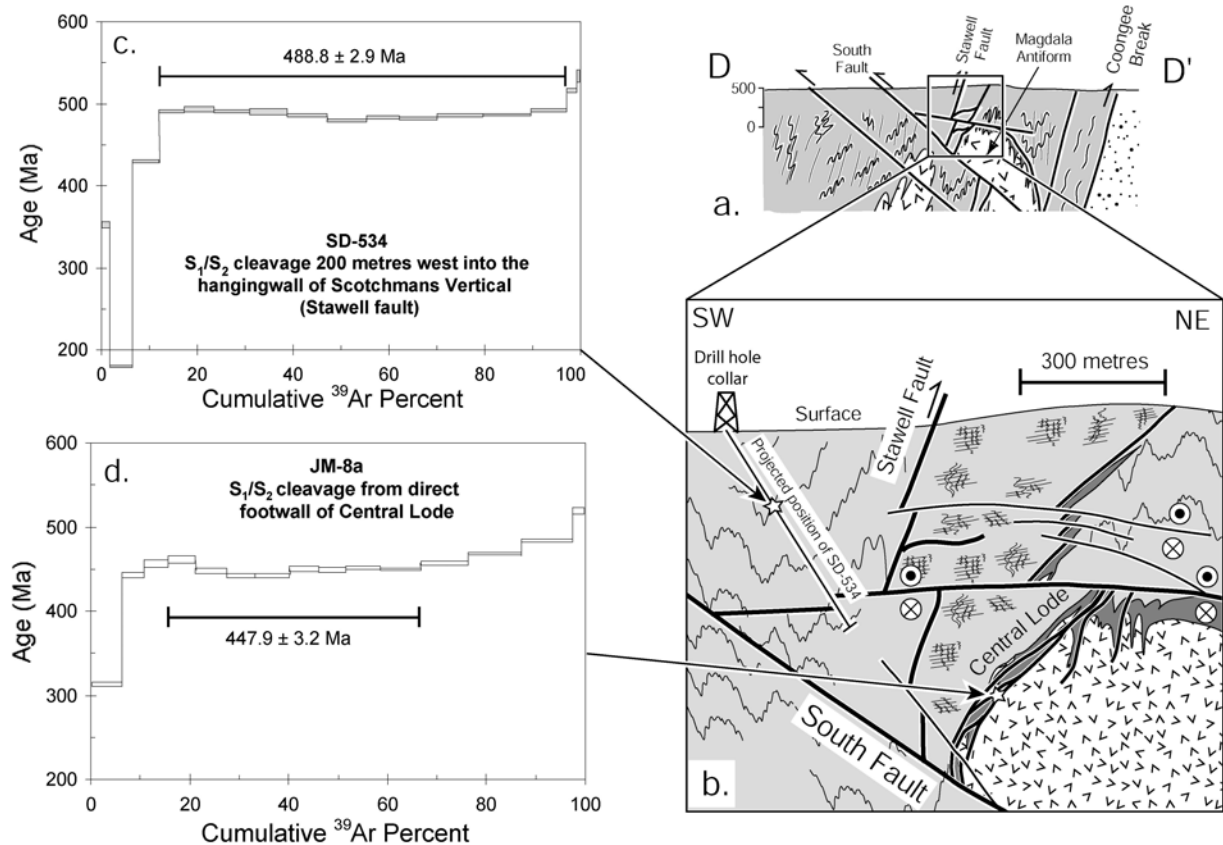
Fig 1.7. ^{40}Ar/^{39}Ar data with structural profile through the Coongee Break south of the Stawell pluton, detail of the Coongee Break highlights sample localities. Section line modified from Miller & Wilson 2002 and references therein. Vertical scale equals horizontal scale. Au symbols correspond to drill hole segments with significant gold values. Errors on age steps are 1σ. Stratigraphic units same as Fig 1.3.
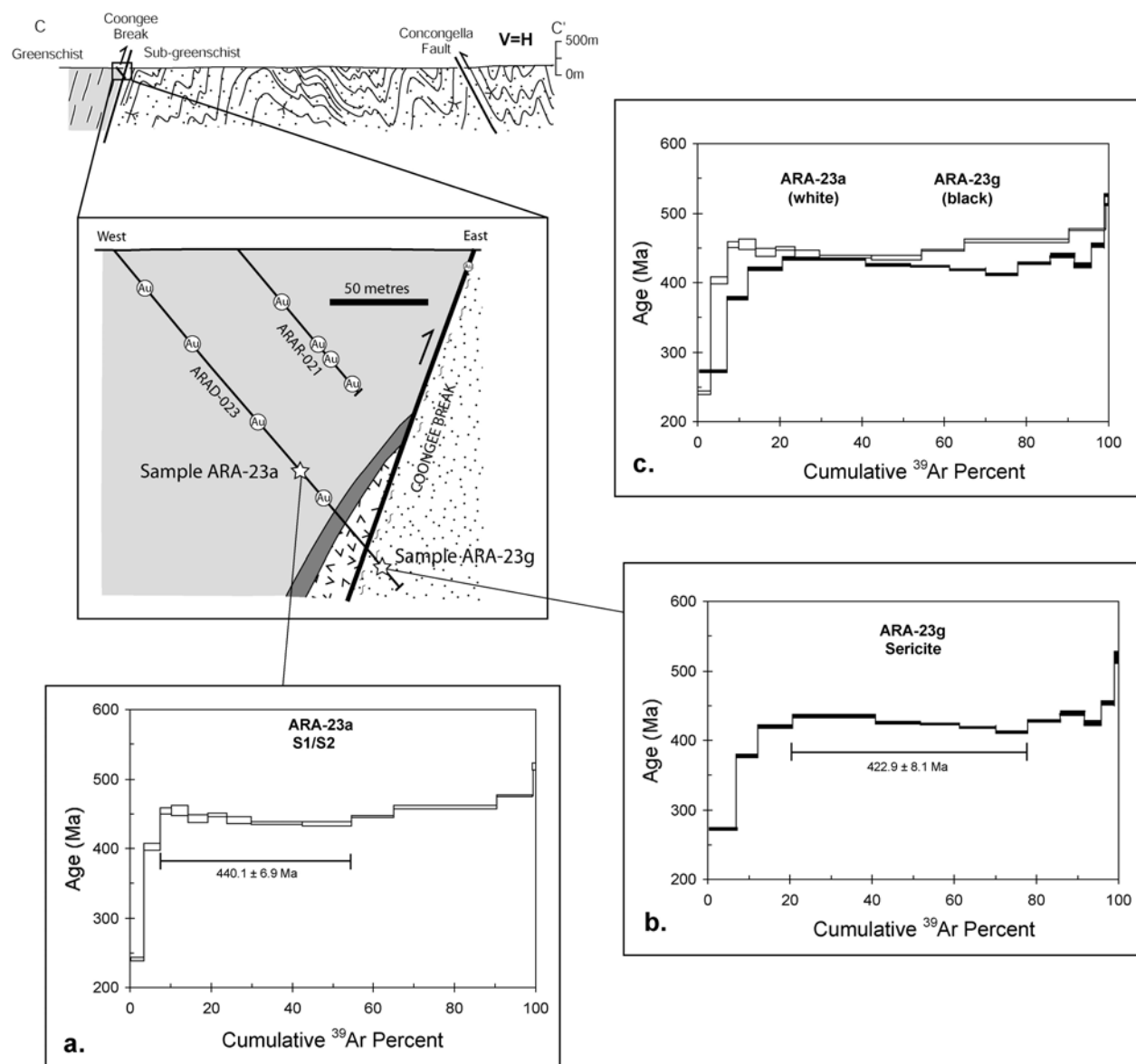
Fig 1.8. (a, b) Profile through the Stawell gold mine, Stawell (modified from Miller & Wilson 2002 and references therein). Stratigraphic units same as Fig 1.3. (c) ^{40}Ar/^{39}Ar spectrum, sample **SD-534** is a pelite 250 m east of the Stawell Fault. Errors on age steps are 1σ. (d) ^{40}Ar/^{39}Ar spectrum, sample **JM-8a** is a pelite in the direct footwall of the Central Lode sampled from the –619 Level of the Stawell Gold Mine. Errors on age steps are 1σ.

ARA-23g is a sample of a shale-rich unit from Cambrian sediments ~ 10 m east of the Coongee Break southwest of the Stawell pluton (Fig 1.8). The sample contains a single cleavage defined by fine-grained white mica; some detrital mica was also observed in thin section. The sample does not show any of the structural complexity observed in **ARA-23a** and is sub-greenschist in grade.

Furnace ^{40}Ar/^{39}Ar analyses of white mica concentrates **SD534, ARA-23a, ARA-23g, and JM-8a** produced sigmoidal-shaped age spectra. This sigmoidal shape is typical of slate samples and is considered to result from a combination of ^{40}Ar loss (low temperature steps), ^{39}Ar recoil redistribution between white mica, quartz, chlorite and defect structures (low and intermediate steps), and release of argon from older mica populations (detrital and/or metamorphic) at higher temperatures (see discussion by Fergusson & Phillips 2001). Recoil

loss of ^{39}Ar from the samples is considered to be a minor factor (<2%), given local metamorphic grades (see Dong *et al.* 1995), the use of aggregated sericite samples, and concordance with other dating results in the region (see below).

Furnace analyses of a white mica concentrate from sample **SD–534** produced the least discordant age spectrum with apparent ages ranging from 182 Ma to 536 Ma (Fig 1.7c). The youngest apparent ages are associated with the lowest temperature heating steps and are probably due to argon loss from low retention sites. Elevated apparent ages at the highest temperature steps are attributed to a minor input from detrital micas. It is suggested that the slight discordance between intermediate temperature steps is due largely to minor recoil redistribution of ^{39}Ar$_K$ between white mica, chlorite and quartz. If correct, then the mean result for these steps may provide the best estimate for the age of this sample. Steps 4 to 14 have a mean age of 488.8 ± 2.9 Ma (95% conf.; 85.1% of gas released, MSWD = 6.3). This age is inferred to represent either the age of metamorphism or a cooling age for the metamorphic mica (see discussion) and is distinctly older than ^{40}Ar/^{39}Ar ages on metamorphic fabrics in the eastern Stawell Zone or Bendigo Zone.

Sample JM-8a produced a sigmoidal age spectrum with apparent ages ranging from 312 Ma to 519 Ma (Fig 1.7d). As above, the elevated high temperature apparent ages are considered to result from the presence of some older metamorphic and/or detrital mica grains. The intermediate temperature steps are again slightly discordant, with a mean age of 447.9 ± 3.2 Ma (95% conf.; 47.2% of ^{39}Ar released; MSWD = 3.4). This age is slightly older then the inferred time of gold mineralization (~440 Ma), possibly due to incomplete overprinting of pre-existing metamorphic micas and/or minor recoil loss of ^{39}Ar$_K$ during sample irradiation.

Furnace analyses on **ARA-23a** produced a sigmoidal age spectrum with apparent ages ranging from 239 Ma to 516 Ma (Fig 8a). The low temperature younger ages are attributed to argon loss, whereas the older higher temperature ages are thought to reflect contamination from coarser grained, older metamorphic and/or detrital micas. If the latter steps are ignored, the remaining intermediate temperature steps average 440.1 ± 6.9 Ma (95% conf.; 47.2% of ^{39}Ar released; MSWD = 5.0). **ARA-23a** is surrounded by gold occurrences (note gold marked on drill hole trace in Fig 1.8) and this age is inferred to approximate the timing of the hydrothermal/thermal over print observed in thin section (D$_4$, Fig 1.6h). This age is indistinguishable from a previous ^{40}Ar/^{39}Ar plateau age of 439 ± 1 Ma, determined on gold-related sericite from the Stawell gold deposit (Foster *et al.* 1998). This result is also in agreement with other ^{40}Ar/^{39}Ar and Re-Os age determinations for regional ~440 Ma gold mineralization in western Victoria (Foster *et al.* 1998; Bierlein *et al.* 2001; Arne *et al.* 2001).

Furnace analyses on **ARA-23g** from east of the Coongee Break (Fig 1.8b) produced a sigmoidal age spectrum with apparent ages ranging from 272 Ma to 519 Ma. The decreasing age gradient defining the lower temperature end of the age spectrum has a mean age of 422.9 ± 8.1 Ma (95% conf.; 57.5% of ^{39}Ar released; MSWD = 20.0).

1.4. Discussion

1.4.1 Interpretation of the new ^{40}Ar/^{39}Ar ages

Two clear ^{40}Ar/^{39}Ar age populations have been delineated from the samples of the Moornambool Metamorphic Complex (Fig 1.9a). The oldest grouping at 505 to 490 Ma is interpreted to represent cooling ages on metamorphic minerals. The younger grouping (450

to 440 Ma) was derived from samples directly adjacent to major fault zones associated with hydrothermal alteration and gold mineralisation (Fig 1.9a). These new data indicate that the metamorphism associated with the Moornambool Metamorphic Complex is part of the Delamerian Fold Belt. The ~ 440 to 450 Ma hydrothermal alteration associated with brittle deformation (Figures 1.7d, 1.8a), and associated orogenic gold mineralisation, is the same as deformation documented throughout most of the Lachlan Fold Belt.

The ^{40}Ar/^{39}Ar age plateaux obtained from experiments on amphibole (504 ± 2 Ma) and muscovite (498 ± 2 Ma) indicate that the rocks in the hangingwall of the Moyston Fault cooled rapidly from ~ 500˚C to below ~350˚C at a rate of about 20 to 30˚C per million years (Fig 1.9b). A previously reported 489 Ma ± 2 Ma (2σ) plateau age on biotite from Stawell (Mapani 1995), the 489 Ma age on **SD-534** (Fig 1.7c) and the age spectrum from sample **MM-1-biotite** (Fig 1.4b) suggests that the rocks cooled below 300˚C somewhere between 490 and 480 Ma. The rapid cooling recorded by ^{40}Ar/^{39}Ar ages on muscovite and amphibole from Mount Moornambool precedes the influx of coarse Ordovician turbidites across the Lachlan Fold Belt by about 10 million years (Fig 1.9b).
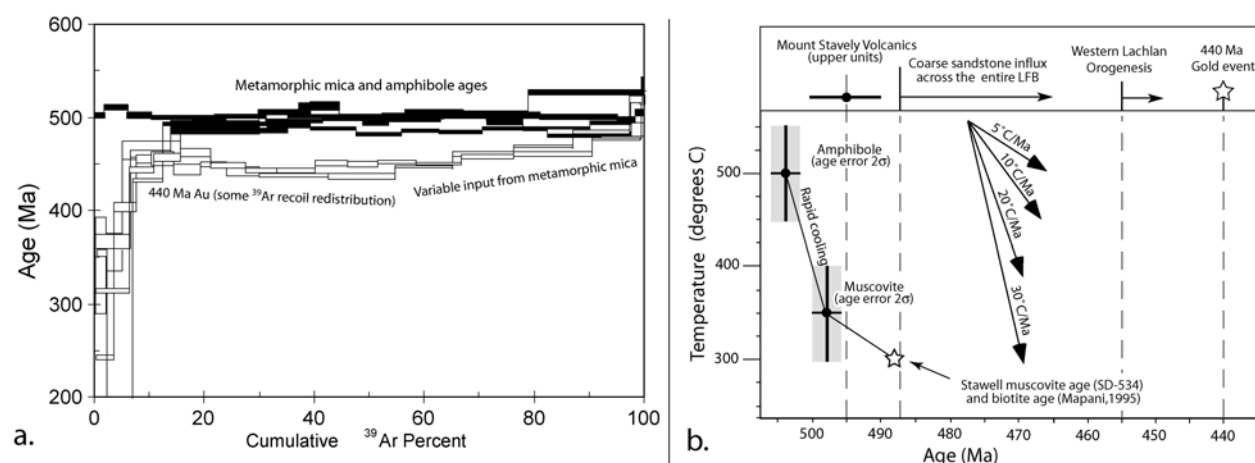
Fig 1.9. (a) All ^{40}Ar/^{39}Ar age spectra from the Moornambool Metamorphic Complex. See text for discussion. (b) Summary of cooling information obtained from ^{40}Ar/^{39}Ar age spectra. Note cooling pre-dates influx of Early Ordovician turbidites (Lancefieldian) into Bendigo-Ballarat Zone of the western Lachlan Fold Belt. Error bars for amphibole and muscovite age data are 2σ. Age of Mount Stavely Volcanics from Stuart-Smith and Black (1999). See text for discussion.

The *ca.* 490 Ma age from **SD-534** is similar to ^{40}Ar/^{39}Ar ages obtained by Wright & Dallmeyer (1991) from Robertson Bay Group slates in an along strike continuation of the Stawell zone rocks into the Ross Orogen of Antarctica (500 to 490 Ma ages; Fig 1.10). The ^{40}Ar/^{39}Ar ages in Antarctica were also interpreted to represent ages of metamorphism. Strong existing structural and stratigraphic correlations between rocks in southeastern Australia and Antarctica (e.g., Flöttman & Kleinschmidt 1993) are now matched by identical ^{40}Ar/^{39}Ar ages on slates from the western boundaries of the Robertson Bay Group and Stawell Zones (Fig 1.10).

The Stawell gold deposit in the eastern zone of the Moornambool is an orogenic gold deposit (Groves *et al.* 1998) and there is a strong link between gold mineralisation and Lachlan-aged orogenesis. This gold mineralisation occurred during D_4 brittle deformation after the D_1, D_2 and D_3 deformations produced ductile S_1, S_2 and S_3 cleavages (Miller & Wilson 2002). The

orogenic gold deposits in the western Lachlan record evidence of supra-lithostatic fluid pressures (Cox 1995) and are associated with extensive alteration halos (Bierlein *et al.* 2000). These deposits are classic examples of mis-oriented faults that require high fluid pressures to reactivate (Sibson & Scott 1998).
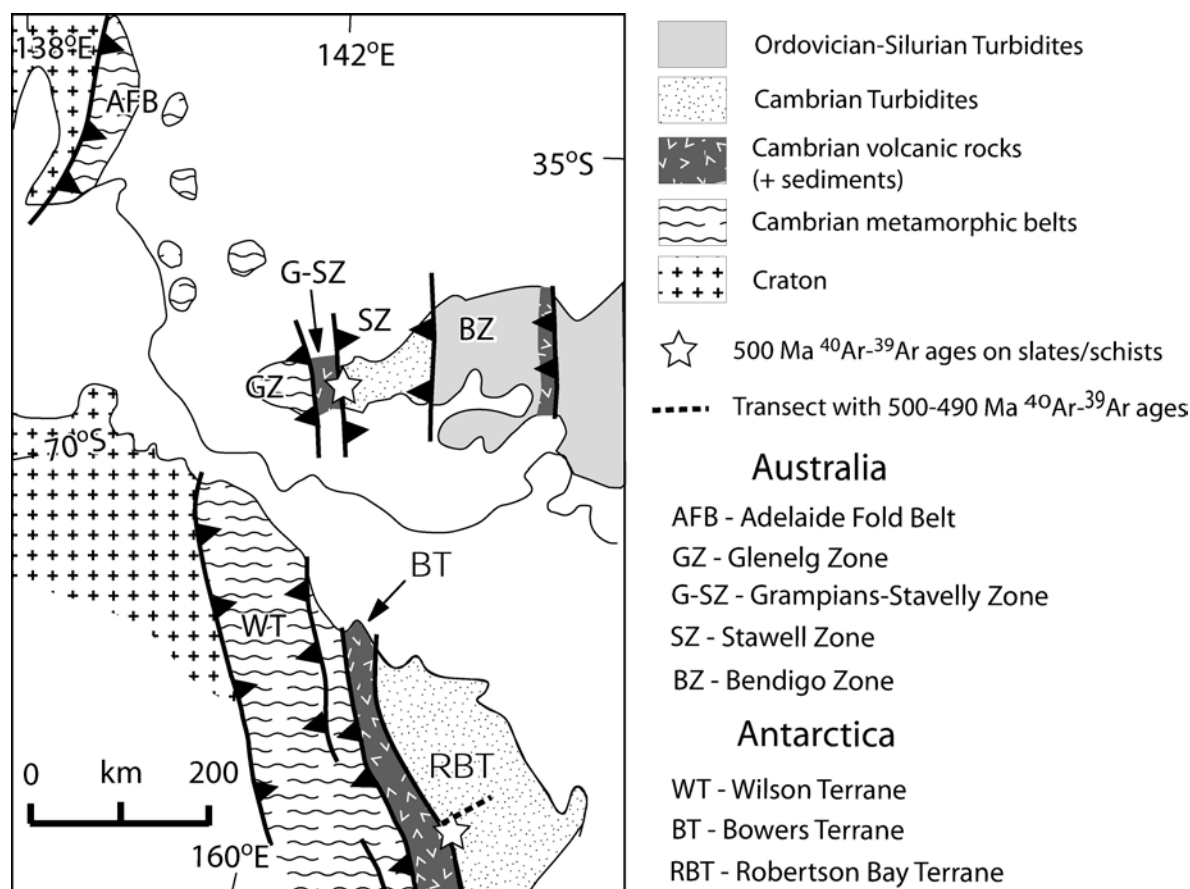
Fig 1.10. Antarctica – Australia correlation (modified from Flöttman & Kleinschmidt 1993). Geochronology in Northern Victoria Land from Wright & Dallmeyer 1991). Note that the Bowers Terrane and Grampian-Stavely Zone that have been correlated have complex magmatic systems, of variable chemistry, which were emplaced over the entire Cambrian time period from ca 530 Ma (Allibone & Wysoczanski 2002) to *ca.* 490 Ma (e.g. VandenBerg *et al.* 2000; Crawford *et al.* 2003b). The full extent of the Proterozoic volcanic rocks (e.g., Direen & Crawford 2003) and related continental fragments (Cayley *et al.* 2002; Crawford *et al.* 2003b) has not been resolved. See text for discussion.

Even though samples **ARA-23a**, and **JM-8a** have micro-structural similarities to **SD-534** (i.e. they contain composite S_1/S_2 fabrics; Figures 1.6a, e, f), the step-heating experiments indicate **ARA-23a**, and **JM-8a** have been thermally or hydrothermally overprinted during late-stage deformation and associated gold lode formation. This is supported by micro-structural evidence from **ARA-23a** that delineates a biotite over growth post the S_1/S_2 fabrics (Fig 1.6h). This sample must have been exposed to a late stage thermal event that locally exceeded the biotite isograd. Major contractional orogenesis in the western Lachlan Fold Belt occurred between 455 and 440 Ma and samples **ARA-23a**, and **JM-8a** are adjacent to gold lodes previously dated at 440 Ma (Foster *et al.* 1998, 1999). Our interpretation is that the samples closest to the lodes (i.e., **ARA-23** and **JM-8a**) were infiltrated by hydrothermal fluids during the late-stage D_4 gold event (in contrast to **SD-534**). Recent work has suggested that

thermally reactivated diffusion is less effective in resetting the ^{40}Ar/^{39}Ar system compared to recrystallisation and/or infiltration of hydrothermal fluids (Maurel *et al.* 2003).

In summary the 440 to 450 ages obtained from samples **ARA-23a**, and **JM-8a** are interpreted to be related to a late-stage short-lived hydrothermal event. The higher temperature steps from the step-heating spectra are inferred to represent an input of inherited argon from incompletely reset Cambrian metamorphic micas (Fig 1.9a) and/or a minor component of detrital mica (e.g., last two steps of Fig 1.7c). The sample furthest away from the gold lodes (**SD-534**) preserves the older metamorphism associated with D$_1$ and D$_2$ deformation (~490 Ma), which occurred at least 40 to 50 million years before mineralisation.

Delineating the exact contribution of detrital mica to a ^{40}Ar/^{39}Ar spectrum is problematic (e.g. Dunlap 1997). An alternate interpretation for the samples dated in the eastern zone could be that the *ca* 490 Ma age calculated from **SD-534** represents a Cambrian detrital age and that the samples with ages of 440 to 450 Ma (**ARA-23a, JM-8a**) just represent greater degrees of out-gassing during the Lachlan Orogeny. In this scenario the newly identified Delamerian metamorphism would be restricted to the western zone of the Moornambool Metamorphic Complex – this is still a major revision to existing tectonic models that argue these rocks cooled in the hangingwall of a major craton-verging thrust during Lachlan orogenesis (Fig 1.2a). However, based on detrital zircon provenance, the rocks to the west of the Coongee Break have been correlated with the Early Cambrian turbidites in the Adelaide Fold Belt (Squire *et al.* 2003), and any detrital mica from the eastern zone of the Moornambool Metamorphic Complex should be 515 Ma or older (not 490 Ma). This is in marked contrast to the rocks east of the Coongee Break where 500 to 600 Ma detrital zircons (Williams *et al.* 1994; Veevers 2000) and 490 to 550 Ma detrital mica grains (Turner *et al.* 1996; Foster et al., 1998) have been previously documented in the Late Cambrian sediments (St Arnaud beds; Fig 1.4). We argue that an alternate interpretation of the *ca* 490 Ma ^{40}Ar/^{39}Ar age on **SD-534** being a Cambrian detrital age is at odds with the existing structural, metamorphic and detrital age data.

1.4.2 Revision of the boundary between the Lachlan and Delamerian Fold Belts

Results from this study indicate that the region between the Yarramyljup Fault and the Coongee Break defines a reworked orogenic zone containing deformation and sedimentation related to both the Delamerian and Lachlan Fold Belts (Fig 1.3). The new ^{40}Ar/^{39}Ar ages highlight that the metamorphism of the rocks defining the Moornambool Metamorphic Complex are Cambrian and thus the Coongee Break potentially defines the current exposed boundary between the Delamerian and Lachlan Fold Belts.

Magnetic and structural trends (lineaments) within the western and eastern Stawell Zone have previously been used to argue the entire Stawell Zone is part of the Delamerian Fold Belt (Glen 1992). These lineaments in the Styawell appear to be truncated by the Avoca Fault (Figures 1.1, 1.3). The folded turbidites to the east of the Avoca Fault are Early Ordovician in age (Figures 1.1, 1.3), which confines any surficial expression of Delamerian deformation to the west of that fault. 490 to 500 Ma detrital zircons and mica grains identified within the eastern Stawell Zone (Williams *et al.* 1994; Veevers 2000; Foster *et al.* 1998) indicate these rocks can only have been deformed by the end-stage of the Delamerian Orogeny (i.e. ~ 490 Ma). Existing ^{40}Ar/^{39}Ar geochronology in the eastern Stawell Zone has focussed on the intra zone faults producing ages consistent with the Lachlan Orogeny (Foster *et al.* 1998). There is currently no age constraint on the folding within the eastern Stawell Zone between the intra-zone faults.

In their Antarctic study of turbidites deformed at low metamorphic grades in the Roberston Bay Terrane Dallmeyer & Wright (1992) produced ^{40}Ar/^{39}Ar ages in the range 500 to 490 Ma across a 70 km wide transect moving east from the contact with the Bowers Group (Fig 1.10). Based on the truncation of the structural trends against the Avoca Fault, and inferring an equivalent width of Late Cambrian deformation in the Stawell Zone to that identified in the along-strike continuation of the system in Antarctica, we argue some of the folding in the eastern Stawell Zone could be Late Cambrian in age. More geochronology needs to be done in the eastern Stawell Zone to assess this.
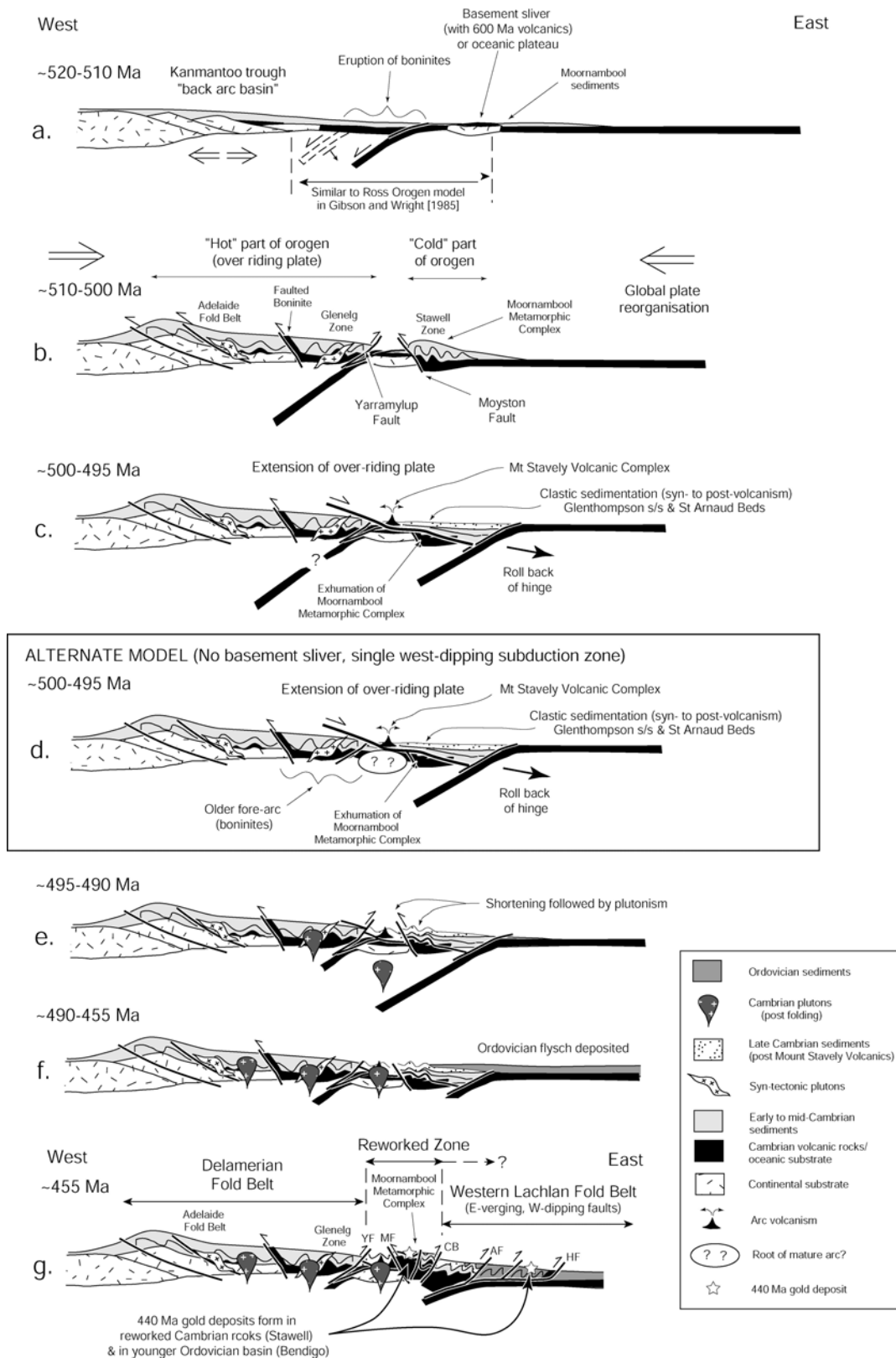
Fig 1.11. Revised geological evolution of the Delamerian and Lachlan Fold Belts, see text for discussion. Fault abbreviations are the same as Fig 1.3.

1.4.3 Revision to the location of world class 440 Ma orogenic gold deposits

Placing the Moornambool Metamorphic Complex into the Delamerian Fold Belt resolves a major problem in structural complexity noted between the two largest 440 Ma primary gold deposits at Bendigo and Stawell (Miller & Wilson 2002; Fig 1.3): the gold-deposits at Stawell within the Moornambool Metamorphic Complex are structurally complex with gold mineralisation occurring very late in the structural evolution (D_4); in contrast some of the Bendigo lodes formed during the first phase of folding in the Bendigo Zone (i.e., D_1). The Ordovician sediments that host the gold lodes at Bendigo were not even deposited until after the cessation of the Cambrian deformation that affected the Moornambool Metamorphic Complex (Stawell). We conclude that the 440 Ma Stawell gold deposit is in a reworked part of the Cambrian Delamerian Fold Belt, while the 440 Ma Bendigo deposit formed in younger Ordovician sequences.

1.4.4 Significance of Moornambool Metamorphic Complex

The western zone of the Moornambool Metamorphic Complex records peak metamorphic conditions of approximately 7-8 kbar, and temperatures of ~540 - 590°C (Phillips *et al.* 2002) and a geothermal gradient of about 25°C/km. At Stawell, in the eastern zone of the complex, some of the metamorphic amphibole cores have a glaucophane-rich composition (Appendix 1 of Wilson *et al.* 1992). In contrast, the metamorphism west of the Grampians-Stavely Zone reflects geothermal gradients substantially above a standard geotherm (e.g., peak metamorphic conditions in the Glenelg Zone are 5.5 kbar and 640°C (Gray *et al.* 2002)) and reflect a geothermal gradient of about 40°C/km. The difference in the geothermal gradients associated with high grade metamorphism between the Glenelg and western region of the Stawell Zone suggest that this region of the Delamerian Fold Belt has a metamorphic field gradient with some similarity to a paired metamorphic belt (high-temperature-low pressure vs lower temperature-higher pressure metamorphic belts e.g. Miyashiro 1973). Whilst the rocks at Stawell are not high-pressure-low-temperature blueschists, as would occur in a paired metamorphic belt, the variation in geothermal gradient is still consistent with a west-dipping subduction zone.

1.4.5 The Delamerian Fold Belt

During the early Cambrian the eastern margin of Gondwana was composed of multiple fragments of continental crust that were relics of the earlier Proterozoic rifting at 600 Ma (e.g., rocks exposed in the Tyennan orogen; Crawford *et al.* 2003b). The Delamerian Fold Belt is typified by craton-verging thrusts and syn-tectonic plutons in the Adelaide Fold Belt and the Glenelg Zone (Jenkins & Sandiford 1992; Gibson & Nihill 1992; Flöttman *et al.* 1994, 1995). Tholeiitic-boninitic-ultramafic rocks within the Grampians-Stavely Zone are inferred to represent an intra-oceanic arc that collided with a continent at about 510 Ma, with most models arguing for eastward (present day coordinates) dipping subduction (Crawford & Berry 1992; Münker & Crawford 2000; VandenBerg *et al.* 2000). West-dipping subduction has, however, also been proposed (Crawford & Keays 1978; Finn *et al.* 1999; Flöttman & Kleinschmidt 1993; Spaggiari *et al.* 2003; Boger & Miller 2004; Foden *et al.* 2004; Foster *et al.* 2005).

The Glenelg, Grampians-Stavely and Stawell Zones have similar stratigraphy, structural relationships (Flöttman & Kleinschmidt 1993) and geophysical properties (Finn *et al.* 1999) to the rocks in Northern Victoria Land. The 500 Ma cooling ages from the western Stawell Zone are the same as $^{40}Ar/^{39}Ar$ ages along the same inferred geological boundary in Northern Victoria Land defined by the western margin of the Robertson Bay Terrane turbidites (Fig 1.10; Wright & Dallmeyer 1991). These marked similarities directly along strike should not

exist if there was a change in the Cambrian subduction polarity from the Ross to Delamerian systems (i.e. west to east-dipping respectively). We argue that for its entire length, the Cambrian subduction zone dipped towards the Gondwana supercontinent (i.e., the same as the models for the Ross Orogen of Weaver *et al.* 1984; Gibson & Wright 1985; Kleinschmidt & Tessensohn 1987; Borg & DePaolo 1991; Rowell *et al.* 1993; Grunow *et al.* 1996; Goodge & Dallmeyer 1996; Goodge 1997). The variations in geothermal gradients in the Delamerian Fold Belt (higher in the west, lower in the east) is also consistent with west-dipping subduction. However, the different Early and Late Cambrian magmatic events preserved are complex and substantial shortening has affected the sequences (Fig 1.3). Furthermore the possible existence of 600 Ma basalts related to continental break up (Direen & Crawford 2003) complicates efforts to correlate units along strike (Fig 1.10), because multiple continental fragments (or ribbons) may have existed (Crawford *et al.* 2003b, also note Ross Orogen model of Goodge & Dallmeyer 1996). In our reconstruction (Fig 1.11) we have assumed Tasmania was an outboard microcontinent and the east-dipping Cambrian subduction preserved in the rock record of the Tyennan Orogen (Crawford *et al.* 2003b) does not correlate along strike with the western Victorian Cambrian system.

The Delamerian Fold Belt could reflect deformation related to the cessation or lock-up of westward-dipping subduction (present day coordinates) due to the accretion of a continental fragment, or alternately an oceanic plateau (Figures 1.11a, b). Accretion of a continental fragment has previously been proposed for the Antarctic Ross Orogen in Northern Victoria Land (Gibson & Wright, 1985), and this mechanism does not require an east-dipping subduction zone. In our model the inferred continental fragment is capped by mafic volcanic rocks (Fig 1.11a) that erupted during *ca.* 600 Ma rifting associated with continental break up (Direen & Crawford 2003). Accretion of continental ribbons has been proposed as a key mechanism driving orogenesis in convergent margins (Lister *et al.* 2001).

An alternate model is that the final consolidation of the Gondwana supercontinent caused a global plate reorganisation that initiated the Delamerian and Ross Orogenies (Boger & Miller 2004). In this model no continental fragment is required to cause the Delamerian orogenesis and the Grampians-Stavely Zone represents an eastward migration of arc-related volcanism and plutonism (Finn *et al.* 1999; Fig 1.11d).

In either of the above scenarios the western part of the system (Adelaide Fold Belt, Glenelg Zone) represents deformation of the hot over-riding plate, whereas the Moornambool Metamorphic Complex reflects metamorphism of rocks that once comprised the colder incoming plate (Figures 1.11a, b). The Early Cambrian basin in the western part of the Delamerian Fold Belt formed in a back-arc basin/region during the initial stage of subduction (Kanmantoo Trough Fig 1.11a). Boninites are unusual in modern settings and are inferred to erupt in the fore-arc region (Crawford *et al.* 1989), this rock type occurs in the Glenelg and Grampians-Stavely Zone and is depicted as erupting in the fore-arc of a retreating Early Cambrian subduction zone (Fig 1.11a).

The Delamerian Yarramjylup and Moyston Faults either formed on the margins of an underlying Proterozoic basement block (and verge towards a "mini-craton"; Fig 1.11b) or alternatively localised on either side of a Late Cambrian arc marked by the presence of the Mount Stavely Volcanic Complex (Fig 1.3). The western boundary of the lithospheric block underlying the Grampians-Stavely Zone defines the eastern-most extent of syn-tectonic plutonism which is controlled by the location of the Early Cambrian basin (Fig 1.11b; Kanmatoo Trough; Flöttman *et al.* 1994, 1995).

The $^{40}Ar/^{39}Ar$ ages on amphibole and muscovite from Mount Moornambool suggest that the observed rapid cooling was either immediately prior to, or synchronous with, the eruption of the Stavely Volcanic rocks (Fig 1.9b). These volcanic rocks have been related to post-collisonal extension (Crawford *et al.* 2003b) and are overlain and inter-layered with Late Cambrian sandstones that are folded and intruded by post-tectonic I-type plutons (VandenBerg *et al.* 2000). The rapid cooling of the Moornambool Metamorphic Complex, the eruption of the Mount Stavely Volcanic Complex, the deposition and deformation of the Late Cambrian sandstones and post-tectonic plutonism, occurred in a very short interval (505 to 490 Ma) (Foster *et al.* 1998; Stuart-Smith & Black 1999; VandenBerg *et al.* 2000; Foden *et al.* 2002a).

Based on correlations with the Tyennan Orogen (Crawford & Berry 1992; Fig 1.1b), the calc-alkaline volcanic rocks within the Mount Stavely Volcanic Complex are inferred to have erupted above a short-lived west-dipping subduction zone following the first phase of Delamerian orogenesis (Fig 1.11c). Two west-dipping subduction zones have previously been proposed to explain the distribution of arc-related rocks and orogenesis within the Ross orogen (Kleinschmidt & Tessensohn 1987). However, if no Proterozoic block exists beneath the Grampians-Stavely Zone then the Mount Stavely Volcanic Complex could have erupted above the same single west-dipping system associated with the Early Cambrian boninites (Fig 1.11d). Irrespective of which model is correct, we relate the rapid cooling and exhumation of the Moornambool Metamorphic Complex to extension that occurred in the overriding plate of a west-dipping subduction zone (Figures 11c, d) due to roll back of the subducting lithospheric slab (Lister *et al.* 2001). This was time equivalent to the eruption of the Mount Stavely Volcanic Complex and with the formation of localised Late Cambrian depocentres (Figures 1.11c, d). Extensional events at *ca.* 500 Ma have already been identified by structural, sedimentological and geochronological studies within the Tyennan Orogen of Tasmania (Hall 1998; Foster *et al.* 2002; Crawford *et al.* 2003b).

Compared to the Moornambool Metamorphic Complex the rocks to the east of the Coongee Break have lower metamorphic grade, less structural complexity (Phillips *et al.* 2002), and distinct detrital zircon provenances (Squire *et al.* 2003). The Late Cambrian turbidites within the eastern Stawell Zone (St Arnaud Beds) are interpreted to represent sediments that were deposited into a syn-orogenic basin deposited over the exhumed metamorphic rocks (Fig 1.11c). We infer that the St Arnaud Beds in the eastern Stawell Zone and the Glenthompson Sandstone in the Grampians-Stavely Zone (Figures 1.3, 1.4) were part of the same depositional system (Fig 1.11c).

The exhumed metamorphic rocks, the overlying Late Cambrian sediments (St Arnaud Beds and Glenthompson Sandstone), and the calc-alkaline volcanic rocks, were then folded prior to the intrusion of Late Cambrian post-tectonic plutons marking the end of the Delamerian Orogeny (Fig 1.11e) (VandenBerg *et al.* 2000). This final stage of Delamerian folding is temporally equivalent to the start of clastic sedimentation into the adjacent basin at about 490 Ma (Fig 1.11f). The current juxtaposition of the sub-greenschist low-grade Cambrian footwall rocks with the amphibolites in the hangingwall of the east-dipping Moyston Fault (and across the Coongee Break) reflects a combination of latest stage Delamerian compression (Fig 1.11e) and later reverse reactivation of the fault during the Lachlan Orogeny (Fig 1.11g). This explains the differences in metamorphism, deformation (Phillips *et al.* 2002), detrital zircon U-Pb ages (Squire *et al.* 2003; Williams *et al.* 1994) and $^{40}Ar/^{39}Ar$ ages across the Coongee Break and the Moyston Fault.

Arc-related magmatism preserved in the eastern sub-province of the Lachlan Fold Belt (Fig 1.1b; Butera *et al.* 2001) indicates that by ~480 Ma subduction had migrated several hundred kilometres to the east, well outboard of the Delamerian system. This is consistent with the $^{40}Ar/^{39}Ar$ cooling ages on post-tectonic A-type plutons that range from 490 to 485 Ma (Turner *et al.* 1996).

1.4.6 The Lachlan Belt

The deformation in the western Lachlan Fold Belt occurred about 40 million years after the Delamerian Orogeny and has a markedly uniform metamorphic grade with dominantly west-dipping faults that verge away from the craton. Unlike the Delamerian Fold Belt, there is little direct evidence that basement blocks controlled the vergence of the fault systems that disrupt the Cambro-Ordovician rocks. The turbidites are folded into tight to isoclinal folds above a low angle décollement, while the volcanic substrate is inferred to have deformed independently via duplexing (Fergusson *et al.* 1986; Cox *et al.* 1991; Gray & Foster 1998). None of the faults have large vertical offsets such as that preserved by the Delamerian Moyston Fault. Thrust-bounded slices of the volcanic substrate preserve evidence of transitional blueschist metamorphism (Spaggiari *et al.* 2002), and the plutonism occurred 40 to 60 million years after the main stage of deformation. The Lachlan orogeny deformed older, colder and denser oceanic crust and the marked change between the Delamerian and Lachlan styles of metamorphism probably reflects the cooling of the underlying volcanic substrate.

The dominant east-vergence of the fault system (Fig 1.11g), combined with transitional blueschist-facies metamorphism, has been used as evidence that the geometry reflects an accretionary wedge that formed due to the under-thrusting of oceanic crust above a subduction zone (Fig 1.2b; Gray & Foster 1998; Foster *et al.* 1999). This subduction is inferred to have closed a small ocean basin inboard, or to the west of, a major convergent margin (Gray & Foster 2000). Alternate models of a doubly-vergent orogen characterised by synchronous craton-verging thrusts (Moyston and Heathcote Faults; Fig 1.2a) are no longer tenable. This is because the metamorphism and marked cooling in the direct hangingwall of the Moyston Fault (e.g. Mount Moornambool; Fig 1.4) is Cambrian and not Ordovician or Silurian as previously inferred. However, the deformation could still be intra-plate in nature (as argued by VandenBerg *et al.* 2000 and Cayley *et al.* 2002) and may have been driven by continental fragments colliding with the Ordovician arc to the east (Squire & Miller 2003).

The Ordovician to Silurian accretionary wedge in the western Lachlan Fold Belt did not deform unlithified terrigenous turbidites recently deposited onto an incoming sediment starved oceanic plate. Instead the sediments were already lithified prior to accretion which resulted in the formation of chevron folds instead of tectonic mélange (Gray & Foster 1998; Gray & Foster 2000).

The major argument against a subduction zone model is the lack of a volcanic arc (O'Halloran *et al.* 1998). Gray and Foster (2000) argued that the actual amount of under-thrust oceanic crust may have been quite small. The identification of Delamerian deformation in the Stawell Zone reduces the dimensions of the Ordovician wedge. How far the Moornambool Metamorphic Complex extends to the east of the Coongee Break beneath the adjacent Late Cambrian sediments is not known. It is debatable if the system was large enough for oceanic lithosphere to be subducted into the asthenosphere and destroyed.

Therefore, it does not match some definitions of a true subduction zone with a Wadati-Benioff zone extending to depths of up to 700 km beneath the Earth's surface.

The western Lachlan orogenesis is contemporaneous with the proposed collision of a seamount or micro-continent with the Early to Late Ordovician arc preserved in the eastern sub-province of the Lachlan Fold Belt (Fig 1.3; Squire & Miller 2003). We argue that this collision triggered under-thrusting of old cold oceanic crust, possibly via slab-pull forces, reactivating the older Cambrian west-dipping subduction zone and resulting in the formation of a small accretionary wedge in the overlying Ordovician sediment pile (Fig 1.11g).

1.5. Conclusions

The revision of the orogenic boundaries in eastern Australia has resolved some geodynamic problems and has led to a simplification in the understanding of the Tasmanide system. The Cambrian Ross and Delamerian systems of Antarctica and Australia are now inferred to be associated with a subduction zone that dipped towards the Gondwanan supercontinent for its entire length (e.g., models of Gibson, 1987; Goodge, 1997; Finn *et al.* 1999; Spaggiari *et al.* 2003; Boger & Miller 2004; Foden *et al.* 2004; Foster *et al.* 2005). The Delamerian Fold Belt in southeastern Australia is typified by craton-verging thrusting that probably post-dates the blocking of a middle Cambrian subduction zone by continental crust, and is time-equivalent to the final consolidation of Gondwana. Arc-related and post-collisional volcanism were a key part of the system. In contrast, the western Lachlan Fold Belt is typified by faults that verge away from the Australian craton with deformation of an older and colder oceanic substrate. The geometry implies that some under-thrusting of the substrate occurred produced an accretionary wedge, although there was no arc-related volcanism.

Delineating orogenic boundaries is particularly difficult when the nature or diagnostic features of an orogen change across strike. In this case the Delamerian system changes from a high geothermal gradient with syn-tectonic plutonism in the west (Glenelg Zone and Adelaide Fold Belt) to lower geothermal gradients with no syn-tectonic plutonism in the east (Moornambool Metamorphic Complex). The eastern segment of the Delamerian Fold Belt was strongly overprinted by the younger Lachlan Orogeny, which produced a reworked orogenic zone.

1.6 Acknowledgements

1.7 References

ALLIBONE A. & WYSOCZANSKI R. 2002. Initiation of magmatism during the Cambrian-Ordovician Ross orogeny in southern Victoria Land. *Geological Society of America Bulletin,* **114**, 1007-1018.

ARNE D.C., BIERLEIN F.P., MCNAUGHTON N., WILSON C.J.L. & MORAND V.J. 1998. Timing of gold mineralization in western and central Victoria, Australia: New constraints from SHRIMP II analysis of zircon grains from felsic intrusive rocks. *Ore Geology Reviews*, **13**, 251-273.

ARNE D.C., BIERLEIN F.P., MORGAN J.W. & STEIN H.J. 2001. Re-Os dating of sulfides associated with gold mineralization in central Victoria. *Economic Geology*, **96**, 1455-1459.

BIERLEIN F.P., ARNE D.C., MCKNIGHT S., LU J., REEVES S., BESANKO J., MAREK J. & COOKE D. 2000. Wallrock petrology and geochemistry in alteration haloes associated with mesothermal gold mineralization, central Victoria, Australia. *Economic Geology*, **95**, 283-312.

BIERLEIN F.P., ARNE D.C., FOSTER D.A. & REYNOLDS P. 2001, A geochronological framework for orogenic gold in central Victoria, Australia. *Mineralium Deposita*, **36**, 741-767.

BIERLEIN F.P., HUGHES M.J., DUNPHY J. & MCKNIGHT S. 2002. Tectonic and economic implications of trace element, $^{40}Ar/^{39}Ar$ and Sm–Nd data from mafic dykes associated with orogenic gold minerals in central Victoria, Australia: reply. *Lithos*, **63**, 119-123.

BOGER S.D. & MILLER J.MCL 2004. Terminal suturing of Gondwana and the onset of the Ross-Delamerian Orogeny: the cause and effect of an Early Cambrian reconfiguration of plate motions. *Earth and Planetary Science Letters*, **219**, 35-48.

BORG S.G. & DEPAOLO D.J. 1991. A tectonic model of the Antarctic Gondwana marginwith implications for southeastern Australia: Isotope and geochemical evidence. *Tectonophysics*, **196**, 339-358.

BOTTOMLEY R.J. & YORK D. 1976. $^{40}Ar-^{39}Ar$ age determinations on the Owyhee basalt of the Columbia Plateau. *Earth and Planetary Science letters*, **31**, 75-88.

BUTERA K. M., WILLIAMS I.S., BLEVIN P.L. & SIMPSON C.J. 2001. Zircon U-Pb dating of Early Palaeozoic monzonitic intrusives from the Goonumbla area, New South Wales. *Australian Journal of Earth Sciences*, **48**, 457-464.

CAS R.A.F. 1983. Palaeogeographic and tectonic development of the Lachlan Fold Belt of southeastern Australia. *Geological Society of Australia Special Publication*, **10**.

CAYLEY R.A. & TAYLOR D.H. 2001. Geological survey report for the Ararat 1:100000 map sheet. *Geological Survey of Victoria Report*, **121**.

CAYLEY R.A., TAYLOR D.H., VANDENBERG A.H.M. & MOORE D.H. 2002. Proterozoic - Early Palaeozoic rocks and the Tyennan Orogeny in central Victoria: the Selwyn Block and its tectonic implications. *Australian Journal of Earth Science*s, **49**, 225-245.

CHAPPELL B.W., WHITE A.J.R. & HINE R. 1988. Granite provinces and basement terranes in the Lachlan Fold Belt, southeastern Australia. *Australian Journal of Earth Sciences*, **35**, 505-521.

COX S.F. 1995. Faulting processes at high fluid pressures: An example of fault valve behaviour from the Wattle Gully Fault, Victoria, Australia. *Journal of Geophysical Research*, **100**, 12841-12859.

COX S.F., ETHERIDGE M.A., CAS R.A.F. & CLIFFORD B.A. 1991. Deformation style of the Castlemaine area, Bendigo-Ballarat Zone: Implications for the evolution of crustal structure in central Victoria. *Australian Journal of Earth Sciences*, **38**, 151-170.

CRAWFORD A. & KEAYS R.R. 1978. Cambrian greenstone belts in Victoria: marginal sea-crust slices in the Lachlan Fold Belt of southeastern Australia. *Earth and Planetary Science Letters*, **41**, 197-208.

CRAWFORD A., FALLOON T.J. & GREEN D.H. 1989. Classification, petrogenesis and tectonic setting of boninites. *In*: CRAWFORD A.J. ed. *Boninites and related rocks*, pp 1-49. Unwin Hyman, London.

CRAWFORD A. & BERRY R.F. 1992. Tectonic implications of Late Proterozoic-Early Palaeozoic igneous rock associations in western Tasmania. *Tectonophysics*, **214**, 37-56.

CRAWFORD A., DONAGHY A.G., BLACK L. & STUART-SMITH P. 1996. Mt. Read correlates in western Victoria: A new exploration opportunity. *Australian Institute of Geoscientists Bulletin*, **20**, 97-102.

CRAWFORD A., CAYLEY R.A., TAYLOR D.H., MORAND V.J., GRAY C.M., KEMP A.I.S., WOHLT K.E., VANDENBERG A.H.M., MOORE D.H, MAHER S., DIREEN N.G., EDWARDS J., DONAGHY A.G., ANDERSON J.A. & BLACK L.P. 2003a. NEOPROTEROZOIC AND CAMBRIAN: CONTINENTAL RIFTING, CONTINENT-ARC COLLISION AND POST-COLLISIONAL MAGMATISM. *In* BIRCH W.D., ed., *Geology of Victoria*. Geological Society of Australia Special Publication, 23, Geological Society of Australia, Victorian Division, p. 73-93.

CRAWFORD A., MEFFRE S. & SYMONDS P.A.. 2003b. Chapter 25 – 120 to 0 Ma tectonic evolution of the southwest Pacific and analogous geological evolution of the 600 to 220 Ma Tasman Fold Belt System in *Evolution and dynamics of the Australian plate,* HILLIS, R.R. & MÜLLER R. D. (eds.), Geological Society of Australia Special Publication **22**, Sydney, 377-397.

DALLMEYER R.D. & WRIGHT T.O. 1992. Diachronous cleavage development in the Robertson Bay terrane, northern Victoria Land, Antarctica: Tectonic implications. *Tectonics*, **11**, 437-448.

DI VINCENZO G., VITI C. & ROCCHO S. 2003. The effect of chlorite interlayering on 40Ar-39Ar biotite dating: an 40Ar-39Ar laser-probe and TEM investigations of variably chloritised biotites. *Contributions to Mineralogy and Petrology*, **145**, 643-658.

DIREEN N.G. & CRAWFORD A.J. 2003. Fossil seaward-dipping reflector sequences preserved in southeastern Australia: a 600 Ma volcanic passive margin in eastern Gondwanaland. *Journal of the Geological Society, London*, **160**, 985-990.

DONG H., HALL C.M., PEACOR D.R. & HALLIDAY A.N. 1995. Mechanisms of argon retention in clays revealed by laser ^{40}Ar-^{39}Ar dating. *Science*, **267**, 355 359.

DUNLAP W.J. 1997. Neocrystallisation or cooling? ^{40}Ar/^{39}Ar ages of white micas from low-grade mylonites. *Chemical Geology*, **143**, 181-203.

FERGUSSON C.L., GRAY D.R. & CAS R.A.F. 1986. Overthrust terranes in the Lachlan Fold Belt, southeastern Australia. *Geology*, **14**, 519-522.

FERGUSSON C.L. & PHILLIPS D. 2001. ^{40}Ar/^{39}Ar and K-Ar age constraints on the timing of regional deformation, south coast of New South Wales, Lachlan Fold Belt: problems and implications. *Australian Journal of Earth Sciences*, **48**, 395-408.

FINN C., MOORE D., DAMAKE D. & MACKEY T. 1999. Aeromagnetic legacy of early Palaeozoic subduction along the Pacific margin of Gondwana. *Geology*, **27**, 1087-1090.

FLÖTTMANN T. & KLEINSCHMIDT G. 1993. Structural continuity of the Ross and Delamerian orogens of Antarctica and Australia along the margin of the palaeo-Pacific. *Geology*, **21**, 319-322.

FLÖTTMANN T., JAMES P., ROGERS J. & JOHNSON T. 1994. Early Palaeozoic foreland thrusting and basin reactivation at the Palaeo-Pacific margin of the southeastern Australian PreCambrian Craton: a reappraisal of the structural evolution of the southern Australian Fold-thrust Belt. *Tectonophysics*, **234**, 95-116.

FLÖTTMANN T., JAMES P., MENPES R., CESARE P., TWINING M., FAIRCLOUGH M., RANDABEL J. & MARSHAK S. 1995. Kangaroo Island, South Australia: strain and kinematic partitioning during Delamerian basin formation and platform reactivation. *Australian Journal of Earth Sciences*, **42**, 35-49.

FLÖTTMANN T., HAINES P., JAGO J., JAMES P., BELPERIO A. & GUM J. 1998. Formation of reactivation of the Cambrian Kanmantoo trough SE Australia: implications for early Palaeozoic tectonics at eastern Gondwana's plate margin. *Journal of the Geological Society, London*, **155**, 101-115.

FODEN J.D., SANDIFORD M., DOUGHERTY-PAGE J. & WILLIAMS I. 1999. The geochemistry and geochronology of the Rathjen Gneiss: implications for the early tectonic evolution of the Delamerian Orogen. *Australian Journal of Earth Sciences*, **46**, 377-389.

FODEN J.D., BURTT A. & TAYLOR D. 2002a. Geology and Tectonic evolution of the Delamerian Fold Belt in Southern Australia and Western Victoria. *Excursion guide A4, Specialist Group in Geochemistry, Mineralogy and Petrology*, 16th Australian Geological Convention, Adelaide, pp. 68.

FODEN J.D., SONG S-H., TURNER S.P., ELBURG M., SMITH P., VAN DER STELDT B. & VAN PENGLIS, 2002b. Geochemical evolution of lithospheric mantle beneath SE South Australia. *Chemical Geology*, **182**, 663-695.

FODEN J.D., ELBURG M.A., DOUGHERTY-PAGE J. & BURTT A. 2004. The timing and duration of the Delamerian orogeny: correlation with the Ross Orogen and implications for Gondwana assembly. Geological Society of Australia, Abtracts 73, 17th Geological convention, Hobart February, 2004, 158.

FOSTER D.A., GRAY D.R. & OFFLER R. 1996. The western sub-province of the Lachlan Fold Belt: Structural style, geochronology, metamorphism and tectonics. *Specialist Group in Geochemistry, Mineralogy, and Petrology Field Guide No. 1, Geological Society of Australia, Sydney.*

FOSTER D.A., GRAY D.R., KWAK T.A.P. & BUCHER M. 1998. Chronology and tectonic framework of turbidite hosted gold deposits in the western Lachlan Fold Belt, Victoria: ^{40}Ar-^{39}Ar results. *Ore Geology Reviews*, **13**, 229-250.

FOSTER D.A., GRAY D.R. & BUCHER M. 1999. Chronology of deformation within the turbidite-dominated, Lachlan orogen: Implications for the tectonic evolution of eastern Australia and Gondwana. *Tectonics*, **18**, 452-485.

FOSTER D.A. & GRAY D.R. 2000a. Evolution and structure of the Lachlan Fold Belt (Orogen) of Eastern Australia. *Annual Reviews of Earth and Planetary Sciences*, **28**, 47-80.

FOSTER D.A. & GRAY D.R. 2000b. Discussion: Timing of orogenic events in the Lachlan Orogen. *Australian Journal of Earth Sciences*, **47**, 813-818.

FOSTER D.A., GRAY D.R., HARTLEY M. & SPAGGIARI C. 2002. Dating metamorphism and exhumation of Forth Metamorphic Complex, Tasmania with implications for Paleozoic Tectonics of the East Gondwana Margin. *Geoscience 2002: Expanding Horizons*, 16th Australian Geological Convention, Adelaide, p. 116.

FOSTER D.A., GRAY D.R. & SPAGGIARI C. 2005. Timing of subduction and exhumation along the Cambrian East Gondwana margin, and the formation of Paleozoic backarc basins. *Geological Society of America Bulletin* **117**.

GIBSON G.M. 1987. Metamorphism and deformation in the Bowers Supergroup: implications for terrane accretion in Northern Victoria Land, Antarctica. In: Terrane accretion and orogenic belts, LEITCH E.C. & SCHEIBNER E., eds., Geodynamic Series, American Geophysical Union **19**, 207-219.

GIBSON G.M. & WRIGHT T.O. 1985. Importance of thrust faulting in the tectonic development of northern Victoria Land, Antartica. *Nature*, **315**, 480-483.

GIBSON G.M. & NIHILL D.N. 1992. Glenelg River Complex: western margin of the Lachlan Fold Belt or extension of the Delamerian Orogen into western Victoria. *Tectonophysics*, **214**, 69-91.

GLEN R.A. 1992. Thrust, extensional and strike-slip tectonics in an evolving Palaeozoic orogen - a structural synthesis of the Lachlan Orogen of southeastern Australia. *Tectonophysics*, **214**, 341-380.

GLEN R.A., WALSHE J.L., BARRON L.M. & WATKINS J.J. 1998. Ordovician convergent-margin volcanism and tectonism in the Lachlan sector of east Gondwana. *Geology*, **26**, 751-754.

GOODGE J.W. 1997. Latest Neoproterozoic basin inversion of the Beardmore Group, central Transantarctic Mountains, Antarctica. *Tectonics*, **16**, 682-701.

GOODGE J.W. & DALLMEYER R.D. 1996. Contrasting thermal evolution within the Ross Orogen, Antarctica: Evidence from mineral $^{40}Ar/^{39}Ar$ ages. *Journal of Geology*, **104**, 435-458.

GRAEBER F.M., HOUSEMAN G.A. & GREENHALGH S. 2002. Regional teleseismic tomography of the western Lachlan Orogen and the Newer Volcanic Province, southeast Australia. *Geophysical Journal International*, **149**, 249–267.

GRAY D.R., GREGORY R.T. & DURNEY D.W. 1991. Rock buffered fluid-rock interaction in deformed quartz-rich turbidite sequences, southeastern Australia. *Journal of Geophysical Research*, **96**, 19681-19704.

GRAY D.R. & FOSTER D.A. 1998. Character and kinematics of faults within the turbidite-dominated Lachlan Orogen: implications for tectonic evolution of eastern Australia. *Journal of Structural Geology*, **20**, 1691-1720.

GRAY D.R. & FOSTER D.A. 2000. Character and kinematics of faults within the turbidite-dominated Lachlan Orogen: implications for tectonic evolution of eastern Australia: Reply. *Journal of Structural Geology*, **22**, 529-535.

GRAY D.R. & FOSTER D.A. 2001. Character and kinematics of faults within the turbidite-dominated Lachlan Orogen: implications for tectonic evolution of eastern Australia: Reply. *Journal of Structural Geology*, **23**, 145-147.

GRAY C.M., KEMP A.I.S., ANDERSON J.A.C., BUSHELL D.J., FERGUSSON D.J., FITZHERBERT J. & STEVENSON M.D. 2002. Delamerian Glenelg tectonic zone, western Victoria: geology and metamorphism of stratiform rocks. *Australian Journal of Earth Sciences*, **49**, 187-200.

GROVES D.I., GOLDFARB R.J., GEBRE-MARIAM M., HAGEMANN S.G., & ROBERT F. 1998. Orogenic gold deposits: A proposed classification in the context of their crustal distribution and relationship to other gold deposit types. *Ore Geology Reviews*, **13**, 7-27.

GRUNOW A., HANSON R. & WILSON T. 1996. Were aspects of Pan-African deformation linked to Iapetus opening? *Geology*, **24**, 1063-1066.

HAINES P.W. & FLÖTTMAN T. 1998. The Delamerian Orogeny and potential foreland sedimentation : A review of age and stratigraphic constraints. *Australian Journal of Earth Sciences*, **45**, 559-57.

HALL M. 1998. The Structural History of Northern Tasmania and the Bass Strait Connection. In FINDLAYSON, D.M. & JONES, L.E.A., Mineral Systems and the Crust and Upper Mantle of Southeast Australia, *AGSO Record* **1998/2**, 93-97.

HANDLER M.R. & BENNETT V.C. 2001. Constraining continental structure by integrating Os isotopic ages of lithospheric mantle with geophysical and crustal data: an example from southeastern Australia. *Tectonics*, **20**, 177–188.

JENKINS J.F. & SANDIFORD M. 1992. Observations on the tectonic evolution of the southern Adelaide Fold Belt. *Tectonophysics*, **214**, 27-36.

KLEINSCHMIDT G. & TESSENSOHN F. 1987. Early Paleozoic westward directed subduction at the Pacific margin of Antarctica, in: Gondwana six: structure, tectonics, and Geophysics, G.D. MCKENZIE, ed., pp. 89-105, *American Geophysical Union*, Washington, D.C..

KORSCH R.J., BARTON T.J., GRAY D.R., OWEN A.J. & FOSTER D.A. 2002. Geological interpretation of a deep seismic-reflection transect across the boundary between the Delamerian and Lachlan Orogens, in the vicinity of the Grampians, western Victoria. *Australian Journal of Earth Sciences*, **49**, 1057-1075.

LISTER G.S. 2001. Character and kinematics of faults within the turbidite-dominated Lachlan Orogen: implications for tectonic evolution of eastern Australia: Discussion. *Journal of Structural Geology*, **23**, 143-144.

LISTER G.S., FORSTER M.A. & RAWLING T.J. 2001. Episodicity during orogenesis. In: MILLER, J.A., HOLDSWORTH, R.E., BUICK, I.S., & HAND, M. (eds) *Continental Reactivation and Reworking*. Geological Society, London, Special Publications, **184**, 89-113.

LO C-H. & ONSTOTT T.C. 1989. ^{39}Ar recoil artefacts in chloritised biotite. *Geochimica et Cosmochimica Acta*, **53**, 2697-2711.

MAPANI B.S.E. 1995. Structural evolution and gold mineralisation at the Magdala gold mine, Stawell, western Victoria, unpublished PhD thesis, University of Melbourne, Victoria.

MAUREL O., MONIÉ P., RESPAUT J.P., LEYRELOUP A.F. & MALUSKI H. 2003. Pre-metamorphic $^{40}Ar/^{39}Ar$ ages in HP metagranitoids from the Hercynian belt (france). *Chemical Geology*, **193**, 195-214.

McDougall I. & Harrison T.M. 1999. Geochronology and thermochronology by the ^{40}Ar/^{39}Ar method. Second Edition. Oxford Univ. Press, New York.

Meert J.G. 2003. A synopsis of events related to the assembly of eastern Gondwana. *Tectonophysics*, **362**, 1-40.

Miller J.McL., Dugdale L.J. & Wilson C.J.L. 2001. Variable hangingwall palaeotransport during Silurian and Devonian thrusting in the Lachlan Fold Belt – missing gold lodes, synchronous Melbourne Trough sedimentation and Grampians Group fold interference. *Australian Journal of Earth Sciences*, **48**, 901-909.

Miller J.McL. & Wilson C.J.L. 2002. The Magdala Lode System, Stawell, southeastern Australia: structural style and relationship to gold mineralisation across the western Lachlan Fold Belt. *Economic Geology*, **97**, 325-349.

Miller J.McL., Norvick M.S. & Wilson C.J.L. 2002. Basement controls on rifting and the associated formation of ocean transform faults—Cretaceous continental extension of the southern margin of Australia. *Tectonophysics*, **359**, 131-155.

Miyashiro A. 1973. Metamorphism and metamorphic Belts. Allen and Unwin, London, 492pp.

Münker C. & Crawford A.J. 2000. Cambrian arc evolution along the SE Gondwana active margin: A synthesis from Tasmania-New Zealand-Australia-Antarctica correlations. *Tectonics*, **19**, 415-432.

Offler R.L., McKnight S. & Morand V. 1998. Tectonothermal history of the western Lachlan Fold Belt: Insights from white mica studies. *Journal of Metamorphic Geology*, **16**, 531-540.

O'Halloran G. J., Bryan S.E., Cayley R.A., Taylor D.H., Soesoo A., Bons P.D., Gray D.R. & Foster D.A. 1998. Divergent double subduction:Tectonic and petrologic consequences: Comment and Reply. *Geology*, **26**, 1051–1054.

Phillips G., Miller J.McL. & Wilson C.J.L. 2002. Structural and metamorphic evolution of the Moornambool Metamorphic Complex, western Lachlan Fold Belt, southeastern Australia. *Australian Journal of Earth Sciences*, **49**, 891-913.

Powell R. & Holland T. 1994. Optimal geothermometry and geobarometry. *American Mineralogist*, **79**, 120-133.

Preiss W.V. 2000. The Adelaide Geosyncline of South Australia and its significance in Neoproterozoic continental reconstruction. *Precambrian Research*, **100**, 21-63.

Price R.C., Gray C.M. & Frey F.A. 1997. Strontium and isotopic and trace element heterogeneity in the plains basalts of the Newer Volcanic province, Victoria, Australia. *Geochimica et Cosmochimica Acta*, **61**, 171–192.

Renne P., Swisher C.C., Deino A.L., Karner D.B.V., Owens T.L. & DePaolo D.J. 1998. Intercalibration of standards, absolute ages and uncertainties in ^{40}Ar/^{39}Ar dating. *Chemical Geology*, **145**, 117-152.

Rowell A.J., Rees M.N., Duebendorfer E.M., Wallin E.T., Van Schmus W.R. & Smith E.I. 1993. An active Neoproterozoic margin: evidence from the Skelton Glacier area, Transantarctic Mountains. *Journal of the Geological Society, London*, **150**, 677-682.

Sherlock S.C. 2001. Two-stage erosion and deposition in a continental margin setting: an ^{40}Ar/^{39}Ar laser probe study of offshore detrital white micas in the Norwegian sea. *Journal of the Geological Society, London*, **158**, 793-799.

Sibson R.H. & Scott J. 1998. Stress/fault controls on the containment and release of overpressured fluids: Examples from gold-quartz vein systems in Juneau, Alaska; Victoria, Australia and Otago, New Zealand. *Ore Geology Reviews*, **13**, 293-306.

Spaggiari C.V., Gray D.R. & Foster D.A. 2003. Tethyan_ and Cordilleran-type ophiolites of eastern Australia: implications for the evolution of the Tasmanides. In Dilek Y. & Robinson P.T. (eds) *Ophiolites in Earth History*. Geological Society, London, Special Publications, **218**, 517-539.

Squire R. & Miller J.McL. 2003. Synchronous compression and extension in East Gondwana: tectonic controls on world class gold deposits at 440 Ma. *Geology*, **31**, 1073-1076.

Squire R., Campbell I.H., Allen C., Wilson C.J.L. 2003. U-Pb in detrital-zircon LA-ICP-MS age dating of early Palaeozoic sandstones from the Lachlan Orogen: sediment provinces and implications for tectonic evolution. In: Reddy, S.M., Fitzsimmons, I.C.W. & Collins, A.S., eds.. SGTSG Field Meeting Kalbarri, 22-26 September 2003, *Geological Society of Australia Abstracts*, **72**, 72 p.

Steiger R.H. & Jager E. 1977. Subcommission on geochronology: Convention on the use of decay constants in geo- and cosmochronology. *Earth and Planetary Science Letters*, **36**, 359-362.

Stuart-Smith P.G. & Black L.P. 1999. Willaura sheet 7422, Victoria 1:100000 map geological report. *Australian Geological Survey Organisation Record*, **1999/38**.

Taylor D.H. & Cayley R.A. 2000. Character and kinematics of faults within the turbidite-dominated Lachlan Orogen: implications for tectonic evolution of eastern Australia: Discussion. *Journal of Structural Geology*, **22**, 523-528.

TAYLOR D.H. & CAYLEY R.A. 2002. Tectonic and economic implications of trace element, ^{40}Ar/^{39}Ar and Sm–Nd data from mafic dykes associated with orogenic gold minerals in central Victoria, Australia: comment. *Lithos*, **63**, 115-118.

TETLEY N., MCDOUGALL I. & HEYDEGGER H.R. 1980. Thermal neutron interferences in the ^{40}Ar/^{39}Ar dating technique. *Journal of Geophysical Research*, **85**, 7201-7205.

TURNER S.P., KELLEY S.P., VANDENBERG A.H.M., FODEN J.D. & SANDIFORD M. 1996. Source of the Lachlan Fold Belt flysch linked to convective removal of the lithospheric mantle and rapid exhumation of the Delamerian-Ross fold belt. *Geology*, **24**, 941-944.

VANDENBERG A.H.M. 2000. Reply: Timing of orogenic events in the Lachlan Orogen. *Australian Journal of Earth Sciences*, **47**, 818-822.

VANDENBERG A.H.M., WILLMAN C.E., MAHER S., SIMONS B.A., CAYLEY R.A., TAYLOR D.H., MORAND V.J., MOORE D.H. & RADOJKOVIC A. 2000. The Tasman Fold Belt System in Victoria, *Geological Survey of Victoria Special Publication*, pp. 462.

VEEVERS J.J. 2000. Chapter 17 Antarctic Beardmore-Ross and Mirny Provences saturate Paleozoic-Mesozoic east Gondwanaland with 0.6 – 0.5 Ga zircons. In: VEEVERS, J.J. ed., *Billion-year earth history of Australia and neighbours in Gondwanaland*. Gemoc Press, Sydney, 110-130

WEAVER S.D., BRADSHAW J.D. & LAIRD M.G. 1984. Geochemistry of Cambrian volcanics of the Bowers Group and implications for early Paleozoic tectonic evolution of northern Victoria Land, Antarcti*ca. Earth and Planetary Science Letters*, **68**, 128-140.

WILLIAMS I.S., CHAPPELL B.W., CROOK K.A.W. & NICOLL R.S. 1994. In search of the Early Palaeozoic flysch in the Lachlan Fold belt, southeastern Australia. *Geological Society of Australia Abstracts* **37**, 464.

WILSON C.J.L, WILL T.M., CAYLEY R.A. & CHEN S. 1992. Geological framework and tectonic evolution in western Victoria, Australia. *Tectonophysics*, **214**, 93-127.

WRIGHT T.O. & DALLMEYER R.D. 1991. The age of cleavage development in the Ross orogen, northern Victoria Land, Antarctica: evidence from ^{40}Ar/^{39}Ar whole-rock slate ages. *Journal of Structural Geology*, **13**, 677-690.

⁴⁰Ar/³⁹Ar data files for Chapter 1

GPUNFOL (amphibole), GR 6597 586604 AGD66, mass = 3.33 mg, J-value = 0.0098241 ± 0.0000491

Temp (C)	Cumulative ^{39}Ar(%)	^{40}Ar/^{39}Ar	^{37}Ar/^{39}Ar	^{36}Ar/^{39}Ar	Vol. ^{39}Ar x 10^{-15} mol	%Rad. ^{40}Ar	Ca/K	^{40}Ar*/^{39}Ar	Age (Ma)	±1σ (Ma)
800	6.3	28.94	4.5066	0.0226	1.36	78.40	8.59	22.78	364.39	7.74
900	13.7	30.96	14.5113	0.0109	1.60	94.30	27.90	29.54	459.66	3.57
980	29.8	32.39	14.9716	0.0089	3.52	96.60	28.80	31.66	488.59	6.58
1010	37.2	33.34	14.6159	0.0079	1.59	97.40	28.10	32.85	504.54	2.38
1030	39.4	35.76	14.2474	0.0149	0.48	91.80	27.40	33.17	508.93	5.99
1070	44.5	33.68	14.5878	0.0075	1.12	97.80	28.10	33.35	511.25	3.90
1100	56.8	32.95	14.4098	0.0081	2.66	97.20	27.70	32.39	498.46	2.73
1130	67.3	33.29	14.3889	0.0078	2.30	97.50	27.70	32.83	504.27	2.59
1170	79.2	33.31	14.4250	0.0080	2.57	97.30	27.70	32.77	503.57	2.05
1450	100.0	40.73	13.1041	0.0267	4.52	83.90	25.20	34.51	526.70	2.71
Total		335.34	133.7683	0.1233	21.70			32.09	494.39	3.74

MM-1 (muscovite), GR 6600 58605 AGD66, mass = 0.56 mg, J-value = 0.0097560 ± 0.0000488

Temp (C)	Cumulative ^{39}Ar(%)	^{40}Ar/^{39}Ar	^{37}Ar/^{39}Ar	^{36}Ar/^{39}Ar	Vol. ^{39}Ar x 10^{-15} mol	%Rad. ^{40}Ar	Ca/K	^{40}Ar*/^{39}Ar	Age (Ma)	±1σ (Ma)
600	1.6	36.03	0.0137	0.0108	1.84	91.10	0.03	32.82	501.11	2.60
700	6.0	34.87	0.0301	0.0044	4.89	96.20	0.06	33.54	510.66	2.18
750	10.2	33.91	0.0330	0.0038	4.82	96.60	0.06	32.77	500.51	2.84
780	21.8	33.98	0.0291	0.0045	13.10	96.00	0.06	32.62	498.47	1.94
810	31.2	33.68	0.0261	0.0031	10.63	97.20	0.05	32.71	499.64	2.18
840	41.4	33.11	0.0291	0.0025	11.58	97.70	0.06	32.36	494.99	1.95
870	48.9	33.32	0.0412	0.0027	8.45	97.50	0.08	32.50	496.92	2.31
900	53.7	33.17	0.0114	0.0029	5.42	97.30	0.02	32.29	493.99	3.13
950	63.2	33.46	0.0258	0.0032	10.71	97.10	0.05	32.48	496.64	2.44
1000	81.2	33.44	0.0202	0.0021	20.42	98.10	0.04	32.80	500.85	3.01
1050	95.4	33.25	0.0307	0.0020	16.05	98.20	0.06	32.65	498.88	2.33
1100	98.6	33.50	0.0865	0.0035	3.57	96.80	0.16	32.43	495.95	2.72
1150	100.0	34.66	0.0643	0.0053	1.60	95.40	0.12	33.08	504.58	3.11
Total		440.39	0.4414	0.0508	113.07			32.65	498.87	2.44

MM-1 (biotite), GR 6600 58605 AGD66, mass = 0.48 mg, J-value = 0.0097560 ± 0.0000488

Temp (C)	Cumulative ^{39}Ar(%)	^{40}Ar/^{39}Ar	^{37}Ar/^{39}Ar	^{36}Ar/^{39}Ar	Vol. ^{39}Ar x 10^{-15} mol	%Rad. ^{40}Ar	Ca/K	^{40}Ar*/^{39}Ar	Age (Ma)	±1σ (Ma)
550	1.8	449.56	1.6348	1.4504	1.37	4.70	3.11	21.18	338.80	51.30
600	5.0	185.01	0.7677	0.5512	2.34	12.00	1.46	22.16	353.09	19.71
650	15.5	99.51	0.3087	0.2352	7.88	30.10	0.59	29.99	462.96	9.60
700	35.0	37.06	0.1584	0.0186	14.54	85.10	0.30	31.55	484.12	2.50
730	52.1	33.79	0.1267	0.0037	12.81	96.70	0.24	32.69	499.32	1.95
760	63.5	33.33	0.1043	0.0020	8.54	98.20	0.20	32.73	499.88	2.87
800	71.3	33.35	0.1659	0.0018	5.78	98.30	0.32	32.81	500.93	2.68
850	77.9	32.93	0.1663	0.0022	4.98	98.00	0.32	32.26	493.69	2.51
900	82.3	32.66	0.1763	0.0033	3.27	97.00	0.34	31.68	485.80	2.05
980	92.0	32.13	0.1302	0.0033	7.25	96.90	0.25	31.15	478.74	2.29
1050	97.6	32.54	0.1034	0.0043	4.15	96.10	0.20	31.26	480.16	2.51
1150	100.0	34.59	0.3472	0.0100	1.82	91.50	0.66	31.67	485.68	7.58
Total		1036.47	4.1900	2.2861	74.73			31.33	481.12	4.73

ARA-23a (sericite), mass = 1.81 mg, J-value = 0.0098585 ± 0.0000493

Drill hole ARAD-23 drill hole collar GR 6675 58792 AGD66, sample 146 metres down hole

Temp (C)	Cumulative ^{39}Ar(%)	^{40}Ar/^{39}Ar	^{37}Ar/^{39}Ar	^{36}Ar/^{39}Ar	Vol. ^{39}Ar x 10^{-15} mol	%Rad. ^{40}Ar	Ca/K	^{40}Ar*/^{39}Ar	Age (Ma)	±1σ (Ma)
500	3.2	15.07	0.0254	0.0023	3.22	95.30	0.05	14.36	238.79	2.31
525	7.3	25.84	0.0229	0.0020	4.04	97.70	0.04	25.23	400.77	4.73
550	10.0	29.35	0.0277	0.0014	2.70	98.50	0.05	28.92	452.46	4.00
575	14.1	29.25	0.0155	0.0009	4.10	99.00	0.03	28.96	453.12	7.43
600	19.1	28.21	0.0115	0.0002	4.97	99.70	0.02	28.11	441.33	5.45
625	23.7	28.71	0.0151	0.0006	4.64	99.30	0.03	28.52	446.93	2.70
650	29.7	28.19	0.0208	0.0007	6.04	99.20	0.04	27.97	439.28	5.26
700	42.2	27.81	0.0069	0.0004	12.49	99.40	0.01	27.65	434.91	2.06
750	54.5	27.71	0.0159	0.0004	12.26	99.50	0.03	27.57	433.74	2.92
800	64.9	28.40	0.0060	0.0003	10.34	99.60	0.01	28.32	444.15	1.34
900	90.5	29.37	0.0067	0.0000	25.59	99.90	0.01	29.33	458.24	2.46
1000	99.2	30.58	0.0132	0.0001	8.67	99.80	0.03	30.52	474.50	1.70
1200	100.0	36.25	0.2190	0.0089	0.84	92.70	0.42	33.62	516.38	4.93
Total		364.74	0.4067	0.0183	99.89			28.08	440.92	2.97

ARA-23g (sericite), mass = 0.41 mg, J-value = 0.0098932 ± 0.0000495

Drill hole ARAD-23 drill hole collar GR 6675 58792 AGD66, sample 210 metres down hole

Temp (C)	Cumulative ^{39}Ar(%)	^{40}Ar/^{39}Ar	^{37}Ar/^{39}Ar	^{36}Ar/^{39}Ar	Vol. ^{39}Ar x 10^{-15} mol	%Rad. ^{40}Ar	Ca/K	^{40}Ar*/^{39}Ar	Age (Ma)	±1σ (Ma)
500	6.6	16.73	0.0074	0.0010	2.64	98.20	0.01	16.43	271.71	2.23
525	12.0	23.67	0.0002	0.0005	2.11	99.30	0.00	23.50	377.10	2.27
550	20.3	26.61	0.0001	0.0005	3.33	99.40	0.00	26.44	419.13	2.22
575	30.2	27.74	0.0119	0.0006	3.90	99.30	0.02	27.53	434.60	2.41
600	40.6	30.33	0.0050	0.0094	4.16	90.80	0.01	27.54	434.63	2.31
625	51.6	27.13	0.0394	0.0009	4.37	98.90	0.07	26.84	424.83	1.38
650	61.1	26.85	0.0023	0.0003	3.76	99.60	0.00	26.73	423.34	1.58
675	70.0	26.63	0.0292	0.0009	3.55	98.90	0.06	26.35	417.89	1.49
700	77.9	26.25	0.0444	0.0013	3.12	98.50	0.08	25.86	411.00	1.94
750	85.8	27.85	0.0718	0.0028	3.15	97.00	0.14	27.02	427.32	2.34
800	91.5	28.54	0.0521	0.0023	2.26	97.50	0.10	27.83	438.80	2.96
850	95.9	27.62	0.0578	0.0029	1.75	96.90	0.11	26.76	423.76	3.75
900	98.9	29.96	0.0913	0.0037	1.20	96.30	0.17	28.86	453.12	3.13
1000	100.0	33.82	0.0995	0.0003	0.45	99.70	0.19	33.70	519.12	8.95
Total		379.74	0.5124	0.0272	39.75			26.15	415.12	2.23

SD-534 (sericite), mass = 1.81 mg, J-value = 0.0088565 ± 0.0000620

Drill hole SD-534 on Stawell Mine Lease, sample 188 metres down hole

Temp (C)	Cumulative ^{39}Ar(%)	^{40}Ar/^{39}Ar	^{37}Ar/^{39}Ar	^{36}Ar/^{39}Ar	Vol. ^{39}Ar x 10^{-15} mol	%Rad. ^{40}Ar	Ca/K	^{40}Ar*/^{39}Ar	Age (Ma)	±1σ (Ma)
500	1.6	25.30	0.0078	0.0027	1.61	96.80	0.01	24.50	354.22	3.25
550	6.4	12.30	0.0225	0.0012	4.93	97.20	0.04	11.96	181.62	0.95
600	12.0	30.61	0.0181	0.0002	5.69	99.80	0.03	30.54	431.89	2.18
625	17.3	35.52	0.0054	0.0001	5.36	99.90	0.01	35.51	493.27	1.89
650	23.4	35.75	0.0142	0.0003	6.22	99.80	0.03	35.66	495.12	2.73
675	30.9	35.47	0.0200	0.0000	7.61	100.00	0.04	35.47	492.84	1.49
700	38.9	35.42	0.0125	0.0001	8.10	100.00	0.02	35.40	492.05	3.67
725	47.1	35.07	0.0025	0.0001	8.39	99.90	0.00	35.05	487.67	1.68
750	55.4	34.65	0.0088	0.0003	8.39	99.70	0.02	34.57	481.85	1.79
780	62.3	34.82	0.0001	0.0000	7.00	100.00	0.00	34.80	484.72	1.69
820	70.1	34.86	0.0016	0.0005	7.92	99.60	0.00	34.73	483.77	1.56
860	79.8	35.09	0.0001	0.0000	9.90	100.00	0.00	35.08	488.11	1.84
900	89.7	35.27	0.0125	0.0006	10.11	99.50	0.02	35.09	488.22	1.46
940	97.2	35.62	0.0081	0.0002	7.57	99.80	0.02	35.55	493.76	1.45
1000	99.3	37.77	0.0779	0.0008	2.16	99.40	0.15	37.56	518.08	2.70
1200	100.0	42.02	3.0941	0.0111	0.73	92.70	5.89	39.05	535.84	7.09
Total		535.55	3.3063	0.0182	101.69			33.67	470.88	1.95

JM-8a (sericite), Mass = 1.21 mg, J-value = 0.0099106 ± 0.0000496

Footwall of Central Lode -619RL Stawell Mine

Temp (C)	Cumulative ^{39}Ar(%)	^{40}Ar/^{39}Ar	^{37}Ar/^{39}Ar	^{36}Ar/^{39}Ar	Vol. ^{39}Ar x 10^{-15} mol	%Rad. ^{40}Ar	Ca/K	^{40}Ar*/^{39}Ar	Age (Ma)	±1σ (Ma)
500	6.0	20.81	0.0310	0.0058	4.20	91.60	0.06	19.06	312.16	2.80
525	10.6	29.08	0.0256	0.0037	3.22	96.20	0.05	27.98	441.47	3.22
550	15.6	29.59	0.0096	0.0021	3.46	97.80	0.02	28.96	455.18	4.13
575	21.1	29.68	0.0049	0.0012	3.83	98.70	0.01	29.30	459.94	4.52
600	27.4	28.64	0.0024	0.0009	4.44	99.00	0.00	28.36	446.81	3.30
625	33.1	28.29	0.0098	0.0011	3.95	98.80	0.02	27.94	441.03	2.91
650	40.2	28.15	0.0055	0.0007	4.98	99.20	0.01	27.92	440.74	2.55
675	46.2	28.70	0.0035	0.0005	4.17	99.40	0.01	28.52	449.11	2.75
700	51.6	28.70	0.0016	0.0007	3.81	99.10	0.00	28.44	447.97	3.12
750	58.5	28.84	0.0052	0.0008	4.83	99.10	0.01	28.59	450.10	1.79
800	66.8	28.77	0.0143	0.0007	5.74	99.10	0.03	28.53	449.18	1.33
850	76.3	29.13	0.0027	0.0004	6.69	99.50	0.01	29.00	455.73	2.42
900	87.1	29.95	0.0011	0.0003	7.56	99.60	0.00	29.83	467.24	1.74
1000	97.7	31.31	0.0011	0.0010	7.38	99.00	0.00	30.99	483.20	2.05
1100	100.0	35.08	0.0307	0.0049	1.61	95.80	0.06	33.61	518.69	3.74
Total		434.72	0.1491	0.0249	69.87			28.47	448.42	2.61

Chapter 2: Using the ^{40}Ar/^{39}Ar technique to date sericite: a case study on a complex gold deposit, Stawell, southeastern Australia

J. McL. Miller and D. Phillips

Summary

A discussion of the causes behind discordance in ^{40}Ar/^{39}Ar spectra obtained from fine-grained mica is presented. The ^{40}Ar/^{39}Ar technique is then applied to alteration within the samples from various phases of alteration and gold mineralisation that are structurally well-constrained within the Stawell gold deposit in western Victoria. Although the majority of the samples fall within the previously constrained age brackets (from ^{40}Ar/^{39}Ar dating and U-Pb dating of intrusions), precision is limited by the discordant nature of most age spectra. One sample of wall rock sericite from a 440 Ma gold lode (age confirmed by pyrite dating presented in Chapter 3) gave a ca. 400 Ma age, which reflects overprinting from hydrothermal fluids linked to the 400 Ma Stawell intrusion. This highlights the danger in relying too much on ^{40}Ar/^{39}Ar ages from fine-grained wall-rock sericite adjacent to gold lodes, even within structurally well-constrained systems such as Stawell. The majority of age spectra are complicated by a combination of ^{39}Ar recoil, inherited detrital and metamorphic mica and multiple phases of alteration. Although the use of vacuum encapsulation may improve age constraints with respect to characterising the amount of ^{39}Ar loss, the age spectra are complicated by a combination of factors, thus limiting the usefulness of this approach. We believe the way forward is to date mica encapsulated within pyrites to overcome recoil loss of ^{39}Ar and minimise the affects of younger hydrothermal and thermal events.

2.1 Introduction

The dating of sericite by the ^{40}Ar/^{39}Ar technique has been applied to many mineral deposits, with a particular focus on gold deposits that lack the intrusive relationships for the application of U-Pb dating methods (e.g., Foster, et al., 1998; Bierlein, et al., 2001). In many cases, the multiple deformation, alteration and thermal events, that are often associated with gold-bearing terranes, complicate the interpretation of ^{40}Ar/^{39}Ar age spectra and raise questions as to the validity of the sericite age results. Furthermore, compared to coarse-grained mica (i.e., >100 μm diameter), the fine-grained nature of sericite (<30 μm diameter) means it is more susceptible to loss of ^{40}Ar and recoil loss/ redistribution of ^{39}Ar$_K$ (e.g. Fergusson and Phillips, 2001). These phenomena can lead to discordant ^{40}Ar/^{39}Ar age spectra, geologically meaningless ages and/or ages that reflect younger thermal events post-dating sericite growth.

Discordant ^{40}Ar/^{39}Ar spectra are almost diagnostic of step-heating experiments on fine-grained mica (e.g. Wright and Dallmeyer, 1991; Foster, et al., 1998; Bierlein, et al., 2001; Fergusson and Phillips, 2001) and it is difficult to assess which steps should be averaged to produce an age and to ascertain if this age has any geological significance (e.g., Fergusson and Phillips, 2001; Sherlock et al., 2003). In spite of this, many publications quote mean ages for particular segments of age spectra with no explanation as to the rationale or interpretation behind the choice of a given segment.

The Stawell gold deposit in western Victoria, Australia has a well characterized structural evolution (e.g. Watchorn and Wilson, 1989; Miller and Wilson, 2002, 2004a, 2004b), with key events being bracketed by U-Pb SHRIMP ages on intrusive rocks (e.g. Arne et al., 1998). In addition, there is general agreement in the literature on the timing of the main phase of gold mineralisation (ca. 440 Ma; e.g. Foster et al., 1998; Bierlein et al., 1999; 2001). In this chapter we apply the $^{40}Ar/^{39}Ar$ technique to different stages of alteration and contact metamorphism associated with the Stawell gold system. Apart from providing geochronological constraints on the evolution of this world-class gold system, this study addresses possible causes of $^{40}Ar/^{39}Ar$ age spectra discordance and assesses various interpretative models and the geological significance of $^{40}Ar/^{39}Ar$ ages obtained from fine-grained mica.

2.2 $^{40}Ar/^{39}Ar$ geochronology

2.2.1 Brief summary of technique

The $^{40}Ar/^{39}Ar$ technique uses the decay of ^{40}K to ^{40}Ar to determine the age of a sample and in this sense is identical to the more conventional K-Ar method (MacDougall and Harrison, 1999). In the $^{40}Ar/^{39}Ar$ technique samples are irradiated in a nuclear reactor to convert a portion of the non-radiogenic ^{39}K to $^{39}Ar_K$ ($^{39}Ar_K = ^{39}Ar$ produced from irradiation of ^{39}K). The $^{39}Ar_K$ acts as a proxy parent isotope with the $^{40}Ar*/^{39}Ar_K$ ratio used to calculate an age. One advantage of the $^{40}Ar/^{39}Ar$ technique is that the daughter and 'parent' products can be measured simultaneously on the same aliquot of sample.

In a $^{40}Ar/^{39}Ar$ step-heating experiment samples are progressively step-heated *in vacuo* by either a laser or vacuum furnace until fusion. The gas released from each step is purified and 5 isotopes of argon are measured using a static mass spectrometer. $^{40}Ar/^{39}Ar$ ages are calculated after correcting the data for system backgrounds, radioactive decay of $^{37}Ar_{Ca}$ and $^{39}Ar_K$, mass discrimination, isotopic interferences, fluence gradients and atmospheric contamination (refer to MacDougall and Harrison, 1999). $^{40}Ar/^{39}Ar$ age spectra are obtained by combining results from a step-heating experiment in order of increasing temperature or cumulative release of $^{39}Ar_K$.

A plateau age represents a flat portion of the age spectrum and is normally defined as comprising at least three consecutive steps that are within 2σ of the plateau age and contain more than 50% of the gas released. The term "mean age" is commonly used to define the mean of age steps that do not fit the criterion for a plateau.

The mechanisms by which argon is released from a mineral during an $^{40}Ar/^{39}Ar$ heating experiment has been a controversial issue and has important implications for interpreting discordant $^{40}Ar/^{39}Ar$ age spectra. The key issue is whether the heating experiment unmasks fossil ^{40}Ar gradients preserved in a mineral (e.g., Harrison and McDougall, 1980) or merely reflects degassing due to dehydroxylation, delamination and/or phase changes induced by the heating experiment (e.g. Wartho, 1995; Sletten and Onstott, 1998).

2.2.2 Closure temperature

An important concept related to the $^{40}Ar/^{39}Ar$ technique is that of closure temperature (e.g. McDougall and Harrison, 1999). Above the closure temperature for argon diffusion in a particular mineral, $^{40}Ar^*$ produced will escape via diffusion and no age will be recorded by the K-Ar isotopic system. Once the mineral cools below a certain temperature, accumulation of $^{40}Ar^*$ will begin to exceed diffusive loss. Below the closure temperature, a mineral quantitatively retains $^{40}Ar^*$ and hence records age information – this age is defined as a cooling age. The closure temperature of a given mineral varies as a function of cooling rate, composition, and grain size.

A short-lived geological heating event may reset the rim of an existing mineral (i.e., the rim of the mineral loses ^{40}Ar via diffusion). The argon gas residing in the "centre" of the mineral may retain either part, or all, of the $^{40}Ar^*$ produced since crystallisation. If the $^{40}Ar/^{39}Ar$ heating experiment does record a fossil ^{40}Ar gradient, then the $^{40}Ar^*$ released from the lowest temperature steps may provide information on the age of the younger event, whereas the higher temperature steps, which extract gas from the "centre" of the mineral, may yield ages approaching the age of crystallisation. In this case, an age spectrum with a 'staircase' pattern would be expected. For micas the effective diffusion dimension for argon may be the physical grain size (e.g. Hames and Bowring, 1994), although internal structures may also have a strong control on the diffusion length scale (e.g. Dunlap, 1997).

The concept of closure temperature only relates to whether $^{40}Ar^*$ can be retained by the mineral lattice and may differ from the growth temperature of the mineral. It is possible for micas to grow below the closure temperature for argon diffusion. In this situation, provided that there are no later thermal disturbances, the $^{40}Ar/^{39}Ar$ age derived from a step heating experiment would represent a crystallisation age. This situation may also apply to micas that grew in short-lived thermal events, such as hydrothermal alteration associated with post-peak metamorphic gold deposits or contact metamorphism adjacent to a shallow level pluton. Mean or plateau $^{40}Ar/^{39}Ar$ ages obtained on micas from rocks within the Lachlan Fold Belt of southeastern Australia (e.g. Foster et al, 1998; 1999) and in central Australia (e.g. Dunlap, 1997) have previously been interpreted as deformation-induced neo-crystallisation ages that directly date mica growth during cleavage or fabric development as a result of deformation or hydrothermal alteration, rather than the time that the mineral cooled through the closure temperature for argon diffusion.

2.2.3 Recoil loss/redistribution of $^{39}Ar_K$

Low-grade samples (lower to sub-greenschist facies) can in some cases be affected by the recoil of $^{39}Ar_K$ during irradiation (e.g. Reuter and Dallmeyer 1989; Ferguson and Phillips, 2001). This is a consequence of the $^{39}K(n, p)^{39}Ar_K$ reaction during irradiation in a nuclear reactor. The $^{39}Ar_K$ nuclei recoil variable distances, with a mean recoil length-scale of 0.08 μm (e.g. Lo and Onstott, 1989). This phenomenon can cause loss and/or redistribution of $^{39}Ar_K$ in fine-grained samples, often producing markedly discordant $^{40}Ar/^{39}Ar$ age spectra (e.g. Lo and Onstott, 1989; Reuter and Dallmeyer, 1989).

The effect of $^{39}Ar_K$ recoil loss/redistribution is generally negligible for large grains (>100 μm), but may be significant in fine-grained micas. Recoil loss of $^{39}Ar_K$ will result in anomalously old apparent ages due to loss of $^{39}Ar_K$ from grain margins (Reuter and Dallmeyer 1989; Fergusson and Phillips, 2001). The amount of $^{39}Ar_K$ loss is controlled by

the grain size and edge morphology. Minerals with poorly defined amorphous margins have high surface to volume ratios and are more prone to $^{39}Ar_K$ recoil loss (e.g. Reuter and Dallmeyer, 1989; Lo and Onstott, 1989; Dong et al., 1995). The only way to assess recoil loss of $^{39}Ar_K$ is by comparison of standard $^{40}Ar/^{39}Ar$ age spectra with conventional K-Ar and/or by vacuum encapsulation $^{40}Ar/^{39}Ar$ experiments (Dong et al., 1995). Work done by Dong et al. (1995) showed a correlation between $^{39}Ar_K$ recoil loss and illite crystallinity (IC), with poorly crystallised phyllosilicates (high IC values) exhibiting most recoil loss of $^{39}Ar_K$.

For fine-grained, impure mineral separates the recoil problem is complicated by $^{39}Ar_K$ redistribution into surrounding mineral phases (e.g., quartz, albite or chlorite) and defect structures. These impurities may preferentially release the $^{39}Ar_K$ at different temperatures to the mica. For example chlorite has two out-gassing periods, one at low temperature, and the other between 700 and 900°C, which is a temperature range that commonly defines a major part of a sericite $^{40}Ar/^{39}Ar$ age spectra (Lo and Onstott, 1989). Chlorite contains negligible amounts of potassium and, as a result, only releases the redistributed $^{39}Ar_K$, thus producing discordant age spectra (Fig 2.1a). Typically, mica/chlorite mixtures exhibit $^{40}Ar/^{39}Ar$ age spectra with younger apparent ages in the central part, due to the degassing of $^{39}Ar_K$ from chlorite (i.e. lower $^{40}Ar*/^{39}Ar_K$ ratios). In contrast, if the $^{39}Ar_K$ recoils into albite or quartz, then the $^{39}Ar_K$ is released at higher temperatures producing progressively younger apparent ages at the higher temperature end of the spectrum (e.g. Reuter and Dallmeyer, 1987; Fig 2.1b). Sletten and Onstott (1998) have also argued that $^{39}Ar_K$ recoil redistribution into K-poor phases can lead to the production of staircase $^{40}Ar/^{39}Ar$ age spectra that resemble an $^{40}Ar*$ diffusive loss profile (Fig 2.1c).

The above summary highlights that $^{39}Ar_K$ recoil redistribution can potentially cause anomalously low apparent age steps during a step-heating experiment due to differential degassing of $^{39}Ar_K$ from K-poor phases. The corollary is that $^{39}Ar_K$ recoil loss from K-rich minerals produce anomalously old apparent age steps, sometimes producing significant discordance in the resulting age spectra (e.g, Fergusson and Phillips, 2001) (Fig 2.2).
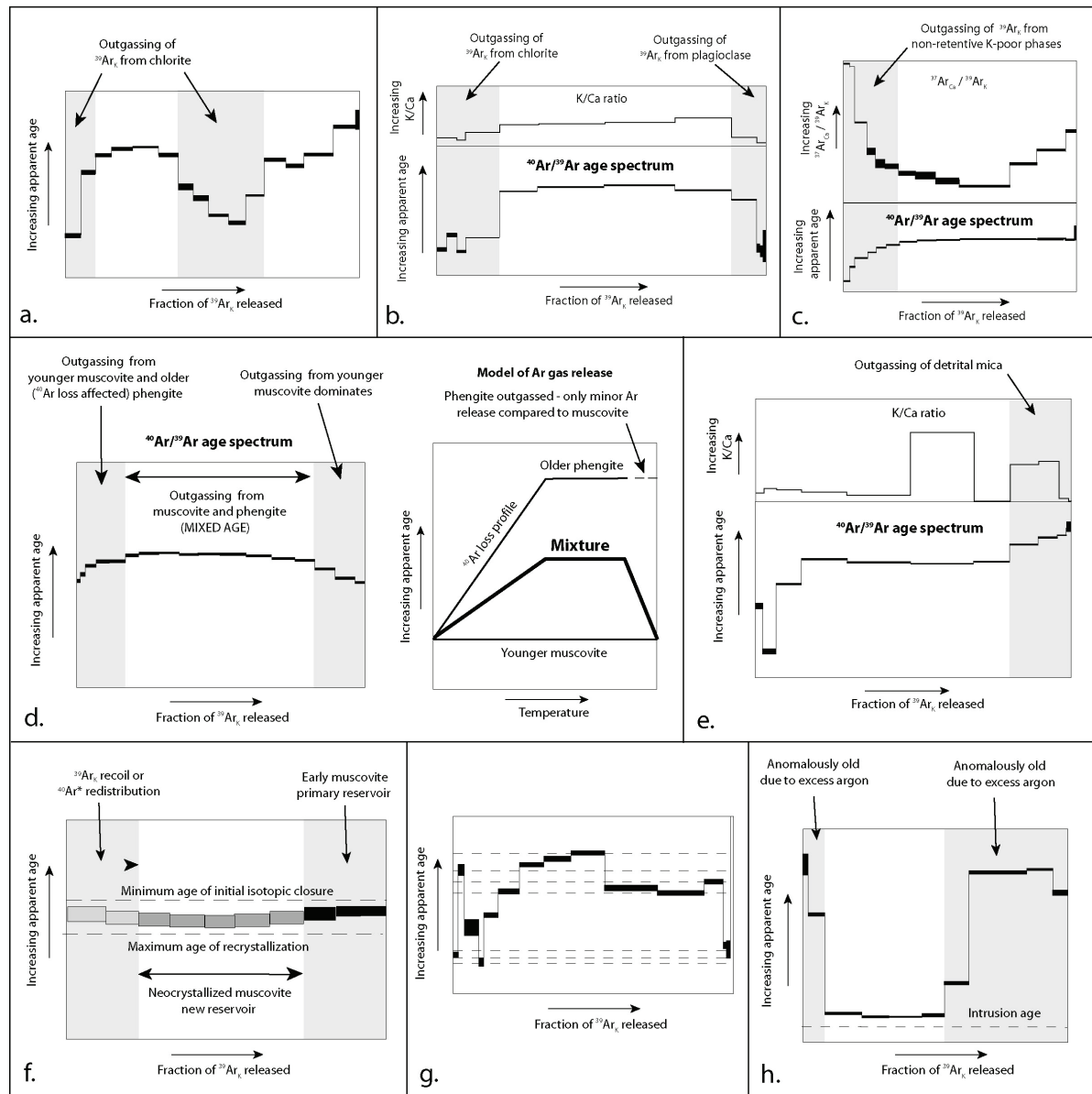
Fig 2.1. Examples of discordant spectra with different interpretations proffered for the cause of the discordance. a) from Lo and Onstott (1989); b) from Reuter and Dallmeyer (1987); c) from Sletten and Onstott (1998); d) from Wijbrans and McDougall (1986); e) from Reuter and Dallmeyer (1987); f) from Alexandrov et al. (2002); g) from Forster and Lister (2004); h) from Kelley (2002).
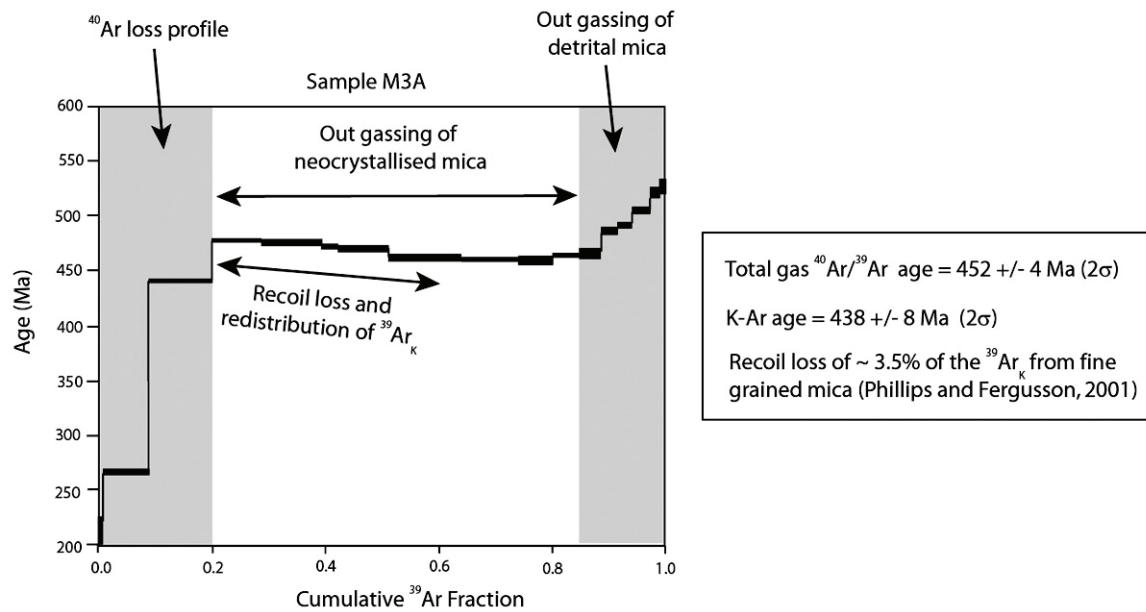
Fig 2.2. Example of recoil affected spectra from Fergusson and Phillips (2001). K-Ar dating gave a younger age than the $^{40}Ar/^{39}Ar$ ages indicating ~3.5% loss of ^{39}Ar. These authors interpreted the spectrum as affected by geological loss of ^{40}Ar (producing younger ages at low temperatures) with the decreasing gradient in the central part of the spectrum representing recoil loss/redistribution of ^{39}Ar. The high temperature ages were inferred to reflect degassing of detrital mica.

2.2.4 Additional causes for discordant spectra

Apart from $^{39}Ar_K$ recoil, other major causes of discordance in $^{40}Ar/^{39}Ar$ age spectra include: 1) multiple mica populations (metamorphic and/or detrital) with different compositions and/or grain sizes resulting in different degassing profiles during the heating experiment, causing discordant spectra, and 2) excess argon.

A sample with more than one mica population represents a heterogeneous system. During a step-heating experiment the degassing behaviour will depend upon relative grain size distributions and the composition of the different mica populations. For example phengite and muscovite have different release patterns for argon and may produce discordant spectra if a mixed age populations exist (Fig 1d; Wijbrans and McDougall, 1986). The presence of detrital mica in a sample can result in elevated apparent ages – particularly in the higher temperature steps (Fig 1.1e; Reuter and Dallmeyer, 1987; Dunlap, 1997).

Some workers have argued that discordant saddle shaped spectra are produced by micro-scale deformation processes, such as partial recrystallisation in the presence of hydrothermal fluids (e.g. Cheilletz et al., 1999; Alexandrov et al., 2002; Forster and Lister, 2004). Alexandrov et al., (2002) argued that this can produce multiple isotopic reservoirs that degas at different times due to composition and grain size variations and residence of an argon component in deformation induced "low activation energy sites" (Fig 2.1f). The resulting sigmoidal age spectra (Fig 2.1f) were interpreted as follows: 1) high temperature steps reflect degassing from older coarser grained primary muscovite; 2) lower temperature steps reflect degassing of younger finer grained mica that experienced minor $^{39}Ar_K$ recoil loss/redistribution, or alternatively, deformation-induced redistribution of $^{40}Ar*$ into low-activation-energy sites.

Forster and Lister (2004) have argued that discordant spectra represent degassing of different microstructural and microchemical domains that degas via a combination of dehydroxylation and diffusion. These authors argue that by applying a method of asymptotes and limits to age spectra, a range of age maximum and minimum age estimates with geological significance can be obtained from complex age spectra (Fig 2.1g). Whereas most interpretations of $^{40}Ar/^{39}Ar$ age spectra utilise variations on this theme as a matter of course, the method fails to account for spectra that have been affected by recoil loss/redistribution of $^{39}Ar_K$.

Excess argon is defined as radiogenic ^{40}Ar, present in fluid inclusions or the mineral lattice, that has not been generated by *in situ* decay of potassium. ^{40}Ar from contamination by either modern (or ancient) atmosphere or meteroic water is taken into account by the measurement of ^{36}Ar during a sample analysis ($^{40}Ar/^{36}Ar = 295.5$ in air and meteoric waters). The presence of excess argon often produces saddle shaped spectra with the base of the saddle usually inferred to be the closest estimate of the true age (Fig 2.1h, e.g., McDougall and Harrison, 1999; Kelley, 2002). In some cases excess argon may be present within fluid inclusions in the K-bearing mineral or in impurities such as quartz (e.g. Cumbest et al., 1994; Kendrick et al., 2001a, b). Heating experiments on fluid inclusion-rich quartz highlight that the quartz degasses argon in two distinct temperature ranges at 400 – 600°C and >1200°C (Kendrick et al. a, b). Therefore, fluid inclusion-bearing quartz impurities in sericite mineral separates will not outgas significant amounts of excess argon through the temperature range for argon release from sericite (600 to 1200°C).

2.3 Geological context to geochronology

The Magdala and Wonga gold deposits occur in the >5 million ounce Stawell gold field in the Victorian gold province of southeastern Australia (Figures 1.3, 2.3; Miller and Wilson, 2002, 2004a, b). The gold deposits are hosted within poly-deformed rocks that have 3 major phases of Cambrian-aged ductile deformation (D_1 to D_3) prior to D_4 brittle faulting (Watchorn and Wilson, 1989; Miller and Wilson 2002).

The 5 million ounce Magdala deposit occurs on the western flank of the Magdala basalt dome (Fig 2.3) and is part of the 440 Ma gold mineralization event in western Victoria (Foster et al., 1998; Arne et al., 2001; Bierlein et al., 2002; Squire and Miller, 2003). This orogenic deposit formed at high fluid pressures during D_4 brittle deformation and later D_5 sinistral wrenching (Fig 2.4, Watchorn and Wilson, 1989; Miller and Wilson, 2002). The Magdala deposit was dismembered by northwest-dipping thrust faults between 425 and 414 Ma (Miller and Wilson, 2004) and then intruded by Late Silurian quartz-feldspar-porphyritic intrusions (413±3 Ma U-Pb age on zircons; Arne et al., 1998) (Fig 2.4).

The smaller Wonga gold deposit (~300,000 oz Au) is an intrusion-related gold deposit associated with a suite of reduced diorites that formed between 413 and 400 Ma (Miller and Wilson, 2004b). The age constraints are based on cross-cutting relationships, with the Wonga Gold lodes overprinting Late Silurian porphyry dikes, and being intruded and metamorphosed by the youngest granite phase of the early Devonian Stawell pluton (Fig 2.4, Wilson et al., 1999) (401±4 Ma; Arne et al., 1998). Apart from the close temporal and spatial relationship to plutonism, the Wonga lodes also have structural and geochemical characteristics that distinguish them from the Magdala lodes (Miller and Wilson, 2004b).

The final major stage of brittle deformation in the Stawell-Ararat fault zone was associated with the formation of northeast-dipping dip-slip reverse faults. The Wonga deposit now lies in the footwall of a fault that formed during this event (Fig 2.3). These faults are associated with hydrothermal alteration that overprints the hornfels adjacent to the ~400 Ma Stawell pluton (Miller and Wilson, 2004a, 2004b) and are best typified by the South fault (Fig 2.3; Miller and Wilson, 2004). The age of faulting (~380 - 400 Ma; Fig 2.4) is constrained by correlations with regional orogenic events (Miller et al., 2001).
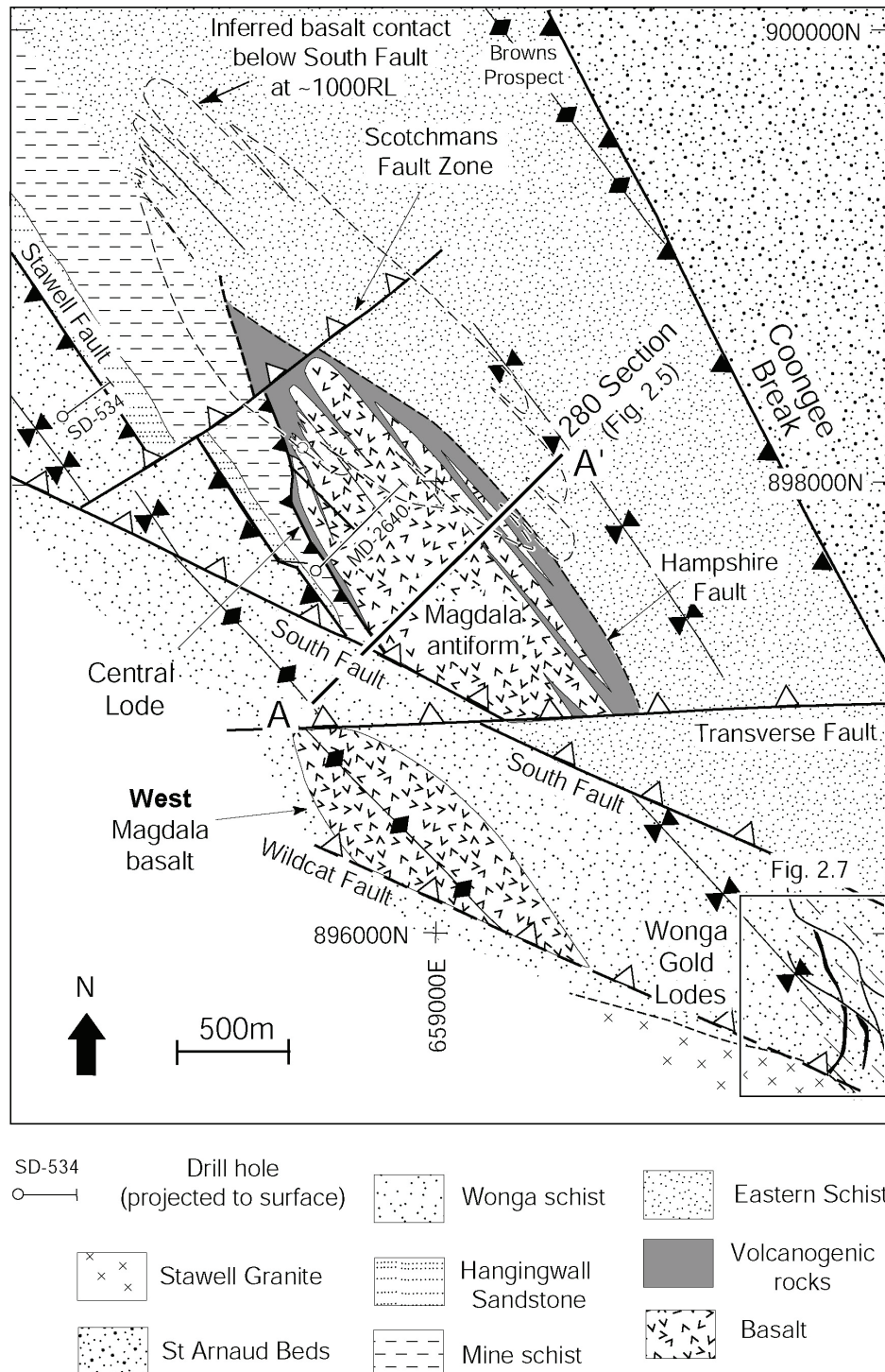
Fig2.3.   Geological map at −500 RL of the Magdala and Wonga Mines. The inferred position of the offset basalt below the South Fault (at approximately −1000 RL) is marked as a dashed outline. AMG grid northings

(and eastings) are marked. Early mineralising faults have black teeth (e.g. Stawell Fault); later faults that dismember the system, and in some cases further mineralise it, are marked with white teeth (e.g. Scotchmans Fault Zone). Antiform and synform traces to the east of the Magdala Antiform are also shown. Marked on the map are the sampled drill holes, the location of section line for Fig 2.5 and the location of Fig 2.7.

| ca. 490-500 Ma | $^{40}Ar/^{39}Ar$ ages (see Chapter 1) |
| Ductile deformation D_1, D_2, D_3 deformation | |

| ca. 488 Ma (?) | $^{40}Ar/^{39}Ar$ age on hydrothermal biotite = 488+2Ma (Mapani, 1995) |
| Initiation of D_4 brittle deformation | |

| ca. 440 Ma Fault-valve behavior Magdala Au mineralization D4 brittle deformation | **Samples JM-23, JM-23f, ARC-23** $^{40}Ar/^{39}Ar$ age on sericite = 439 +/- 2 Ma (Foster et al., 1998) |

| ca. 425 Ma Sinistral wrenching (Au) D5 deformation | |

| ~ 420 - 414 Ma Southeast-directed fault transport dismemberment of gold lodes | |

| 413 Ma Porphyry dyke emplacement | U-Pb zircon age = 413 +/- 2 Ma (Arne et al., 1998) |

| ~ 413 - 400 Ma Wonga intrusion-related Au & reduced plutonism (diorites) | **Sample BW-1** |

| 400 Ma Oxidized plutonism | U-Pb zircon age = 401 +/- 2 Ma (Arne et al., 1998) **Sample JM-42a** |

| ~ 400 - 380 Ma Southwest-directed fault transport Late brittle deformation/ fault gouge and hydrothermal alteration | **Sample JM-42a** |

Fig 2.4. Time line for the evolution of the Stawell gold field with samples that have been dated placed into this history.

2.4 Rationale for $^{40}Ar/^{39}Ar$ sample selection

Sericite-bearing samples were collected from a range of altered wall rocks and quartz veins. Exact sample locations are given in the data tables. The sample localities focussed on: 1) the 440 Ma orogenic gold lodes and 2) the later intrusion-related gold lodes and associated hydrothermal and intrusive overprints.

Samples from the D_4 440 Ma gold lodes were selected to investigate the reliability of age data from fine-grained sericite samples and to characterise the shape of release spectra from such material (Samples **JM-23f, JM23c, JM-23**; Fig 2.4).

The younger intrusion-related gold lodes have tight age constraints from SHRIMP U-Pb dating of zircons. A sample from one of these lodes was selected to assess the extent of possible $^{39}Ar_K$ recoil loss (Sample **BW-1**; Fig 2.4). Samples of the hornfels surrounding the ~400 Ma Stawell pluton as well as the hydrothermal alteration related to late-stage faulting (South Fault age) that overprints the contact aureole were also collected. These samples (Samples **JM-42a** and **JM-43b**; Fig 2.4) were analysed to assess of the affects of $^{39}Ar_K$ recoil on samples with a homogenous mica population (i.e. ~400 Ma old).

Also included are the $^{40}Ar/^{39}Ar$ age results reported in chapter1 from several samples of the earlier S_2 and S_3 ductile cleavages adjacent to 440 Ma orogenic gold lodes (Samples **MM-1 (muscovite)**, **MM-1 (biotite)**, **GPUNFOL**, **ARA-23a**, **ARA-23g, SD534** and **JM-8A**). These were included to highlight the affects of metamorphic and/or detrital mica on the age spectra.

2.5 $^{40}Ar/^{39}Ar$ Analytical procedures

Samples were crushed in a disk mill and then washed, dried and sieved. All samples contained mica 30μm or less in diameter, resulting in highly statically charged mineral separates. As a result 75-125μm sieve size fractions were used with the separate containing aggregates of fine-grained mica/sericite. For the smaller sieve size fractions, magnetic and non-magnetic minerals were removed using a magnetic separator. These samples were then hand picked under an optical microscope. Sample purity was monitored by observing a small quantity of each separate in oil on microscope slides. The purity of the samples was also estimated after the step-heating experiments by comparing the amount of argon released with the mass of the sample. All samples were >80% pure using a standard formula for muscovite. All samples were bathed overnight in dilute nitric acid and washed in deionised distilled water and then acetone prior to being shipped for irradiation.

The grains were wrapped in aluminium packets and placed into an aluminium irradiation canister together with aliquots of the flux monitor GA1550 (Age = 98.8 ± 0.5 Ma; Renne et al., 1998). Packets containing K_2SO_4 were placed at either end of the canister to monitor ^{40}Ar production from potassium. Samples were irradiated in two separate batches.

Samples **JM-23, JM-23c, JM-23Fb, JM-43b, JM-42a, and BW-1** were placed in an irradiation canister that was also cadmium-lined and irradiated for 40 hours in position 5C of the McMaster University reactor, Hamilton, Ontario. Correction factors for interfering reactions are as follows: $(^{36}Ar/^{37}Ar)_{Ca} = 2.54\ (\pm\ 0.09)\ x\ 10^{-4}$; $(^{39}Ar/^{37}Ar)_{Ca} = 6.51\ (\pm\ 0.31)\ x\ 10^{-4}$; (Bottomley and York, 1976); $(^{40}Ar/^{39}Ar)_K = 0.0010\ (\pm\ 0.005)$. K/Ca = 1.90 x $^{39}Ar/^{37}Ar$.

After irradiation, the samples were loaded into tin-foil packets and step-heated in a tantalum furnace. $^{40}Ar/^{39}Ar$ analyses were carried out on a VG3600 mass spectrometer using a Daly photomultiplier detector. Mass discrimination was monitored by analyses of standard air volumes.

The reported data have been corrected for system backgrounds, mass discrimination, fluence gradients and atmospheric contamination. Errors associated with the age determinations are one sigma uncertainties and exclude errors in the age of the fluence monitor GA1550 (±0.5 Ma, 1σ). The error associated with the plateau age determinations exclude the uncertainty in the J-value. A plateau age is defined as comprising at least three consecutive steps that are within 2σ error of the mean age and that represent >50% of the gas released. The term "mean age" is used to define the mean of age steps that do not fit the criterion for a plateau. Spectra for all samples are provided in Appendix with data tables at the end of this chapter. Decay constants are those of Steiger and Jager (1977).

2.6 Description of samples and $^{40}Ar/^{39}Ar$ age experiments

Sample JM-23 is an intensely hydrothermally altered fragment of wall rock sampled from a narrow band of rock (< 1 metre wide) between Scotchmans Vertical and Scotchmans Flat (the "Hangingwall reefs") on the 278N cross cut, -145 RL, Magdala Mine (Figures 2.5 and 2.6). The "Hangingwall reefs" produced about 1.4 million ounces of gold in historical production at a grade of 9 to 30 grams per tonne (Watchorn, 1986). The sample is directly adjacent to one of these historical stopes. Sample **JM-23** is part of the Mine Schist, though none of the metamorphic fabrics characteristic of the Mine Schist are preserved and the sample contains fine-grained sericite inter-layered with chlorite. Furnace analyses (Fig 2.6b) of a 75-125 μm mica concentrate produced an age spectrum with a sigmoidal shape and a total gas age of 432.3 ± 2.0 Ma. Apparent ages increase initially from 327 Ma to 451 Ma, before progressively decreasing to 428 Ma. Higher temperature steps show an increasing age gradient up to 452 Ma, with the final step having an apparent age of 418 Ma. The intermediate temperature steps (i.e., steps 4 to 15) have a mean age of 438.9 ± 2.0 Ma (88.3% of gas released, size of step-weighting). The ~439 Ma age is considered to approximate the age of alteration associated with the formation of the "Hangingwall reefs". The sigmoidal shape may reflect $^{39}Ar_K$ recoil loss/redistribution related to chlorite inter-layered with sericite (e.g., Lo and Onstott, 1989).

Sample JM-23c is a strongly foliated pelite within the Mine Schist, sampled from between Scotchmans Lower Flat and Hangingwall lode on the 278N cross cut, -145 RL, Magdala Mine (Figures 2.5, 2.6). This sample has a strong S_1/S_2 cleavage defined by white mica with minor chlorite (the fabrics are sub-parallel), and an intense S_3 crenulation cleavage marked by strong pressure solution and only minor mica growth. Furnace analyses (Fig 2.6c) of a 75-125 μm mica concentrate again produced a sigmoidal age spectrum with apparent ages generally increasing from 228 Ma to 469 Ma, before decreasing to 437 Ma, followed by a high temperature age increase to 469 Ma. The total gas age of **JM-23c** is 435.8 ± 1.8 Ma. The intermediate steps (i.e., steps 5 to 15) have a mean age of 448.5 ± 1.6 Ma (86.7% of gas released; size of step-weighting). This age is inferred to approximate the time of hydrothermal overprinting. The older high temperature ages could represent input from older metamorphic or detrital micas, with the sigmoidal shape of the age spectra possibly reflecting recoil redistribution of $^{39}Ar_K$ into chlorite.

Sample JM-23Fb is a sericite separate from a quartz-calcite vein parallel to Hangingwall Lode sampled on the 278N cross cut, -145 RL, Magdala Mine (Figures 2.5, 2.6). Furnace analyses (Fig 2.6d) of a 75-125 μm mica size fraction produced an age spectrum with apparent ages that decrease from 432 Ma to 384 Ma for a total-gas age of 401.4 ± 1.7 Ma. The decreasing age gradient (steps 2 to 12) has a mean age of 400.4 ± 1.5 Ma (92.0% of gas released; size of step-weighting). This age is inferred to approximate the age of alteration associated with intrusion-related deformation/ reactivation of Hangingwall Lode (calcite is commonly associated with late-stage South Fault structures). The decreasing age gradient may reflect $^{39}Ar_K$ recoil redistribution between mica and other phases such as quartz.
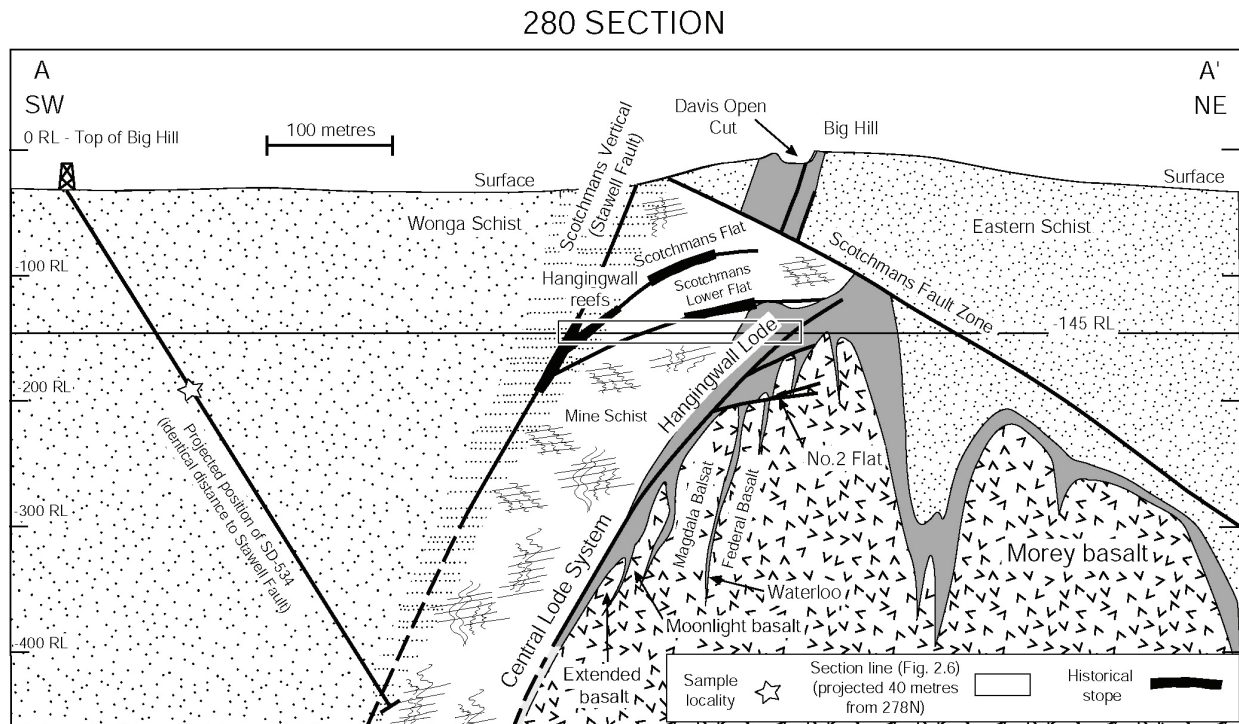
280 SECTION

Fig 2.5. Geological profile of the Magdala Antiform at 280 section. Section line for Fig 2.6 is projected onto section (actual section line position is 278 section, which is 40 metres southwest of 280 Section). Projected position of drill hole SD-534 is also marked on section; actual drill hole location is marked on Fig 2.3.

Sample BW-1 is from intensely hydrothermal altered wall-rock adjacent to Wonga-style mineralisation intersected by the under-the-south-fault drilling program beneath the Magdala orebody (drill hole MD-2640 – sample 800.5 m down drill hole marked on Fig 2.3). The ore is defined as Wonga-style due to its distinctive mineralogy (arsenopyrite and stibnite), distinctive sulphur isotopes (magmatic values for arsenopyrite which is different to the arsenopyrite associated with Magdala-style ore), and distinctive sulphide form (the arsenopyrite is asicular not euhedral). Unlike the Magdala deposit/mine (Fig 2.7), the ore is not overprinted by contact metamorphism associated with the Stawell pluton. Furnace analyses (Fig 2.8a) of a 75-125 μm mica size fraction produced a somewhat saddle-shaped age spectrum apparent ages ranging from 402 to 424 Ma, with a total-gas age of 410.5 ± 2.1 Ma. Steps 5 to 11 satisfy the plateau criteria with a weighted mean age of 405.1 ± 0.9 Ma (52.8% of gas released). The total-gas age is preferred as an estimate for the time of hydrothermal alteration associated with Wonga-style intrusion-related gold. This is because the plateau age may underestimate the age of mineralisation as it does not account for $^{39}Ar_K$ recoil redistribution. However, if the initial gradient defined by the lower temperature steps is due solely to $^{39}Ar_K$ recoil loss (with no redistribution) then the plateau age is more reliable.

The highest temperature steps produced older apparent ages, which could indicate a minor input from metamorphic/detrital mica.

Sample WM-42a is a hornfels from the –289 RL of the Wonga Mine (Figures 2.7, 2.8) that formed due to contact metamorphism adjacent to the Stawell pluton. The sample contains aggregates of fine-grained biotite (<50 μm in diameter) intergrown with quartz and also aggregates of sillimanite; no older metamorphic fabrics (S_1, S_2, S_3 etc.) are preserved. Furnace analysis (Fig 2.8b) of a 75-125 μm biotite separate produced an age spectrum with apparent ages ranging from 235 Ma (low temperature step) to 406 Ma (high temperature step) for a total-gas age of 398.2 ± 1.5 Ma. Steps 15 to 18 satisfy the plateau criteria with a weighted mean plateau age of 397.2 ± 0.8 Ma (58.5% of gas released). Excluding the younger lower temperature results, the remaining steps of the age spectrum (steps 6 to 17) exhibit a mean age of 400.2 ± 1.4 Ma (94.4% of gas released, size of step-weighting). Reasons for the slight discordance associated with the biotite age spectrum are unclear, but could be related to minor alteration-induced recoil loss/redistribution of $^{39}Ar_K$. Given this uncertainty, the age of 400.2 ± 1.4 Ma is the preferred cooling age for the biotite associated with contact metamorphism. Significantly, this age is identical to a cooling age obtained on coarse-grained biotite from the adjacent Stawell granite (400.9 ± 1.7 Ma, Bucher, 1998).
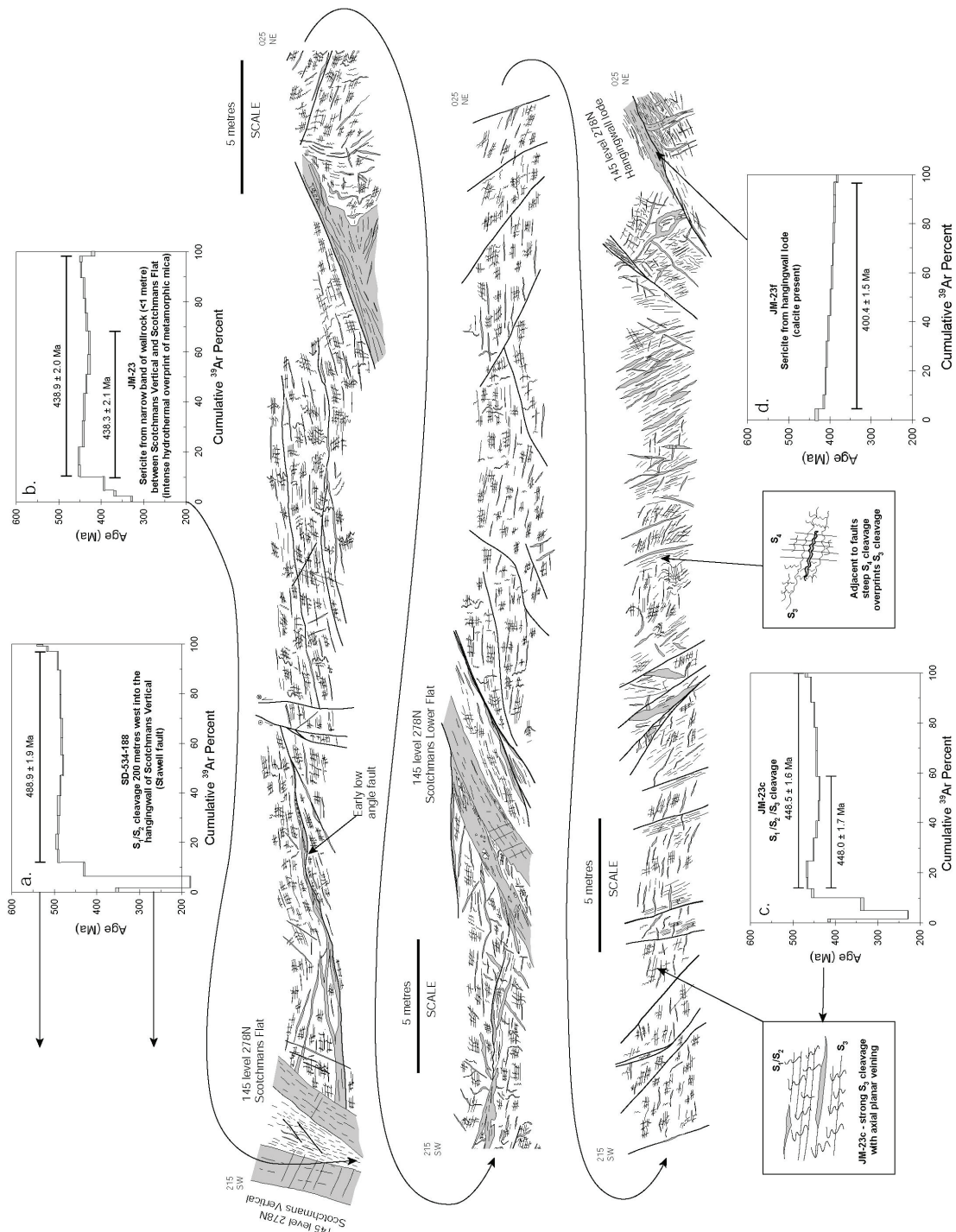
Fig 2.6. ^{40}Ar/^{39}Ar data (and sample locations) with structural profile from the Stawell Fault (Scotchmans Vertical) to the Hangingwall Lode. Errors are 1σ. Grey regions are quartz veins, thick lines are faults, thin lines represent cleavages, bedding surfaces, or joints. Results from sample SD-534 is described in chapter 1.
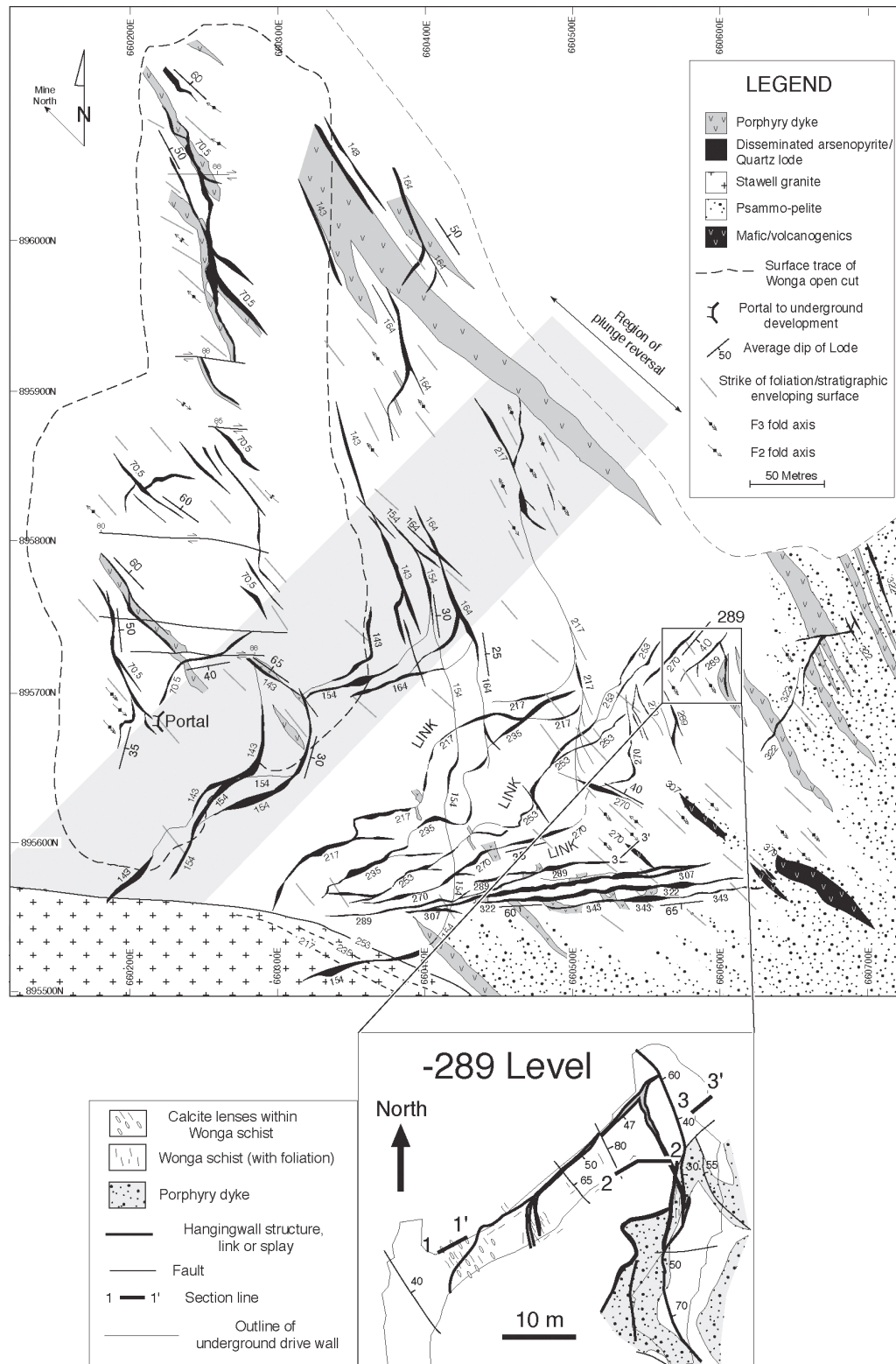
Fig 2.7. Composite level plan for the −70.5 RL of the Wonga open cut and the underground levels from −143 RL to −164 RL and −217 RL to 379 RL. Section lines for Fig 2.8 are marked on the geological map of the -289 RL.
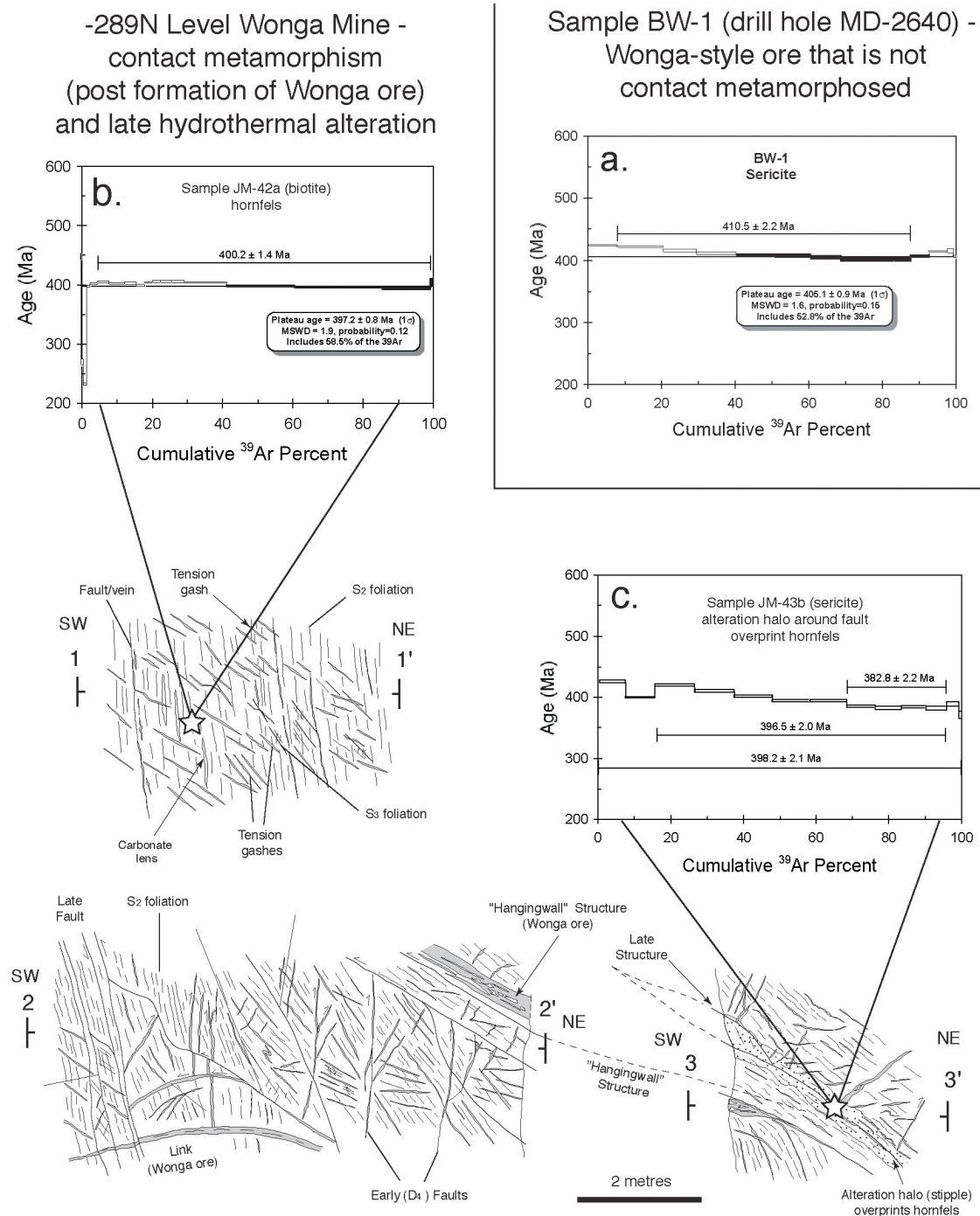
Fig 2.8. $^{40}Ar/^{39}Ar$ data with structural profiles from the –289 RL (Wonga Mine). Sample locations for **JM-43b** and **JM-42a** are marked on sections. Errors are 1σ. Grey regions are quartz veins, thick lines are faults, thin lines represent cleavages, bedding surfaces, or joints.

Sample WM-43b derives from intense hydrothermal alteration around a "South Fault age" structure on the –289 RL of the Wonga Mine (Figures 2.7, 2.8). The alteration assemblage comprises mainly sericite, silica and pyrite, which completely replaces the biotite related to contact metamorphism and is associated with a mineral lineation indicative of dip slip movement on the faults. Furnace analysis (Fig 2.8c) of a 75-125 μm sized separate produced an discordant age spectrum with apparent ages generally decreasing with increasing temperature from 425 to 388 Ma. Steps 3 to 11 have a mean age of 396.5 ± 2.0 Ma (83.9% of

gas released, size of step-weighting) and this is the preferred estimate for the age of alteration associated with this phase of faulting. The decreasing age gradient may again reflect $^{39}Ar_K$ recoil loss and/or redistribution between mica and quartz. If the sample has suffered significant recoil loss of $^{39}Ar_K$, then the high temperature steps averaging 382.8 ± 2.2 Ma (26.7% of ^{39}Ar released; size-of-step weighting) may provide a better estimate of the time of alteration. Although it is argued that an age of ~397 Ma is the most likely age of alteration, it can be stated with reasonable confidence that the age lies between 397 and 383 Ma. This phase of alteration, associated with southwest-directed transport on "South Fault age" structures, has already been assigned to deformation related to the Tabberabberan orogeny (Miller et al., 2001). This orogeny caused folding of the sediments in the Melbourne Zone and is inferred to have occurred between 400 Ma and 370 Ma.

2.7 Discussion

The interpretation of $^{40}Ar/^{39}Ar$ step-heating spectra obtained from fine-grained sericite samples can be complicated and compromised by the interplay of several factors such as multiple mica populations (e.g. hydrothermal sericite plus inherited detrital or metamorphic micas), loss of $^{40}Ar*$ due to alteration or younger thermal events, excess argon contamination, recoil loss/redistribution of $^{39}Ar_K$ and *in-vacuo* structural break-down. Despite the litany of potential problems, the current study yielded $^{40}Ar/^{39}Ar$ ages (Fig 2.9) that, for the majority of samples, are broadly consistent with available geochronological and geological constraints (Fig 2.4). In this regard the Stawell $^{40}Ar/^{39}Ar$ dating program was surprisingly successful in that it delineated the ca. 440 Ma Magdala gold deposition event, the younger age of the Wonga alteration (ca. 405 to 410 Ma) and the post-400 Ma hydrothermal alteration event related to the Tabberabberan orogeny. Furthermore, an important result was obtained from sample JM-23Fb, which was selected from one of the major 440 Ma Magdala gold lodes, but produced a substantially younger age than expected. This ca. 400 Ma age has been interpreted to result from resetting by hydrothermal fluids linked to the Stawell pluton – a result that has been confirmed by dating mica inclusions in pyrite from the same sample (see Chapter 3). This outcome clearly highlights the danger in simply collecting so-called 'grab samples' from a lode and assuming the sericite age produced is the true age of mineralisation.

Although the above ages are within expected limits, determining precise ages and assigning realistic uncertainties to the ages is more problematic, due to the discordant nature of the age spectra and the, often, complex interplay of the aforementioned complicating factors. In order to address this issue, we now examine the age spectra from those samples that have the most restrictive age constraints from other dating methods and attempt to isolate the factors responsible for discordance in each case.

A number of sericite samples from this study exhibit linear age gradients (e.g., sample JM-23Fb) with ages progressively decreasing with increasing temperature. We interpret these gradients to reflect reactor-induced recoil redistribution and/or loss of ^{39}Ar. Support for this interpretation comes from results of combined K-Ar and $^{40}Ar/^{39}Ar$ studies on fine-grained micas from Bateman's Bay slates (Fergusson and Phillips, 2001). Recoil loss of ^{39}Ar from samples produces elevated $^{40}Ar*/^{39}Ar$ ratios and hence anomalously old apparent ages. As recoil loss of ^{39}Ar preferentially affects grain margins, the effect is most pronounced during initial low temperature heating steps. Therefore, low temperature ages will be too old, with the higher temperature steps providing the best age estimates. Recoil redistribution of ^{39}Ar produces decreased $^{40}Ar*/^{39}Ar$ ratios in potassium-rich phases and increased $^{40}Ar*/^{39}Ar$ ratios

in potassium-poor minerals (e.g. chlorite, quartz) – the sequence of argon release from these phases will then dictate the shape of the resultant age spectrum. For example, release of argon from sericite during initial heating steps would produce anomalously elevated apparent ages, with argon release at high temperatures from quartz resulting in apparent ages that are too young.

If it is assumed that age spectra with decreasing age gradients are solely due to recoil redistribution of ^{39}Ar between sericite and other phases present (e.g. chlorite, quartz), with no ^{39}Ar loss, then the average of all age steps should provide the best estimate for the time of sericite crystallisation. This approach would average out steps that are too old (^{39}Ar redistribution from K-rich phases) and steps that are too young (uptake of ^{39}Ar by K-poor phases). In the case of sample BW-1, the lowest temperature ages (>420 Ma) are older than a U-Pb age for a cross-cutting dyke (413 ± 2 Ma; Arne et al., 1998), which could be explained by recoil loss or redistribution of ^{39}Ar. Averaging the age gradient (but excluding the last few steps) produces an acceptable age of 410.5 ± 2.2 Ma (Figures 2.8a, 2.10a), which lies within the age range for this phase of mineralisation (413 ± 2 Ma to 400 ± 2 Ma Ma), as bracketed by U-Pb dating of cross-cutting felsic intrusions (Fig 2.4). At the same time, the youngest age obtained from sample BW-1 (402 ± 3 Ma) is also within the above age range, which means that recoil loss of ^{39}Ar$_K$ alone could also account for this age spectrum. Consequently, separation of recoil loss and redistribution effects is not possible with the current samples. Intuitively, it might be expected that both processes operate in fine-grained multi-phase samples.

Recent work on clay samples by Dong et al. (1995) revealed a linear correlation between the amount of recoil loss and illite crystallinity indices. Based on crystallinity indices available for the Stawell region, the anticipated amount of ^{39}Ar recoil loss is estimated at ~2-3%, which would equate to an overall age overestimate of ~8 – 12 Ma. In reality, the situation is more complex in that the decreasing age gradients mask evidence of ^{40}Ar loss. Dong et al. (1995) suggest that ^{40}Ar and ^{39}Ar recoil loss would take place from similar lattice sites and that these effects offset one another to a large extent. If correct, then the above approach of averaging all steps that form a decreasing apparent age spectrum may provide a reasonable estimate for the age of sericite crystallisation.

The complexity of age spectra increases further when other mica populations are present in a sample. Fergusson and Phillips (2001) demonstrated that coarse detrital muscovite grains outgas at higher temperatures (>800°C) than fine-grained sericite and result in increasing apparent ages for the higher temperature steps. Therefore, we attribute the older, high temperature ages from samples such as BW-1 in terms of detrital/metamorphic muscovite contamination (Fig. 2.8a) – consequently, these steps are excluded from any age estimate for the time of sericite formation. Separation of signatures from multiple sericite populations with similar grain size distributions is, however, far more difficult, if not impossible. The only way to reduce the risk of this complication is to select samples with only one dominant cleavage fabric.

An additional complication is that age spectra with anomalously old initial ages steps may be affected by excess argon contamination, rather than recoil loss/redistribution of ^{39}Ar (e.g. hornfels sample JM43b; Fig. 2.8). Recognition of the presence of excess argon is often a non-trivial task. In order to investigate this possibility further, we undertook step-heating analyses of quartz-rich separates from selected samples. In all cases, quartz released argon in two pulses, at very low temperatures (<600°C) and at high temperatures (>1200°C). Although

measured $^{40}Ar/^{36}Ar$ ratios were higher than the atmospheric ratio of 295.5, the amount of ^{40}Ar released was small, suggesting that excess argon contamination is not an important factor in the current samples.

Other factors that could affect the age spectra of sericite such as *in-vacuo* structural break-down are also difficult to evaluate using the current data. A number of studies have shown that micas undergo dehydroxylation reactions during *in-vacuo* heating and do not release argon by volume diffusion mechanisms. The consequence of this is homogenisation of age spectra and suppression of diffusion-related age gradient effects. In other words, this process should not cause discordance in mica age spectra.

In summary, it is suggested that the discordance of the current age spectra is largely due to recoil redistribution (±loss) of ^{39}Ar (which produces decreasing age gradients) and contamination by detrital grains (resulting in elevated high temperature apparent ages). Therefore, the 'best' age estimates from the current spectra may be obtained by averaging those steps forming part of the decreasing age gradients (e.g. Fig. 2.8, 2.9, 2.10). However, it is still problematic ascertaining which age steps should be averaged to give a reasonable age estimate. The approach adopted in this study is to consider only the decreasing age steps in an age spectrum, excluding any high temperature older steps. However, to compensate for the 'masking' effect of these older steps, a similar proportion of low temperature steps are omitted from the final age estimate (e.g. Fig. 2.8a). Uncertainties in these ages are then based on the variance of the mean age, weighted by the square of the Mean Square Weighted Deviates (MSWD). However, given the uncertainties in the relative effects of all complicating factors that could influence the age spectra of fine-grained sericite concentrates, it is unlikely that uncertainties will be better than 2-3%, (1σ) at best. Consequently, we believe that the pyrite dating method documented in chapter 3 may provide a way forward in applying the $^{40}Ar/^{39}Ar$ technique to dating fine-grained mica associated with ore deposits.
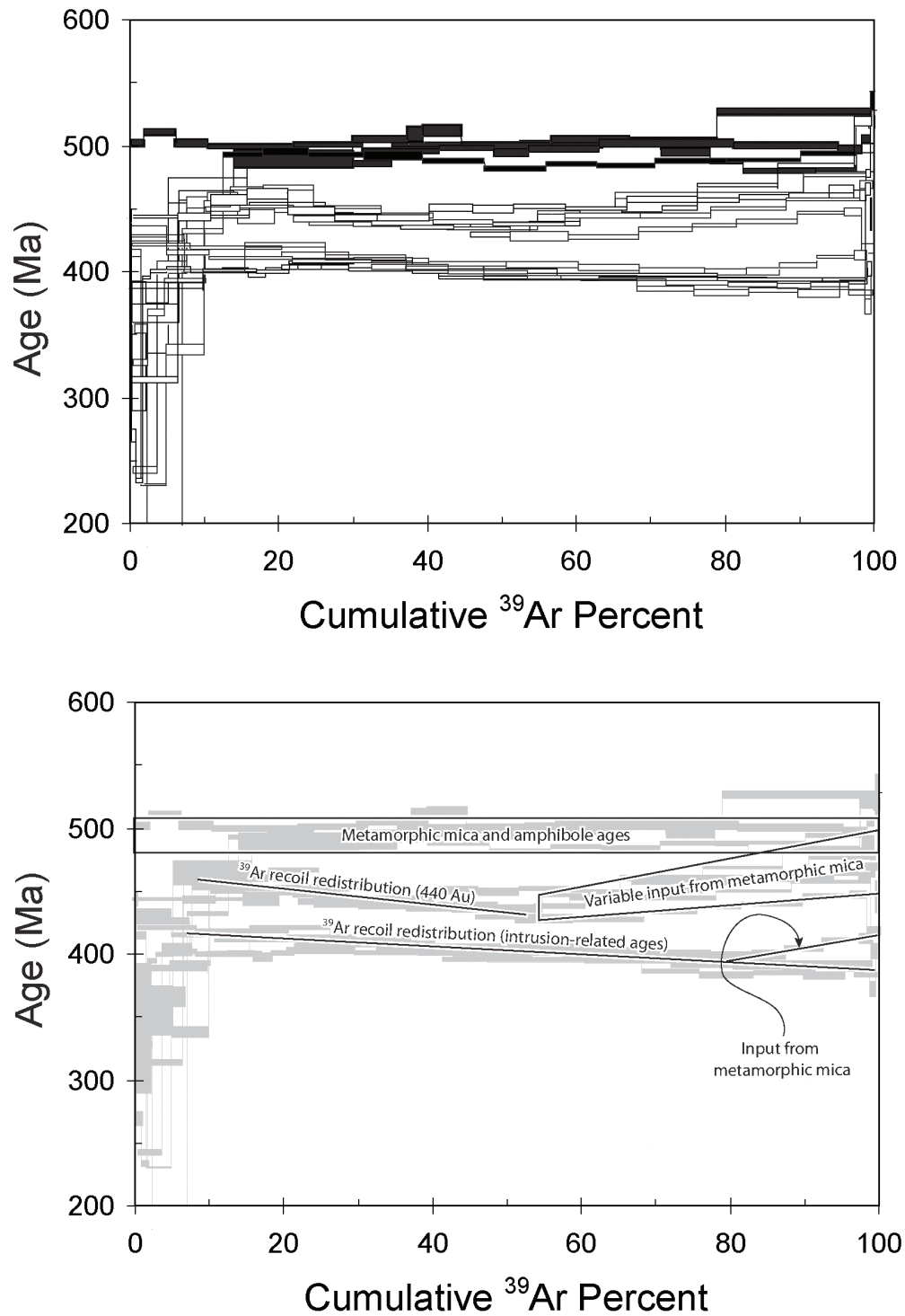
Fig 2.9. All [40]Ar/[39]Ar age spectra from the Moornambool Metamorphic Complex and Stawell gold mine. Lower diagram highlights interpretation of age spectra. See text for discussion.
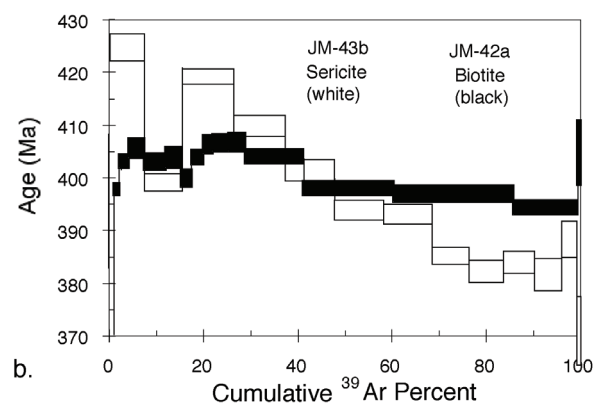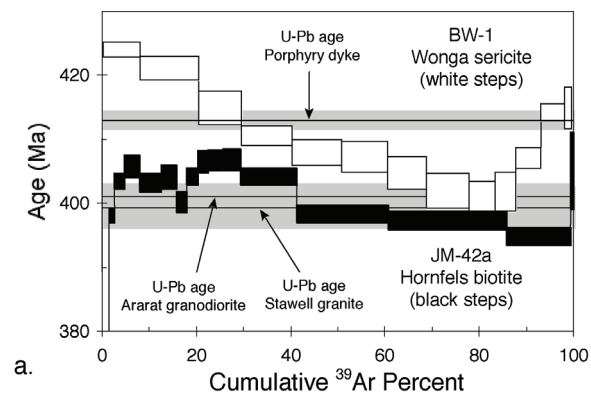
Fig 2.10 ^{40}Ar/^{39}Ar intrusion-related age data –see text for discussion.

2.8 References

ALEXANDROV, P., RUFFET, G., CHEILLETZ, A., 2002. Muscovite recrystallization and saddle-shaped ^{40}Ar/^{39}Ar age spectra: Example from the Blond granite (Massif Central, France). Geochemica et Cosmochimica Acta, 66, 1793-1807.

ARNE, D.C., BIERLEIN, F.P., MCNAUGHTON, N., WILSON, C.J.L., MORAND, V.J., 1998. Timing of gold mineralization in western and central Victoria, Australia: New constraints from SHRIMP II analysis of zircon grains from felsic intrusive rocks. Ore Geology Reviews, 13, 251-273.

ARNE D.C., BIERLEIN F.P., MORGAN J.W. & STEIN H.J. 2001. Re-Os dating of sulfides associated with gold mineralization in central Victoria. Economic Geology, 96, 1455-1459.

BIERLEIN F.P., FOSTER D.A., MCKNIGHT S. & ARNE D.C. 1999. Timing of gold mineralization in the Ballarat goldfields, central Victoria: constraints from ^{40}Ar-^{39}Ar results: Australian Journal of Earth Sciences 46, 301-309.

BIERLEIN F.P., ARNE D.C., MCKNIGHT S., LU J., REEVES S., BESANKO J., MAREK J. & COOKE D. 2000. Wallrock petrology and geochemistry in alteration haloes associated with mesothermal gold mineralization, central Victoria, Australia. Economic Geology, 95, 283-312.

BIERLEIN F.P., ARNE D.C., FOSTER D.A. & REYNOLDS P. 2001, A geochronological framework for orogenic gold in central Victoria, Australia. Mineralium Deposita, 36, 741-767.

BOTTOMLEY, R.J. AND YORK, D., 1976. ^{40}Ar-^{39}Ar age determinations on the Owyhee basalt of the Columbia Plateau. Earth and Planetary Science letters, 31, 75-88.

CHEILLETZ, A., RUFFET, G., MARIGNAC, C., KOLLI, O., GASQUET, D., FÉRAUD, G., BOUILLIN, J.P., 1999, 40Ar/39Ar dating of shear zones in the Variscan basement of Greater Kabylia (Algeria). Evidence of an Eo-alpine event at 128 Ma (Hautervian-Barremian boundary): geodynamic consequences, Tectonophysics, 306, 97-116.

CUMBEST, R.J., JOHNSON, E.L., ONSTOTT, T.C., 1994, Argon composition of metamorphic fluids: implications for 40Ar/39Ar geochronology, Geological Society of America Bulletin, 106, 942-951.

DONG H., HALL C. M., PEACOR D. R., HALLIDAY, A. N., 1995. Mechanisms of argon retention in clays revealed by laser 40Ar-39Ar dating. Science, 267, 355 359.

DUNLAP, W.J. 1997. Neocrystallisation or cooling? ^{40}Ar/^{39}Ar ages of white micas from low-grade mylonites. Chemical Geology, 143, 181-203.

FERGUSSON, C. L., PHILLIPS D., 2001. ^{40}Ar/^{39}Ar and K-Ar age constraints on the timing of regional deformation, south coast of New South Wales, Lachlan Fold Belt: problems and implications. Australian Journal of Earth Sciences, 48, 395-408.

FOSTER, D.A., GRAY, D.R., KWAK, T.A.P., BUCHER, M., 1998. Chronology and tectonic framework of turbidite hosted gold deposits in the western Lachlan Fold Belt, Victoria: ^{40}Ar-^{39}Ar results. Ore Geology Reviews, 13, 229-250.

FOSTER, D.A., GRAY, D.R., BUCHER, M., 1999. Chronology of deformation within the turbidite-dominated, Lachlan orogen: Implications for the tectonic evolution of eastern Australia and Gondwana. Tectonics, 18, 452-485.

FORSTER, M.A. AND LISTER, G.S., 2004, The interpretation of ^{40}Ar/^{39}Ar age spectra produced by mixing: application of the method of asymptotes and limits, Journal of Structural Geology, 26, 287-305.

HAMES, W.E., BOWRING, S.A., 1994. An empirical evaluation of the argon diffusion geometry in muscovite, Earth and Planetary Science Letters, 124, 161-167.

HARRISON, T.M., AND MCDOUGALL, I., 1980. Investigations of an intrusive contact, northwest Nelson, New Zealand-II. Diffusion of radiogenic and excess 40Ar revealed by 40Ar/39Ar spectrum analyses, Geochimica et Cosmochimica Acta, 44, 2005-2020.

KELLEY, S., 2002, Excess argon in K-Ar and Ar-Ar geochronology, Chemical Geology, 188, 1-22.

KENDRICK M.A., BURGESS R., PATTRICK R.A.D., AND TURNER G., 2001a, Halogen and Ar-Ar age determinations of inclusions within quartz veins from porphyry copperdeposits using complementary noble gas extraction techniques. Chemical Geology, 177, 351-370.

KENDRICK M.A., BURGESS R., PATTRICK R.A.D., AND TURNER G., 2001b, Noble gas and halogen evidence on the origin of Cu-Porphyry mineralising fluids. Geochimica et Cosmochimica Acta, 65, 2651-2668.

KENDRICK, M.A., MILLER, J.McL. & PHILLIPS, D., (in review, a), Evaluation of ^{40}Ar-^{39}Ar quartz-fluid-inclusion ages: examples from the Mt Isa Inlier: Geochimica et Cosmochimica Acta.

KENDRICK, M.A., PHILLIPS, D. & MILLER, J.McL., (in review, b). Stepwise heating of quartz: Implications for fluid inclusion analysis and the solubility of noble gases and halogens in quartz: Geochimica et Cosmochimica Acta.

LO, C-H., ONSTOTT, T. C., 1989. 39Ar recoil artefacts in chloritised biotite. Geochimica et Cosmochimica Acta, 53, 2697-2711.

MacDougall, I. and Harrison, T.M., 1999. Geochronology and thermochronology by the ^{40}Ar/^{39}Ar method. Second Edition. Oxford Univ. Press, New York.

Miller, J.McL., Dugdale, L.J., Wilson, C.J.L. 2001. Variable hangingwall palaeotransport during Silurian and Devonian thrusting in the Lachlan Fold Belt – missing gold lodes, synchronous Melbourne Trough sedimentation and Grampians Group fold interference. Australian Journal of Earth Sciences, 48, 901-909.

Miller, J.McL and Wilson, C.J.L. 2002. The Magdala Lode System, Stawell, southeastern Australia: structural style and relationship to gold mineralisation across the western Lachlan Fold Belt. Economic Geology, 97, 325-349.

Miller J.McL. & Wilson C.J.L. 2004a. Application of structural analysis to faults associated with a heterogeneous stress history: the reconstruction of a dismembered gold deposit, Stawell, western Lachlan Fold Belt, southeastern Australia. Journal of Structural Geology.

Miller J.McL. & Wilson C.J.L. 2004b. Stress controls on intrusion-related gold lodes: Wonga gold mine, Stawell, Western Lachlan Fold Belt, southeastern Australia. Economic Geology 99, 941-963.

Offler, R.L., McKnight, S., Morand, V., 1998. Tectonothermal history of the western Lachlan Fold Belt: Insights from white mica studies. Journal of Metamorphic Geology, 16, 531-540.

Onstott, T. C., Mueller, C., Vroluk, P. J., Pevear, D. R., 1997. Laser ^{40}Ar/^{39}Ar microprobe analyses of fine-grained illite. Geochimica et Cosmochimica Acta, 61, 3851 3861.

Renne, P., Swisher, C.C., Deino, A.L., Karner, D.BV., Owens, T.L., DePaolo, D.J., 1998. Intercalibration of standards, absolute ages and uncertainties in ^{40}Ar/^{39}Ar dating. Chemical Geology, 145, 117-152.

Reuter, A., Dallmeyer, R. D., 1987. Significance of 40Ar/39Ar age spectra of whole-rock and constituent grain size fractions from anchizonal slates, Chemical Geology, 66, 73-88.

Reuter, A., Dallmeyer, R. D., 1989. K-Ar and ^{40}Ar/^{39}Ar dating of cleavage formed during very low-grade metamorphism: a review. In: Daly, J. S., Cliff, R. A., Yardley, B.W.D. (eds). Evolution of Metamorphic Belts. Geological Society of London Special Publication, 43, 161-171.

Sherlock, S.C., Kelley, S.P., Zalasiewicz, J.A., Schofield, D.I., Evans, J.A, Merriman, R.J., Kemp, S.J., 2003. Precise dating of low-temperature deformation:Strain fringe analysis by 40Ar-39Ar laser microprobe. Geology, 31, 219-222.

Sletton, V.W., and Onstott, T.C., 1998, The effect of the instability of muscovite during in vacuo heating on 40Ar/39Ar step-heating spectra, Geochemica et Cosmochimica Acta, 62, 123-141.

Smith, P.E., Evensen, N.M., York, D., Szatmari, P. and de Oliveira, D.C., 2001, Single-crystal ^{40}Ar-^{39}Ar dating of pyrite: No fool's clock: Geology, v. 29, p. 403-406.

Steiger, R.H., Jager, E., 1977. Subcommission on geochronology: Convention on the use of decay constants in geo- and cosmochronology. Earth and Planetary Science Letters, 36, 359-362.

Squire R. & Miller J.McL. 2003. Synchronous compression and extension in East Gondwana: tectonic controls on world class gold deposits at 440 Ma. Geology, 31, 1073-1076.

Tetley, N., MacDougall, I. and Heydegger, H.R., 1980. Thermal neutron interferences in the ^{40}Ar/^{39}Ar dating technique. Journal of Geophyscial Research, 85, 7201-7205.

Wartho, J., 1995. Apparent argon diffusive loss ^{40}Ar/^{39}Ar spectra in amphiboles, 134, 393-407.

Watchorn, R.B., Wilson, C.J.L., 1989. Structural setting of gold mineralization at Stawell, Victoria, Australia, in The Geology of Gold Deposits: The perspective in 1988, ECONOMIC GEOLOGY MONOGRAPH 6, 292-309.

Wijbrans, J.R., and McDougall, I., 1986, 40Ar/39Ar dating of white micas from an Alpine high-pressure metamorphic belt on Naxos (Greece): the resetting of the argon isotopic system, Contributions to Mineralogy and Petrology, 93, 187-194.

Wilson, C.J.L, Xu, G., Moncrieff, J., 1999. The Structural Setting and Contact Metamorphism of the Wonga Gold Deposit, Victoria, Australia. Economic Geology, 94, 1305-1328.

Wright T.O. & Dallmeyer R.D. 1991. The age of cleavage development in the Ross orogen, northern Victoria Land, Antarctica: evidence from ^{40}Ar/^{39}Ar whole-rock slate ages. Journal of Structural Geology, 13, 677-690.

$^{40}Ar/^{39}Ar$ data files for Chapter 2

$^{40}Ar/^{39}Ar$ Step-Heating Analytical
Results

Temp (C)	Cumulative ^{39}Ar(%)	$^{40}Ar/^{39}Ar$	$^{37}Ar/^{39}Ar$	$^{36}Ar/^{39}Ar$	Vol. ^{39}Ar x 10^{-15} mol	%Rad. ^{40}Ar	Ca/K	$^{40}Ar*/^{39}Ar$	Age (Ma)	±1s (Ma)
JM-23 (sericite)										
Mass = 1.13 mg										
J-value = 0.0089084 ± 0.0000445										
500	1.8	22.34	0.0002	0.0001	1.2	99.8	0	22.32	327.13	2.54
550	4.3	25.34	0.0298	0.0001	1.62	99.9	0.06	25.32	366.97	2.26
600	9.7	27.45	0.0028	0.0005	3.59	99.4	0.01	27.29	392.56	1.8
625	14.3	31.89	0.0001	0.0001	3	99.9	0	31.87	450.87	2.27
650	21.6	31.99	0.0139	0	4.81	100	0.03	31.98	452.24	1.1
675	32.1	31.22	0.0045	0.0002	6.92	99.8	0.01	31.16	441.95	2.12
700	43.2	30.93	0.0134	0	7.29	100	0.03	30.92	438.89	1.81
725	50.8	30.55	0.0074	0	5	100	0.01	30.54	434.16	1.39
760	58.6	30.13	0.0066	0.0001	5.16	99.9	0.01	30.1	428.61	3.75
800	68.1	30.07	0.0197	0.0001	6.25	100	0.04	30.04	427.86	2.11
830	75.2	30.58	0.0043	0.0002	4.67	99.8	0.01	30.51	433.76	1.84
870	81.3	30.8	0.0066	0	3.99	100	0.01	30.79	437.25	1.45
920	89.4	31.15	0.0075	0.0004	5.35	99.6	0.01	31.03	440.36	1.73
960	95.8	31.6	0.0098	0	4.2	100	0.02	31.6	447.41	1.55
1000	98.1	31.64	0.0001	0.0001	1.52	99.9	0	31.61	447.56	3.48
1150	100	29.33	0.0002	0.0001	1.28	99.9	0	29.28	418.18	3.3
		477	0.1269	0.0021	65.84			30.4	432.32	2.01

$^{40}Ar/^{39}Ar$ Step-Heating Analytical
Results

Temp (C)	Cumulative ^{39}Ar(%)	$^{40}Ar/^{39}Ar$	$^{37}Ar/^{39}Ar$	$^{36}Ar/^{39}Ar$	Vol. ^{39}Ar x 10^{-15} mol	%Rad. ^{40}Ar	Ca/K	$^{40}Ar*/^{39}Ar$	Age (Ma)	±1s (Ma)
JM-23c (sericite)										
Mass = 1.40 mg										
J-value = 0.0088915 ± 0.0000489										
500	1.2	32.39	0.0002	0.0115	1.06	89.5	0	29	413.88	3.16
550	4.5	15.16	0.0154	0	3.01	99.9	0.03	15.15	227.96	0.82
600	9.6	23.21	0.0235	0.0006	4.59	99.3	0.04	23.06	336.49	4.37
625	13.3	32.3	0.0355	0.0006	3.33	99.4	0.07	32.11	453.09	2.59
650	17.9	33.44	0.0116	0.0012	4.09	98.9	0.02	33.08	465.19	1.7
675	24.5	33.16	0.0404	0.0001	6.01	100	0.08	33.15	466.03	1.58
700	33.8	32.14	0.0105	0.0009	8.3	99.2	0.02	31.88	450.18	1.49
725	40.7	31.46	0.0001	0.0004	6.21	99.7	0	31.35	443.54	1.92

Chapter 2

Temp (C)	Cumulative ^{39}Ar(%)	^{40}Ar/^{39}Ar	^{37}Ar/^{39}Ar	^{36}Ar/^{39}Ar	Vol. ^{39}Ar x 10^{-15} mol	%Rad. ^{40}Ar	Ca/K	^{40}Ar*/^{39}Ar	Age (Ma)	±1s (Ma)
760	48.9	31.01	0.0001	0.0003	7.38	99.7	0	30.92	438.22	1.78
800	58.5	31	0.0155	0.0006	8.71	99.4	0.03	30.82	436.88	1.58
840	68.6	31.38	0.0001	0.0001	9.09	99.9	0	31.37	443.78	1.71
880	78.2	31.44	0.0135	0.0003	8.65	99.7	0.03	31.34	443.5	1.7
920	88.3	31.88	0.0245	0.0003	9.06	99.8	0.05	31.8	449.22	1.53
970	98.4	32.38	0.0001	0	9.07	100	0	32.37	456.37	1.2
1050	100	33.68	0.0002	0.0011	1.45	99	0	33.36	468.58	3.16
		456.01	0.191	0.0179	90.01			30.73	435.76	1.8

^{40}Ar/^{39}Ar Step-Heating Analytical Results

Temp (C)	Cumulative ^{39}Ar(%)	^{40}Ar/^{39}Ar	^{37}Ar/^{39}Ar	^{36}Ar/^{39}Ar	Vol. ^{39}Ar x 10^{-15} mol	%Rad. ^{40}Ar	Ca/K	^{40}Ar*/^{39}Ar	Age (Ma)	±1s (Ma)

JM-23f (sericite)

Mass = 1.01 mg
J-value = 0.0088733 ± 0.0000532

500	4.7	31.42	0.0488	0.0031	6.11	97.1	0.09	30.52	432.31	4.39
550	10.4	29.32	0.0124	0.0005	7.25	99.5	0.02	29.18	415.41	1.99
600	21.5	28.91	0.0007	0	14.37	100	0	28.9	411.79	1.01
625	32.3	28.75	0.0001	0.0002	13.91	99.8	0	28.68	409	1.46
650	42.6	28.35	0.0001	0	13.37	100	0	28.34	404.72	1.6
675	53.4	27.95	0.0001	0	13.83	100	0	27.94	399.56	0.99
700	63	27.67	0.0001	0	12.38	100	0	27.66	395.98	1.63
730	72	27.54	0.0001	0	11.59	100	0	27.53	394.27	1.25
770	80.5	27.39	0.0016	0.0002	11	99.8	0	27.34	391.78	1.7
820	87	27.33	0.004	0.0003	8.42	99.7	0.01	27.25	390.68	2.01
880	91.7	27.33	0.0125	0.0007	6.11	99.2	0.02	27.12	388.97	2.09
950	96.8	27.39	0.0107	0.0005	6.49	99.5	0.02	27.25	390.7	1.86
1050	100	27.05	0.0076	0.0011	4.17	98.8	0.01	26.73	384.02	1.46
		366.4	0.0987	0.0067	129			28.09	401.44	1.65

^{40}Ar/^{39}Ar Step-Heating Analytical Results

Temp (C)	Cumulative ^{39}Ar(%)	^{40}Ar/^{39}Ar	^{37}Ar/^{39}Ar	^{36}Ar/^{39}Ar	Vol. ^{39}Ar x 10^{-15} mol	%Rad. ^{40}Ar	Ca/K	^{40}Ar*/^{39}Ar	Age (Ma)	±1s (Ma)

BW-1 (sericite)

Mass = 1.52 mg
J-value = 0.0088399 ± 0.0000707

550	7.8	30.54	0.0126	0.0019	16.35	98.1	0.02	29.97	424	1.15
600	20.3	29.77	0.0103	0.0001	25.96	99.9	0.02	29.74	421.13	1.91
625	29.3	29.46	0.0085	0.0007	18.85	99.3	0.02	29.25	414.9	2.67
650	40.2	29.07	0.0196	0.0006	22.64	99.4	0.04	28.9	410.45	1.59

Temp (C)	Cumulative 39Ar(%)	40Ar/39Ar	37Ar/39Ar	36Ar/39Ar	Vol. 39Ar x10-15 mol	%Rad. 40Ar	Ca/K	40Ar*/39Ar	Age (Ma)	±1s (Ma)
675	50.7	28.87	0.0037	0.0006	22.01	99.4	0.01	28.69	407.81	2.08
700	60.5	28.65	0.0192	0	20.34	100	0.04	28.63	407.07	2.43
730	68.8	28.47	0.0014	0.0001	17.29	99.9	0	28.44	404.61	2.53
780	77.7	28.23	0.0042	0.0001	18.69	99.9	0.01	28.22	401.78	2.76
830	83.4	28.18	0.0017	0.0001	11.77	99.9	0	28.16	400.98	2.34
890	87.8	28.24	0.0002	0.0001	9.28	99.9	0	28.2	401.59	3.04
950	92.9	28.62	0.0014	0	10.66	100	0	28.62	406.92	1.64
1000	98	29.19	0.0006	0	10.55	100	0	29.19	414.11	1.37
1050	99.6	29.27	0.0001	0.0001	3.42	99.9	0	29.24	414.82	3.24
1150	100	28.58	0.0599	0.0002	0.8	99.8	0.11	28.53	405.67	2.27
Total		405.16	0.1433	0.0047	208.6			28.91	410.52	2.14

^{40}Ar/^{39}Ar Step-Heating Analytical Results

Temp (C)	Cumulative 39Ar(%)	40Ar/39Ar	37Ar/39Ar	36Ar/39Ar	Vol. 39Ar x10-15 mol	%Rad. 40Ar	Ca/K	40Ar*/39Ar	Age (Ma)	±1s (Ma)

JM-42a (biotite)

Mass = 1.67 mg
J-value = 0.0089495 ± 0.0000313

500	0.3	40.03	0.3555	0.0291	0.56	78.6	0.68	31.46	447.53	5.11
550	0.7	19.72	0.3283	0.0057	0.83	91.6	0.62	18.08	270.56	5.29
600	1.8	15.92	0.1846	0.0014	2.12	97.5	0.35	15.52	234.59	1.77
625	2.9	27.62	0.0808	0.0001	2.29	99.9	0.15	27.6	398.25	1.11
650	5	28.37	0.1352	0.0012	4.14	98.8	0.26	28.02	403.63	1.19
675	8.3	28.27	0.1186	0.0003	6.68	99.8	0.23	28.2	405.94	1.72
700	12.6	28.02	0.1118	0.0001	8.7	99.9	0.21	28	403.43	1.48
725	16	28.2	0.1353	0.0005	6.71	99.5	0.26	28.07	404.29	1.89
750	18.2	27.89	0.2447	0.0005	4.5	99.5	0.47	27.77	400.43	1.57
800	20.5	28.12	0.4455	0.0003	4.58	99.8	0.85	28.07	404.35	1.28
850	22.7	28.35	0.7477	0.0006	4.44	99.6	1.42	28.25	406.65	1.62
900	25.8	28.31	0.8998	0.0004	6.25	99.9	1.71	28.28	406.97	1.58
950	29.5	28.38	0.7201	0.0006	7.4	99.6	1.37	28.28	407.03	1.67
1000	41.5	28.23	0.215	0.0006	24.05	99.5	0.41	28.08	404.42	1.29
1050	60.7	27.71	0.0832	0.0003	38.61	99.7	0.16	27.63	398.56	1.28
1100	85.8	27.58	0.0492	0.0001	50.33	99.9	0.09	27.55	397.56	1.45
1150	99.3	27.44	0.1034	0.0004	27.22	99.6	0.2	27.35	394.97	1.35
1200	100	28.93	0.7953	0.0029	1.32	97.3	1.51	28.14	405.25	5.96
		497.09	5.7543	0.0449	200.7			27.6	398.22	1.47

^{40}Ar/^{39}Ar Step-Heating Analytical Results

Temp (C)	Cumulative 39Ar(%)	40Ar/39Ar	37Ar/39Ar	36Ar/39Ar	Vol. 39Ar x10-15 mol	%Rad. 40Ar	Ca/K	40Ar*/39Ar	Age (Ma)	±1s (Ma)

Chapter 2

JM-43b (sericite)

Mass = 1.30 mg
J-value = 0.0089637 ±
0.0000314

550	7.2	30.38	0.021	0.0026	6.68	97.5	0.04	29.63	424.88	2.62
600	15.3	27.85	0.0201	0.0008	7.55	99.1	0.04	27.6	398.84	1.66
650	26.3	29.36	0.0069	0.0006	10.19	99.4	0.01	29.19	419.28	1.49
680	37.2	28.88	0.0108	0.0015	10.13	98.5	0.02	28.45	409.74	1.98
710	47.7	28.11	0.0117	0.0011	9.72	98.8	0.02	27.78	401.15	2.09
740	58	27.34	0.0084	0.0005	9.64	99.4	0.02	27.19	393.47	1.93
780	68.4	27.29	0.0148	0.0005	9.59	99.4	0.03	27.13	392.73	1.98
820	76.2	26.99	0.0305	0.0016	7.27	98.2	0.06	26.51	384.62	1.6
870	83.5	26.52	0.0175	0.0008	6.8	99.1	0.03	26.28	381.65	2.18
920	90.2	26.77	0.0173	0.0012	6.19	98.6	0.03	26.41	383.36	2.17
980	96	26.64	0.0136	0.0014	5.36	98.5	0.03	26.24	381.05	3.14
1040	99.2	26.8	0.042	0.0001	2.99	99.8	0.08	26.76	387.89	3.5
1120	100	28.58	0.0113	0.0107	0.77	88.9	0.02	25.41	370.22	6.66
		361.52	0.2261	0.0236	92.87			27.56	398.23	2.11

Chapter 3: Testing time for the fool's clock: ^{40}Ar/^{39}Ar dating of hydrothermally overprinted pyrite

D. Phillips and J. McL. Miller

Summary

Previous studies have speculated that pyrite may armour potassium-bearing mineral inclusions from alteration-induced argon loss, thus providing improved ^{40}Ar/^{39}Ar age results. To test this hypothesis, matrix muscovite and pyrite crystals hosting muscovite inclusions were selected from three variably overprinted orogenic gold deposits and analysed by combined single crystal ^{40}Ar/^{39}Ar laser-probe and *in vacuo* crushing methods. Pyrite grains from the ~2.60 Ga Mt Charlotte gold deposit exhibit evidence of minor argon loss, but give concordant high temperature ages averaging 2594 ± 8 Ma (2σ), indistinguishable from previous age estimates. Matrix mica from the ~2.63 Ga Kanowna Belle gold deposit yielded a discordant age spectrum with all ages younger than 2.5 Ga, indicating substantial ^{40}Ar* loss related to mid-Proterozoic thermal overprinting. Crushing and low temperature heating experiments on pyrite crystals from Kanowna Belle produced anomalously old apparent ages (up to 7.0 Ga) – however, in contrast to the matrix mica, total-gas pyrite ages generally approach or overlap the inferred time of gold mineralization. This behaviour is attributed to diffusion of ^{40}Ar* to internal muscovite/pyrite grain boundaries in response to the mid-Proterozoic thermal event, with limited external loss of argon. Matrix mica from the ~440 Ma Stawell gold deposit, hydrothermally overprinted at ~400 Ma, exhibits a discordant age spectrum attributed to recoil loss/redistribution of ^{39}Ar$_K$. High temperature steps from most Stawell pyrite grains give ages averaging 436 ± 4 Ma, within error of the inferred time of gold mineralisation. However, it is unclear whether these results are also affected by recoil effects. It is concluded that pyrite acts as a partially closed system for argon, but that the ^{40}Ar/^{39}Ar 'pyrite' dating method has the potential to 'see through' later thermal/alteration events and resolve controversial aspects of ore deposit geochronology.

3.1 Introduction

Pyrite contains negligible structural potassium and would normally be a poor candidate for ^{40}Ar/^{39}Ar geochronology - unless it contains potassium-bearing mineral inclusions. ^{40}Ar/^{39}Ar dating of 'pyrite' was first attempted by York et al. (1982), who obtained an imprecise isochron age of 2500 ± 240 Ma (2σ) for analyses of bulk pyrite samples from the Archaean Geco sulphide deposit in Ontario, Canada. These authors attributed the potassium and argon in pyrite to encapsulated silicate or fluid inclusions. More recently, Smith et al. (2001) used the ^{40}Ar/^{39}Ar laser probe method to analyse single pyrite grains from igneous intrusions in Brazil. These grains yielded similar ages to co-existing amphibole, suggesting that at least some pyrite samples can provide precise and reliable age information. The potassium content of the pyrite grains was attributed to the presence of microscopic inclusions of feldspar, amphibole and phlogopite.

Although the results reported by Smith et al. (2001) are tantalizing, there has been no further application of the 'pyrite' dating method. Possible reasons include the higher radioactivity of pyrite compared to minerals typically used for ^{40}Ar/^{39}Ar dating, contamination of analytical lines by sulphur leading to elevated system blanks, and the fact that there may be no incentive to date 'pyrite' when co-existing potassium-rich minerals are present. Nonetheless, there are circumstances in which the dating of pyrite hosting potassium-bearing inclusions may be particularly useful. Smith et al. (2001) noted that phlogopite from one igneous intrusion yielded a younger age than either co-existing pyrite or amphibole, which they attributed to post-crystallization alteration. These authors concluded that pyrite protects potassium-bearing inclusions from alteration and may act as a 'time capsule', inhibiting both diffusive loss of ^{40}Ar and recoil loss of ^{39}Ar.

In this study, we test the hypothesis that pyrite is capable of armouring potassium-bearing inclusions and investigate whether the ^{40}Ar/^{39}Ar 'pyrite' dating method can 'see through' younger alteration/thermal events. To this end, we selected pyrite samples containing muscovite inclusions from two well-constrained Archaean gold deposits in Western Australia and from the Ordivician/Silurian Stawell gold deposit in Victoria, all of which have undergone variable degrees of hydrothermal/thermal overprinting.

3.2 Geology and sample selection

Gold-bearing pyrite samples were selected from the Mt Charlotte and Kanowna Belle deposits, both located in the Eastern Goldfields Province of the Yilgarn craton, Western Australia. The Eastern Goldfields Province is a late Archean granite-greenstone terrane comprising deformed and metamorphosed volcanics and sediments intruded by granites and felsic volcanics (e.g. Witt, 1993; Groves et al., 1995). Gold mineralization is hosted by a variety of greenstones and generally post-dates peak metamorphism (e.g. Yeats et al., 1999). Previous geochronological work on hydrothermal muscovite related to gold stockwork systems at Mount Charlotte yielded reproducible ^{40}Ar/^{39}Ar ages averaging 2602 ± 8 Ma (2σ), which were interpreted to represent the time of gold deposition (Kent and McDougall, 1995). The age of the Kanowna Belle lode-gold deposit is constrained by cross-cutting felsic porphyry dykes to be less than ~2655 Ma, with mineralization considered to have occurred at ~2630 Ma, based on reset U-Pb zircon ages, Pb-Pb ages of ore-related galena and an affinity with similar gold deposits in the region (Ross et al., 2004).

Sample MC1 was taken from a quartz stockwork vein at Mt Charlotte (drill-hole MC263; 92 m) and comprises mainly quartz, muscovite (<0.15 mm) and pyrite (0.15 – 0.50 mm). This sample was selected to test the efficacy of the pyrite dating method on samples that exhibit only minor argon loss, as evidenced from analyses of MC1 matrix mica. Two samples, GD1 (drill-hole GDD438; 351 m) and K1 (drill-hole KDU1640; 200 m), were collected from the Kanowna Belle mine and also contain abundant muscovite (<0.15 mm) and pyrite (0.20 – 0.50 mm). The latter two samples were selected to determine the effects of mid-Proterozoic thermal events that have overprinted GD1 matrix muscovite. Pyrite grains from all three samples contain relatively coarse (up to 0.15 mm) muscovite inclusions (Fig. 3-1), enabling direct comparisons with matrix muscovite from the same samples and also minimizing ^{39}Ar$_K$ recoil loss/redistribution problems.
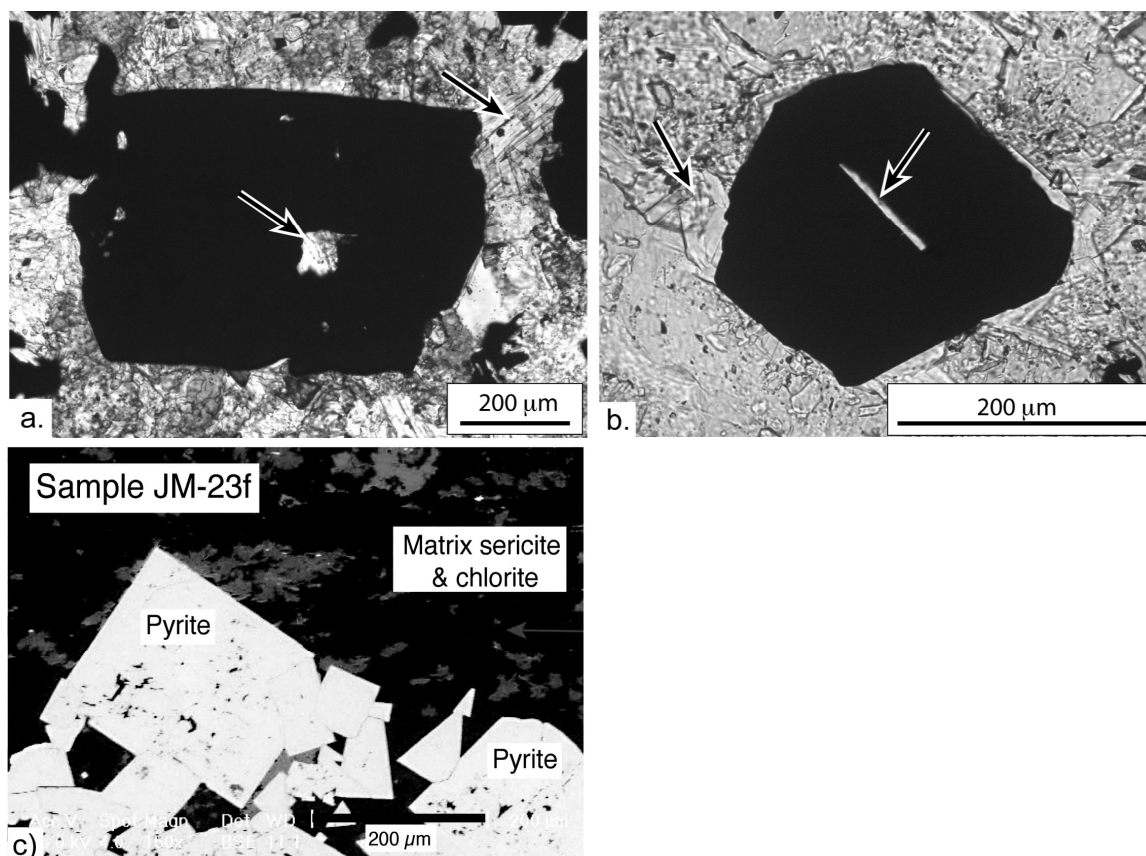
Fig 3-1. Photomicrograph showing muscovite inclusions in pyrite grains from a) Mount Charlotte sample MC1. Note the relatively coarse grain-size of the muscovite inclusion. Arrows point to matrix and included mica grains. b) Kanowna Belle sample GD1. Note again the relatively coarse grain-size of the muscovite inclusion. c) Stawell mine sample JM-23f, showing the presence of abundant, fine-grained inclusions of matrix minerals in euhedral pyrite grains.

A single sample (JM-23f) was collected from the Stawell gold deposit in western Victoria. Gold mineralisation in the region is associated with brittle deformation along the flanks of basalt domes that are overlain by deformed turbidite sequences. The main phase of gold deposition has been dated at ~440 Ma (e.g. Foster et al., 1998). Sample JM-23f was cut from a quartz-calcite vein in the Hangingwall Lode of the Magdala mine and comprises quartz, calcite, sericite, pyrite and minor biotite (Fig. 3-1c). This sample was selected to determine whether pyrite could preserve ~440 Ma gold mineralisation ages despite hydrothermal overprinting by infiltrating fluids from the nearby Stawell pluton, which has a U-Pb SHRIMP age of 399 ± 3 Ma (see Frederickson and Gane, 1998).

3.3 Analytical methods and results

Muscovite and pyrite separates from samples MC1, GD1, K1 and JM-23f, together with the flux monitors GA1550 (98.8 ± 0.5 Ma; Renne et al., 1998) and Hb3gr (1072 Ma; Turner et al., 1971) were irradiated in position 5c of the McMaster Nuclear Reactor, Hamilton, Ontario. Muscovite step-heating analyses were conducted in a tantalum resistance furnace linked to a VG 3600 mass spectrometer equipped with a Daly detector. Laser step-heating and crushing analyses of pyrite crystals were achieved

using a Spectron Nd-YAG laser and modified Nupro® valve connected to a Micromass 5400 mass spectrometer, also with a Daly detector. Analytical procedures generally followed those described by Fergusson et al. (2005). Sulphur contamination of the laser extraction line was minimized through the use of copper sample holders and a silver mesh filter. ^{40}Ar/^{39}Ar analytical results are summarized in Table 3-1, with the full data-set listed in Appendix 3. Unless otherwise stated, uncertainties are quoted at the two sigma level.

TABLE 1. Summary of ^{40}Ar/^{39}Ar step-heating analytical results

Locality	Sample No	Mineral	Sample wt (mg)	No grains	Low temp ages (Ma) Minimum	Maximum	Fusion ages (Ma) Minimum	Maximum	Total-gas age (Ma) Minimum	Maximum	Plateau age (Ma)	Isochron age (Ma)
Mount Charlotte	MC263	muscovite*	0.58		2033 ± 18			2663 ± 14		2565 ± 12	2564 ± 9	
		'pyrite'**		12	2052 ± 24	2604 ± 23	2578 ± 14	2626 ± 24	2550 ± 16	2603 ± 39		2594 ± 8
Kanowna Belle	GD1	muscovite*	0.97		1605 ± 15			2495 ± 11		2344 ± 14		
		'pyrite'**		15	2466 ± 14	4014 ± 18	1945 ± 52	2565 ± 14	2252 ± 20	2714 ± 22		
	K1	'pyrite'**		14	2495 ± 44	4050 ± 39	2131 ± 12	2604 ± 16	2341 ± 24	2786 ± 26		

Note: uncertainties in reported ages are at the two sigma level.
*Muscovite separates were heated incrementally from 500ūC to 1450ūC (15 and 24 steps, respectively).
**Single pyrite crystals (12 - 15 per sample) containing muscovite inclusions were laser step-heated in two to five increments.

Matrix muscovite from Mount Charlotte sample MC1 yielded a somewhat saddle-shaped age spectrum with apparent ages ranging from 2033 ± 18 Ma to 2663 ± 14 Ma for a total-gas age of 2565 ± 12 Ma (Fig. 3-2a). Both the total-gas and the statistically applicable plateau age (2561 ± 9 Ma) are distinctly younger than the ~2600 Ma ages reported by Kent and McDougall (1995). Twelve pyrite grains from sample MC263 were individually step-heated in two to five increments. Although some grains yielded younger low temperature ages (Fig. 3-2b), the high temperature results are concordant and define an isochron with an age of 2594 ± 8 Ma and a ^{40}Ar/^{36}Ar ratio of 294 ± 5 (Fig. 3-2c). The pyrite age is thus older than the average muscovite age from this sample, but indistinguishable from the results of Kent and McDougall (1995).

Matrix muscovite from Kanowna Belle sample GD1 produced a highly discordant age spectrum, with apparent ages ranging from 1606 ± 16 to 2495 ± 11 Ma, giving a total-gas age of 2344 ± 16 Ma (Fig. 3-3a). Step-heating analyses of pyrite grains from samples GD1 (n = 15) and K1 (n = 14) yielded distinctive age spectra, characterized by anomalously old low temperature ages (up to 4.05 Ga) and younger high temperature results (>1.80 Ga) (Fig 3-3b). Pyrite total-gas ages for samples GD1 and K1 are similar and range from 2252 ± 20 to 2714 ± 22 Ma and from 2341 ± 24 to 2786 ± 26 Ma, respectively, although most results are between 2550 and 2620 Ma (Fig. 3-3c). Seven of the older total-gas ages are concordant, with a mean age of 2625 ± 9 Ma.

To investigate the source of the anomalously old, low temperature, ages obtained from the Kanowna Belle pyrite grains, comparative crushing experiments were undertaken on pyrite from samples GD1 (n = 10; 0.81 mg) and MC1 (n = 20; 0.82 mg). Crushing released relatively large quantities of ^{40}Ar from GD1 (~1.5x10^{-10} mol/g), but only minor amounts of ^{39}Ar$_K$, resulting in an average apparent age of 6980 ± 45 Ma and a ^{40}Ar/^{36}Ar ratio of 3393 ± 68. Mass balance estimates indicate that gas proportions released by

crushing are similar to those out-gassed during low temperature heating, suggesting that this component is located in low retention sites. In contrast, crushing of pyrite grains from MC1 produced lower $^{40}Ar^*$ yields (1.53×10^{-11} mol/g) and $^{40}Ar/^{36}Ar$ ratios as low as 445 ± 4, consistent with the more concordant ages obtained from this sample.
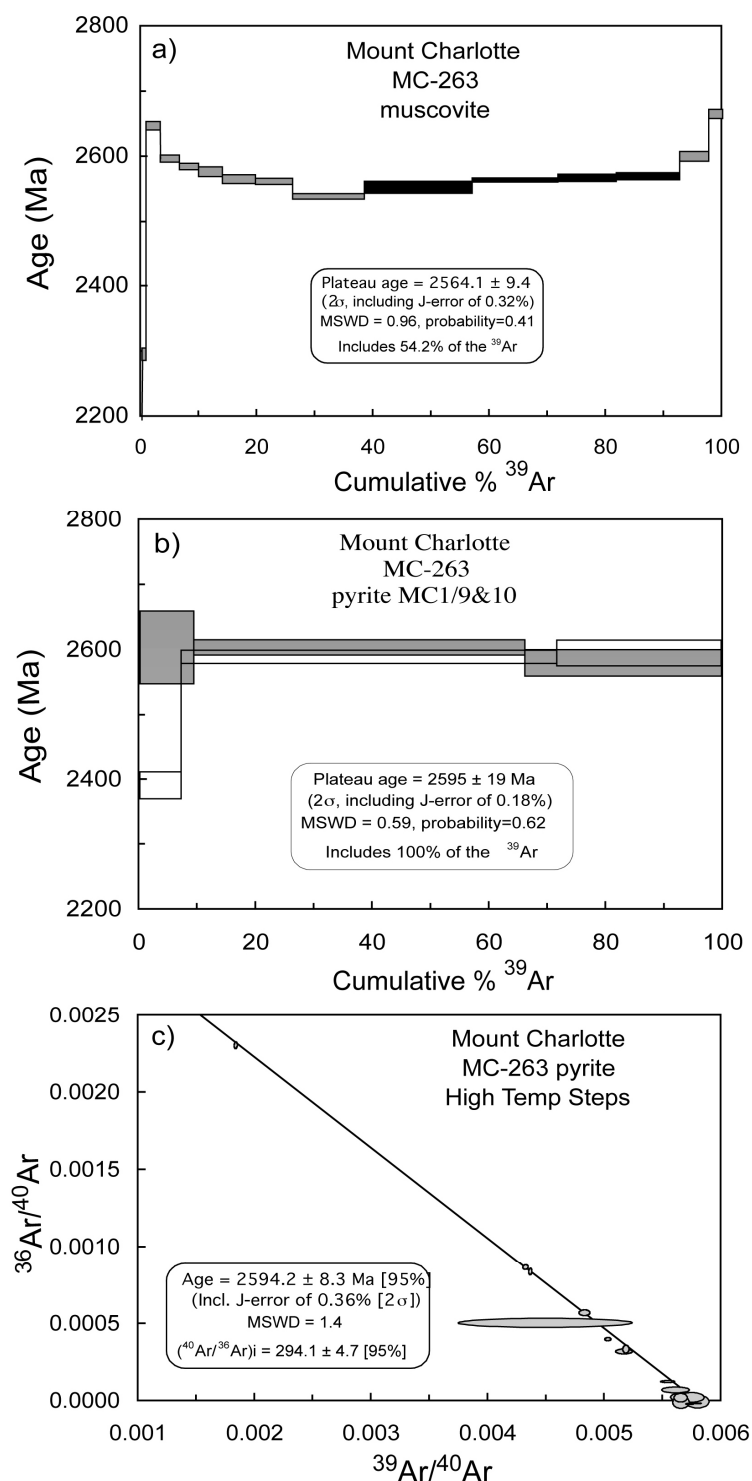
Fig 3-2. a) $^{40}Ar/^{39}Ar$ step-heating age spectrum for matrix muscovite from Mount Charlotte sample MC1. Box heights are $\pm 1\sigma$ uncertainties. b) Laser step-heating results for two single pyrite grains from sample MC1, illustrating the two main types of spectra obtained. Grains such as MC1/9 exhibit plateau ages (dark grey boxes), whereas other crystals (e.g. MC1/10) give younger low temperature apparent ages. c) Inverse isochron plot showing high temperature results for 12 MC1 pyrite grains.
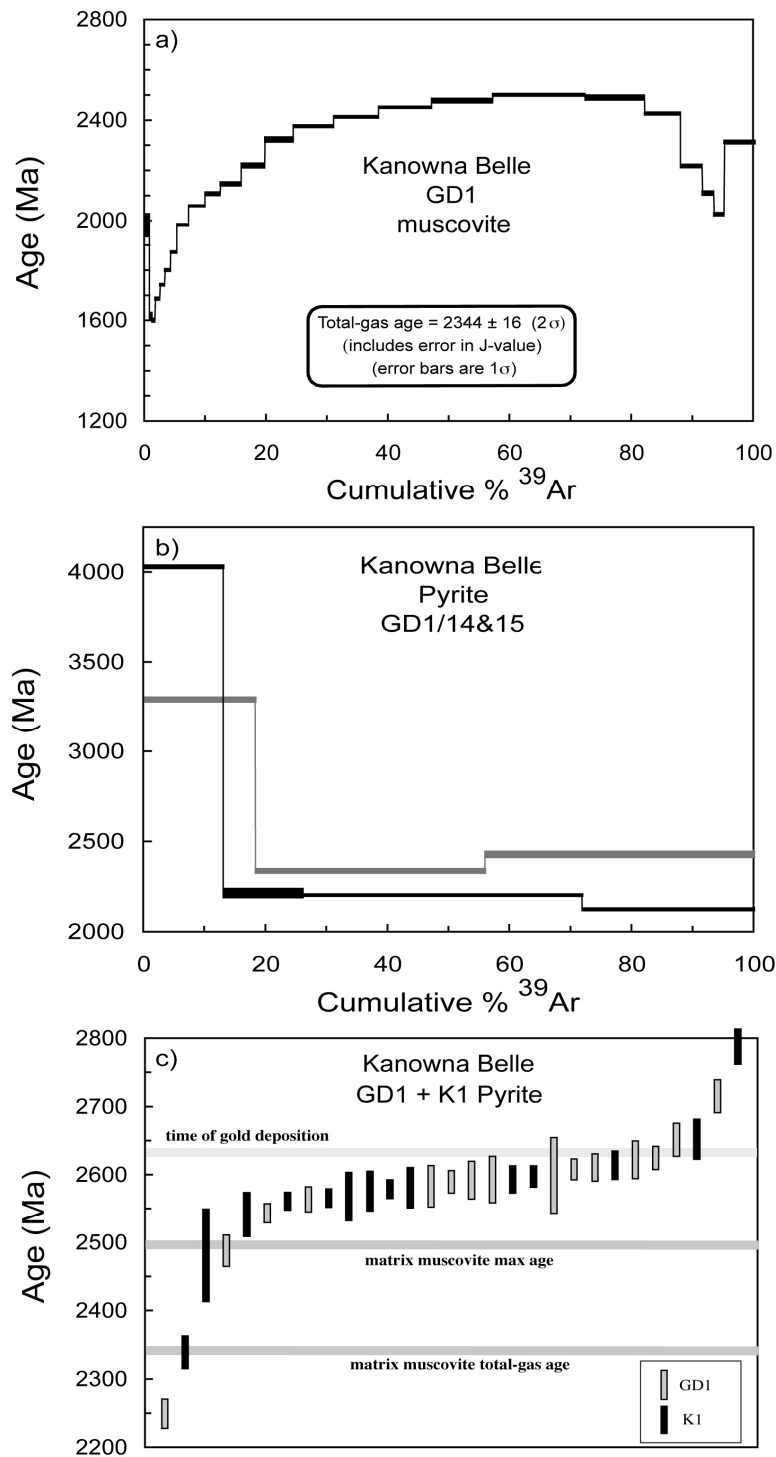
Fig 3-3. a) ^{40}Ar/^{39}Ar age spectrum for a muscovite separate from Kanowna Belle sample GD1. Box heights represent ±1σ errors. b) Representative age spectra for two single pyrite grains from GD1 and K1; only 2 of 29 spectra are shown for clarity. c) Summary of total-gas ages for single pyrite grains from samples GD1 and K1 (error boxes are ±2σ), illustrating that most ages are intermediate between the maximum matrix muscovite ages (<2500 Ma) and the time of gold mineralization (~2630 Ma; Ross et al., 2004).
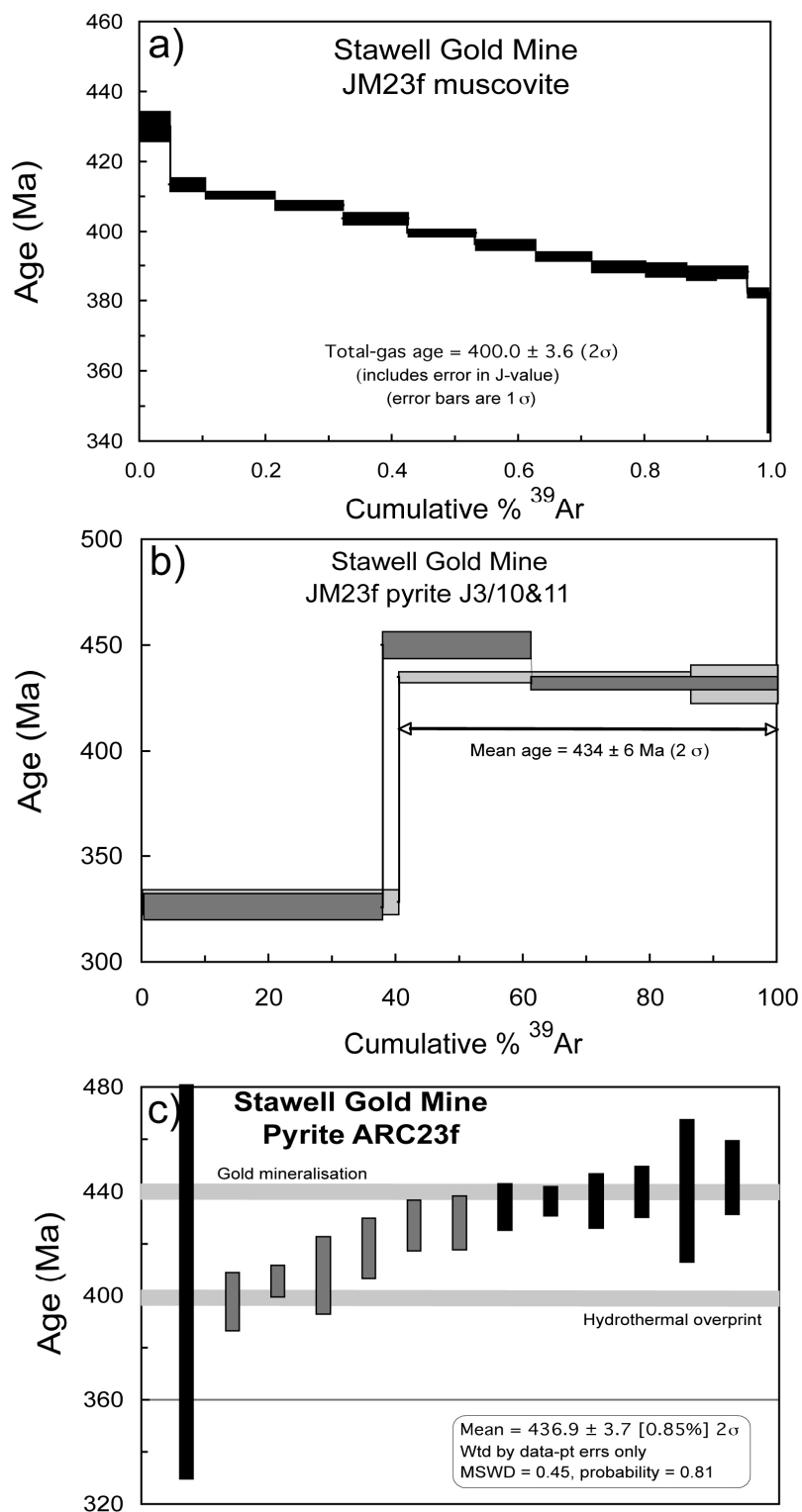
Fig 3-4. a) ^{40}Ar/^{39}Ar age spectrum for a sericite separate from Stawell sample JM-23f (box heights are ±1σ errors). b) Representative age spectra for two single pyrite grains from sample JM-23f. c) Summary of high temperature ages for single pyrite grains from sample JM-23f (error boxes are ±2σ).

Matrix sericite from Stawell sample JM-23f is characterised by a highly discordant age spectrum, with apparent ages decreasing with increasing temperature from 430 ± 8 Ma to 343.1 ± 8 Ma (Fig. 3-4a). The total-gas age for the sample is 400 ± 3 Ma. Possible explanations for the discordance include excess argon contamination and recoil loss/redistribution of $^{39}Ar_K$. In contrast to the matrix sericite results, $^{40}Ar/^{39}Ar$ laser probe analyses of single pyrite grains generally show increasing apparent ages with increasing temperature, a pattern that is more consistent with $^{40}Ar^*$ loss than $^{39}Ar_K$ recoil loss (Fig. 3-4b). Total-gas ages range from 306 ± 9 Ma to 419 ± 6 Ma, whereas most high temperature steps vary from 400 to 445 Ma (Fig. 3-4c). Nine of thirteen pyrite grains have concordant high temperature ages averaging 435 ± 4 Ma. The five oldest high temperature steps average 438 ± 4 Ma.

3.4 Discussion

$^{40}Ar/^{39}Ar$ laser probe analyses of single pyrite grains from sample MC263 provide the most precise estimate (2594 ± 8 Ma) for the timing of gold mineralization at Mount Charlotte. The younger average age obtained for matrix muscovite from this sample is suggestive of minor argon loss, possibly related to later hydrothermal alteration. That some pyrite crystals from MC263 also exhibit evidence of argon loss (Fig. 3-2b) is noteworthy and demonstrates that pyrite is not the perfect 'time capsule' suggested by Smith et al. (2001). It is well known that sulphide minerals such as pyrite are retentive of noble gasses, including helium (e.g. Turner and Stuart, 1992), which suggests that argon loss by volume diffusion through pyrite may not be the controlling mechanism for argon loss. Rather, it is suggested that pyrite behaves as a partially closed system, in which some inclusions are exposed to the surroundings through fractures, sub-grain boundaries and/or by virtue of their location at pyrite grain boundaries (Fig. 3-5). Exposed inclusions, which are more susceptible to argon loss, are then preferentially out-gassed during initial heating of the pyrite, with argon from armoured inclusions released at higher temperatures. This explanation can account for both argon loss from pyrite and the discrepancy between the MC263 pyrite and muscovite results - and may also explain the scattered results reported by York et al. (1982) for total-fusion analyses of pyrite from the Geco mine samples.
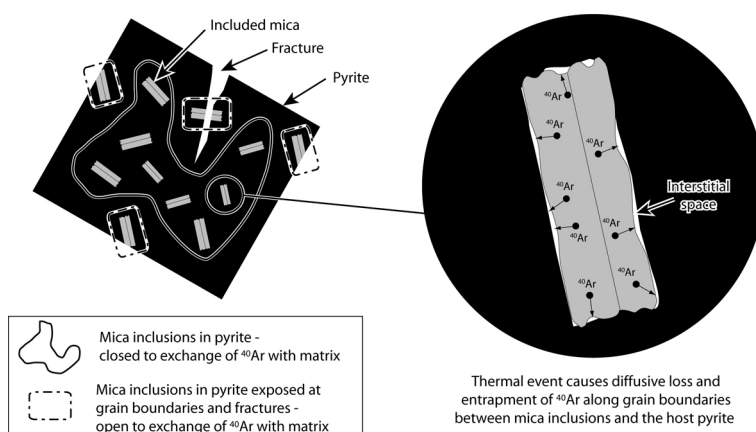
Fig 3-5. Diagram illustrating possible muscovite inclusion geometries in pyrite. Muscovite inclusions exposed to the surroundings behave as open systems and can incur argon loss; armored inclusions will act as closed systems. During thermal events, argon will diffuse to and accumulate at inclusion/pyrite grain boundaries. This grain boundary component is released during the first step-heating and crushing experiments.

The discordant ^{40}Ar/^{39}Ar step-heating spectrum obtained from the Kanowna Belle matrix muscovite implies significant argon loss, which is attributed to mid-Proterozoic thermal events that affected the northern parts of the Eastern Goldfields Province. The Kanowna Belle pyrite step-heating spectra are clearly unusual and atypical of samples that have experienced argon loss. Our preferred explanation for these out-gassing profiles involves (partial?) diffusive redistribution of ^{40}Ar* from the muscovite inclusions to internal inclusion/pyrite grain boundaries, in response to mid-Proterozoic heating (Fig. 3-5). The dense structure of pyrite and the preferential partitioning of noble gases to defects and fluid phases (e.g. Trull and Kurz, 1993; Kelley et al., 1997) results in the effective retention of argon within pyrite. This grain boundary component is then preferentially released during crushing and low temperature heating analyses.

Similar out-gassing behavior has been observed previously in ^{40}Ar/^{39}Ar studies of biotite inclusions in thermally overprinted garnet (Kelley et al., 1997) and for clinopyroxene inclusions in diamonds entrained in kimberlite magmas (Burgess et al., 1992). In both cases, ^{40}Ar* was shown to accumulate along inclusion/host grain boundaries in response to post-encapsulation heating, with gas loss only occurring on brittle failure of the host mineral and exposure of internal inclusion/host grain boundaries to the surroundings.

If the ^{40}Ar* grain boundary component is retained quantitatively by the Kanowna Belle pyrite grains, then the total-gas ages should provide an estimate of the time of muscovite crystallization. However, as pyrite appears to be a variably closed system (Fig. 3-5), argon loss from exposed inclusions would be expected to yield younger ages ranging up to the time of mineralization. For samples GD1 and K1, all but two total-gas ages are similar to, or younger, than the inferred time of gold mineralization (~2630 Ma). Of this group, the oldest five samples have a mean age of 2625 ± 9 Ma, within error of the preferred time of gold deposition (~2630 Ma; Ross et al., 2004).

An alternative explanation for the anomalously old ages, obtained from crushing and low temperature experiments on the Kanowna Belle pyrite samples, is release of excess ^{40}Ar from fluid inclusions. Although we cannot totally discount contributions from fluid inclusions, the presence of excess argon is not supported because: 1) the majority of total-gas ages obtained from Kanowna Belle pyrite grains are similar or younger than the inferred time of gold mineralization; 2) pyrite from two widely separated samples form different structural zones in the Kanowna Belle deposit produced almost identical total-gas results; 3) K/Cl ratios for GD1 pyrite grains (~10 – 120) are poorly correlated with apparent age; 4) Mt Charlotte pyrite grains contain negligible excess argon.

Excess argon contamination could, however, account for the two anomalously old Kanowna Belle pyrite grains (Fig. 3c), although incorporation of older detrital/xenocrystic inclusions in pyrite is also a possible explanation. In this regard, Dunlap (1997) has demonstrated that detrital muscovite grains are able to survive Greenschist facies metamorphism.

Taken at face value, the Stawell pyrite results appear similar to those from Mt Charlotte, in that the highest temperature steps approach the inferred time of gold mineralisation (439 ± 2 Ma; Foster et al., 1998). In fact, 9 of 13 pyrite grains have similar high

temperature ages, with a mean age of 436 ± 4 Ma, which is within error of previously reported ages for this deposit. However, the age spectra obtained from the pyrite grains are quite different to that of the matrix sericite (Fig. 3-4a,b). The sericite pattern, of decreasing apparent ages with increasing temperature, could be due to either excess argon contamination or recoil loss/redistribution of $^{39}Ar_K$, with any $^{40}Ar*$ loss masked by these effects. Given the fine grain size of the matrix sericite and a total-gas age (400 ± 3 Ma) that is similar to the nearby Stawell granite, recoil loss/redistribution is considered to be the most likely explanation for the sericite age discordance. The fact that the pyrite grains exhibit different age spectrum patterns suggests either, that the mica inclusions in pyrite are unaffected by recoil loss/redistribution of $^{39}Ar_K$, or that recoil affects mica inclusions in a different way to matrix sericite. If recoil loss from mica inclusions is minimal, then the younger low temperature pyrite ages are best explained by argon loss from inclusions exposed to the surroundings. In this case, the high temperature apparent ages would provide the best constraints on the age of pyrite crystallisation (~440 Ma). Alternatively, recoil loss of ^{39}Ar from mica inclusions could embed into pyrite and other included matrix phases and/or along pyrite/inclusion grain boundaries. Preferential release of recoiled ^{39}Ar during low temperature heating would result in lower $^{40}Ar/^{39}Ar$ ratios and younger apparent ages. In this case, the total-gas ages would provide the most appropriate constraints on the time of pyrite crystallisation and would imply a minimum age for gold mineralisation of ~420 Ma. Resolution of this issue requires analyses of additional well-constrained samples. Nonetheless, the use of either total-gas or high temperature ages for the Stawell pyrite grains would indicate formation prior to the ~400 Ma hydrothermal event that overprinted sample JM-23f.

Many ore deposits, including orogenic gold systems, have proven extremely difficult to date in the past, due to multiple episodes of gold mineralization, post-depositional hydrothermal alteration events and/or the presence of fine-grained white micas that are susceptible to recoil loss/redistribution of ^{39}Ar (e.g. Kerrich et al., 1994; Hanes et al., 1994; Witt et al., 1996; Kent and McDougall, 1996; Fergusson and Phillips, 2001). The current study highlights the potential of the 'pyrite' dating method to 'see through' younger thermal events. Therefore, combined analyses of matrix mica and mica inclusions in pyrite could provide improved age constraints for many hydrothermally overprinted gold systems, and give new insights into controversies surrounding the age of deposits such as Val D'Or in Canada (e.g. Kerrich, 1994; Hanes et al., 1994).

3.5 Acknowledgements

References

Burgess, R., Turner, G. and Harris, J.W., 1992, ^{40}Ar-^{39}Ar laser probe studies of clinopyroxene inclusions in eclogitic diamonds: Geochimica et Cosmochimica Acta, v.56, 389-402.

Dunlap, W.J., 1997, Neocrystallisation or cooling? ^{40}Ar/^{39}Ar ages of white micas from low-grade mylonites: Chemical Geology, v.143, 181-203.

Fergusson, C.L., and Phillips, D., 2001, ^{40}Ar/^{39}Ar and K-Ar age constraints on the timing of regional metamorphism, south coast of New South Wales, Lachlan Fold Belt: problems and implications: Australian Journal of Earth Sciences, v.48, 395-408.

Fergusson, C.L., Fanning, C.M., Phillips, D. and Ackerman, B.R., 2005, Structure, detrital zircon U-Pb ages and ^{40}Ar/^{39}Ar geochronology of the Early Palaeozoic Girilambone Group, central New South Wales: subduction, contraction and extension associated with the Benambran Orogeny: Australian Journal of Earth Sciences, v.52, 137-159.

Foster, D.A., Gray, D.R., Kwak, T.A.P. and Bucher, M., 1998, Chronology and tectonic framework of turbidite hosted gold deposits in the western Lachlan Fold Belt, Victoria: ^{40}Ar-^{39}Ar results: Ore Geology Reviews, v.13, 229-250.

Frederickson, D.C. and Gane, M., 1998, Stawell Gold Deposit, in Berkman, D.A. and Mackenzie, D.H., eds., Geology of Australian and Papua New Guinean Mineral Deposits: The Australasian Institute of Mining and Metallurgy, Melbourne, 535-542.

Groves, D.I., Ridley, J.R., Bloem, E.M.J., Gebre-Mariam, M., Hageman, S.G., Hronsky, J.M.A., Knight, J.T., McNaughton, N.J., Ojala, J., Vielriecher, R.M., McCuaig, T.C. and Holyland, P.W., 1995, Lode gold deposits of the Yilgarn block: Products of late Archaean crustal-scale over-pressured hydrothermal systems: Geological Society of London, Special Publication 95, p. 155-172.

Hanes, J.A., Archibald, D.A. and Hodgson, C.J., 1994, Dating of Archean auriferous quartz vein deposits in the Abitibi Greenstone Belt, Canada: ^{40}Ar/^{39}Ar evidence for a 70- to 100-M.Y.-time gap between plutonism-metamorphism and mineralization – A reply: Economic Geology, v.89, 687-690.

Kelley, S.P., Barlett, J.M. and Harris, N.B.W., 1997, Pre-metamorphic Ar-Ar ages from biotite inclusions in garnet: Geochimica et Cosmochimica Acta, v.61, 3873-3878.

Kent, A.J. and McDougall, I., 1995, ^{40}Ar/^{39}Ar and U-Pb age constraints on the timing of gold mineralization in the Kalgoorlie gold field, Western Australia: Economic Geology, v.90, 845-859.

Kent, A.J. and McDougall, I., 1996, ^{40}Ar/^{39}Ar and U-Pb age constraints on the timing of gold mineralization in the Kalgoorlie gold field, Western Australia – A reply: Economic Geology, v.91, 795-799.

Kerrich, R., 1994, Dating of Archean auriferous quartz vein deposits in the Abitibi Greenstone Belt, Canada: ^{40}Ar/^{39}Ar evidence for a 70- to 100-M.Y.-time gap between plutonism-metamorphism and mineralization – A discussion: Economic Geology, v.89, 679-687.

Krapez, B., Brown, S.J.A., Hand, J., Barley, M.E., Cas, R.A.F., 2000, Age constraints on recycled crustal and supracrustal sources of Archean metasedimentary sequences, Eastern Goldfields Province, Western Australia: evidence from SHRIMP zircon dating: Tectonophysics, v.322, 89-133.

Renne, P.R., Swisher, C.C., Deino, A.L., Karner, D.B., Owens, T.L., and DePaolo, D.J., 1998, Intercalibration of standards, absolute ages and uncertainties in ^{40}Ar/^{39}Ar

dating: Chemical Geology, v.145, 117-152.

Ross, A.A., Barley, M.E., Brown, S.J.A., McNaughton, N.J., Ridley, J.R., and Fletcher, I.R., 2004: Precambrian Research, v.128, 105-142.

Smith, P.E., Evensen, N.M., York, D., Szatmari, P. and de Oliveira, D.C., 2001, Single-crystal ^{40}Ar-^{39}Ar dating of pyrite: No fool's clock: Geology, v. 29, p. 403-406.

Trull, T.W., and Kurz, M.D., 1993, Experimental measurements of ^{3}He and ^{4}He mobility in olivine and clinopyroxene at magmatic temperatures: Geochimica Cosmochimica Acta, v.57, 1313-1324.

Turner, G., and Stuart, F., 1992, Helium/heat ratios and deposition temperatures of sulphides from the ocean floor: Nature, v.357, 581-583.

Turner, G., Huneke, J.C., Podosek, F.A., and Wasserburg, G.J., 1971, ^{40}Ar-^{39}Ar ages and cosmic ray exposure ages of Apollo 14 samples: Earth and Planetary Science Letters, v.12, 19-35.

Witt, W.K., 1993, Gold minerlization in the Menzies-Kambalda region, Eastern Goldfields, Western Australia: Australian Geological Survey Report, v.39, 165p.

Witt, W.K., Swager, C.P. and Nelson, D.R., 1996, ^{40}Ar/^{39}Ar and U-Pb age constraints on the timing of gold mineralization in the Kalgoorlie gold field, Western Australia – A discussion: Economic Geology, v.91, 792-795.

Yeats, C.J., McNaughton, N.J., Ruettger, D., Bateman, R., Groves, D.I., Harris, J.L. and Kohler, E., 1999, Evidence for diachronous Archean lode gold mineralization in the Yilgarn craton, Western Australia: A SHRIMP U-Pb study of intrusive rocks: Economic Geology, v. 94, 1259-1276.

York, D., Masliwec, A., Kuybida, P., Hanes, J.A., Hall, C.M., Kenyon, W.J., Spooner, E.T.C. and Scott, S.D., 1982, ^{40}Ar/^{39}Ar dating of pyrite: Nature, v.300, 52-53.

Appendix 3:

SUPPLEMENTARY $^{40}Ar/^{39}Ar$ DATA TABLES.

$^{40}Ar/^{39}Ar$ step-heating results obtained on matrix muscovite samples from the Mount Charlotte (MC1), Kanowna Belle (GD1) and Stawell (JM-23f) mines are listed in Table A. Analytical results for pyrite grains containing muscovite inclusions from Mount Charlotte (MC1), Kanowna Belle (GD1, K1) and Stawell (JM-23f) are listed in Table B. All data have been corrected for mass spectrometer backgrounds, radioactive decay and mass discrimination. The molar values for ^{40}Ar, ^{39}Ar, ^{38}Ar, ^{37}Ar and ^{36}Ar have NOT been corrected for isotopic interferences. Correction factors for the interference corrections are given in the footnotes to each table.

Table A. $^{40}Ar/^{39}Ar$ step-heating analytical results for matrix muscovite samples from Mount Charlotte (MC1) and Kanowna Belle (GD1).

Temp (ūC)	Cum.% ^{39}Ar	^{40}Ar (x10^{-13}mol)	±	^{39}Ar (x10^{-14}mol)	±	^{38}Ar (x10^{-16}mol)	±	^{37}Ar (x10^{-16}mol)	±	^{36}Ar (x10^{-16}mol)	±	$^{40}Ar*$ (%)	Ca/K	±	$^{40}Ar*/^{39}Ar$	±	Age (Ma)	±
MC1^a muscovite																		
Mass = 0.58 mg																		
J-value = 0.01698 ± 0.000027																		
500	0.28	0.3415	0.0007	0.0225	0.0001	0.6027	0.0174	0.9542	0.3382	0.2204	0.0058	80.95	0.7420	0.2630	122.84	0.95	2032.6	9.4
600	0.96	0.8906	0.0017	0.0559	0.0004	5.2475	0.0291	1.6470	0.2566	0.1483	0.0078	95.15	0.5156	0.0804	151.60	1.09	2297.6	9.4
700	3.34	3.8573	0.0068	0.1947	0.0008	1.2901	0.0425	9.8428	2.4106	0.1214	0.0245	99.08	0.8848	0.2167	196.31	0.93	2645.1	6.6
750	6.58	5.0478	0.0089	0.2649	0.0009	1.1457	0.0239	8.9202	0.4858	0.1026	0.0118	99.40	0.5893	0.0322	189.42	0.73	2595.7	5.3
780	9.93	5.1544	0.0094	0.2734	0.0007	1.2484	0.0267	14.544	1.7180	0.0776	0.0182	99.56	0.9311	0.1100	187.75	0.63	2583.5	4.6
810	14.02	6.2565	0.0110	0.3343	0.0016	1.1081	0.0665	18.171	2.5830	0.0627	0.0375	99.71	0.9516	0.1354	186.70	1.02	2575.8	7.5
840	19.67	8.5563	0.0154	0.4620	0.0014	1.2617	0.0369	15.042	2.2838	0.0138	0.0924	99.95	0.5699	0.0865	185.14	0.89	2564.3	6.5
860	26.09	9.7059	0.0170	0.5252	0.0013	1.3588	0.0675	11.045	2.8483	0.0185	0.0290	99.94	0.3681	0.0949	184.73	0.60	2561.3	4.4
900	38.40	18.324	0.0330	1.0061	0.0022	2.8342	0.0662	40.152	6.3547	0.1801	0.0669	99.71	0.6986	0.1106	181.65	0.55	2538.3	4.1
950	56.95	27.957	0.0511	1.5162	0.0094	4.2523	0.2543	72.289	5.9811	0.4995	0.1404	99.48	0.8346	0.0693	183.49	1.22	2552.1	9.1
1000	71.59	22.166	0.0386	1.1969	0.0016	2.9773	0.1468	24.403	15.076	0.0968	0.0657	99.86	0.3568	0.2205	184.97	0.44	2563.1	3.2
1050	81.73	15.463	0.0272	0.8292	0.0029	2.2664	0.0869	32.819	7.6150	0.3110	0.0764	99.41	0.6928	0.1608	185.42	0.78	2566.4	5.7
1100	92.59	16.539	0.0286	0.8877	0.0024	2.5035	0.1077	28.570	4.5056	0.1813	0.1084	99.67	0.5633	0.0889	185.75	0.69	2568.9	5.1
1150	97.58	7.7757	0.0137	0.4080	0.0020	1.2907	0.0544	11.552	1.5934	0.1066	0.0503	99.59	0.4956	0.0684	189.83	1.04	2598.7	7.5
1450	100.0	4.3789	0.0075	0.1975	0.0008	1.4677	0.0246	8.5562	1.8137	1.5298	0.0214	89.68	0.7584	0.1608	198.89	0.97	2663.2	6.8
Total															185.17	0.79	2564.5	5.9
GD1^b muscovite																		
Mass = 0.97 mg																		
J-value = 0.018756 ± 0.000047																		
500	0.69	10.828	0.0282	0.2295	0.0011	6.3014	0.1277	2.7984	0.3054	28.357	0.2843	22.61	0.2134	0.0233	106.71	3.89	1982.8	43.9
525	1.09	1.1590	0.0034	0.1335	0.0010	0.3300	0.0052	0.0456	0.0659	4.4118	0.0361	89.47	0.0060	0.0086	77.67	1.03	1621.6	14.2
550	1.62	1.4972	0.0046	0.1777	0.0011	0.3019	0.0041	1.1706	0.1075	4.4654	0.0070	90.79	0.1153	0.0106	76.51	0.54	1605.5	7.6
575	2.41	2.2960	0.0063	0.2620	0.0012	0.4715	0.0083	0.7476	0.0809	4.4317	0.0229	94.41	0.0499	0.0054	84.72	0.52	1690.1	6.8
600	3.23	2.4856	0.0069	0.2720	0.0005	0.4845	0.0082	1.6150	0.0785	4.4118	0.0151	95.08	0.1039	0.0051	86.90	0.35	1744.5	4.5
625	4.14	2.9600	0.0083	0.3033	0.0010	0.6123	0.0218	1.3496	0.0818	6.6221	0.0190	93.76	0.0779	0.0047	91.50	0.44	1802.6	5.5
650	5.19	3.6291	0.0089	0.3500	0.0007	0.8334	0.0094	3.4757	0.1492	7.7474	0.0290	93.90	0.1738	0.0075	97.35	0.40	1874.1	4.8
675	7.07	7.1379	0.0204	0.6273	0.0014	1.4659	0.0144	3.8110	0.8048	1.4759	0.0144	93.87	0.1063	0.0225	106.82	0.41	1984.1	4.6
700	9.75	10.777	0.0274	0.8937	0.0020	1.9309	0.1080	4.3421	1.9587	2.1347	0.0176	94.13	0.0850	0.0384	113.51	0.40	2057.9	4.4
725	12.30	10.542	0.0277	0.8496	0.0045	1.4562	0.0476	4.1344	0.0913	1.7340	0.0750	95.12	0.0852	0.0019	118.04	0.75	2106.2	7.9
750	15.65	14.129	0.0361	1.1161	0.0063	1.9289	0.1155	6.6787	0.4184	1.8021	0.0241	96.21	0.1047	0.0066	121.80	0.76	2145.4	7.9
775	19.62	17.637	0.0482	1.3222	0.0092	2.0697	0.0243	0.8446	0.2732	1.9625	0.0282	96.69	0.0112	0.0036	128.97	0.97	2217.8	9.6
820	24.27	22.189	0.0586	1.5490	0.0117	3.0871	0.0259	7.0253	0.3678	1.9350	0.0256	97.41	0.0794	0.0042	139.54	1.12	2319.5	10.5
850	30.81	31.989	0.0788	2.1788	0.0073	4.7557	0.0952	17.092	0.5037	1.1698	0.0433	98.90	0.1373	0.0041	145.22	0.61	2371.9	5.5
875	38.23	37.739	0.0987	2.4729	0.0061	4.1238	0.0438	7.7975	1.3420	2.7589	0.0582	97.82	0.0552	0.0095	149.29	0.55	2408.4	4.9
900	46.95	45.356	0.1269	2.9059	0.0020	5.0430	0.0502	12.658	0.7267	2.5125	0.1464	98.35	0.0762	0.0044	153.51	0.47	2445.6	4.1
925	56.97	53.545	0.1521	3.3387	0.0169	6.0992	0.0969	9.4437	2.1912	4.2625	0.4453	97.63	0.0495	0.0115	156.58	1.00	2472.3	8.6
950	72.15	82.044	0.2032	5.0583	0.0161	9.8687	0.5047	27.240	2.4379	5.1000	0.1293	98.15	0.0942	0.0084	159.20	0.65	2494.6	5.5
975	81.85	52.097	0.1312	3.2311	0.0239	4.3451	0.6271	10.838	7.2899	3.5865	0.0568	97.95	0.0587	0.0395	157.94	1.24	2483.8	10.6
1000	87.71	30.180	0.0733	1.9536	0.0067	3.5930	0.0497	14.345	1.2506	2.4378	0.1627	97.60	0.1285	0.0112	150.79	0.68	2421.8	6.0
1050	91.34	16.057	0.0420	1.2108	0.0049	2.1442	0.0305	5.5141	0.7911	1.5705	0.0252	97.09	0.0797	0.0114	128.76	0.63	2215.7	6.2
1100	93.24	7.7427	0.0204	0.6338	0.0038	1.2176	0.0390	3.8051	0.5089	0.8375	0.0166	96.78	0.1051	0.0141	118.25	0.79	2108.4	8.3
1150	94.91	6.3031	0.0159	0.5556	0.0025	1.1209	0.0396	1.7221	0.2202	0.5594	0.0120	97.36	0.0542	0.0069	110.44	0.58	2024.4	6.4
1450	100.0	24.096	0.0613	1.6952	0.0069	3.5853	0.0625	7.9985	0.2513	2.0947	0.0943	97.41	0.0826	0.0026	138.47	0.69	2309.5	6.5
Total															142.21	0.78	2344.3	7.2
JM23f muscovi																		
Mass = 1.01mg																		
J-value = 0.008885 ± 0.0000																		
500	0.047	4.4853	0.0128	1.4267	0.0147	2.1344	0.1300	6.7448	0.7486	0.5530	0.0400	96.37	0.0827	0.0092	30.30	0.33	430.1	4.2
550	0.103	4.9631	0.0176	1.6918	0.0059	2.1984	0.0441	2.0333	0.7698	0.1947	0.0232	98.84	0.0210	0.0080	29.00	0.15	413.6	1.9
600	0.214	9.6983	0.0226	3.3536	0.0047	4.3499	0.0663	0.2347	0.8596	0.1715	0.0348	99.48	0.0012	0.0045	28.77	0.08	410.6	1.1
625	0.321	9.3349	0.0222	3.2459	0.0086	4.1368	0.0511	0.1746	0.0808	0.2420	0.0455	99.23	0.0009	0.0004	28.54	0.11	407.7	1.4
650	0.424	8.8458	0.0294	3.1185	0.0090	4.0405	0.0792	0.1746	0.0986	0.1304	0.0246	99.56	0.0010	0.0006	28.24	0.13	403.9	1.6
675	0.530	9.0244	0.0234	3.2273	0.0029	4.0374	0.0968	0.1746	0.0491	0.0393	0.0347	99.87	0.0009	0.0003	27.93	0.08	399.9	1.1
700	0.626	7.9962	0.0249	2.8883	0.0097	3.7530	0.0718	0.1746	0.2053	0.0318	0.0452	99.88	0.0011	0.0012	27.65	0.13	396.3	1.7
730	0.715	7.4516	0.0214	2.7045	0.0054	3.5817	0.0307	0.8405	0.1545	0.0344		99.39	0.0011	0.0054	27.38	0.10	392.9	1.3
770	0.800	7.0340	0.0273	2.5670	0.0061	3.2616	0.0507	0.3976	0.3658	0.2138	0.0165	99.10	0.0027	0.0025	27.15	0.13	389.9	1.6
820	0.865	5.3690	0.0164	1.9636	0.0079	2.6373	0.0365	0.7625	0.2420	0.1664	0.0427	99.08	0.0068	0.0022	27.09	0.15	389.1	2.0
880	0.912	3.9004	0.0129	1.4265	0.0035	2.0061	0.0369	1.7309	0.5484	0.1551	0.0552	98.83	0.0212	0.0067	27.02	0.16	388.2	2.1
950	0.962	4.1499	0.0129	1.5147	0.0048	2.0129	0.0685	1.5636	0.5417	0.1814	0.0334	98.71	0.0181	0.0063	27.04	0.14	388.5	1.8
1050	0.994	2.6316	0.0074	0.9722	0.0017	1.3528	0.0337	0.7187	0.3965	0.1577	0.0198	98.23	0.0129	0.0071	26.59	0.11	382.6	1.4
1200	1.000	0.4751	0.0012	0.1825	0.0014	0.3053	0.0181	2.0377	0.1641	0.1525	0.0144	90.55	0.1954	0.0158	23.57	0.31	343.1	4.1
Total															27.94	0.13	400.0	1.7

1. Errors are one sigma uncertainties and exclude uncertainties in the J-value.
2. Data are corrected for mass spectrometer backgrounds, discrimination and radioactive decay.
3. Corrections: $(^{36}Ar/^{37}Ar)_{Ca}$ = 2.70 (±0.03) x 10^{-4}, $(^{39}Ar/^{37}Ar)_{Ca}$ = 6.80 (±0.04) x 10^{-4}, $(^{40}Ar/^{39}Ar)_K$ = 0.0301 ± 0.0005^a; 0.0286 ± 0.0006^b; $^{36}Cl/^{38}Cl$ = 316 (Roddick, 1983).
4. J-value is based on an age of 98.8 ± 0.5 Ma for GA-1550 biotite (Renne et al., 1998).

Table B. ^{40}Ar/^{39}Ar laser probe analytical results for pyrite grains from Mount Charlotte (MC1) and Kanowna Belle (GD1, K1).

Sample No	Step No	Cum.% ^{39}Ar	^{40}Ar (x10^{-14}mol)	±	^{39}Ar (x10^{-16}mol)	±	^{38}Ar (x10^{-17}mol)	±	^{37}Ar (x10^{-16}mol)	±	^{36}Ar (x10^{-17}mol)	±	^{40}Ar* (%)	Ca/K	±	^{40}Ar*/^{39}Ar	±	Age (Ma)	±
Mount Charlotte pyrite MC1 [a]																			
J-value = 0.018631 ± 0.000034																			
MC1/1	1	3.71	0.1574	0.0006	0.0875	0.0026	0.0805	0.0273	0.1703	0.0537	0.1966	0.0183	63.17	3.410	1.081	113.74	7.11	2052.2	76.6
	2	100.0	5.2444	0.0097	2.2709	0.0063	1.2641	0.0436	0.2289	0.0378	4.6518	0.0477	73.78	0.176	0.029	170.40	0.89	2578.1	7.2
MC1/2	1	72.44	3.9147	0.0079	2.2671	0.0135	0.5788	0.0186	6.8369	0.1344	0.2342	0.0119	98.36	5.288	0.109	170.19	1.09	2576.4	8.7
	2	100.0	1.5203	0.0034	0.8610	0.0068	0.1640	0.0125	0.1270	0.0485	0.0396	0.0388	99.22	0.258	0.099	175.22	1.96	2616.5	15.5
MC1/3	1	43.66	1.3925	0.0031	0.7793	0.0015	0.2304	0.0256	0.0918	0.0380	0.4380	0.0205	90.69	0.206	0.085	162.08	0.93	2509.8	7.8
	2	100.0	2.3008	0.0042	1.0055	0.0007	0.5599	0.0330	0.0248	0.0147	1.9756	0.0306	74.62	0.043	0.026	170.74	1.00	2580.8	8.0
MC1/4	1	72.41	3.4270	0.0062	1.9653	0.0092	0.4232	0.0152	17.822	0.1114	0.4579	0.0153	96.46	15.968	0.125	169.26	0.89	2568.9	7.2
	2	100.0	1.4342	0.0038	0.7441	0.0017	0.2137	0.0405	0.0272	0.0145	0.5214	0.0233	89.25	0.064	0.034	172.02	1.13	2591.1	9.0
MC1/5	1	34.50	3.6625	0.0069	2.2002	0.0059	0.4387	0.0555	3.8744	0.1107	0.2064	0.0082	98.41	3.085	0.089	164.01	0.55	2525.9	4.6
	2	100.0	7.2034	0.0131	4.1728	0.0207	0.6053	0.0139	0.6307	0.0354	0.1367	0.0108	99.43	0.265	0.015	171.66	0.91	2588.2	7.3
MC1/6	1	73.06	5.3254	0.0098	2.7695	0.0061	0.9318	0.0243	4.7469	0.0977	2.1582	0.0216	88.08	3.003	0.062	169.57	0.56	2571.4	4.5
	2	100.0	5.5336	0.0097	1.0204	0.0038	2.6605	0.0159	0.6189	0.0514	12.725	0.0750	32.05	1.062	0.088	173.88	2.46	2605.9	19.5
MC1/7	1	37.32	1.1711	0.0025	0.6773	0.0052	0.0927	0.0370	8.1486	0.2450	0.1726	0.0079	96.20	21.229	0.660	167.72	1.41	2556.4	11.5
	2	100.0	2.1811	0.0041	1.1282	0.0101	0.2802	0.0275	0.0009	0.0009	0.7617	0.0215	89.67	0.001	0.001	173.34	1.68	2601.6	13.4
MC1/8	1	6.62	0.4766	0.0009	0.3291	0.0077	0.1527	0.0170	3.1886	0.1173	0.1849	0.0093	89.07	17.070	0.746	129.86	3.20	2218.0	31.4
	2	60.14	5.2498	0.0094	2.6441	0.0080	0.7885	0.0387	1.0512	0.0329	2.2399	0.0344	87.39	0.696	0.022	173.57	0.74	2603.4	5.9
	3	100.0	4.0733	0.0071	1.9685	0.0125	0.7267	0.0271	0.1079	0.0503	2.4244	0.0495	82.40	0.096	0.045	170.51	1.36	2579.0	11.0
MC1/9	1	9.21	0.2203	0.0006	0.1143	0.0042	0.0927	0.0116	1.4374	0.0730	0.0835	0.0088	89.33	22.198	1.396	173.68	6.86	2604.3	54.4
	2	66.09	1.2360	0.0026	0.6997	0.0042	0.1232	0.0361	0.2757	0.0946	0.0708	0.0217	98.31	0.690	0.237	173.70	1.45	2604.4	11.5
	3	100.0	0.7187	0.0019	0.4170	0.0106	0.0052	0.0052	0.0366	0.0114	0.0222	0.0201	99.08	0.154	0.048	170.76	2.40	2581.0	19.3
MC1/10	1	7.13	0.3987	0.0011	0.2175	0.0017	12.1341	1.1606	3.7182	0.0958	0.2814	0.0135	80.19	30.270	0.817	148.72	2.28	2394.5	20.3
	2	71.66	3.5079	0.0070	1.9481	0.0137	0.3775	0.0172	3.5192	0.0737	0.5652	0.0158	95.31	3.165	0.070	171.83	1.29	2589.5	10.3
	3	100.0	1.5220	0.0034	0.8549	0.0116	0.1386	0.0117	0.3676	0.0578	0.1618	0.0191	96.86	0.753	0.119	172.50	2.46	2594.9	19.6
MC1/11	1	11.93	0.4810	0.0012	0.2717	0.0035	0.1411	0.0195	2.3820	0.0921	0.2231	0.0154	86.69	15.437	0.630	154.42	2.65	2444.6	23.0
	2	19.69	0.3368	0.0008	0.1760	0.0042	0.0514	0.0171	0.5862	0.0971	0.0565	0.0069	95.17	5.844	0.978	182.60	4.55	2673.7	34.7
	3	21.93	0.1127	0.0004	0.0507	0.0055	0.0232	0.0149	0.1206	0.0790	0.0601	0.0021	84.32	4.164	2.767	187.48	20.49	2710.6	153.3
	4	46.49	0.9773	0.0021	0.5575	0.0074	0.1051	0.0223	2.3212	0.1557	0.0636	0.0178	98.26	7.307	0.500	172.73	2.50	2596.7	19.9
	5	100.0	2.2685	0.0042	1.2112	0.0098	0.2670	0.0174	0.5641	0.0718	0.4456	0.0155	94.20	0.815	0.104	176.48	1.52	2626.4	11.9
MC1/12	1	47.56	5.1136	0.0092	2.9612	0.0091	0.5901	0.0474	4.0943	0.1644	0.3941	0.0142	97.77	2.422	0.098	169.00	0.62	2566.8	5.1
	2	59.38	1.2769	0.0033	0.7353	0.0087	0.1034	0.0217	0.6708	0.0884	0.0749	0.0260	98.29	1.597	0.211	170.79	2.33	2581.2	18.7
	3	100.0	4.4068	0.0094	2.5269	0.0075	0.3288	0.0180	0.1749	0.0632	0.0728	0.0104	99.50	0.121	0.044	173.53	0.64	2603.1	5.1
MC1/Cr1	1	61.12	3.6625	0.0071	0.3990	0.0018	2.6270	0.0305	3.1787	0.8132	8.2384	0.0685	33.61	14.019	3.587	310.18	5.58	3452.6	27.6
MC1/Cr2	2	100.0	0.8801	0.0023	0.2564	0.0039	0.5427	0.0388	5.7800	3.9520	1.2946	0.0413	57.07	40.069	27.40	198.97	5.81	2794.6	41.5
Kanowna Belle pyrite GD1																			
J-value = 0.018756 ± 0.000047																			
GD1/1	1	48.93	2.0029	0.0036	0.9836	0.0068	0.3613	0.0136	0.1567	0.0208	0.1519	0.0122	97.75	0.279	0.0370	199.08	1.48	2793.0	10.5
	2	100.0	1.4889	0.0031	1.0266	0.0130	0.2304	0.0290	0.3431	0.0797	0.1101	0.0287	97.82	0.585	0.1361	141.89	2.00	2330.5	18.4
GD1/2	1	60.53	10.9952	0.0193	5.2954	0.0254	1.5317	0.0511	0.4886	0.0613	1.3300	0.0290	96.42	0.161	0.0203	200.21	1.04	2801.1	7.4
	2	100.0	10.0938	0.0188	3.4532	0.0105	4.1596	0.0830	0.7275	0.1342	18.7378	0.1190	45.14	0.369	0.0680	131.97	1.22	2236.5	11.9
GD1/3	1	100.0	4.4810	0.0090	2.4167	0.0223	0.6479	0.0502	0.1747	0.0243	0.8776	0.0172	94.20	0.127	0.0177	174.68	1.67	2609.9	13.2
GD1/4	1	16.39	2.4255	0.0051	1.1448	0.0089	0.6262	0.0273	0.3583	0.0523	0.2576	0.0112	96.86	0.548	0.0801	205.27	1.68	2836.7	11.7
	2	100.0	9.9389	0.0179	5.8404	0.0270	0.9174	0.0465	0.8604	0.0254	0.2148	0.0223	99.35	0.258	0.0077	169.09	0.85	2565.3	6.9
GD1/5	1	43.18	3.0801	0.0061	1.1353	0.0125	0.9608	0.0431	0.0315	0.0237	2.9870	0.0420	71.33	0.049	0.0366	193.53	2.45	2753.0	17.9
	2	100.0	4.0062	0.0082	1.4942	0.0079	1.3848	0.0356	0.1744	0.0512	5.7697	0.0742	57.43	0.204	0.0599	154.00	1.77	2438.8	15.3
GD1/6	1	49.98	3.9241	0.0074	1.9470	0.0147	0.0903	0.0027	0.2821	0.0669	1.2721	0.0252	90.41	0.254	0.0602	182.24	1.48	2668.7	11.3
	2	100.0	3.1448	0.0062	1.9486	0.0106	0.6328	0.0341	0.3044	0.0780	1.7558	0.0498	83.49	0.273	0.0701	134.76	1.10	2263.5	10.5
GD1/7	1	45.15	1.7814	0.0033	0.6413	0.0072	0.3733	0.0320	0.0621	0.0108	0.5651	0.0163	90.62	0.169	0.0296	251.73	2.98	3134.3	17.6
	2	100.0	2.7174	0.0069	0.7791	0.0057	1.3474	0.0201	0.2215	0.0250	6.4010	0.0673	30.39	0.498	0.0564	106.03	2.81	1965.2	31.8
GD1/8	1	82.90	5.0767	0.0100	2.4506	0.0118	1.2881	0.0483	0.4756	0.0728	0.2929	0.0136	98.29	0.340	0.0520	203.65	1.08	2825.4	7.5
	2	100.0	1.0429	0.0028	0.5057	0.0014	0.4868	0.0271	0.3442	0.0913	1.7459	0.0375	50.54	1.192	0.3162	104.29	2.28	1945.4	26.0
GD1/9	1	68.36	9.1899	0.0160	4.7393	0.0238	8.4505	0.1087	0.4404	0.0282	1.6651	0.0410	94.64	0.163	0.0104	183.53	1.02	2678.6	7.7
	2	100.0	3.1705	0.0066	2.1934	0.0084	4.9633	0.0353	0.2483	0.0335	0.1287	0.0175	98.80	0.198	0.0267	142.83	0.67	2339.1	6.1
GD1/10	1	79.85	7.7219	0.0146	4.1018	0.0161	4.7420	0.0789	1.3605	0.0777	0.9480	0.0259	96.38	0.581	0.0333	181.47	0.82	2662.8	6.3
	2	100.0	1.5534	0.0029	1.0349	0.0049	8.9509	0.1127	0.1965	0.1061	0.3861	0.0189	92.70	0.332	0.1795	139.17	0.90	2305.2	8.4
GD1/11	1	39.78	3.3003	0.0061	1.2126	0.0148	0.5612	0.0272	2.3670	0.0463	0.4116	0.0156	96.36	3.421	0.0788	262.63	3.27	3197.6	18.6
	2	100.0	2.9519	0.0052	1.8334	0.0068	0.8656	0.0252	0.5637	0.0548	2.3749	0.0244	76.22	0.538	0.0523	122.75	0.67	2144.7	6.8
GD1/12	1	57.63	4.6252	0.0090	2.2445	0.0026	0.7803	0.0096	0.1553	0.0269	1.4454	0.0306	90.75	0.121	0.0209	187.03	0.61	2705.0	4.6
	2	100.0	2.3575	0.0044	1.6505	0.0091	0.3710	0.0261	0.3335	0.0630	0.4346	0.0172	94.54	0.354	0.0669	135.06	0.85	2266.3	8.1
GD1/13	1	44.51	6.2025	0.0115	3.6497	0.0177	1.4915	0.0500	1.1239	0.0272	1.5806	0.0245	92.47	0.539	0.0133	157.18	0.85	2466.2	7.2
	2	65.91	1.9676	0.0039	1.7554	0.0109	0.2659	0.0284	0.3890	0.0321	0.0327	0.0093	99.50	0.388	0.0321	111.55	0.75	2026.4	8.1
	3	85.87	1.9318	0.0049	1.6364	0.0192	0.2685	0.0177	0.2646	0.1437	0.0633	0.0039	99.02	0.283	0.1537	116.90	1.40	2084.0	14.8
	4	100.0	1.2827	0.0025	1.1589	0.0118	0.2511	0.0365	0.8191	0.1611	0.0916	0.0142	97.92	1.238	0.2437	108.43	1.18	1992.1	13.1
GD1/14	1	18.04	3.3350	0.0057	1.1444	0.0090	1.0173	0.0331	0.2956	0.0787	0.5584	0.0172	95.05	0.452	0.1204	277.04	2.29	3277.9	12.5
	2	55.77	3.4133	0.0072	2.3939	0.0194	0.4156	0.0565	0.2110	0.1467	0.0314	0.0180	99.71	0.154	0.1072	142.18	1.21	2333.1	11.2
	3	100.0	4.2860	0.0095	2.8076	0.0308	0.8767	0.0413	1.8584	0.2412	0.4577	0.0332	99.21	1.159	0.1510	152.27	1.74	2423.7	15.2
GD1/15	1	12.90	7.4137	0.0150	1.6280	0.0078	1.3219	0.0535	0.5013	0.2366	0.6555	0.0409	97.39	0.539	0.2544	443.59	2.44	4013.6	8.8
	2	25.96	2.1703	0.0048	1.6476	0.0306	0.3035	0.0385	0.1920	0.1284	0.0923	0.0185	98.73	0.204	0.1365	130.07	2.45	2218.0	24.1
	3	71.75	7.4768	0.0142	5.7774	0.0181	0.8553	0.0264	0.4677	0.1024	0.0802	0.0159	99.67	0.142	0.0310	128.99	0.48	2207.4	4.7
	4	100.0	4.3700	0.0091	3.5644	0.0132	0.8048	0.0361	1.6274	0.0661	0.1716	0.0199	99.85	0.799	0.0326	121.23	0.54	2129.1	5.6
GD1/Cr1	1	0.50	13.4246	0.0233	0.4988	0.0075	3.7101	0.0616	8.8053	5.0867	4.0053	0.0508	91.24	31.267	18.069	2485.4	38.3	6954.8	27.2
	2	1.00	14.0451	0.0258	0.5086	0.0109	3.9716	0.0823	21.5428	2.7216	4.1658	0.0638	91.37	76.337	9.791	2598.4	57.9	7033.3	39.4

Table B (cont.).

Sample No	Step No	Cum.% ^{39}Ar	^{40}Ar (x10^{-14}mol)	±	^{39}Ar (x10^{-16}mol)	±	^{38}Ar (x10^{-17}mol)	±	^{37}Ar (x10^{-16}mol)	±	^{36}Ar (x10^{-17}mol)	±	^{40}Ar* (%)	Ca/K	±	^{40}Ar*/^{39}Ar	±	Age (Ma)	±
Kanowna Belle pyrite K1[b]																			
J-value = 0.016652 ± 0.000027																			
K1/1	1	38.14	19.751	0.0351	8.6284	0.0337	2.3784	0.1459	5.5375	0.5154	0.7240	0.0585	98.93	1.124	0.1047	226.55	1.00	2819.5	6.3
	2	73.04	13.805	0.0262	7.8946	0.0380	1.1946	0.0851	3.0266	0.6274	0.1979	0.0560	99.58	0.671	0.1391	174.17	0.93	2455.4	7.1
	3	100.0	9.9146	0.0178	6.0981	0.0236	0.9128	0.0449	0.6441	0.1755	0.2001	0.0202	99.39	0.185	0.0504	161.61	0.70	2355.9	5.7
K1/2	1	15.75	2.5645	0.0045	0.4771	0.0057	3.4492	0.0423	0.9539	0.1610	0.5112	0.0122	94.15	3.503	0.5927	506.75	6.18	4049.7	19.7
	2	27.11	0.3763	0.0008	0.3441	0.0078	0.0573	0.0359	0.7692	0.2243	0.0786	0.0271	93.96	3.919	1.1461	102.91	3.31	1801.0	36.6
	3	100.0	3.3428	0.0065	2.2053	0.0135	0.3109	0.0201	0.8311	0.1110	0.0966	0.0169	99.15	0.660	0.0882	150.33	0.99	2261.7	8.5
K1/3	1	10.34	1.0292	0.0019	0.5232	0.0082	0.2411	0.0133	0.3118	0.0943	0.3085	0.0137	91.15	1.043	0.3160	179.39	2.93	2495.2	22.1
	2	100.0	8.8531	0.0162	4.5371	0.0251	0.6496	0.0515	0.3149	0.1313	0.1309	0.0209	99.55	0.121	0.0507	194.26	1.14	2603.9	8.1
K1/4	1	37.31	0.7863	0.0018	0.4009	0.0029	0.1074	0.0177	0.1366	0.0818	0.1146	0.0127	95.69	0.596	0.3570	187.73	1.69	2556.9	12.3
	2	100.0	1.2933	0.0034	0.6740	0.0098	0.1553	0.0319	0.7012	0.1781	0.0449	0.0113	99.00	1.822	0.4635	190.11	2.85	2574.2	20.6
K1/5	1	31.42	2.0586	0.0044	0.9418	0.0166	0.3478	0.0359	0.4035	0.3643	0.1979	0.0237	97.16	0.750	0.6772	212.43	3.84	2728.4	25.4
	2	100.0	2.8237	0.0056	2.0548	0.0074	0.3221	0.0304	0.1425	0.2123	0.1211	0.0192	98.72	0.121	0.1808	135.66	0.62	2131.4	5.8
K1/6	1	100.0	5.8901	0.0115	3.0285	0.0150	1.2864	0.0472	6.9594	0.6306	0.1699	0.0154	99.23	4.028	0.3655	193.29	1.04	2597.0	7.4
K1/7	1	100.0	3.7781	0.0073	1.6879	0.0144	0.4376	0.0165	0.5621	0.2050	0.1512	0.0172	98.82	0.583	0.2127	221.23	1.97	2785.7	12.6
K1_8	1	100.0	1.0989	0.0023	0.6015	0.0146	0.3360	0.0260	0.0478	0.4270	0.1022	0.0212	97.24	0.139	1.2424	177.68	4.44	2482.2	33.7
K1_9	1	100.0	17.193	0.0299	9.0183	0.0378	1.5937	0.0693	3.2553	0.3504	0.7254	0.0523	98.75	0.632	0.0681	188.31	0.87	2561.2	6.3
K1_10	1	100.0	6.1721	0.0129	3.2976	0.0375	0.5963	0.0460	0.6057	0.3903	0.1733	0.0360	99.16	0.321	0.2072	185.63	2.17	2541.6	15.9
K1_11	1	16.82	0.9918	0.0020	0.2895	0.0025	0.2475	0.0430	0.0611	0.1700	0.1573	0.0172	95.31	0.369	1.0276	326.54	3.40	3359.4	15.9
	2	77.09	1.6769	0.0033	1.0376	0.0060	0.1361	0.0117	0.0824	0.1232	0.0880	0.0165	98.44	0.139	0.2077	159.10	1.08	2335.4	8.9
	3	100.0	0.6847	0.0016	0.3946	0.0076	0.1160	0.0144	0.3385	0.2987	0.0142	0.0165	99.41	1.502	1.3258	172.60	3.56	2443.2	27.6
K1/12	1	31.64	3.3886	0.0063	1.5731	0.0084	0.4826	0.0493	0.6177	0.0849	0.3353	0.0147	97.08	0.687	0.0946	209.16	1.22	2706.6	8.1
	2	100.0	6.1630	0.0110	3.3975	0.0125	0.4932	0.0229	0.1087	0.1478	0.2054	0.0191	99.00	0.056	0.0761	179.59	0.75	2496.7	5.7
K1/13	1	26.17	1.9830	0.0041	0.9917	0.0036	0.2808	0.0231	0.4401	0.1041	0.1444	0.0141	97.85	0.777	0.1838	195.73	0.93	2614.2	6.5
	2	78.21	3.7542	0.0071	1.9714	0.0285	0.2946	0.0281	0.3751	0.1943	0.0563	0.0147	99.55	0.333	0.1726	189.60	2.77	2570.5	20.0
	3	100.0	1.5932	0.0029	0.8252	0.0060	0.1321	0.0301	0.0827	0.1450	0.1117	0.0158	97.92	0.175	0.3075	189.05	1.53	2566.5	11.1
K1/14	1	24.74	1.3993	0.0025	0.5271	0.0033	0.2903	0.0164	0.9430	0.1378	0.1670	0.0159	96.52	3.135	0.4585	256.54	1.91	2999.1	10.9
	2	100.0	2.8428	0.0052	1.6014	0.0104	0.2181	0.0457	0.0349	0.0397	0.0994	0.0253	98.95	0.038	0.0434	175.66	1.27	2466.8	9.7
Stawell Mine pyrite J3[c]																			
J-value = 0.008649 ± 0.000040																			
J3/1a	1	100.0	1.0675	0.0022	1.9869	0.0123	0.8428	0.0124	1.2267	0.1121	1.6968	0.0251	53.08	1.0809	0.0990	28.53	0.43	397.9	5.3
J3/2a	1	50.14	0.6461	0.0017	1.4914	0.0078	1.7472	0.0451	0.2519	0.1226	1.5468	0.0290	29.25	0.2956	0.1439	12.67	0.59	187.6	8.3
J3/2b	2	100.0	0.5005	0.0027	1.4831	0.0099	0.2229	0.0282	0.1854	0.0578	0.1792	0.0172	89.37	0.2187	0.0682	30.16	0.44	418.2	5.4
J3/3a	1	43.51	0.3852	0.0010	0.9052	0.0127	0.3608	0.0192	0.7090	0.0554	0.5078	0.0228	61.14	1.3714	0.1088	26.03	0.84	366.3	10.6
J3/3b	2	100.0	0.4025	0.0022	1.1749	0.0061	0.0479	0.0411	0.1875	0.1552	0.0758	0.0196	94.40	0.2793	0.2313	32.35	0.55	445.0	6.7
J3/4a	1	55.08	0.7773	0.0021	1.8872	0.0149	0.6184	0.0312	1.0807	0.0676	0.8698	0.0229	66.98	1.0025	0.0632	27.60	0.44	386.2	5.5
J3/4b	2	81.56	0.3206	0.0011	0.9069	0.0121	0.1541	0.0314	0.2747	0.1333	0.1197	0.0083	88.96	0.5302	0.2574	31.45	0.52	434.0	6.3
J3/4c	3	100.0	1.0650	0.0029	0.6324	0.0085	0.6441	0.0389	0.9802	0.0363	2.9085	0.0394	19.36	2.7154	0.1071	32.64	1.95	448.6	23.7
J3/5a	1	74.55	0.6714	0.0016	0.8294	0.0113	0.6111	0.0379	0.9511	0.0881	1.3815	0.0327	39.28	2.0084	0.1881	31.82	1.26	438.6	15.4
J3/5b	2	93.20	0.1075	0.0004	0.2075	0.0083	0.0341	0.0211	0.1542	0.0782	0.1437	0.0262	60.57	1.3006	0.6617	31.40	3.95	433.5	48.4
J3/5c	3	100.0	0.6810	0.0029	0.0757	0.0017	0.4574	0.0223	0.1932	0.0320	2.2658	0.0404	1.697	4.4756	0.7488	15.30	16.26	224.2	224.1
J3/6a	1	63.06	0.9912	0.0022	2.7961	0.0164	0.7050	0.0488	0.4514	0.0753	0.8728	0.0165	73.94	0.2825	0.0472	26.21	0.24	368.7	3.1
J3/6b	2	100.0	0.5799	0.0019	1.6379	0.0076	0.2313	0.0185	0.3847	0.0626	0.2095	0.0193	89.30	0.4111	0.0667	31.62	0.39	436.1	4.8
J3/7a	1	54.81	2.1033	0.0046	5.2471	0.0103	1.6299	0.0321	1.9767	0.0490	2.4602	0.0404	65.45	0.6594	0.0164	26.24	0.25	369.0	3.2
J3/7b	2	100.0	1.4818	0.0032	4.3266	0.0082	0.5452	0.0409	2.4903	0.1919	0.3897	0.0212	92.28	1.0077	0.0777	31.62	0.17	436.1	2.1
J3/8a	1	52.64	3.2102	0.0066	4.1031	0.0094	2.9550	0.0303	8.2162	0.2402	6.7880	0.0739	37.69	3.5090	0.1029	29.53	0.56	410.3	7.0
J3/8b	2	100.0	1.6692	0.0039	3.6990	0.0267	0.9481	0.0538	17.9354	0.1191	1.8330	0.0374	68.35	8.5134	0.0836	30.95	0.39	427.9	4.8
J3/9a	1	65.12	0.9831	0.0023	2.1180	0.0175	0.8688	0.0312	0.8873	0.0671	1.4442	0.0255	56.61	0.7333	0.0558	26.28	0.43	369.5	5.5
J3/9b	2	100.0	0.5927	0.0021	1.1340	0.0046	0.2846	0.0414	0.0627	0.0309	0.8798	0.0208	56.10	0.0967	0.0476	29.32	0.58	407.8	7.3
J3/10a	1	37.63	1.3976	0.0031	2.1949	0.0084	1.1330	0.0449	0.8160	0.0699	3.0185	0.0332	36.18	0.6508	0.0558	23.04	0.48	327.9	6.2
J3/10b	2	61.08	0.7222	0.0025	1.3680	0.0079	0.4631	0.0819	0.2497	0.0534	0.9242	0.0211	62.36	0.3194	0.0684	32.83	0.53	450.8	6.4
J3/10c	3	100.0	0.8478	0.0023	2.2700	0.0123	0.3777	0.0214	0.4966	0.0845	0.4616	0.0144	83.89	0.3829	0.0652	31.33	0.27	432.6	3.4
J3/11a	1	40.37	2.2006	0.0041	3.1271	0.0117	2.8232	0.0342	0.8822	0.0487	4.3883	0.0439	35.83	0.4938	0.0273	23.15	0.44	329.3	5.8
J3/11b	2	86.32	1.2225	0.0045	3.5592	0.0153	0.6529	0.0286	0.7659	0.0659	0.3425	0.0117	91.69	0.3766	0.0324	31.50	0.21	434.6	2.6
J3/11c	3	100.0	0.5027	0.0016	1.0601	0.0052	0.2831	0.0178	0.7007	0.0613	0.5822	0.0251	65.83	1.1573	0.1014	31.23	0.73	431.3	9.0
J3/12a	1	45.04	4.9765	0.0107	9.6610	0.0376	5.0518	0.0752	4.6502	0.2332	8.3048	0.0747	50.71	0.8426	0.0424	26.13	0.27	367.6	3.5
J3/12b	2	71.76	1.8231	0.0047	5.7298	0.0164	0.7645	0.0341	0.5189	0.0690	0.4121	0.0165	93.36	0.1585	0.0211	29.67	0.15	412.1	1.8
J3/12c	3	78.37	0.4636	0.0026	1.4183	0.0087	0.1883	0.0361	0.2154	0.1142	0.1729	0.0215	88.93	0.2658	0.1410	29.07	0.51	404.6	6.4
J3/12d	4	100.0	1.4673	0.0037	4.6392	0.0167	0.7068	0.0279	1.6059	0.1086	0.4861	0.0213	90.21	0.6059	0.0410	28.54	0.19	398.0	2.4
J3/13a	1	38.96	1.0784	0.0023	2.4277	0.0047	1.0229	0.0207	0.9137	0.1132	1.6635	0.0296	54.43	0.6588	0.0816	24.18	0.38	342.7	4.8
J3/13b	2	75.90	0.8249	0.0020	2.3017	0.0166	0.3719	0.0155	1.3740	0.0402	0.3775	0.0175	86.53	1.0451	0.0315	31.03	0.33	428.9	4.0
J3/13c	3	100.0	0.5374	0.0020	1.5024	0.0051	0.2630	0.0232	1.8833	0.0756	0.2671	0.0195	85.52	2.1955	0.0884	30.61	0.42	423.8	5.2

1. Errors are one sigma uncertainties and exclude uncertainties in the J-value.
2. Data are corrected for mass spectrometer backgrounds, discrimination and radioactive decay.
3. Corrections: $(^{36}Ar/^{37}Ar)_{Ca}$ = 2.70 (±0.03) x 10^4, $(^{39}Ar/^{37}Ar)_{Ca}$ = 6.80 (±0.04) x 10^4; $(^{40}Ar/^{39}Ar)_K$ = 0.0286 ± 0.0006; 0.0301 ± 0.0005; 0.0271 ± 0.0007; $^{36}Cl/^{38}Cl$ = 316 (Roddick, 1983).
4. J-value is based on an age of 98.8 ± 0.5 Ma for GA-1550 biotite (Renne et al., 199

Chapter 4: Analysis of noble gases and halogens in complex fluid inclusion assemblages by stepwise heating of quartz.

M.A. Kendrick, D. Phillips and J.McL. Miller

Summary

Stepped heating and crushing experiments have been used to investigate the noble gas and halogen degassing behaviour of quartz in detail. Samples with diverse character were selected from the Eloise and Osborne, Iron Oxide Copper Gold (IOCG) ore deposits, and the Railway Fault, 13 km south of the Mt Isa Mine, in the Proterozoic Mt Isa Inlier of northeast Australia.

Quartz has been shown to have a bimodal degassing profile with mechanical decrepitation of fluid inclusions accounting for the release of gas at temperatures of <700 °C. Changes in the Br/Cl, I/Cl, Ar/Cl and $^{40}Ar/^{36}Ar$ composition of gas released at different temperatures up to 700 °C can be related to the decrepitation of different types of fluid inclusion observed by microthermometry.

This is advantageous for the IOCG samples that are characterized by complex fluid inclusion assemblages; the ultra high salinity, multi solid (MS) and liquid-vapour-daughter (LVD) fluid inclusions, with a predominantly primary origin, decrepitate at higher temperatures than lower salinity liquid-vapour (LV) and monophase (M) fluid inclusions that have a predominantly secondary origin.

Three of the IOCG samples have interpreted primary MS and LVD fluid inclusions characterized by molar Br/Cl values of between 0.25×10^{-3} and 0.66×10^{-3}, I/Cl between 0.37×10^{-6} and 5.0×10^{-6} and $^{40}Ar/^{36}Ar$ of <1000. These low values are most easily explained by the involvement of halite dissolution water in IOCG genesis. One of the IOCG samples has Br/Cl of $1.3-2.0\times10^{-3}$ and I/Cl of 10×10^{-6}, similar to juvenile magmatic fluids in Phanerozoic Porphyry Copper Deposits. This sample also has a slightly elevated $^{40}Ar/^{36}Ar$ of 2236.

Step heating reveals limited variation within the more homogenous population of LV fluid inclusions from the Railway Fault. The samples have mean values of 8.1×10^{-3} for Br/Cl; $9.4-12\times10^{-6}$ for I/Cl; <2000 for $^{40}Ar/^{36}Ar$; and $4.7-4.8\times10^{-6}$ $cm^3cm^{-3}H_2O$ for ^{36}Ar concentration. The Br/Cl values are similar to those previously reported for basinal brines present in silicic alteration at the Mt Isa Mine and the additional data can be explained by interaction of such a bittern brine with fine grained sedimentary rocks in the subsurface.

The second mode of quartz degassing occurs between 1200 and 1450 °C, it releases a greater volume of gas than the first degassing mode. Several lines of evidence including microscope observations indicate that the gas released at high temperature is also from the fluid inclusion reservoir. However, its release may be triggered by a metastable phase

transition of quartz (~1200 ºC) and caution is required in interpretation of the fluid compositions obtained at these temperatures.

4.1   Introduction

Simultaneous analysis of fluid inclusion noble gas and halogen compositions by extended Ar-Ar methodology (neutron irradiation and noble gas mass spectrometry) has been demonstrated as a powerful technique for unravelling the origin of hydrothermal fluids in Phanerozoic ore deposits from a variety of tectonic settings (eg. Böhlke and Irwin, 1992ab; Turner et al., 1993; Irwin and Roedder, 1995; Kendrick et al., 2001ab; 2002ab; 2005a). The fluid Br/Cl value is widely regarded as behaving conservatively in the Earth's crust and characteristic values indicate different fluid origins. Similarly, the noble gases are inert elements and have isotopic compositions that vary by orders of magnitude between the crust or mantle, and the modern hydrosphere or atmosphere (eg. Ballentine et al., 2002).

The technique is advantageous because the high sensitivity of noble gas mass spectrometers to noble gas isotopes allows the determination of Cl, Br, I, K and U in very small sample sizes from irradiation-produced nucleogenic noble gas isotopes: $^{38}Ar_{Cl}$, $^{80}Kr_{Br}$, $^{128}Xe_{I}$, $^{39}Ar_{K}$, $^{134}Xe_{U}$. Furthermore, fluid inclusion noble gas concentrations can be obtained from thermometric salinity measurements and the Ar/Cl ratio (Kelley et al., 1986; Turner and Bannon, 1992). When coupled with laser ablation, analysis of small groups of fluid inclusion is possible (Böhlke and Irwin, 1992c; Irwin and Roedder, 1995; Kendrick et al., 2001a). However, simultaneous measurement of the naturally occurring noble gas isotopes of Ar, Kr and Xe is more easily attained in thick section sized samples of 10's of mg (Kendrick et al., 2001a). In some circumstances, Ar-Ar age information can be obtained from either the fluid inclusions or other impurities within the quartz (Kelley et al., 1986; Turner and Bannon, 1992; Kendrick et al., 2001a; but see Kendrick et al., 2005b).

In the present contribution, we explore the potential for stepped heating to resolve different types of fluid inclusion hosted by quartz. This approach does not have the spatial resolution of laser ablation but seeks to exploit the different decrepitation temperatures of specific fluid inclusion types within complex fluid inclusion assemblages. It has the potential advantage that a population of fluid inclusions can be characterised rapidly. It is advantageous over *in vacuo* crushing because $^{38}Ar_{Cl}$ retention in daughter minerals (Kendrick et al., 2001a) is minimized by daughter mineral dissolution during the heating cycle.

The stepped heating experiments continue to temperatures of 1560°C and together with limited crushing experiments provide insight into the siting of the noble gases, halogens and K within quartz samples. Understanding the distribution of impurities between grain boundaries, micron-sized fluid inclusions, mineral impurities or the quartz matrix (either nanometre-sized defects, substitutions for Si^{4+} or channels parallel to the c-axis), is critical to understanding geochemical data (e.g. Barker and Robinson, 1984; Ihinger and Zink, 2000; Grant et al., 2003; Watson and Cherniak, 2003; Götze et al., 2004).

The focus of this study (Part I) is on understanding the degassing behaviour of quartz and demonstrating that stepped heating experiments can be related to fluid inclusion

decrepitation temperatures.   The Ar-Ar systematics of the samples are examined in further detail in Part II (Kendrick et al., 2005b). The study is of additional interest because it represents the first application of the combined noble gas and halogen technique to Proterozoic ore deposits and is the first on Australian localities.

Fig 4-1 (Kendrick et al., 2005)
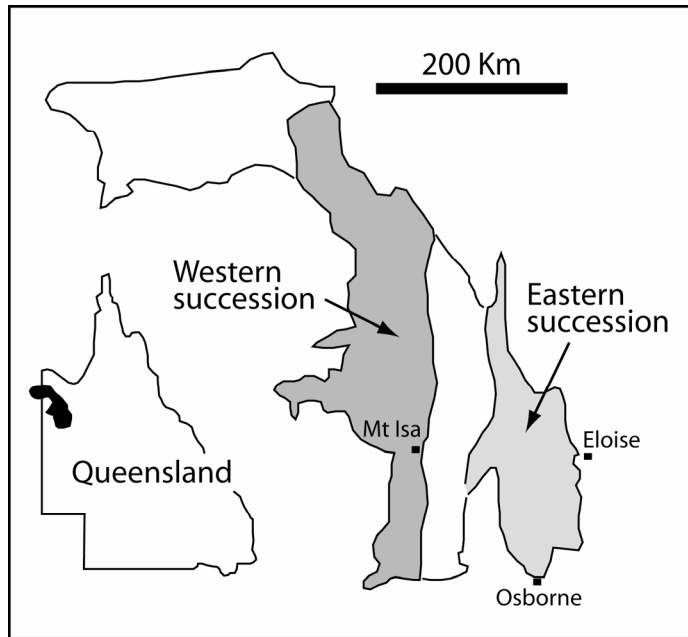
Fig 4-1. Locality map indicating the position of the Mt Isa Inlier within western Queensland, northeast Australia, and the locations of Osborne, Eloise and Mt Isa.

4.2   Samples and microthermometry

Four quartz vein samples were selected from the Eloise (1530 Ma; Baker et al., 2001) and Osborne (1595 Ma; Gauthier et al., 2001) Iron-Oxide-Copper-Gold (IOCG) deposits of the Eastern Succession, of the Proterozoic Mt Isa Inlier, northeast Australia (Fig 4-1). An additional sample was obtained from the Railway Fault, 13 km south of the Mt Isa Copper Mine, in the Western Succession.

Detailed microthermometry has been reported previously for the Eloise samples (Baker, 1998). It is duplicated here for the sample splits analysed and for the Osborne and Railway Fault samples. However, additional emphasis was placed on determination of the fluid inclusion decrepitation temperatures. This was done by mapping the positions of five to fifteen selected primary, pseudo-secondary and secondary fluid inclusions in several ~1 mm^2 wafer fragments and then recording the temperatures of vapour disappearance, daughter mineral dissolution and decrepitiation during a single heating cycle to 600 ºC which destroys the sample. A heating rate of 10 ºC min^{-1} was used for this purpose giving an estimated accuracy of ±10 ºC.

4.2.1 Eloise and Osborne fluid inclusion types

The IOCG samples from Eloise and Osborne include five different types of primary and secondary fluid inclusion with different relative abundances (Table 1). Both the primary and the secondary fluid inclusions have previously been attributed to stage II/III mineralization at Eloise (Baker, 1998) and the Ar-Ar systematics also suggest near synchronous formation of secondary fluid inclusions in the Osborne samples (Kendrick et al., 2005b). In order of decreasing salinity the types comprise:

1) Ultra high salinity multi-solid (MS) fluid inclusions with up to five daughter minerals that usually have a primary origin. During heating, vapour disappearance occurred before daughter mineral dissolution at 80-200 ºC, sylvite was the first salt to dissolve and the halite cube remained to between 400 and ~500 ºC. Carbonate and unidentified daughter minerals, that probably include pyrosmalite [$(Fe,Mn)_8Si_6O_{15}(OH,Cl)_{15}$] or Fe-chloride (Baker, 1998), sometimes remained undissolved at 600 ºC or at the point of decrepitation. Based on the NaCl-H$_2$0 system these fluid inclusions have salinities of at least 40-65 wt %.

2) High salinity liquid-vapour-daughter (LVD) fluid inclusions in which halite is the only daughter mineral are present as both primary and pseudosecondary as well as secondary fluid inclusions. Vapour disappearance occurred between 80 and 200 ºC before halite dissolution which usually occurred between 100 and 300 ºC but occasionally at 400 ºC, indicating salinities of 26-45 wt. %.   Complete homogenisation occurred before decrepitation.

3) Liquid-vapour (LV) fluid inclusions are predominantly on trails indicating a secondary or pseudosecondary origin. They have first melting temperatures as low as -50 ºC indicating a Ca-rich composition, meaning that salinities expressed as wt. % NaCl eq. are over estimated. Final melting occurred between -44 ºC and -5 ºC suggesting variable salinity of approximately 5-26 wt %. Vapour disappearance occurred over a similar interval to the MS and LVD fluid inclusions, between 80-200 ºC.

4 and 5) Monophase (M) and carbon dioxide (CO_2) fluid inclusions are predominantly on trails indicating a secondary origin.

The mean decrepitation temperatures are slightly different for each of the samples, but in general, LV fluid inclusions decrepitate at lower temperatures than LVD fluid inclusions and, where present, MS fluid inclusions decrepitate at the highest temperatures or remained undecrepitated by 600 ºC (Table 2). Most CO_2 fluid inclusions remain undecrepitated at 600 ºC, but some decrepitate around ~400 ºC.

4.2.2 Railway Fault fluid inclusions

Primary LV fluid inclusions define growth zones in sample AW02-002 from the Railway Fault. This sample is included because accidentally trapped mica present within the fluid inclusions represents the major K reservoir, and enables us to evaluate the effect mica impurities have on Ar outgassing and Ar-Ar age determination (see also, Part II; Kendrick et al., 2005b).

The LV fluid inclusions have variable degrees of fill, between 10 and 90%, and final melting occurred in two modes. Most fluid inclusions have final melting temperatures of between -3 ºC and -15 ºC with a mean value of -8 ºC. This indicates a mean salinity of ~12 wt % NaCl eq., but first melting occurred at -35 ºC and -27 ºC in two fluid inclusions suggesting Ca^{2+} in addition to Na^+ and therefore that 12 wt % is an upper limit on salinity. A minor group of fluid inclusions had final melting temperatures between -0.5 ºC and 0 ºC indicating negligible salinity. Homogenisation temperatures varied between 160 and 380 ºC, however some of the highest values may result from necking down or leakage. The highest homogenisation temperature observed concurrently in several fluid inclusions of the same growth zone was 300 ºC. Significant numbers of fluid inclusions began to decrepitate at ~300 ºC and continued to do so up to 600 ºC. The wafer could be seen to 'twitch' around 400 ºC when the greatest number of fluid inclusions were decrepitating.

The data indicate considerable inter growth zone variability in T_h and T_m but the ranges are similar to those reported for NaCl-rich 'group 3' inclusions within silicic alteration at the Mt Isa Mine (Heinrich et al., 1989). The sense of movement, strike direction and relative age of the Railway Fault together with the high Cu-content of fluid inclusions in this sample have previously been used to suggest a link with Cu mineralization (~1523 Ma; Perkins et al., 1999) at the Mt Isa mine (A. Wilde, Pers. Comm. 2005).

Table 1. Fluid inclusion relative abundance.

Sample	Primary	MS	LVD	LV	M	CO_2	Cap. Mica
Eloise							
EL 48177	<20%	2-15%	30-60%	10-15%	0%	10-20%	No
EL 48179	<10%	0-2%	10-40%	50-60%	5-20%	10-20%	No
Osborne							
OS 37A	<10%	2-4%	10-25%	40-60%	0%	15-20%	?
OS 37B	<50%	20-60%	10-30%	20-40%	0-15%	5-20%	No
Railway Fault							
AW02-002	100%	0%	0%	100%	0%	0%	Yes

Primary – maximum proportion of pseudo-secondary and isolated fluid inclusions considered to have a primary origin; MS – multisolid fluid inclusions; liquid, vapour, halite + 1 or more other daughter minerals; LVD – liquid-vapour and halite; LV liquid-vapour; M – monophase; CO_2 – liquid carbon dioxide fluid inclusions.

Table 2. Decrepitation Temperatures ^{o}C

Sample	n	MS		LVD		LV		M		CO_2
Eloise										
EL 48177	26	>600	510->600	418	340-450	515	340->600	295	250-340	>600
EL 48179	22			511	428-580	392	300-530			>600
Osborne										
OS 37A	59	437	390->600	415	240-590	412	340-485	415	410-420	>600
OS 37B	39	543	450->600	481	390->600	437	240-560			>600
Railway Fault										
AW02-002	26					~400	300-600			

n – number of decrepitation measurements for the sample. The mean decrepitation temperature and the range of decrepitation temperatures is given for each fluid inclusion type for which there are measurements.

4.3   Noble gas and halogen Methodology

4.3.1 Sample preparation and Irradiation

High purity quartz separates were obtained by crushing the off-cuts, from the thick sections used for microthermometry, and hand picking under a binocular microscope. The quartz chips were cleaned in an ultrasonic bath using distilled water and acetone and the cleaned chips were wrapped in Al-foil and packed into a silica glass tube.

The packed samples were irradiated for 150 MWH in position 5c of the McMaster University nuclear reactor, Canada (Irradiation designated UM#4). The neutron fluence was monitored using the Hb3Gr (1072 Ma) and GA1550 (98.8 Ma) irradiation monitors. J values were obtained from both monitors, while the additional β and α parameters were obtained from Hb3Gr alone (Appendix A; Kelley et al., 1986). J and β were used to calculate the fluence of fast and thermal neutrons (together approximately 10^{19} neutrons cm^{-2}), and thus to determine the abundance of Ca, Cl, and K measured as $^{37}Ar_{Ca}$, $^{38}Ar_{Cl}$, and $^{39}Ar_K$ respectively. Ar-isotopes were corrected for mass discrimination, ^{37}Ar and ^{36}Cl (producing ^{36}Ar) decay after irradiation, and other Ar-interference-reactions based on irradiated pure CaF_2 and K_2SO_4.

The Br/Cl and I/Cl values are proportional to the measured $^{80}Kr_{Br}/^{38}Ar_{Cl}$ and $^{128}Xe_I/^{38}Ar_{Cl}$ values. The minimum analytical uncertainty is determined by the reproducibility of atmospheric Kr/Ar and Xe/Ar values over the period of analysis. At the 1 sigma level these were 1.5-3% and 3-5% respectively, compared to 0.1-0.2% for the $^{40}Ar/^{36}Ar$ value. However, uncertainty is increased in very low gas volume extraction steps and the absolute uncertainty is determined by the relative fluxes of resonant and thermal neutrons. A suitable monitor for resonant neutrons was not available at the time of irradiation, but three sample duplicates have been included in a fully monitored irradiation that included the Shallowater meteorite (I-Xe) standard and confirm that the resonance correction is similar to previous irradiations. The calculated Br/Cl plus I/Cl values are reduced by factors of 1.3 and 1.7, respectively when resonance is taken into account (Johnson et al., 2000; Kendrick et al., 2001ab; 2002a; 2005a), the resulting uncertainty in Br/Cl and I/Cl is estimated at 10%.

4.3.2 Gas extraction and analysis

Following irradiation, 20-130 mg of quartz chips were loaded in Cu-foil packets and placed in a vacuum sample chamber coupled to a tantalum-resistance-furnace and MAP 215-50 mass spectrometer at the University of Melbourne. Smaller quantities (20-50 mg) of samples AW02-002b and EL 48177 were also loaded into modified nupro® valves for *in vacuo* crushing, in these cases the crushed residue was later loaded in Cu-foil packets and the resistance furnace, as above.

The extraction line and loaded samples were baked at a temperature of 130°C to remove absorbed atmosphere and achieve UHV. Care was taken not to exceed 130°C so as to avoid premature decrepitation of fluid inclusions although slightly higher temperatures may have been obtained during sample irradiation.

Each sample was cyclically heated in a stepwise fashion from an idle temperature of 100°C up to a maximum of 1560°C. The temperature selected for each step was determined by the volume of gas measured in the previous step and varies for each sample (Appendix B). Heating to the desired step temperature was achieved over 3 minutes and each step had a duration of 20 minutes. Stepwise *in vacuo* crushing comprised 3 to 6 crushes.

Extracted gases were expanded into the extraction line, isolated from the cooling furnace, and purified over a period of 15 minutes using one hot and one cold Zr-Al getter (SAES st 101). The purified noble gases (Ar, Kr, Xe) were then admitted to the mass spectrometer and isotopically analysed sequentially over a period of 50 minutes with 9 complete cycles of measurement. Ar isotopes were measured using a Faraday detector while Kr and Xe isotopes were analysed at a relative gain of ~400 using a Johnson electron multiplier.

4.3.3 Instrument blanks

Instrument blanks for stepwise heating were close to the Faraday background noise level of 1.5×10^{-11} cm^{-3} STP for ^{36}Ar, ^{37}Ar, ^{38}Ar, and ^{39}Ar and accounted for between 1% and 10% of the total ^{40}Ar gas released by a typical sample. The blanks increased by up to 4 times at high temperature and where ^{36}Ar was detected had an atmospheric ^{40}Ar/^{36}Ar composition. In all cases, the halogen derived noble gas isotopes, ^{80}Kr$_{Br}$ and ^{128}Xe$_{I,}$ had a blank level of <10% and in many cases <1% of sample gas. The atmospheric ^{84}Kr and ^{129}Xe machine blanks were not detectable or close to the multiplier background noise level (1.5 and 1.2×10^{-14} cm^{-3} STP, for Kr and Xe respectively). However, it was found that the empty Cu-foil capsule made a significant contribution to the ^{84}Kr and ^{129}Xe blank at temperatures of <600°C. Although, believed to represent absorbed atmosphere this component was preferentially enriched in the heavier noble gases Xe>Kr>Ar meaning that the ^{84}Kr/^{36}Ar and ^{129}Xe/^{36}Ar ratios determined at <600°C are unreliable and are not reported.

Instrument blanks for *in vacuo* crushing were lower than cold furnace blanks. Only ^{40}Ar was significantly above the Faraday detection limit, but due to the large volume of gas released by *in vacuo* crushing, this accounted for as little as 0.1-1%, exceptionally reaching 5%, of the sample gas. Kr and Xe isotopes are below or very close to the multiplier detection limit. Where measured, ^{84}Kr accounts for <1% of the typical sample gas and is presumed to have an atmospheric origin. Sample gas abundance data are reported in Appendix B.

4.4 Sample degassing

4.4.1 Degassing profiles

The degassing behaviour of quartz was examined in detail by stepped heating samples from Eloise, Osborne and the Railway Fault in 9-26 increments. All of the samples behaved in a consistent manner similar to samples previously reported from the UK (Kelley et al., 1986), suggesting that the profiles presented in Figure 4-2 are typical for

quartz. Sample AW02-002 which includes accidentally trapped mica was analysed in the most detail and is emphasised throughout this section.

Chlorine-derived $^{38}Ar_{Cl}$ was degassed bimodally from each sample. Approximately 26% of the $^{38}Ar_{Cl}$ was released from sample AW02-002a during the low temperature degassing peak (L <700 °C), 62% was released during the high temperature peak (H ~1200-1450 °C) and only 6% was released in the intervening temperature interval (Table 3; Appendix B). The low temperature peak corresponds with a dewatering peak, previously reported for unrelated quartz (Barker and Robinson, 1984; Fig 4-2a), but the relationship of the high temperature peak to dewatering is unclear because of the lack of dewatering data at high temperature.

In sample AW02-002b analysed by combined *in vacuo* crushing and stepped heating, 58 % of $^{38}Ar_{Cl}$ was released by crushing, compared to only 20% released during stepped heating of the uncrushed sample at <700 ºC (Table 3). Crushing reduced approximately two thirds of the sample to a grainsize of <90 μm, but left sufficient coarse material that many fluid inclusions could have remained intact (Fig 4-3). During stepped heating of the crushed residue both the high and low temperature peaks were similarly reduced in size (Fig 4-2b). Together these observations suggest that $^{38}Ar_{Cl}$ released in both the low and high temperature degassing peaks has a common origin in fluid inclusions.

The degassing profile of $^{36}Ar_{atm}$ is similar to $^{38}Ar_{Cl}$ indicating that most $^{36}Ar_{atm}$ is also contained in fluid inclusions. The small differences in the profiles are explained by variations in fluid $Cl/^{36}Ar$ values and by the presence of adsorbed $^{36}Ar_{atm}$ introduced as a modern atmospheric contaminant. The degassing profiles of $^{36}Ar_{atm}$ and $^{38}Ar_{Cl}$ are most different at low temperature where the atmospheric contaminant is most likely to be released (Fig 4-2).

The degassing profiles of excess $^{40}Ar_E$ and potassium-derived $^{39}Ar_K$ are similar to the $^{38}Ar_{Cl}$ and $^{36}Ar_{atm}$ degassing profiles for samples EL 41877, EL 41879 and OS 37B (Fig 4-4abd), implying that Ar, K and Cl are all hosted by the fluid inclusions in these samples. The small variations in the profiles indicate fluids with different compositions are released at different temperatures. In samples AW02-002a and –b, $^{39}Ar_K$ outgassing is unrelated to outgassing of $^{40}Ar_E$♣, $^{36}Ar_{atm}$ or $^{38}Ar_{Cl}$ and in this sample K is hosted predominantly within accidentally trapped mica that is present within the fluid inclusions as a discrete sub-reservoir (Fig 4-4ef). The poor correlation between $^{39}Ar_K$ and $^{40}Ar_E$ (or $^{38}Ar_{Cl}$) in sample OS 37A (Fig 4-4c) may also be explained by the presence of very minor mica impurities.

The degassing patterns of the nucleogenic and atmospheric Kr and Xe isotopes; $^{80}Kr_{Br}$, $^{128}Xe_I$, $^{84}Kr_{atm}$ and $^{129}Xe_{atm}$, are similar to nucleogenic $^{38}Ar_{Cl}$ and atmospheric $^{36}Ar_{atm}$. This suggests that fluid inclusions are the dominant reservoir of all trapped noble gases and halogens in natural quartz. Mineral impurities can be a significant reservoir of K and radiogenic $^{40}Ar_R$ but the quartz matrix does not appear to be a significant host to either K, the   halogens   or   the   noble   gases.

♣ $^{40}Ar_E$ = excess ^{40}Ar: ^{40}Ar not attributed to an atmospheric source ($^{40}Ar_A = 295 \times ^{36}Ar_{atm}$) or produced within the sample by radiogenic decay of K since the time of trapping, $^{40}Ar_R$. $^{40}Ar_E = {}^{40}Ar_{total} - {}^{40}Ar_A - {}^{40}Ar_R$
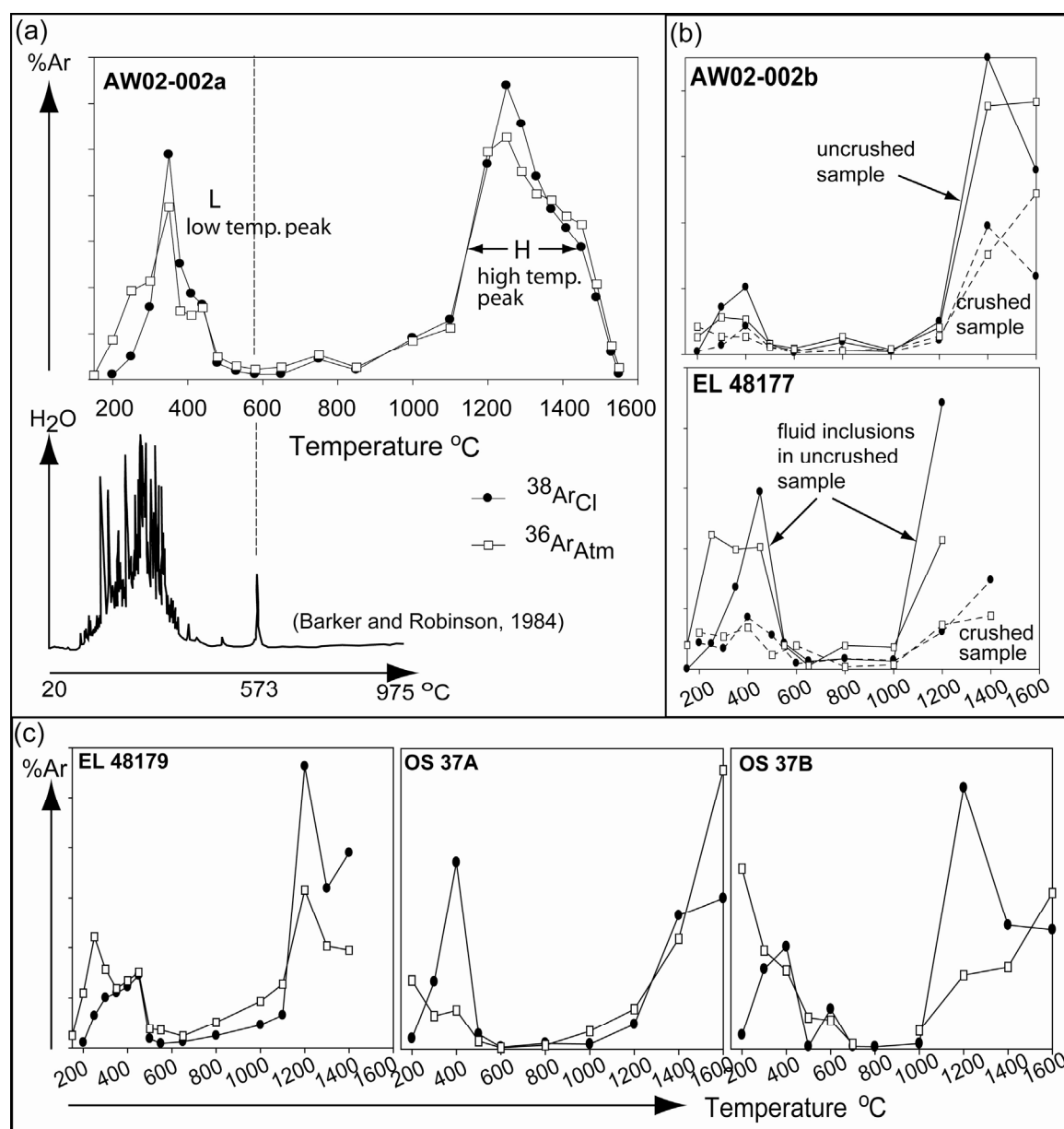
Fig 2 (Kendrick et al., 2005)

Fig 4-2. Quartz degassing profiles for Cl-derived $^{38}Ar_{Cl}$ and atmospheric $^{36}Ar_{atm}$. (a) The highest resolution degassing profile (26 steps) for sample AW02-002a is compared with a previously published dewatering profile (Barker and Robinson, 1984). (b) The degassing profiles for crushed (dashed lines) and uncrushed (solid lines) splits of samples AW02-002b and EL 48177. (c) Degassing profiles for samples EL 48179, OS37B and OS37.

Fig 3 (Kendrick et al., 2005)
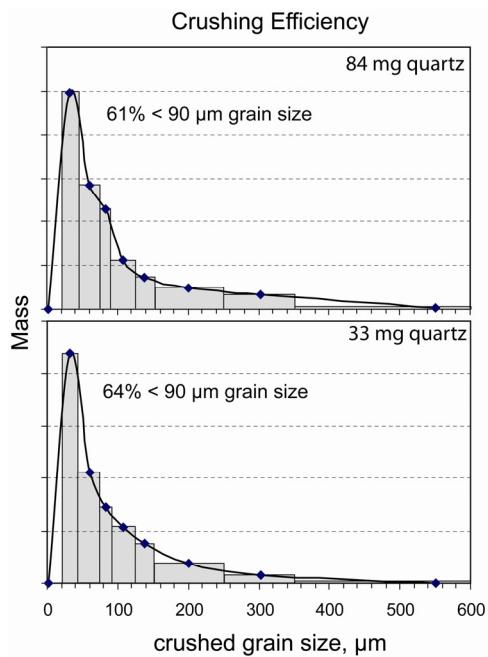
Fig 4-3. Grainsize distribution plots for quartz samples crushed in modified nupro valves. The size fractions have been determined by sieving and are; <45 μm in size; 45-75 μm; 75-90 μm; 90-125 μm; 125-150 μm; 150-250 μm, 250-354 μm; and >354 μm. The area under the curve is equal to 100%. Crushing efficiency appears fairly independent of the quantity of sample crushed up to 84 mg.

Fig 4 (Kendrick et al., 2005)
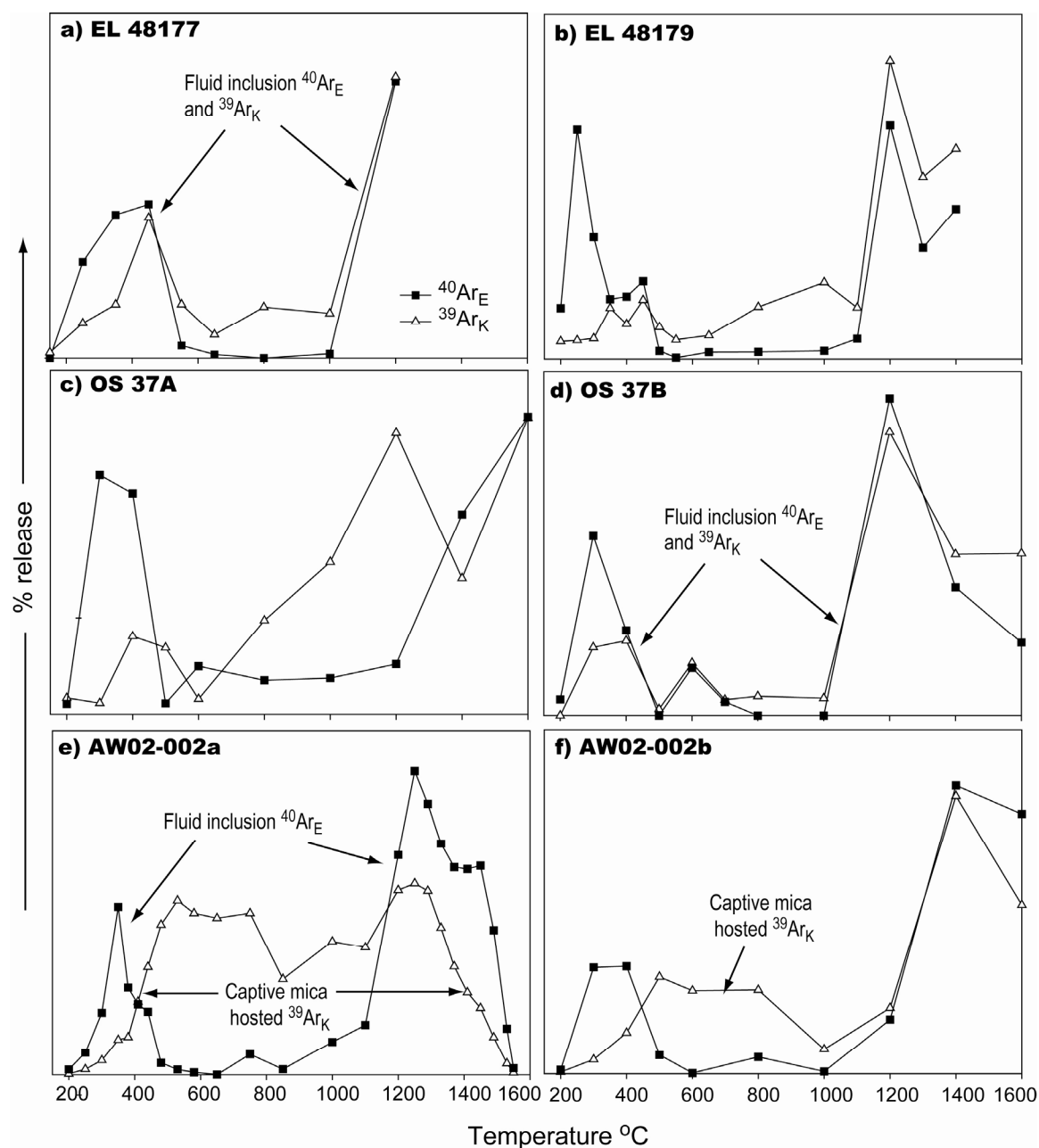
Fig 4-4. Quartz degassing profiles for K-derived $^{39}Ar_K$ and excess $^{40}Ar_{E.}$. (a and b) The Eloise samples have similar $^{39}Ar_K$ and $^{40}Ar_E$ degassing profiles suggesting that both species originate in the fluid inclusions (see also Fig 4-2). (c) The $^{39}Ar_K$ and $^{40}Ar_E$ degassing profiles of sample OS 37A are poorly correlated. (d) Fluid inclusion degassing profiles for sample OS 37B. (e and f) Sample AW02-002 has a $^{40}Ar_E$ degassing profile similar to those of $^{38}Ar_{Cl}$ and $^{36}Ar_{atm}$ (see Fig 4-2) indicating an origin in the fluid inclusions, but K-derived $^{39}Ar_K$ has a unimodal degassing profile that is unrelated to fluid inclusion degassing. Nb - $^{40}Ar_E$ has been calculated from the measured ^{40}Ar and K and ages of 1530 Ma for Eloise, 1595 Ma for Osborne and 1523 Ma for the Railway Fault.

Table 3. Noble gas and halogen degassing data

Sample	Crush or peak	$^{38}Ar_{Cl}$ %	$^{40}Ar/^{36}Ar$	Br/Cl ($\times 10^{-3}$)	I/Cl ($\times 10^{-6}$)
Eloise					
EL 48179	L	30	1331	0.72	2.3
	H	64	1472	0.34	1.5
EL 48177	L	?	1033	0.56	2.9
	H	?	1962	0.48	3.0
EL 48177	C	54	1012	0.88	2.9
	L	23	519	0.25	0.85
	H	21	1180	0.45	2.7
Osborne					
OS37A	L	?	514	1.5	17
	H	?	401	1.2	9.1
OS37B	L	32	374	0.58	3.6
	H	51	592	0.40	2.9
Railway Fault					
AW02-002a	L	28	1431	8.1	9.4
	H	62	2139	3.8	4.0
AW02-002b	L	20	1029	8.1	12
	H	50	706	6.5	4.1
AW02-002b	C	58	810	12	16
	L	8	421	6.1	11
	H	22	640	5.8	4.6

1. *L – gas extracted at <700 °C. H- gas extracted between 1200 and 1450 °C. C – gas extracted by in vacuo crushing.*

2. *'?' question marks indicate samples incompletely outgassed at high temperature.*

3. *The measured $^{40}Ar/^{36}Ar$ values have been corrected for post-entrapment production of radiogenic $^{40}Ar_R$ based on K abundance and ages of 1530 Ma for Eloise (Baker et al., 2001), 1595 Ma for Osborne (Gauthier et al., 2001) and an assumed age of 1523 Ma for the Railway Fault that is tentatively correlated to the age of Mt Isa (Perkins et al., 1999).*

4.4.2 High temperature fractionation

The average Br/Cl and I/Cl values of fluid inclusion gases released during the low temperature (<700 ºC) degassing peak are systematically higher than the Br/Cl and I/Cl values measured during the high temperature (1200-1450 ºC) peak (Fig 4-5; Table 3). However, this trend is not observed in samples that are crushed prior to stepped heating (Table 3). In contrast to the halogens, the initial $^{40}Ar/^{36}Ar$ values that have been corrected for post entrapment production of radiogenic $^{40}Ar_R$, exhibit non-systematic variation between the low and high temperature degassing peaks (Fig 4-5b).

In addition to the variation described above that is seen in all of the samples, sample AW02-002a studied in the most detail, exhibits a dramatic increase in both F-values[1] and the Br/Cl plus I/Cl values[2] at temperatures of greater than ~1450°C (Fig 4-6). Because both the F-values and the Br/Cl plus I/Cl values are measured as Kr/Ar and Xe/Ar ratios, the sudden increase in all the values at ~1450°C indicates that the low volumes of gas released at the highest temperatures is enriched in the heavy noble gases on the order Xe>Kr>Ar.

---

[1] F-values = Fractionation values of atmospheric Xe or Kr relative to Ar. $F^{129}Xe = (^{129}Xe/^{36}Ar)_{sample}/(^{129}Xe/^{36}Ar)_{air}$; $F^{84}Kr = (^{84}Kr/^{36}Ar)_{sample}/(^{84}Kr/^{36}Ar)_{air}$.
[2] Br/Cl is measured as $^{80}Kr_{Br}/^{38}Ar_{Cl}$ and I/Cl is measured as $^{128}Xe_I/^{38}Ar_{Cl}$

Fig 5 (Kendrick et al., 2005)
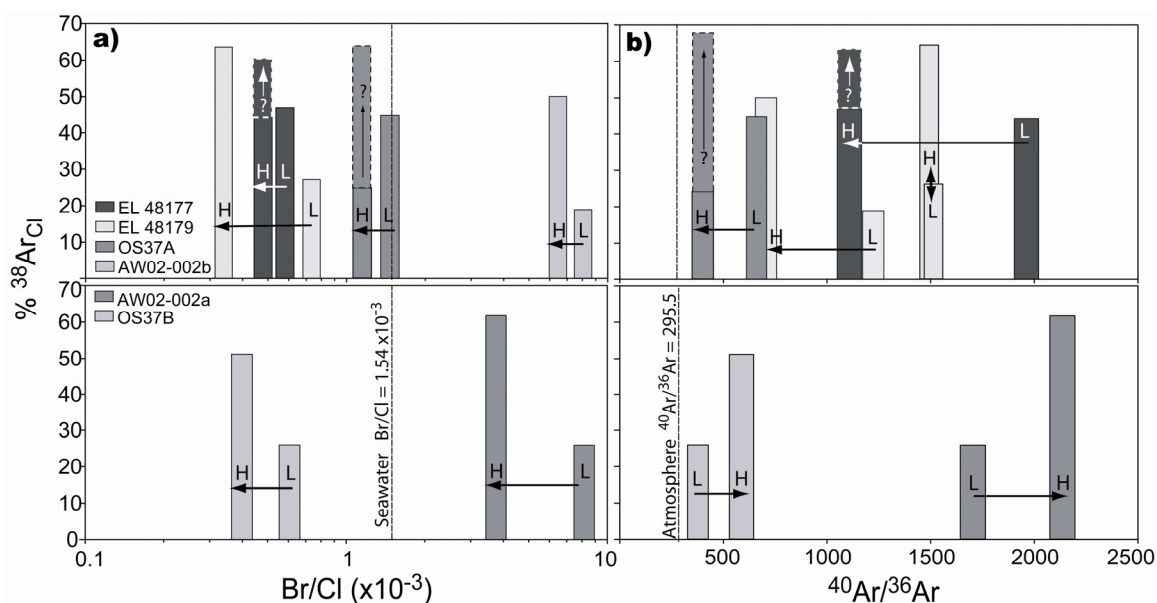
Fig 4-5; Plots showing the composition of gas and the proportion of Cl-derived $^{38}Ar_{Cl}$ outgassed during the high (H; 1200-1450 ℃) and low (L; <700 ℃) temperature peaks of outgassing (see Fig 4-2). (a) Br/Cl values of gas released at high temperature are systematically lower than at low temperature, the arrows indicate increasing temperature. A greater volume of gas is released during the high temperature peak than is released during the low temperature peak. (b) The initial $^{40}Ar/^{36}Ar$ value of gas released at high and low temperatures vary non-systematically. The initial $^{40}Ar/^{36}Ar$ values are corrected for post-entrapment production of radiogenic $^{40}Ar_R$. Nb - Samples EL 48177 and OS37A were incompletely outgassed, the dashed boxes indicate an unknown volume of unmeasured gas.

Fig 6 (Kendrick et al., 2005)

The figure plot contains the following labeled elements:

Left axis: Br/Cl ($\times 10^{-3}$), I/Cl ($\times 10^{-6}$), ranging 0 to 600.

Right axis: $F^{84}Kr$, $F^{129}Xe$, ranging 0 to 25.

X axis: Temperature ^{o}C, ranging 200 to 1600.

Legend (AW02-002a):
- $F^{84}Kr$
- $F^{129}Xe$
- Br/Cl
- I/Cl

Annotation: Sudden elevation of the F-values and Br/Cl plus I/Cl, also measured as noble gas ratios, maybe explained by sample melting.
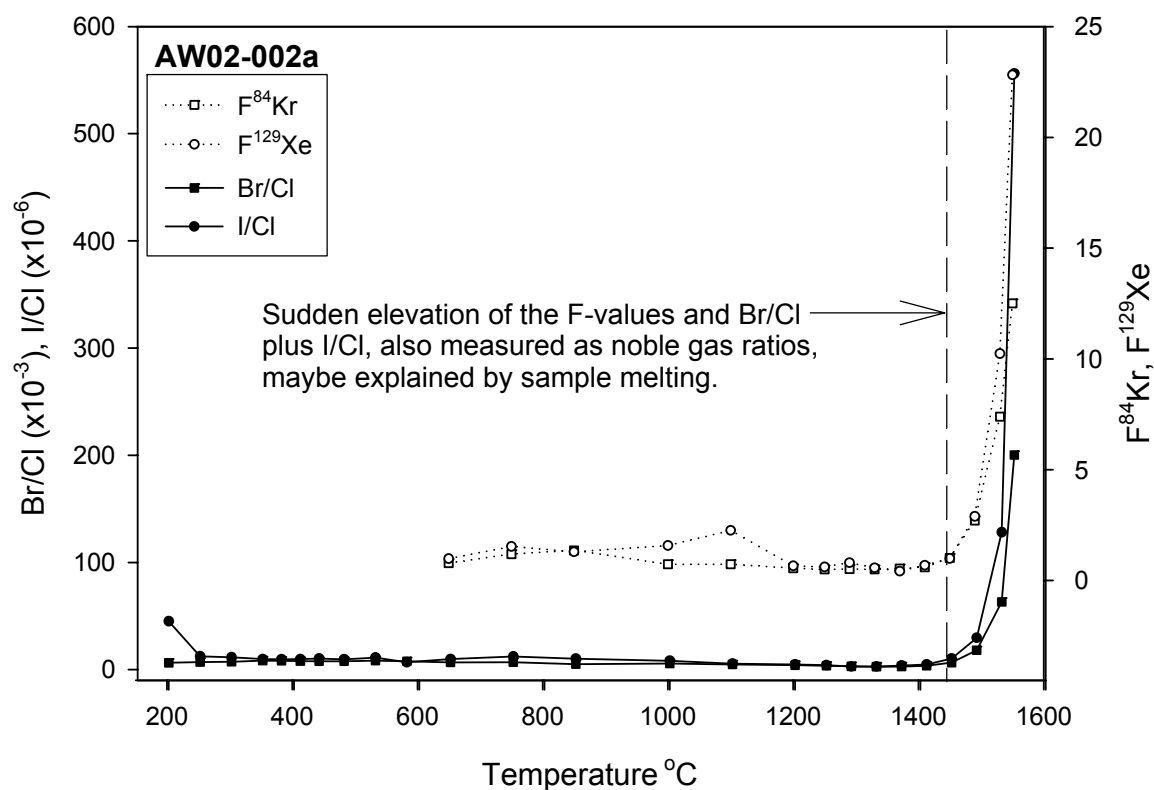
Fig 4-6.   Sample AW02-002a Kr and Xe F-values and apparent Br/Cl plus I/Cl values as a function of temperature. At 1530 ºC the apparent Br/Cl value is geologically unrealistic and both I/Cl and F-values are highly elevated. The F-values are noble gas fractionation values relative to air (FX = [X/^{36}Ar]/[X/^{36}Ar]$_{air}$) and the Br/Cl plus I/Cl values are measured as $^{80}Kr_{Br}/^{38}Ar_{Cl}$ and $^{128}Xe_{I}/^{38}Ar_{Cl}$. The sudden increase in both values at high temperature could be explained by the preferential retention of Ar>Kr>Xe in molten quartz.

4.4.3 Fluid inclusion decrepitation

To better understand the degassing profiles described above, we highlight important aspects of the fluid inclusion decrepitation behaviour observed on the fluid inclusion stage (Tables 1 and 2), and the appearance of selected samples after heating to 1100 ºC and 1400 ºC in the tantalum resistance furnace.

On heating to 600 ºC trails of secondary fluid inclusions were seen to 'unzip' with the largest fluid inclusions decrepitating first and the smallest fluid inclusions decrepitating at the highest temperature. Decrepitation of a given trail could proceed almost instantaneously or gradually over ~100 ºC and different trails decrepitated at different temperatures. Sometimes a fluid inclusion was seen to leak before it decrepitated. The daughter minerals usually dissolved before the fluid inclusion decrepitated. However, in the most saline MS fluid inclusions decrepitation frequently occurs before dissolution of the last one or two daughter minerals.

In all of the samples, heating to 600 ºC appears to decrepitate the majority of fluid inclusions, but not all of them. However, it is virtually impossible to see into the smallest fluid inclusions of <2μm and some of the decrepitated fluid inclusions may have only partially leaked. Fluid inclusion size as well as type is an important control on decrepitation temperature and the different fluid inclusion types exhibit considerable overlap in their decrepitation temperature (Table 2).

4.4.3.1 After heating to 1100 ºC and 1400 ºC

After heating to 1100 ºC, before the second major degassing peak (Fig 4-2), each of the samples retained a similar appearance to that attained after heating to only 600 ºC on the fluid inclusion stage. Rare LV fluid inclusions can still be observed in samples OS 37A and AW02-002 (Fig 6d and 7b). However, the majority of fluid inclusions appear to be vapour dominated and are either completely decrepitated or have partially leaked (Figs 4-5, 4-6 and 4-7).

After heating to 1400°C, after the second major degassing peak (Fig 4-2), the samples have a radically different appearance: Micro-fracturing has affected samples EL 48179 (Fig 4-7de) and AW02-002 (Fig 4-9d). Explosive decrepitation has occurred in sample OS 37A and AW02-002 which results in 50-100 μm pits, from which further fractures propagate (Figs 4-8g and 4-9e). A vapour-dominated fluid inclusion remained intact and has a negative crystal shape in sample EL 48179 (Fig 4-7f). However most intriguingly, samples OS 37A and AW02-002 have developed an entirely new radial fabric (Figs 4-8f and 4-9f) and in sample OS 37A a network of interconnected fluid inclusion 'tubules' that include a fluid phase (Fig 4-8h).

Fig 7 (Kendrick et al., 2005)
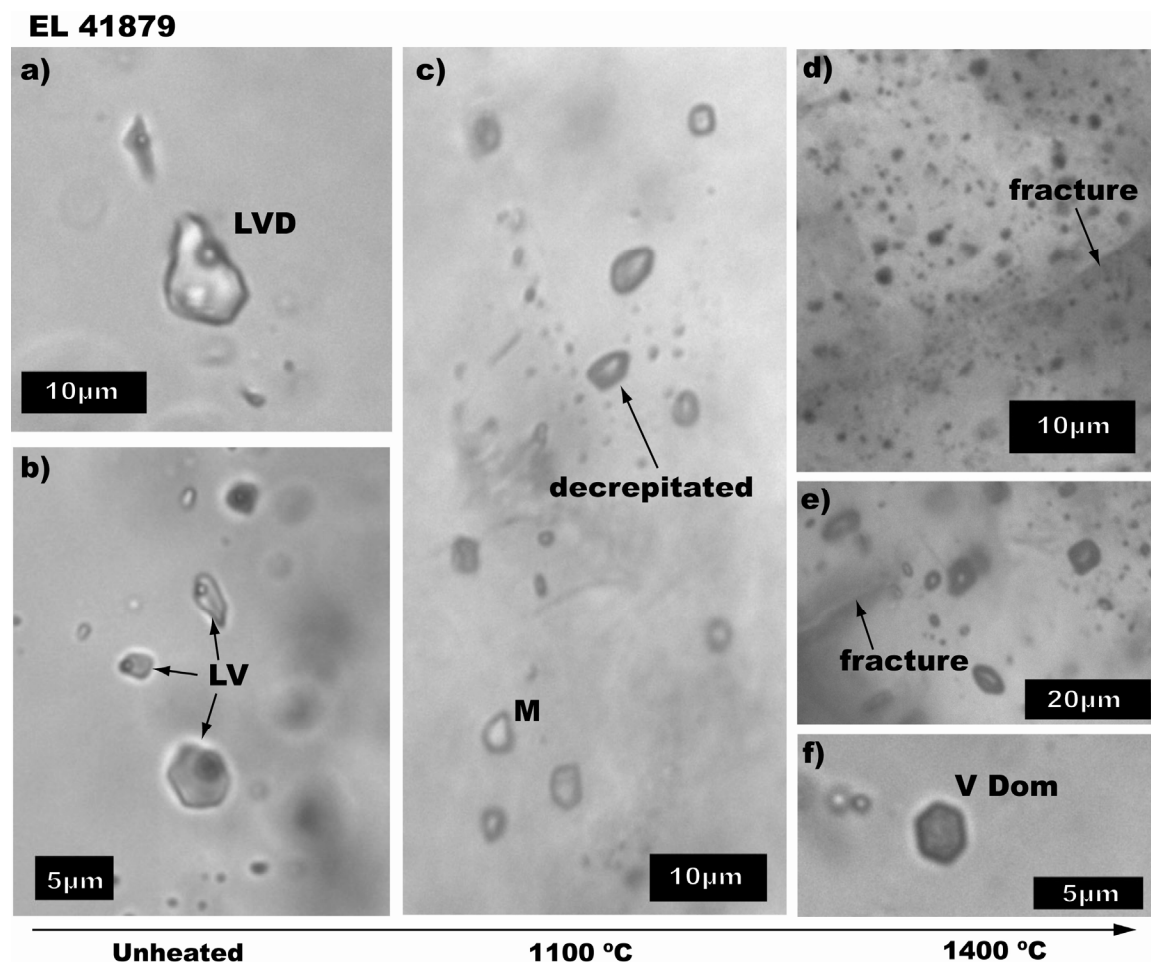
Fig 4-7. Photomicrographs of sample EL 48179 from Eloise. (a and b) Before heating. (c) After heating to 1100 °C in the UHV resistance furnace. (d, e and f) After heating to 1400°C in the UHV resistance furnace. In the samples heated to 1100 °C vapour dominated fluid inclusions can be difficult to distinguish from those that have decrepitated. However, careful observation confirms many inclusions remain in tact.
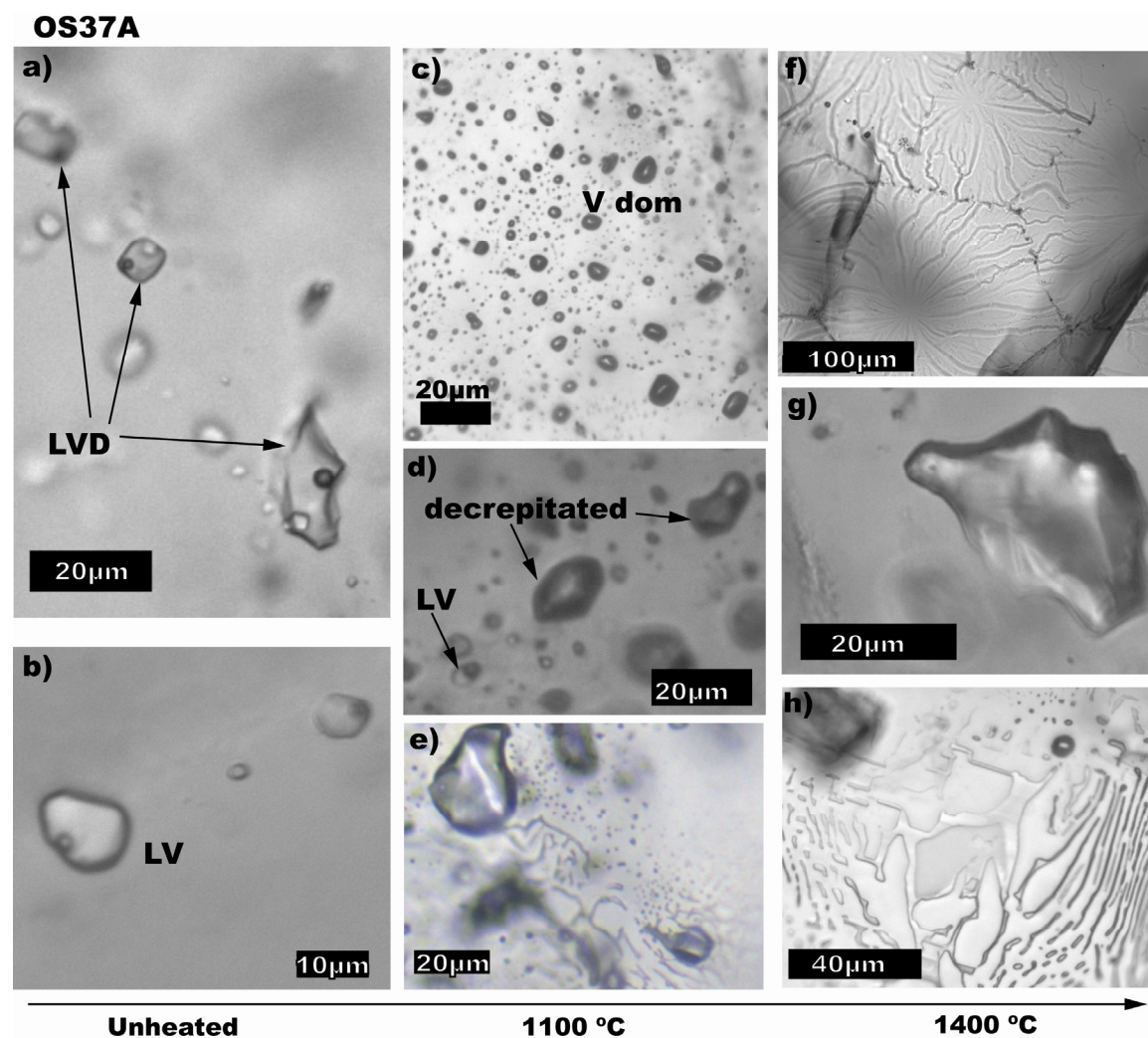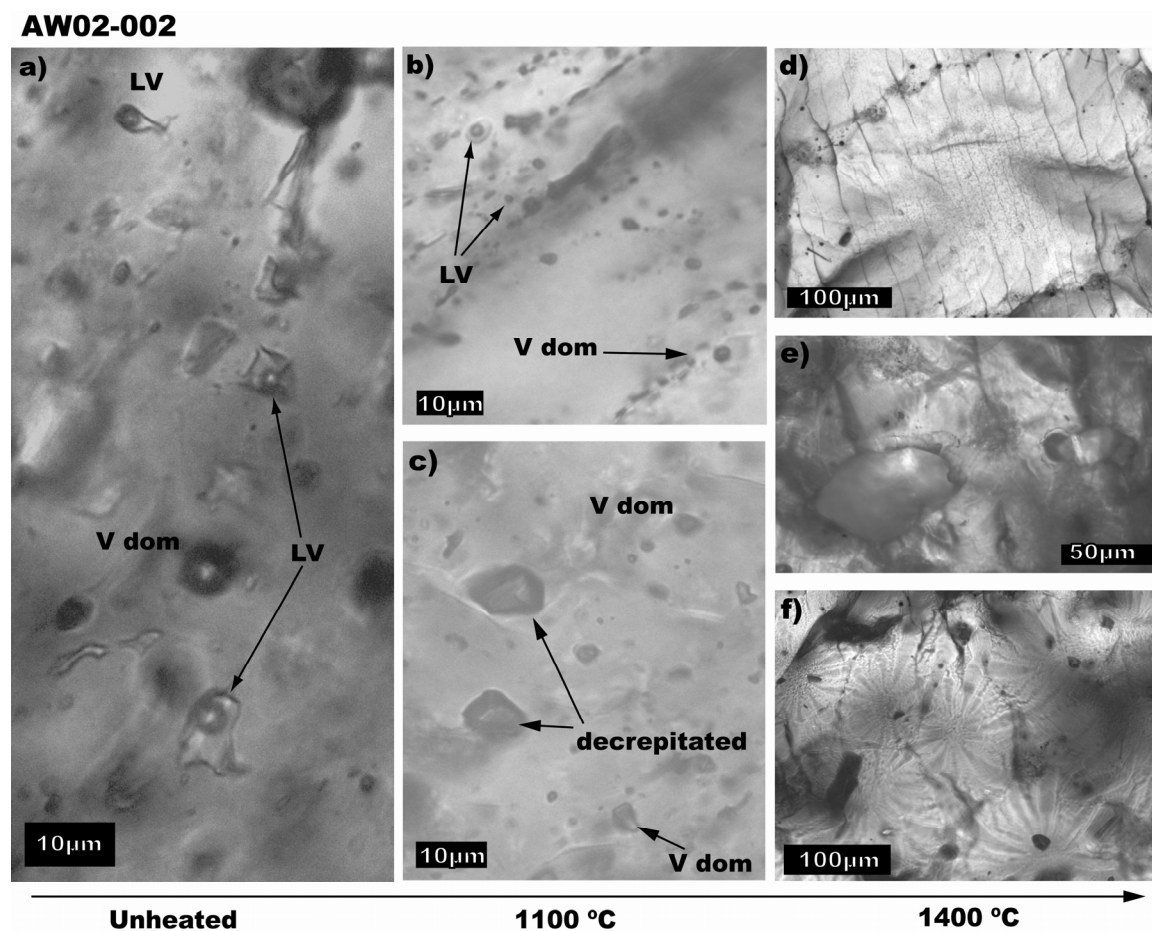
Fig 8 (Kendrick et al., 2005)

Fig 4-8. Photomicrographs of sample OS 37A from Osborne. (a and b) Before heating. (c, d and e) After heating to 1100°C in the UHV resistance furnace. (f,g and h) After heating to 1400°C in the UHV resistance furnace.

Fig 9 (Kendrick et al., 2005)

Fig 4-9. Photomicrographs of sample AW02-002 from the Railway Fault. (a) Before heating. (b and c) After heating to 1100 °C in the UHV resistance furnace. (d, e, and f) After heating to 1400°C in the UHV resistance furnace.

4.4.4 Interpretation of degassing profiles

The bimodal nature of the quartz degassing profile (Fig 4-2) suggests that diffusion is not the primary control on the release of noble gases during stepped heating. Microscopic observations indicate that Ar-degassing from quartz at low temperature (<700 °C) is by the decrepitation of fluid inclusions. Although some fluid inclusions remain undecrepitated on the fluid inclusion stage by 600 °C, very little degassing occurs between 600 and 1200 °C (Fig 4-2).

Four lines of evidence suggest that the gas released at high temperature (1200-1450 °C), is also from the fluid inclusion reservoir: 1) A fluid phase has been observed within quartz heated to 1400 °C (Fig 4-8h). 2) Quartz heated to 1400 °C exhibits evidence for explosive decrepitation, while quartz heated to 1100 °C does not (Figs 4-8g and 4-9e). 3) Crushing a sample prior to step heating reduces the size of both the low and high temperature degassing peaks (Fig 4-2b). 4) More gas is released by crushing a sample than is released at <700 °C by stepped heating (Table 3).

4.4.4.1. Gas release triggers

It has previously been observed that the 573 °C phase transition of α-quartz to β-quartz promotes the decrepitation of fluid inclusions (Bodnar et al., 1989). Although our degassing curves are constructed from stepwise heating increments of 50-100 °C and do not have the resolution necessary to identify a degassing spike at 573 °C, a spike is seen at this temperature on the dewatering curve of Barker and Robinson (1984) (Fig 4-2a). Barker and Robinson (1984) reported no further dewatering spikes, but their experiments did not reach temperatures of >1200 °C.

A phase transition is an attractive mechanism to explain the sudden degassing of our samples at ~1200 °C (Fig 4-2). Impure fluid inclusion rich natural-quartz under ultra-high-vacuum may behave quite differently to pure SiO_2 at 1 bar of pressure which transforms from β-quartz to tridymite at 867 °C and from tridymite to cristobalite at 1470 °C (Tuttle and Bowen, 1958). In particular, the temperature of metastable-melting or metastable-phase-transition is extremely sensitive to the rate of heating, particle size, surface conditions and the presence of gaseous, liquid or solid impurities (Hummel, 1984).

Possible phase transitions to explain the sudden release of gas at 1200 °C include a the tridymite-M to tridymite-S transition, or the metastable transition of superheated β-quartz to undercooled β-cristobalite (see Sosman, 1965 or Hummel, 1984). The metastable transition of superheated β-quartz to undercooled β-cristobalite at ~1200 °C (Fenner, 1912), is favoured because this would also explain the absence of any real dewatering spike at 867 °C (Fig 4-2a; Barker and Robinson, 1984) and because the same phase diagram suggests metastable melting of β-cristobalite to undercooled liquid silica could occur at ~1450 °C (see Hummel, 1984).

The radial fabrics that are developed in samples OS 37A and AW02-002a, heated to 1400 °C (Fig 4-8f and 4-9f), may be caused by volume changes associated with the proposed ~1200 °C phase transition. Furthermore, the change in the composition of noble gases released from sample AW02-002a at ~1450 °C (Fig 4-6) could be explained by

metastable melting of this sample. The lightest noble gases are most soluble in silica melts meaning Ar would be retained preferentially relative to Kr and Xe. Although the furnace crucible was empty after analysis of these samples, compatible with melting of the quartz chips, it is possible that not all of the samples behaved in exactly the same way because the heating schedules were slightly different for each sample. Samples analysed more recently, with a new furnace liner, and fewer heating steps at high temperature, were not melted and did not exhibit the degassing pattern of sample AW02-002a.

4.4.4.2 Fluid inclusion analysis

Even though we have shown gas released at both low and high temperature is from fluid inclusions, there are systematic differences in the Br/Cl (and I/Cl) composition of fluid inclusions decrepitated at <700 °C and in the temperature range 1200-1450 °C (Fig 4-5). In the rest of the paper, only Br/Cl and I/Cl compositions measured at <700 °C, that can be related to the observed behaviour of decrepitating fluid inclusions (Table 2), are considered representative of the fluid inclusions composition. Two potential artefacts might contribute to the systematically different Br/Cl and I/Cl compositions that are measured at >1200 °C:

1) Fluid inclusion decrepitation temperature is inversely proportional to size (Bodnar et al., 1989) and small fluid inclusions have been observed to remain preferentially undecrepitated at °600 C. It is possible that very small fluid inclusions (or nano-pore crystal defects) include fluids with non-representative compositions (Roedder, 1984) and they could dominate the composition of fluids released at 1200-1450 °C. However, non-representative compositions in very small melt inclusions are caused by partitioning of elements along the grain boundary into the crystal matrix (Roedder, 1984). Therefore, it could be argued that the noble gas and halogen composition of fluid inclusions will probably be unaffected because neither noble gases or halogens are important constituents of quartz.

2) The role of diffusion is likely to become increasingly important at high temperature and could lead to preferential release of the lightest noble gases, on the order Ar>Kr>Xe. This would reduce the measured $^{80}Kr_{Br}/^{38}Ar_{Cl}$ and $^{128}Xe_I/^{38}Ar_{Cl}$ ratios giving low Br/Cl and I/Cl values at high temperature, as observed.

In contrast to the systematic difference in Br/Cl (and I/Cl) between the low and high temperature degassing peaks, the $^{40}Ar/^{36}Ar$ values exhibit non-systematic variation (Fig 4-5b). The isotopes of Ar are very close in mass and size relative to Kr or Xe. It therefore seems that they are unaffected by the processes controlling the Br/Cl values, and the $^{40}Ar/^{36}Ar$ and Ar/Cl compositions measured at all temperatures are considered representative of the included fluids.

4.5   Noble gas and Halogen geochemistry

4.5.1 Distinguishing primary and secondary fluid inclusions

The stepped heating data for the IOCG samples shows considerable scatter on a $^{40}Ar/^{36}Ar$ versus $Cl/^{36}Ar$ diagram, with the $^{40}Ar_E/Cl$ values ranging between 10^{-4} and 10^{-6} (Fig 4-10). High salinity primary fluid inclusions are expected to have the most elevated $Cl/^{36}Ar$ values. Therefore, the poor correlation between high $Cl/^{36}Ar$ and the highest $^{40}Ar/^{36}Ar$ values of slightly above 2000, indicate that extraction steps most representative of primary fluid inclusions do not have the highest $^{40}Ar/^{36}Ar$ values.

Compared to the IOCG samples, sample AW02-002 from the Railway Fault exhibits more typical behaviour in $^{40}Ar/^{36}Ar$ versus $Cl/^{36}Ar$ space, the data define a binary mixing array (Fig 4-10). In this case the mixing array represents the two groups of primary LV fluid inclusions identified within the sample and has a mean $^{40}Ar_E/Cl$ value of $\sim 2 \times 10^{-4}$. The most saline fluid inclusions with a mean salinity of ~12 wt % NaCl eq. have $^{40}Ar/^{36}Ar$ values of <3000. The less saline group with final melting temperatures of close to zero have lower $^{40}Ar/^{36}Ar$ and $Cl/^{36}Ar$, although the lowest values may also have been affected by atmospheric contamination.

4.5.1.1 IOCG decrepitation profiles

$Cl/^{36}Ar$ values are highest in fluids that have the highest salinity or that have lost ^{36}Ar through devolatilisation. They are plotted as a function of temperature in Figure 4-11a and suggest that the highest salinity primary fluid inclusions dominate decrepitation release from EL 41879 and OS 37B at 400-450 ºC and from EL 41877 and OS 37A at 600-650 ºC. However, this conclusion is weakened by the possibility that atmospheric contamination has affected the extraction steps to different extents.

Atmospheric contamination is expected to be most significant at low temperature where adsorbed gases are first released from the samples surface. Despite this, the highest $^{40}Ar/^{36}Ar$ values are measured at low temperature in the Eloise samples and as suggested not in the same steps as the highest $Cl/^{36}Ar$ values (Fig 4-11ab).

The $^{40}Ar_E/Cl$ value is related to the $^{40}Ar/^{36}Ar$ and $Cl/^{36}Ar$ values (see Fig 4-10), but because neither Cl or $^{40}Ar_E$ are present in the atmosphere, it is unaffected by atmospheric contamination. The lowest $^{40}Ar_E/Cl$ values correspond to fluids with the highest salinity or lowest $^{40}Ar_E$ concentration and were measured between 500 and 650 ºC in all of the samples (Fig 4-11c). Because the variation in $^{40}Ar_E/Cl$ value cannot be explained by air contamination it provides proof that stepped heating is sampling different fluid inclusion types at different temperatures.

The K/Cl values of both Eloise samples and OS 37B are highest at high temperature (Fig 4-11d). The high K/Cl values of 0.15 to 0.3, that are measured at high temperature in these samples are realistic for K-rich MS primary fluid inclusions. Sample OS 37A has a K/Cl value of greater than one at 600 ºC, suggesting the presence of a very minor K-mineral impurity.

Measurement of the highest Cl/^{36}Ar, lowest ^{40}Ar$_E$/Cl, and highest K/Cl values between 500 and 700 ºC, supports the observation made during microthermometry that the highest salinity fluid inclusions decrepitate at the highest temperatures (section 2.1).

Finally, the Br/Cl value is plotted as a function of temperature in Figure 4-12. The IOCG samples have the lowest Br/Cl values between 500 and 700 ºC which is interpreted as evidence that the highest salinity MS and LVD fluid inclusions have the lowest Br/Cl values (Fig 4-12a). The Br/Cl values of sample AW02-002 from the Railway Fault exhibit less systematic variation with temperature, maximum Br/Cl values were measured at 350 and 550 ºC in split-a and at 650 ºC in split-b (Fig 4-12b). The variation in this sample, that has a less variable ^{40}Ar$_E$/Cl value (Fig 4-10) is interpreted reflect variation in primary LV fluid inclusions only.

Fig 10 (Kendrick et al., 2005)
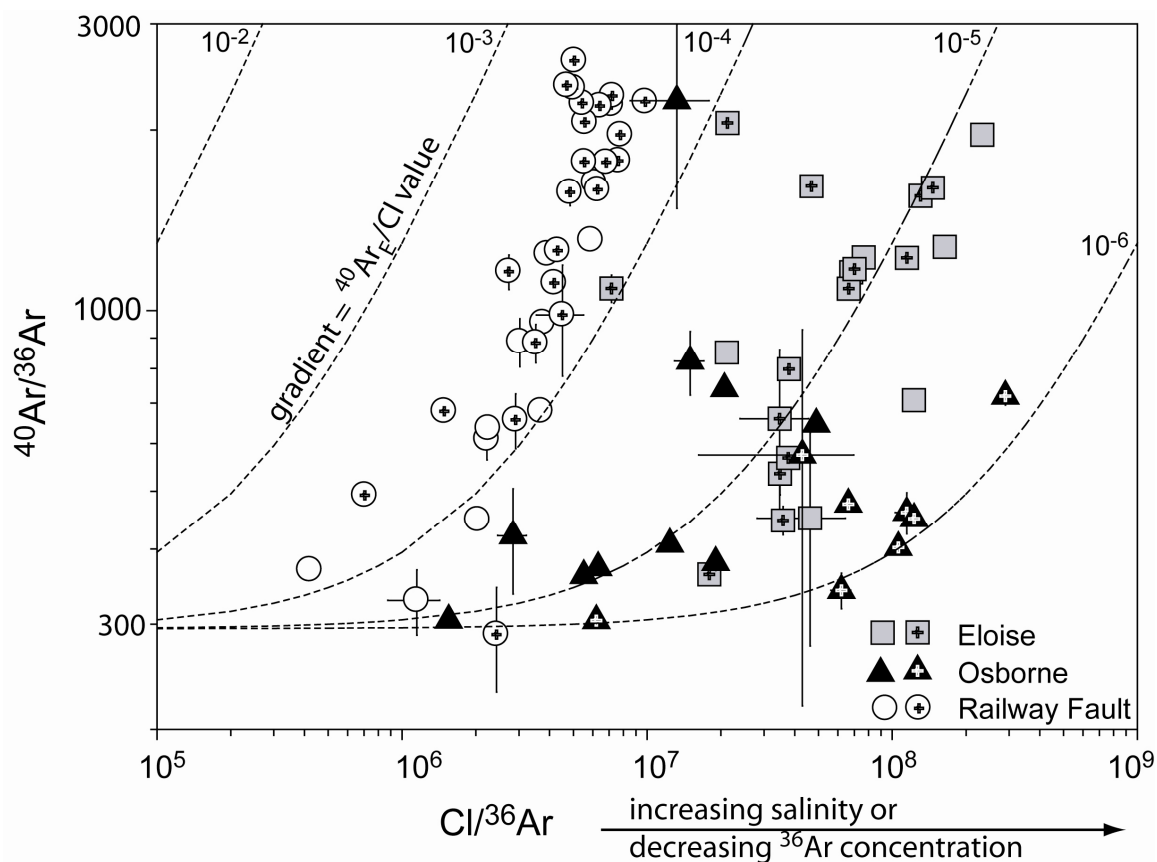
Fig 4-10. Log-log plot of $^{40}Ar/^{36}Ar$ versus $Cl/^{36}Ar$. Legend; Eloise, empty box = EL 48177; crossed box = EL 48179; Osborne, empty triangle = OS 37A; crossed triangle = OS 37B; Railway Fault, empty circle = AW02-002b; crossed circle = AW02-002a. IOCG samples are poorly correlated, the spread in data reflects mixing between a high salinity high $Cl/^{36}Ar$ fluid, a lower salinity fluid with higher $^{40}Ar/^{36}Ar$ value and air with $^{40}Ar/^{36}Ar = 295$ and $Cl/^{36}Ar = 0$. Sample AW02-002 from the Railway Fault exhibits a more typical pattern with less spread in $^{40}Ar_E/Cl$. This is explained by mixing between a high salinity high $^{40}Ar/^{36}Ar$ fluid and a lower salinity fluid with lower $^{40}Ar/^{36}Ar$.

Fig. 11 (Kendrick et al., 2005)
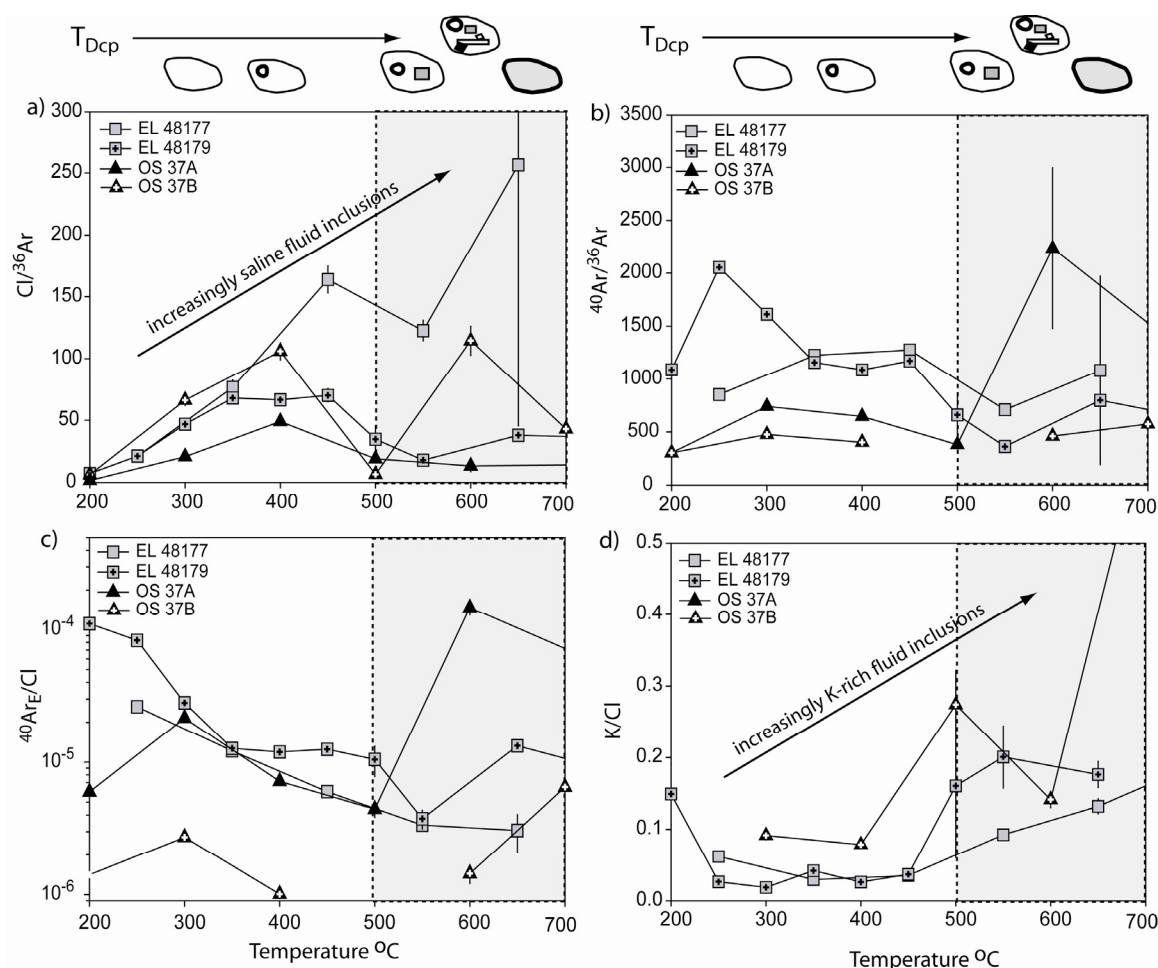
Fig 4-11. Decrepitation profiles for the Eloise and Osborne IOCG deposits. The schematic above the plots indicate the microthermometry observation that the most saline LVD and MS fluid inclusions decrepitate at the highest temperatures of >500 ℃ (see Table 2). (a) The highest $Cl/^{36}Ar$ values are measured at high temperature, suggesting that the most saline primary fluid inclusions decrepitate at this point. (b) The highest $^{40}Ar/^{36}Ar$ values are measured at low temperature in the samples from Eloise. With the exception of one data point Osborne exhibits little variation. (d) The $^{40}Ar_E/Cl$ value is unaffected by atmospheric contamination, the lowest values are measured in the Eloise samples at high temperature, compatible with decrepitation of the highest salinity fluid inclusions at this point. The high $^{40}Ar_E/Cl$ OS 37A data point at 600 ℃ corresponds with the high $^{40}Ar/^{36}Ar$ release from this sample. (c) The highest K/Cl values are measured at high temperature, suggesting K-rich multiphase inclusions decrepitate at this point.

Fig. 12 (Kendrick et al., 2005)
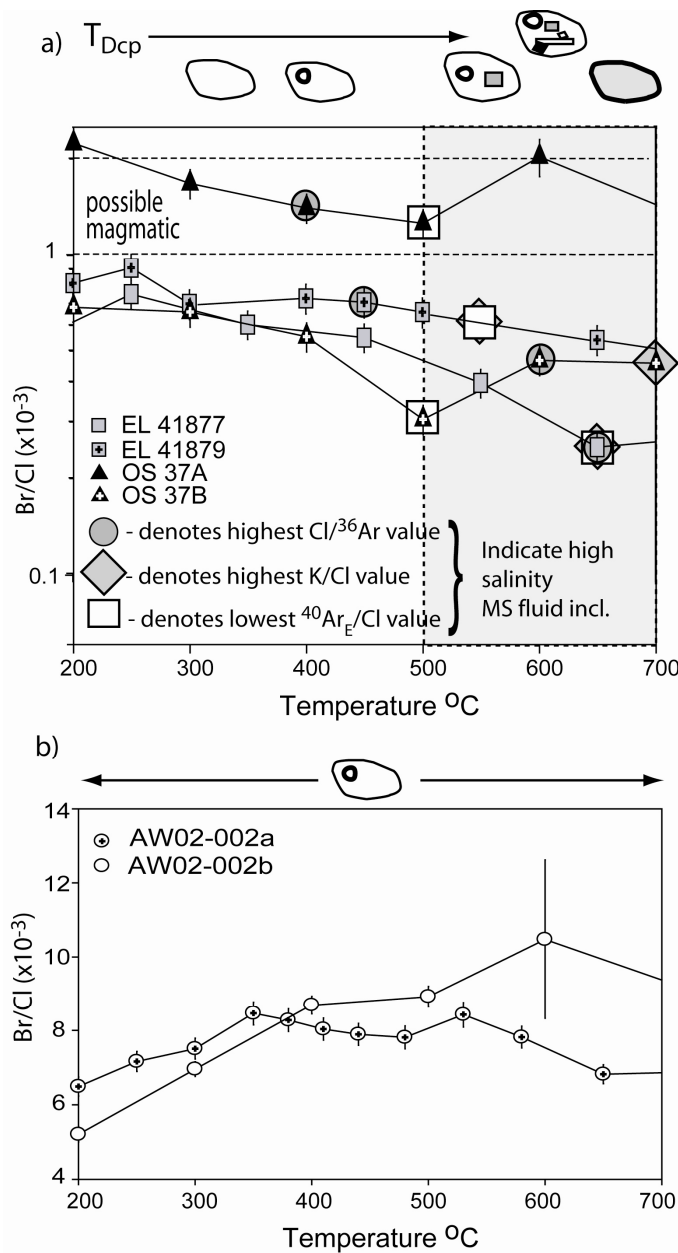
Fig 4-12. Br/Cl decrepitation profiles. (a) For the IOCG deposits Eloise and Osborne. The microthermometric observations are summarized above the plot, these and the fluid Ar/Cl and K/Cl values (Fig 4-11) indicate that the most saline primary fluid inclusions decrepitated above 500 ℃ are characterised by the lowest Br/Cl values. (b) The Railway Fault sample contains only LV fluid inclusions. Br/Cl variation in this sample is less systematic. Nb – analytical uncertainty only is shown for these samples.

4.5.1.2 Comparison with in vacuo crushing

In vacuo crushing was carried out on samples EL 48177 and AW02-002b and in both cases gave higher Br/Cl values than were obtained by stepped heating (Table 3). In the case of sample EL 48177 that is dominated by high salinity LVD fluid inclusions (Table 1), the difference can be explained by the retention of $^{38}Ar_{Cl}$ in daughter minerals which leads to artificially elevated Br/Cl and I/Cl values during *in vacuo* crushing (Kendrick et al., 2001a).

In contrast, the true Br/Cl and I/Cl values are obtained during stepped heating of the uncrushed sample splits. Daughter mineral retention of $^{38}Ar_{Cl}$ does not appear to be significant during stepped heating because: 1) The vast majority of fluid inclusions homogenise before decrepitation. 2) MS fluid inclusions that decrepitate before complete homogenisation retain only the least soluble daughter minerals such as carbonate or pyrosmalite that are not major reservoirs for Cl or $^{38}Ar_{Cl}$. 3) After decrepitation and at temperatures of a few hundred degrees, $^{38}Ar_{Cl}$ is readily released from undissolved daughter minerals: Stepped heating of halite bearing crushed residues yields very low Br/Cl and I/Cl values at 200 ℃, indicating that $^{38}Ar_{Cl}$ is readily liberated from the daughter minerals at this temperature. Therefore, retention of $^{38}Ar_{Cl}$ in undissolved daughter minerals cannot explain the shift to low Br/Cl and I/Cl values that is seen in all samples at 1200-1450 ℃.

Daughter minerals were not observed in the wafer of sample AW02-002. Although it is possible that daughter minerals were present in the split analysed but not in the wafer, two explanations more likely to explain the high Br/Cl values determined by *in vacuo* crushing (Table 3) are that either; 1) *in vacuo* crushing sampled a different population of fluid inclusions compared to stepped heating, or 2) the splits analysed were from significantly different zones within the sample that had real differences in Br/Cl.

In all the other samples analysed from the Mt Isa Inlier to date, *in vacuo* crushing and stepped heating yield similar results when daughter minerals are absent (Kendrick, unpublished data). However, the Br/Cl and I/Cl values determined by stepped heating uncrushed samples usually exhibit greater variation than those determined by *in vacuo* crushing. This is compatible with the selective decrepitation of different fluid inclusion types at different temperatures during stepped heating and the homogenisation of many different fluid inclusion types during *in vacuo* crushing.

4.5.2 Fluid origins

4.5.2.1 Halogens

In order to simplify presentation of the data the weighted mean Br/Cl and I/Cl values of gas released from each sample, in the temperature range 200 to 700 ℃, have been plotted (large symbols in Fig. 4-13). The intra-sample variation is indicated by the composition of individual extraction steps (small symbols in Fig. 4-13) and is far greater than the analytical uncertainty of 1.5-3% for Br/Cl and 3-5% for I/Cl (1σ).

The majority of IOCG samples plot in a field with Br/Cl between 0.3×10^{-3} and 10^{-3} and I/Cl between 10^{-6} and 5×10^{-6} (Fig. 4-13). These values are lower than the range of values

previously determined for Porphyry Copper Deposits (PCD) and Mantle Diamond (0.9-2×10^{-3} and $8\text{-}100 \times 10^{-6}$, Johnson et al., 2000; Kendrick et al., 2001b), that are considered representative of juvenile magmatic fluids derived from a mantle source. Sample OS 37A lies within the above range, compatible with some involvement of juvenile magmatic fluids in IOCG genesis. Such fluids could be derived from the abundant A-type granites within the Cloncurry district (Baker, 1998; Williams, 1998; Mark et al., 2004).

The lowest Br/Cl and I/Cl values are slightly above those of halite dissolution waters (Fig 4-13). These values may represent either incomplete halite dissolution, were NaBr and NaI have been dissolved preferentially relative to NaCl, or it may represent mixing between halite dissolution water and a magmatic fluid (Barton and Johnson, 1996). In either case, halite dissolution must have occurred at high pressure and temperature to enable the exceptional salinities of ~65 wt %, that are much greater than the salinity of surface brines saturated with halite (26 wt %). It is notable that the samples including the highest salinity fluid inclusions, OS 37B and EL 48177, have the least magmatic compositions (Table 1 and Fig 4-13) which supports the idea that evaporites may be the most important source of salinity for IOCG genesis (Barton and Johnson, 1996).

An alternative to halite dissolution might be acquisition of Cl by melting of the abundant metamorphic scapolite that is present within the district and formed by metamorphism of evaporitic rocks (Williams, 1998; Mark and Pollard, 2003). Although little is known about the fractionation of Br and Cl in scapolite, metamorphic scapolite derived from Br-poor evaporitic rocks might also have a Br-poor composition.

AW02-002 has a Br/Cl and I/Cl composition that lies very close to the modern day seawater evaporation trajectory (Fig 4-13; Zherebstova and Volkova, 1966). Silicic alteration at the Mt Isa mine is characterised by fluid inclusions with similarly elevated Br/Cl values (Heinrich et al., 1993). Such values may represent a bittern brine that has been enriched in iodine subsequent to a sub-aerial origin by the evaporation of seawater beyond the point of halite saturation. Iodine enrichment can take place in the sub-surface as a result of fluid interaction with organic-rich sedimentary rocks (Worden, 1996; Kendrick et al., 2005a). As the fluid inclusions are no longer saturated with halite significant dilution has also taken place.
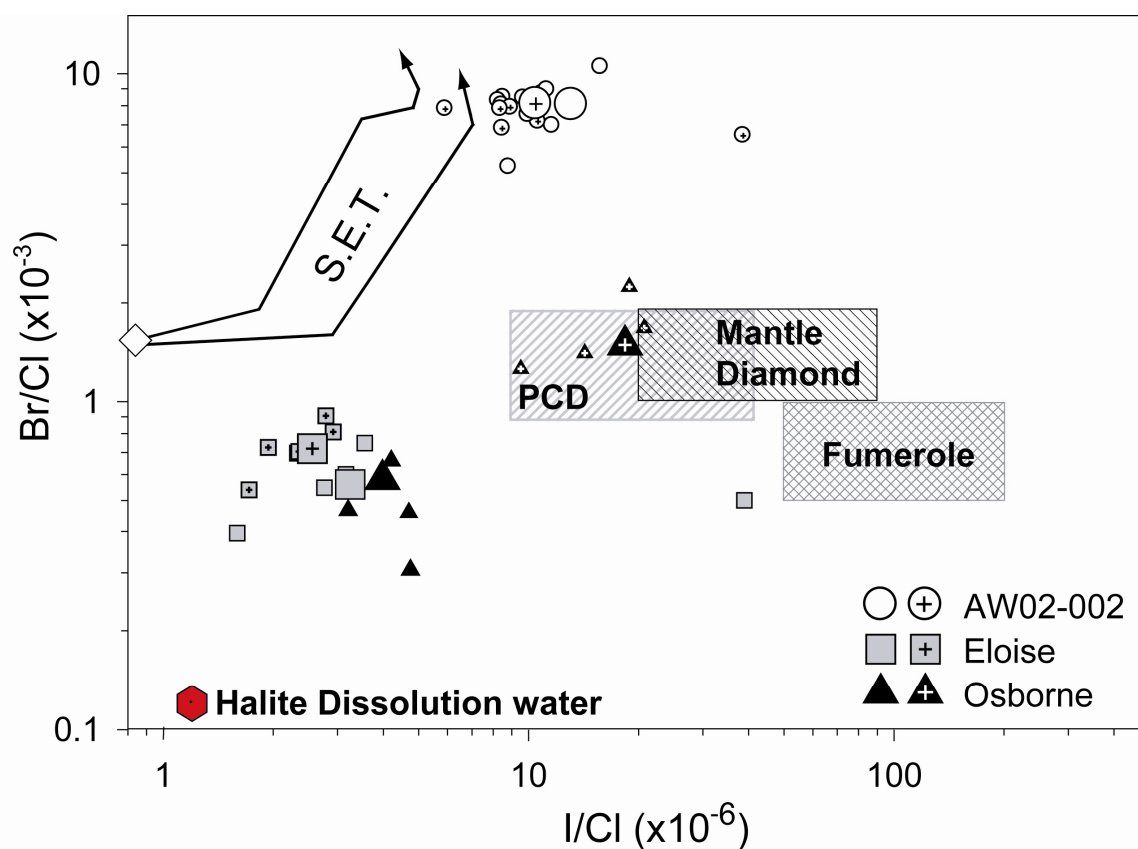
Fig 13 (Kendrick et al., 2005)

Fig 4-13. Br/Cl and I/Cl data for quartz samples from Eloise, Osborne and the Railway Fault. Large data points represent the weighted mean of gas released in the temperature interval 200-700 °C, small data points represent the composition of individual extraction steps. The empty and crossed symbols distinguish individual samples for each of the localities and are the same as in all other figures. The compositions of halite dissolution water (Böhlke and Irwin 1992b), seawater, the seawater evaporation trajectory (S.E.T.; Zherebtsova and Volkova, 1966) and the composition of possible magmatic fluids derived from the mantle (Porphyry Copper Deposit fluids PCD, mantle diamond and volcanic fumeroles; Kendrick et al., 2001b and references therein) are shown for reference.

4.5.2.2 Argon

The Eloise and Osborne IOCG samples have low $^{40}Ar/^{36}Ar$ values from near the atmospheric value of 295, up to a maximum of 2236 in sample OS 37A which has the most mantle-like halogen signature (Figs 4-12 and 4-13; Table 4). These values are orders of magnitude lower than the MORB mantle $^{40}Ar/^{36}Ar$ value of >40,000 (Burnard et al., 1997; Moriera 1998) and, like the halogens, provide strong evidence that an external meteoric or halite dissolution water component has been involved in mineralisation.

The $^{40}Ar_E/Cl$ values are highly variable lying between 10^{-5} and 10^{-6} (Fig 4-10). These values are much lower than the values measured in mantle diamond and the most magmatic PCD fluids (Johnson et al. 2000; Kendrick et al., 2001b) and also favour the involvement of crustal fluids. The maximum $Cl/^{36}Ar$ values, the minimum $^{40}Ar_E/Cl$ values and the maximum salinity of primary fluid inclusions indicate that the IOCG fluids have $^{40}Ar_E$ concentration of 0.4-3 ppm and ^{36}Ar concentration of 1-6 ppb (Table 4). The concentration of ^{36}Ar is slightly lower than that of meteoric water, in the majority of samples that have halite dissolution-like halogen signatures, but sample OS 37A with the magmatic-like halogen signature is enriched in both $^{40}Ar_E$ and ^{36}Ar relative to either meteoric water or mantle fluids (Table 4).

The correction for post-entrapment *in situ* production of radiogenic $^{40}Ar_R$ is straight forward for the IOCG samples, but in sample AW02-002 it is complicated by the presence of accidentally trapped mica in the fluid inclusions. The analytical implications of the accidently trapped mica are evaluated fully in Part II (Kendrick et al., 2005a); here we note only that the sample has a mean $^{40}Ar/^{36}Ar$ value of <2000 (Table 4). This is slightly higher than the maximum values determined for the composition of ore fluids in several MVT districts (Kendrick et al., 2002ab). The maximum $Cl/^{36}Ar$ value of 5.9-9.8×10⁶ and the mean salinity of ~12 wt % NaCl eq. indicate a ^{36}Ar concentration of 8-13 ppb, significantly above the concentration in meteoric water (Table 4). The noble gas and halogen data are compatible with the origin of this fluid as a basinal brine that has been enriched in atmospheric noble gases through interaction with fine grained sedimentary rocks.

Measurement of the heavier, atmospheric noble gases ^{84}Kr and ^{129}Xe was compromised at temperatures of <600 ºC by a blank component associated with the Cu-foil packaging (section 3.3). The $F^{84}Kr$ and $F^{129}Xe$ values obtained by *in vacuo* crushing and at temperatures of over 600 ºC encompass a range from significantly less than the air value of one up to values of greater than ASW (Appendix B). The range in values cannot be explained by mixing between air and ASW alone, phase separation or interaction with fine grained organic-rich sediments may explain the additional fractionation. However, due to the lack of data at <600 ºC, that can be correlated with decrepitation of a given population of fluid inclusions, we make no further comment.

Table 4. Summary of compositions determined for primary fluid inclusions[♣]

Sample	$^{40}Ar/^{36}Ar$ 500-700 °C	$Cl/^{36}Ar$ Max. ×10^6	$^{40}Ar_E/Cl$ Min.	Salinity Max. 1° Wt. %	Max. [^{36}Ar] cm^3 cm^{-3} H$_2$O ×10^{-6}	ppb	Max. [$^{40}Ar_E$] cm^3 cm^{-3} H$_2$O×10^{-3}	ppm	Br/Cl ×10^{-3} 500-700 °C	I/Cl ×10^{-6} 500-700 °C
Eloise										
EL 48177	708-1082	257	3.1	50	0.7	1	0.6	1	0.25-0.40	0.37-1.7
EL 48179	360-800	146	3.8-8.9	40	1.0	2	0.6-1.4	1-3	0.54-0.66	0.39-1.8
Osborne										
OS 37A	520-2236	49	4.4	45	3.5	6	0.8	1	1.3-2.0	10
OS 37B	460-570	289	0.7-1.0	65	0.9	1	0.2-0.3	0.4-0.5	0.31-0.47	3.4-5.0
Railway Fault										
AW02-002a	1921*	9.8		12	4.7	8			8.1	9.4
AW02-002b	728*	5.9		12	7.8	13			8.1	12
Reference values										
Meteoric	295			0	1-1.7	1.6-2.7	0	0	--	--
Halite dissolution		>>0		high					0.1	1.2
Seawater	295	10-17	0	3.5	0.8-1.3		0	0	1.54	0.86
MORB Mantle	>40 000	30	10^{-3}	<8 to ?	<0.1	<0.16	0.03	54	0.9-2	9.3-40

[♣] *Primary MS and LVD fluid inclusions are interpreted to dominate decrepitation release between 500 and 700 ºC for the IOCG samples. Sample AW02-002 includes only primary LV inclusions, the halogen values are averaged over 200-700 ºC and the $^{40}Ar/^{36}Ar$ values are averaged over the entire experiment. *Determination of initial $^{40}Ar/^{36}Ar$ values in samples that include accidentally trapped mica is discussed fully in Part II (Kendrick et al., 2005b). Reference values in Böhlke and Irwin, 1992b; Burnard et al. 1997; Moirea et al., 1998; Johnson et al., 2000; Kendrick et al., 2001b; Ozima and Podesek, 2002.*

4.6 Conclusions

Fluid inclusions are the dominant reservoir for noble gases and halogens in quartz. During stepped heating they degas bimodally in two decrepitation related degassing peaks. Compositional variation in Br/Cl and I/Cl within the first degassing peak (<700 ºC) can be related to the different decrepitation temperatures of different types of fluid inclusion determined by microthermometry. Variations in Cl/Ar and K/Cl can be used as imperfect proxies to confirm if the K-rich ultra-high-salinity fluid inclusions are decrepitated in the expected ranges.

In all the samples analysed a greater volume of gas is released between 1200 and 1450 ºC during the second degassing peak, than is released at <700 ºC. The Br/Cl and I/Cl composition of this gas is systematically shifted to lower values than are obtained at <700 ºC. Release of this gas is probably triggered by a phase transition of quartz and the gas is released from the smallest fluid inclusions within the sample. The low Br/Cl and I/Cl values may indicate that either the small fluid inclusions have non-representative compositions or that diffusion fractionates the noble gas elemental compositions at high temperature. Ar-isotopes are unaffected and appear representative of fluid compositions at all temperatures.

The study has demonstrated the potential of the noble gas and halogen technique to investigate Proterozoic ore deposits with complex fluid inclusion assemblages. Ultra-high salinity, primary fluid inclusions, in three IOCG samples from Eloise and Osborne have Br/Cl and I/Cl values of $0.25\text{-}0.66\times10^{-3}$ and $0.37\text{-}5.0\times10^{-6}$. One of the Osborne samples includes fluids with higher values that are similar to Porphyry Copper Deposits, compatible with the involvement of a juvenile magmatic fluid (e.g. Baker, 1998; Williams, 1998). However, it is the highest salinity samples that have compositions least similar to the magmatic range suggesting that interaction with evaporites is important. Like the halogens, the $^{40}Ar/^{36}Ar$ of <2000 and $^{40}Ar_E/Cl$ values of $10^{-5}\text{-}10^{-6}$ measured in IOCG fluids are most easily explained by the involvement of external crustal fluids.

The Railway Fault sample has basic thermometric properties that are similar to silicic alteration at the Mt Isa mine. The Br/Cl values are also similar at $\sim8.1\times10^{-3}$, and together with I/Cl of $9.4\text{-}12\times10^{-6}$, $^{40}Ar/^{36}Ar$ of <2000 and ^{36}Ar concentration of 8-13 ppb, indicate an origin by the evaporation of seawater beyond the point of halite saturation and subsequent interaction with I-rich sedimentary rocks in the subsurface plus dilution to 12 wt. % NaCl eq.

The intra- and inter-sample variation for each of the deposits studied is large and more detailed work is required to better understand the genesis of the diverse mineralization types within the Mt Isa Inlier.

4.7   Acknowledgements

Appendix A – Irradiation UM#6 undertaken on the 30-Nov-2003.

$J = 0.0186 \pm 0.0001$ $\beta = 4.8 \pm 0.3$ $\alpha = 0.55 \pm 0.01$

J, β and α are determined experimentally from the Hb3Gr standard using K/Cl and K/Ca weight ratios (Kelley et al., 1986).

$$J = \frac{(e^{\lambda t} - 1)}{\left({}^{40}Ar_R/{}^{39}Ar_K\right)} \qquad \beta = \frac{(K/Cl)}{\left({}^{39}Ar_K/{}^{38}Ar_{Cl}\right)} \qquad \alpha = \frac{(K/Ca)}{\left({}^{39}Ar_K/{}^{37}Ar_{Ca}\right)}$$

Calculated neutron flux

Thermal flux $(\phi_t) = 9.6 \times 10^{18} \pm 0.6 \times 10^{18}$ Fast flux $(\phi_f) = 3.52 \times 10^{18} \pm 0.02 \times 10^{18}$

Standard Ar interference corrections obtained from salts

${}^{36}Ar/{}^{37}Ar_{Ca\text{-}salt} = 0.000322 \pm 0.000012$ ${}^{39}Ar/{}^{37}Ar_{Ca\text{-}salt} = 0.000685 \pm 0.000009$

${}^{38}Ar/{}^{39}Ar_{K\text{-}salt} = 0.0124 \pm 0.0001$ ${}^{40}Ar/{}^{39}Ar_{K\text{-}salt} = 0.0295 \pm 0.0023$

Calculation of parent elements

Reaction	*Important neutrons*	*Calculation*
${}^{39}K(n,p){}^{39}Ar$	Fast	K mols $= {}^{39}Ar_K$ cm³ STP $\times (3.647/J)$
${}^{40}Ca(n,\alpha){}^{37}Ar$	Fast	Ca mols $= {}^{37}Ar_{Ca}$ cm³ STP $\times (3.558/J\alpha)$
${}^{37}Cl(n,\gamma\beta){}^{38}Ar$	Thermal	Cl mols $= {}^{38}Ar_{Cl}$ cm³ STP $\times (4.022/\beta J)$ or
		Cl mols $= \dfrac{{}^{38}Ar_{Cl}\,\text{mols}}{\phi t \times \sigma t \times {}^{37}Cl/Cl \times Y}$
${}^{79}Br(n,\gamma\beta){}^{80}Kr$	Thermal + resonant*	Br mols $= \dfrac{{}^{80}Kr_{Br}\,\text{mols}}{\phi t \times \sigma t \times {}^{79}Br/Br \times Y} \div 1.3*$
${}^{127}I(n,\gamma\beta){}^{128}Xe$	Thermal + resonant*	I mols $= \dfrac{{}^{128}Xe_I\,\text{mols}}{\phi t \times \sigma t \times Y} \div 1.7*$

*Where; ϕ_t = thermal neutron flux; σ_t = reaction cross section; Y = yield (cross sections and resonance integrals are given in Irwin and Reynolds, 1995). *Resonance correction factors of 1.3 and 1.7 are based on several previous irradiations (Johnson et al., 2000; Kendrick et al., 2001a; 2002a; 2005a; unpublished data). Nb – ${}^{37}Ar_{Ca}$ is corrected for post irradiation radioactive decay.*

The calculation of Br and I based on thermal neutrons only is a simplification that necesitates incorparation of a resonant neutron correction factor. Based on the equations above Br/Cl and I/Cl values can be determined thus:

$$\frac{Br}{Cl} = \frac{{}^{80}Kr_{Br}}{{}^{38}Ar_{Cl}} \times \text{constant} * \qquad\qquad \frac{I}{Cl} = \frac{{}^{128}Xe_I}{{}^{38}Ar_{Cl}} \times \text{constant} *$$

Uncertainty in the flux of thermal neutrons cancels out. Total uncertainty is determined by the constants* above and is attributed to the resonant neutron correction factor only. Based on the variability of previous irradiations the analytical uncertainty (1.5-3% for Br/Cl and 3-5% for I/Cl) is therefore elevated to 10% (1σ) for both Br/Cl and I/Cl.

Appendix B – Noble gas and halogen data

The tabulated data is corrected for Ar-interference reactions and post irradiation isotope decay. The $^{40}Ar_{corr}$ value is the measured ^{40}Ar value corrected for post entrapment radiogenic production of $^{40}Ar_R$, based upon the measured K abundance of each step and assumed ages of Mt Isa, 1523 Ma; Eloise, 1530 Ma and Osborne, 1595 Ma, the uncorrected value is given in the appendix of Part II. The molar Br/Cl and I/Cl ratios are given in preference to Br and I abundances, because they have lower uncertainty.

Eloise

Temp °C	$^{40}Ar_{corr}$ mols (×10^{-15})	^{36}Ar mols (×10^{-15})	^{84}Kr mols (×10^{-18})	^{129}Xe mols (×10^{-18})	Cl mols (×10^{-9})	K mols (×10^{-9})	Br/Cl (×10^{-3})	I/Cl (×10^{-6})
EL 48177 Combined crushing and stepped heating data								22.5 mg
Cr 1	28.0 ± 0.1	0.17 ± 0.01	0.19 ± 0.01	0.28 ± 0.09	1.29 ± 0.08			
Cr 2	2336.7 ± 7.6	2.46 ± 0.01	56.6 ± 1.5	0.22 ± 0.09	142 ± 9	6.19 ± 0.04	0.89 ± 0.09	1.5 ± 0.2
Cr 3	1029.2 ± 2.3	0.73 ± 0.01	18.1 ± 0.5		78.9 ± 5.1	3.34 ± 0.02	0.87 ± 0.09	5.5 ± 0.6
200	140.31 ± 0.0	0.35 ± 0.01			18.0 ± 1.2		0.11 ± 0.01	0.35 ± 0.04
300	235.9 ± 0.5	0.31 ± 0.01			14.0 ± 0.9	0.41 ± 0.01	0.27 ± 0.03	1.2 ± 0.1
400	226.7 ± 0.7	0.39 ± 0.01			35.4 ± 2.3	1.14 ± 0.03	0.25 ± 0.03	1.0 ± 0.1
500	110.1 ± 0.5	0.135 ± 0.003			23.1 ± 1.5	1.88 ± 0.02	0.32 ± 0.03	0.8 ± 0.1
600	20.2 ± 0.4	0.224 ± 0.002			3.9 ± 0.3	1.75 ± 0.02	0.45 ± 0.05	
800	28.9 ± 0.7	0.02 ± 0.01	0.74 ± 0.01		7.0 ± 0.5	2.1 ± 0.2	0.44 ± 0.04	2.7 ± 0.3
1000	46.4 ± 0.6	0.04 ± 0.01	0.43 ± 0.22		5.5 ± 0.4	1.9 ± 0.2	0.54 ± 0.05	1.6 ± 0.2
1200	299.4 ± 1.6	0.42 ± 0.01	5.98 ± 0.10		25.5 ± 1.7	1.6 ± 0.1	0.44 ± 0.05	2.7 ± 0.3
1400	792.6 ± 2.7	0.51 ± 0.01	7.56 ± 0.16	0.43 ± 0.02	60.9 ± 4.0	2.9 ± 0.1	0.45 ± 0.05	2.6 ± 0.3
Total	5294 ± 9	5.76 ± 0.04			416 ± 12	23.2 ± 0.3		
EL 48177 Stepped heating data								26.0 mg
150	25.8 ± 0.2	0.14 ± 0.01			0.06 ± 0.01	0.17 ± 0.02	0.50 ± 0.07	40.8 ± 9.8
250	675.9 ± 1.8	0.79 ± 0.01			16.8 ± 1.1	1.04 ± 0.08	0.75 ± 0.08	3.7 ± 0.4
350	866.8 ± 2.3	0.71 ± 0.03			54.2 ± 3.5	1.60 ± 0.04	0.60 ± 0.06	3.3 ± 0.4
450	919.7 ± 2.5	0.72 ± 0.01			118 ± 8	4.15 ± 0.03	0.55 ± 0.06	2.9 ± 0.3
550	99.5 ± 0.4	0.141 ± 0.003			17.2 ± 1.1	1.60 ± 0.05	0.40 ± 0.04	1.7 ± 0.2
650	22.2 ± 0.2	0.02 ± 0.02	0.68 ± 0.02		5.3 ± 0.3	0.70 ± 0.03	0.25 ± 0.03	0.4 ± 0.1
800	22.2 ± 0.4	0.14 ± 0.01	1.93 ± 0.03		7.0 ± 0.5	1.52 ± 0.07	0.28 ± 0.03	1.2 ± 0.1
1000	58.3 ± 1.0	0.13 ± 0.05	1.31 ± 0.07		6.0 ± 0.4	1.33 ± 0.07	0.56 ± 0.06	1.3 ± 0.2
1200	1497.7 ± 4.3	0.76 ± 0.01	20.7 ± 1.1	0.91 ± 0.08	178 ± 12	8.34 ± 0.07	0.48 ± 0.05	2.9 ± 0.3
Total	4188 ± 6	3.56 ± 0.06			402 ± 14	20.4 ± 0.2	0.50 ± 0.07	40.8 ± 9.8

Chapter 4

Eloise

Temp °C	$^{40}Ar_{corr}$ mols ($\times 10^{-15}$)	^{36}Ar mols ($\times 10^{-15}$)	^{84}Kr mols ($\times 10^{-18}$)	^{129}Xe mols ($\times 10^{-18}$)	Cl mols ($\times 10^{-9}$)	K mols ($\times 10^{-9}$)	Br/Cl ($\times 10^{-3}$)	I/Cl ($\times 10^{-6}$)
EL 48179 Stepped heating data								**92.0 mg**
200	326.7 ± 0.5	0.30 ± 0.02			2.1 ± 0.1	0.32 ± 0.09	0.81 ± 0.09	3.06 ± 1.3
250	1245.6 ± 3.2	0.606 ± 0.004			12.9 ± 0.8	0.34 ± 0.07	0.91 ± 0.10	2.92 ± 0.4
300	692.2 ± 1.5	0.43 ± 0.01			20.1 ± 1.3	0.38 ± 0.00	0.70 ± 0.07	2.44 ± 0.3
350	375.6 ± 0.5	0.32 ± 0.01			22.0 ± 1.4	0.93 ± 0.06	0.71 ± 0.08	2.35 ± 0.2
400	399.9 ± 1.1	0.37 ± 0.01			24.4 ± 1.6	0.64 ± 0.03	0.73 ± 0.08	2.03 ± 0.2
450	485.0 ± 1.4	0.41 ± 0.02			29.0 ± 1.9	1.07 ± 0.06	0.71 ± 0.08	2.46 ± 0.3
500	68.9 ± 0.5	0.10 ± 0.03			3.6 ± 0.2	0.58 ± 0.36	0.66 ± 0.07	0.39 ± 0.3
550	35.4 ± 0.2	0.098 ± 0.003			1.8 ± 0.1	0.35 ± 0.07		
650	51.1 ± 0.3	0.064 ± 0.002	1.4 ± 0.2	0.44 ± 0.03	2.4 ± 0.2	0.43 ± 0.03	0.54 ± 0.06	1.80 ± 0.5
800	74.6 ± 0.3	0.14 ± 0.01	1.3 ± 0.2	0.48 ± 0.02	4.9 ± 0.3	0.95 ± 0.05	0.45 ± 0.05	2.75 ± 0.3
1000	113.9 ± 0.4	0.26 ± 0.01	2.7 ± 0.1	0.53 ± 0.05	9.1 ± 0.6	1.39 ± 0.01	0.48 ± 0.05	1.99 ± 0.2
1100	198.4 ± 1.2	0.349 ± 0.004	4.4 ± 0.2	0.42 ± 0.02	13.2 ± 0.9	0.94 ± 0.01	0.52 ± 0.06	1.93 ± 0.2
1200	1341.7 ± 3.9	0.86 ± 0.01	22.3 ± 0.9	1.28 ± 0.08	113 ± 7	5.40 ± 0.05	0.51 ± 0.05	2.27 ± 0.2
1300	680.6 ± 1.7	0.56 ± 0.01	7.3 ± 0.4	0.42 ± 0.14	63.9 ± 4.1	3.29 ± 0.02	0.22 ± 0.02	0.87 ± 0.1
1400	853.7 ± 2.4	0.53 ± 0.01	5.3 ± 0.2	0.42 ± 0.06	78.0 ± 5.1	3.80 ± 0.05	0.19 ± 0.02	0.73 ± 0.1
Total	6957 ± 6	5.47 ± 0.05			400 ± 10	20.8 ± 0.4		

Chapter 4

Osborne

Temp °C	$^{40}Ar_{corr}$ mols ($\times 10^{-15}$)	^{36}Ar mols ($\times 10^{-15}$)	^{84}Kr mols ($\times 10^{-18}$)	^{129}Xe mols ($\times 10^{-18}$)	Cl mols ($\times 10^{-9}$)	K mols ($\times 10^{-9}$)	Br/Cl ($\times 10^{-3}$)	I/Cl ($\times 10^{-6}$)
OS 37A Stepped heating data								**41.9 mg**
200	158.9 ± 0.5	0.52 ± 0.01			0.81 ± 0.05	0.19 ± 0.01	2.2 ± 0.2	19.8 ± 2.0
300	186.8 ± 0.9	0.25 ± 0.01			5.2 ± 0.3	0.13 ± 0.03	1.7 ± 0.2	21.7 ± 2.2
400	190.9 ± 0.3	0.296 ± 0.004			14.5 ± 0.9	0.89 ± 0.02	1.4 ± 0.1	14.9 ± 1.5
200	22.9 ± 0.3	0.060 ± 0.002			1.15 ± 0.08	0.76 ± 0.07	1.3 ± 0.1	10.0 ± 1.2
600	25.9 ± 0.2	0.012 ± 0.004			0.15 ± 0.02	0.17 ± 0.16	2.0 ± 0.3	
800	24.8 ± 0.4	0.030 ± 0.004	1.78 ± 0.18	0.68 ± 0.02	0.45 ± 0.03	1.08 ± 0.08	1.0 ± 0.1	8.6 ± 1.6
1000	56.7 ± 2.4	0.13 ± 0.02	3.99 ± 0.17	0.78 ± 0.10	0.38 ± 0.03	1.75 ± 0.05	3.2 ± 0.3	27.8 ± 7.4
1200	113.4 ± 0.7	0.30 ± 0.01	8.28 ± 0.29	1.62 ± 0.03	1.92 ± 0.13	3.23 ± 0.04	1.6 ± 0.2	15.2 ± 1.7
1400	340.9 ± 0.9	0.84 ± 0.01	21.4 ± 0.9	3.63 ± 0.10	10.4 ± 0.7	1.56 ± 0.09	1.1 ± 0.1	8.0 ± 0.8
1600	766.5 ± 2.5	2.12 ± 0.01	79.5 ± 2.3	15.1 ± 0.3	11.7 ± 0.8	3.41 ± 0.06	2.8 ± 0.3	11.6 ± 1.2
Total	1888 ± 4	4.57 ± 0.03			47 ± 1	13.2 ± 0.2		
OS 37B Stepped heating data								**43.2 mg**
200	218.5 ± 0.8	0.718 ± 0.005			4.5 ± 0.3		0.68 ± 0.07	
300	185.7 ± 0.3	0.391 ± 0.005			25.8 ± 1.7	2.37 ± 0.01	0.66 ± 0.07	4.4 ± 0.5
400	125.5 ± 1.0	0.312 ± 0.003			33.0 ± 2.1	2.60 ± 0.04	0.55 ± 0.06	3.4 ± 0.4
500	34.0 ± 0.7	0.12 ± 0.01			0.8 ± 0.1	0.22 ± 0.04	0.31 ± 0.03	5.0 ± 0.7
600	52.0 ± 0.7	0.11 ± 0.01			12.9 ± 0.8	1.8 ± 0.1	0.47 ± 0.05	3.4 ± 0.4
700	11.0 ± 0.2	0.02 ± 0.01	1.04 ± 0.08	0.12 ± 0.10	0.8 ± 0.1	0.55 ± 0.03	0.46 ± 0.05	4.9 ± 1.6
800	11.0 ± 0.2		0.28 ± 0.12	0.092 ± 0.002	0.7 ± 0.0	0.67 ± 0.01	0.55 ± 0.06	2.0 ± 1.0
1000	13.3 ± 0.3	0.07 ± 0.01	1.11 ± 0.12	0.52 ± 0.01	1.7 ± 0.1	0.60 ± 0.11	0.61 ± 0.06	5.3 ± 0.8
1200	210.8 ± 1.0	0.29 ± 0.01	7.88 ± 0.21	0.73 ± 0.03	84.8 ± 5.5	9.9 ± 0.1	0.48 ± 0.05	3.8 ± 0.4
1400	146.5 ± 0.9	0.326 ± 0.004	8.59 ± 0.25	1.24 ± 0.02	40.0 ± 2.6	5.62 ± 0.03	0.22 ± 0.02	1.0 ± 0.1
1600	212.1 ± 1.4	0.62 ± 0.04	19.8 ± 0.7		38.5 ± 2.5	5.7 ± 0.1	0.49 ± 0.05	
Total	1221 ± 3	2.99 ± 0.05			243.6 ± 7.2	30.0 ± 0.2		

Railway Fault

Temp °C	$^{40}Ar_{corr}$ mols ($\times 10^{-15}$)	^{36}Ar mols ($\times 10^{-15}$)	^{84}Kr mols ($\times 10^{-18}$)		^{129}Xe mols ($\times 10^{-18}$)		Cl mols ($\times 10^{-9}$)	K mols ($\times 10^{-9}$)	Br/Cl ($\times 10^{-3}$)	I/Cl ($\times 10^{-6}$)
AW02-002a Stepped heating data										**126 mg**
150	27.7 ± 0.1	0.10 ± 0.003								
200	446.8 ± 1.4	0.91 ± 0.01					0.64 ± 0.04	0.90 ± 0.04	6.5 ± 0.7	40.5 ± 4.9
250	1363.7 ± 4.3	2.01 ± 0.02					3.0 ± 0.2	5.94 ± 0.05	7.2 ± 0.8	11.1 ± 1.2
300	2799.3 ± 9.3	2.23 ± 0.02					9.6 ± 0.6	15.6 ± 0.1	7.5 ± 0.8	10.4 ± 1.1
350	6944.3 ± 23.0	3.91 ± 0.03					29.9 ± 1.9	37.9 ± 0.3	8.5 ± 0.9	8.9 ± 0.9
380	3471.6 ± 11.4	1.56 ± 0.01					15.3 ± 1.0	40.7 ± 0.2	8.3 ± 0.9	8.7 ± 0.9
410	2869.7 ± 12.2	1.46 ± 0.01					11.4 ± 0.7	78.7 ± 0.5	8.0 ± 0.9	8.8 ± 0.9
440	2658.7 ± 14.8	1.63 ± 0.02					9.9 ± 0.6	116.0 ± 0.7	7.9 ± 0.8	9.3 ± 1.0
480	566.8 ± 14.8	0.51 ± 0.01					2.1 ± 0.1	161.6 ± 1.0	7.8 ± 0.8	8.8 ± 0.9
530	270.2 ± 17.0	0.31 ± 0.01					1.1 ± 0.1	187.7 ± 1.2	8.4 ± 0.9	10.1 ± 1.1
580	149.5 ± 15.4	0.23 ± 0.00					0.66 ± 0.04	174.0 ± 1.1	7.8 ± 0.8	6.2 ± 3.2
650	80.5 ± 15.0	0.28 ± 0.02	4.4	0.5	0.20	0.02	0.68 ± 0.04	168.7 ± 1.0	6.8 ± 0.7	8.9 ± 4.6
750	873.7 ± 16.4	0.56 ± 0.03	13.2	0.6	0.62	0.05	2.7 ± 0.2	174.0 ± 1.0	6.9 ± 0.7	11.0 ± 1.3
850	271.3 ± 8.7	0.28 ± 0.06	7.5	0.3	0.26	0.01	1.2 ± 0.1	103.0 ± 0.6	5.3 ± 0.6	9.2 ± 1.1
1000	1402.0 ± 14.6	0.88 ± 0.02	13.0	0.5	1.02	0.02	5.5 ± 0.4	143.7 ± 0.9	5.8 ± 0.6	7.5 ± 0.9
1100	2069.0 ± 16.0	1.17 ± 0.04	17.3	0.6	1.94	0.06	8.0 ± 0.5	137.2 ± 0.9	5.0 ± 0.5	5.0 ± 0.5
1200	9100.1 ± 36.6	5.15 ± 0.04	56.7	2.1	2.48	0.10	28.6 ± 1.9	198.7 ± 1.2	4.3 ± 0.5	4.3 ± 0.5
1250	12064.1 ± 41.1	5.47 ± 0.04	55.0	2.0	2.45	0.07	39.1 ± 2.5	206.1 ± 1.2	3.7 ± 0.4	3.8 ± 0.4
1290	10717.0 ± 37.3	4.70 ± 0.04	48.8	2.3	2.75	0.06	34.0 ± 2.2	197.9 ± 1.2	3.1 ± 0.3	2.6 ± 0.3
1330	9208.4 ± 31.0	4.20 ± 0.03	42.1	1.9	1.74	0.12	27.0 ± 1.8	158.4 ± 1.0	2.8 ± 0.3	2.7 ± 0.3
1370	8358.4 ± 27.4	4.06 ± 0.04	44.3	1.6	1.23	0.26	22.7 ± 1.5	116.6 ± 0.7	3.1 ± 0.3	3.4 ± 0.4
1410	8187.9 ± 24.9	3.70 ± 0.03	44.5	1.6	1.85	0.15	20.1 ± 1.3	88.8 ± 0.5	3.7 ± 0.4	4.4 ± 0.5
1450	8245.0 ± 24.4	3.51 ± 0.02	71.2	2.6	2.56	0.14	17.5 ± 1.1	72.0 ± 0.4	6.6 ± 0.7	9.3 ± 1.0
1490	5628.5 ± 15.1	2.16 ± 0.01	117	4	4.57	0.20	10.9 ± 0.7	40.6 ± 0.3	18 ± 2	27 ± 3
1530	1827.9 ± 2.8	0.77 ± 0.01	114	4	5.78	0.19	3.6 ± 0.2	12.28 ± 0.08	63 ± 7	115 ± 12
1550	308.7 ± 0.9	0.27 ± 0.02	66.6	2.1	4.44	0.12	0.73 ± 0.05	2.29 ± 0.02	200 ± 21	499 ± 52
Total	21649 42	52.0 ± 0.1					306 ± 5	2639 ± 4		

Railway Fault

Temp °C	⁴⁰Ar_corr mols (×10⁻¹⁵)	³⁶Ar mols (×10⁻¹⁵)	⁸⁴Kr mols (×10⁻¹⁸)	¹²⁹Xe mols (×10⁻¹⁸)	Cl mols (×10⁻⁹)	K mols (×10⁻⁹)	Br/Cl (×10⁻³)	I/Cl (×10⁻⁶)
AW02-002b Combined crushing and stepped heating data								**22.9 mg**
Cr 1	128.6 ± 0.6	0.24 ± 0.03	2.9 ± 0.1	0.52 ± 0.03	0.53 ± 0.04	0.35 ± 0.03	9.2 ± 1.0	10.1 ± 1.4
Cr 2	273.0 ± 0.7	0.51 ± 0.02	9.7 ± 0.3	0.44 ± 0.01	1.34 ± 0.10	0.94 ± 0.05	10.9 ± 1.2	13.4 ± 1.7
Cr 3	1126.8 ± 2.4	1.89 ± 0.01	35.2 ± 1.2	1.8 ± 0.1	4.3 ± 0.3	3.44 ± 0.05	12.6 ± 1.3	12.9 ± 1.3
Cr 4	2634.6 ± 7.2	2.93 ± 0.02	66.5 ± 1.8	2.9 ± 0.1	10.7 ± 0.7	7.69 ± 0.05	11.9 ± 1.2	16.2 ± 1.7
Cr 5	2675.6 ± 6.0	3.11 ± 0.02	68.2 ± 1.9	3.6 ± 0.1	10.3 ± 0.7	8.52 ± 0.05	12.6 ± 1.3	18.8 ± 1.9
Cr 6	1669.5 ± 3.0	1.81 ± 0.02	45.5 ± 1.2	2.5 ± 0.2	8.0 ± 0.5	6.46 ± 0.06	12.4 ± 1.3	15.9 ± 1.7
200	330.9 ± 1.1	1.01 ± 0.01			0.26 ± 0.03	2.69 ± 0.04	5.7 ± 0.8	18.9 ± 2.9
300	300.0 ± 0.9	0.65 ± 0.01			0.86 ± 0.06	8.91 ± 0.06	5.9 ± 0.6	12.9 ± 1.5
400	373.8 ± 3.3	0.64 ± 0.02			2.6 ± 0.2	34.9 ± 0.2	5.4 ± 0.6	8.5 ± 1.1
500	180.5 ± 12.2	0.27 ± 0.01			0.71 ± 0.07	130.7 ± 1.0	8.4 ± 1.1	14.1 ± 1.8
600		0.189 ± 0.002			0.14 ± 0.01	74.5 ± 0.5	9.5 ± 1.0	27.6 ± 7.6
800		0.13 ± 0.03	2.1 ± 0.1	0.7 ± 0.0	0.36 ± 0.04	43.4 ± 0.3	6.7 ± 0.9	4.8 ± 1.2
1000	32.3 ± 1.6	0.196 ± 0.004	3.2 ± 0.1	0.7 ± 0.1	0.27 ± 0.02	15.7 ± 0.1	6.4 ± 0.7	19.7 ± 7.4
1200	333.6 ± 2.7	0.67 ± 0.01	12.7 ± 0.4	3.6 ± 0.1	1.32 ± 0.09	23.8 ± 0.1	4.4 ± 0.5	12.5 ± 1.4
1400	2383.0 ± 10.9	3.57 ± 0.02	53.6 ± 1.4	6.1 ± 0.2	11.9 ± 0.8	45.4 ± 0.3	5.9 ± 0.6	3.8 ± 0.4
1600	2730.7 ± 7.9	5.78 ± 0.09	198 ± 6	29.5 ± 0.8	7.2 ± 0.5	18.2 ± 0.1	19.0 ± 3.4	19.6 ± 5.1
Total	15140 ± 22.7	23.6 ± 0.1			61 ± 1	425 ± 1		
AW02-002b Stepped heating data								**23.3 mg**
200	161.6 ± 0.5	0.44 ± 0.01			0.18 ± 0.01	0.67 ± 0.03	5.2 ± 0.6	9.2 ± 7.8
300	1143.3 ± 3.5	0.92 ± 0.02			3.6 ± 0.2	5.9 ± 0.1	7.0 ± 0.7	12.2 ± 1.2
400	1135.6 ± 3.4	0.87 ± 0.02			5.1 ± 0.3	16.9 ± 0.1	8.7 ± 0.9	11.4 ± 1.2
500	232.8 ± 3.5	0.26 ± 0.02			0.8 ± 0.1	39.8 ± 0.2	8.9 ± 0.9	11.8 ± 3.8
600	51.6 ± 3.1	0.16 ± 0.02			0.18 ± 0.04	34.1 ± 0.2	10.5 ± 2.4	16.5 ± 4.3
800	268.0 ± 20.4	0.439 ± 0.003	9.3 ± 0.4	1.1 ± 0.1	1.0 ± 0.1	34.4 ± 0.2	8.3 ± 0.9	12.8 ± 1.4
1000	52.5 ± 1.2	0.117 ± 0.001	3.0 ± 0.1	0.8 ± 0.0	0.24 ± 0.02	10.2 ± 0.1	6.8 ± 0.9	11.4 ± 3.7
1200	644.2 ± 3.8	0.68 ± 0.03	11.1 ± 0.6	1.1 ± 0.0	2.5 ± 0.2	27.1 ± 0.2	4.9 ± 0.5	5.3 ± 0.6
1400	4167.4 ± 20.3	6.13 ± 0.04	64.6 ± 1.8	5.8 ± 0.1	22.6 ± 1.5	113.7 ± 0.7	5.4 ± 0.6	10.1 ± 1.1
1600	3965.2 ± 14.6	6.24 ± 0.04	169 ± 5	18.6 ± 0.4	14.0 ± 0.9	69.2 ± 0.4	16.8 ± 1.7	22.5 ± 2.3
Total	11822 ± 33	16.2 ± 0.1			50 ± 2	352 ± 1		

References

Baker, T., 1998, Alteration, Mineralisation, and Fluid Evolution at the Eloise Cu-Au Deposit, Cloncurry District, Northwest Queensland, Australia. *Econ. Geol.* **93**, p1213-1236.

Baker, T., Perkins C., Blake K.L., and Williams P.J., 2001, Radiogenic and Stable Isotope Constraints on the Genesis of the Eloise Cu-Au Deposit, Cloncurry District, Northwest Queensland. *Econ. Geol.* **96**, p723-742.

Ballentine C.J., Burgess R., and Marty B., 2002, Tracing fluid origin, transport and interaction in the crust. *In* Noble Gases in Geochemistry and Cosmochemistry, (eds. Porcelli D., Ballentine C.J., and Wieler R.), *Reviews in Mineralogy and Geochemistry* **47**, p539-614.

Barker C., and Robinson S.J., 1984, Thermal release of water from natural quartz, *American Mineralogist* **69**, 1078-1081.

Barton M.D., and Johnson D.A., 1996, Evaporitic-source model for igneous related Fe oxide (REE-Cu-Au-U) mineralization. *Geology* **24**, 259-262.

Bodnar R.J., Binns P.R., and Hall D.L., 1989, Synthetic fluid inclusions – VI. Quantitative evaluation of the decrepitation behaviour of fluid inclusions in quartz at one atmosphere confining pressure. *J. metamorphic geol.* **7**, 229-242.

Böhlke J.K. and Irwin J.J., 1992a, Laserprobe analyses of Cl, Br, I, and K in fluid inclusions: Implications for the sources of salinity in some ancient hydrothermal fluids. *Geochim. Cosmochim. Acta* **56**, 203-225 p.

Böhlke J.K. and Irwin J.J., 1992b, Brine history indicated by argon, krypton, chlorine, bromine, and iodine analyses of fluid inclusions from the Mississippi Valley type lead-fluorite-barite deposits at Hansonburg, New Mexico. *Earth Planet. Sci. Lett.* **110**, 51-66 p.

Böhlke J.K. and Irwin J.J., 1992c, Laser microprobe analyses of noble gas isotopes and halogens in fluid inclusions: Analyses of microstandards and synthetic inclusions in quartz. *Geochim. Cosmochim. Acta* **56**, 187-201 p.

Burnard P., Graham D., and Turner G. (1997) Vesicle-specific noble gas analyses of "popping rock"; implications for primordial noble gases in the Earth. *Science* **276**, 568-571.

Fenner C.N.,1913, Stability relations of the silica minerals. *American Journal of Science* **36**, 331-384.

Gauthier L., Hall G., Stein H., Schaltegger U., 2001, The Osborne Deposit, Cloncurry District: A 1595 Ma Cu-Au Skarn Deposit. In A Hydrothermal Odyssey, Extended conference Abstracts, Ed. Williams P.J., James Cook University, Townesville, pp 58-59.

Grant K., Gleeson S.A., and Roberts S., 2003, The high-temperature behavior of defect hydrogen species in quartz: Implications for hydrogen isotope studies. *American Mineralogist* **88**, 262-270.

Götze J., Plötze M., Graupner T., Hallbauer D.K., Bray C.J., 2004, Trace element incorporation into quartz: A combined study by ICP-MS, electron spin

resonance, cathodoluminescence, capillary ion analysis, and gas chromatography. *Geochim. Cosmochim. Acta* **68**, 3741-3759.

Heinrich C.A., Andrew A.S., Wilkins R.W.T., and Patterson D.J., 1989, A Fluid inclusion and stable isotope study of synmetamorphic copper ore formation at Mount Isa, Australia. *Economic Geology* **84**, p529-550.

Heinrich C.A., Bain J.H.C., Fardy J.J., and Waring C.L., 1993, Br/Cl geochemistry of hydrothermal brines associated with Proterozoic metasediment-hosted copper mineralisation at Mount Isa, northern Australia. *Geochim. Cosmochim. Acta* **57**, p2991-3000.

Hummel F.A., 1984, Introduction to phase equalibria in ceramic systems. Pp400 M.Dekker, New York, ISBN 0824771524.

Ihinger, P.H. and Zink, S.I. (2000) Determination of relative growth rates of natural quartz crystals. *Nature* **404**, 865–869

Irwin J.J., and Roedder E., 1995, Diverse origins of fluid inclusions at Bingham (Utah, USA), Butte (Montana, USA), St. Austell (Cornwall, UK) and Ascension Island (mid-Atlantic, UK), indicated by laser microprobe analysis of Cl, K, Br, I, Ba + Te, U, Ar, Kr, and Xe. *Geochim. Cosmochim. Acta* **59(2)**, 295-312.

Johnson L.H., Burgess R., Turner G., Milledge H.J. and Harris J.W., 2000, Noble gas and halogen geochemistry of mantle fluids: Comparison of African and Canadian diamonds. *Geochimica et Cosmochimica Acta* **64**, 717-732.

Kelley S., Turner G., Butterfield A.W., and Shepherd T.J. (1986) The source and significance of argon isotopes in fluid inclusions from areas of mineralisation. *Earth Plan. Sci. Lett*. **79**, 303-318.

Kendrick M.A., Burgess R., Pattrick R.A.D., and Turner G., 2001a, Halogen and Ar-Ar age determinations of inclusions within quartz veins from porphyry copper deposits using complementary noble gas extraction techniques. *Chem. Geol*. **177**, p351-370.

Kendrick M.A., Burgess R., Pattrick R.A.D., and Turner G., 2001b, Noble gas and halogen evidence on the origin of Cu-Porphyry mineralising fluids. *Geochim. Cosmochim. Acta* **65**, p2651-2668.

Kendrick M.A., Burgess R., Pattrick R.A.D., and Turner G. (2002a) Hydrothermal fluid origins in a fluorite-rich Mississippi valley-type deposit: combined noble gas (He, Ar, Kr) and halogen (Cl, Br, I) analysis of fluid inclusions from the South Pennine Orefield, United Kingdom, *Econ. Geol*. **97 (3)**, p435-451.

Kendrick M.A., Burgess R., Leach D. and Pattrick R.A.D. (2002b) Hydrothermal fluid origins in Mississippi valley-type ore deposits: combined noble gas (He, Ar, Kr) and halogen (Cl, Br, I) analysis of fluid inclusions from the Illinois-Kentucky Fluorspar district, Viburnum Trend, and Tri-State districts, mid-continent United States. *Econ. Geol*. **97 (3)**, p452-479

Kendrick M.A., Burgess R., Harrison D., and Bjørlykke A., 2005a, Noble gas and halogen evidence on the origin of Scandinavian sandstone-hosted Pb-Zn deposits. *Geochim. Cosmochim. Acta* **69**, 109-129.

Kendrick M.A., Phillips D., Miller J.McL., 2005b, Part II. Evaluation of ^{40}Ar-^{39}Ar quartz ages: Implications for fluid inclusion retentivity and determination of initial ^{40}Ar/^{36}Ar values in Proterozoic samples. Submitted to GCA.

Mark G., and Pollard P.J., 2003, Contrasting composition of metasomatic and metamorphic scapolite in the Eastern Fold Belt, Northwest Queensland, Australia. In Mineral Exploration and Sustainable Development (eds Eliopoulos et al.). Millpress, Rotterdam, ISBN 90 77017 77 1.

Mark G., Foster D.R.W., Pollard P.J., Williams P.J., Tolman J., Darvall M., and Blake K.L., 2004, Stable isotope evidence for magmatic fluid input during large-scale Na-Ca alteration in the Cloncurry Fe oxide Cu-Au district, NW Queensland, Australia. *Terra Nova* **16**, p54-61.

Moreira M., Kunz J., and Allegre C.J. (1998), Rare gas systematics in popping rock: Isotopic and elemental compositions in the upper mantle. *Science* **279**, p1178-1181.

Ozima M. and Podesek F.A., 2002, Noble Gas Geochemistry, 2nd Edition, Cambridge University Press, Cambridge UK. pp286.

Perkins C., Heinrich C.A. and Wyborn L.A.I., 1999, 40Ar/39Ar Geochronology of Copper Mineralisation and Regional Alteration, Mount Isa, Australia. *Econ. Geol.* **94**, p23-36.

Roedder E., 1984, Fluid Inclusions. Reviews in Mineralogy 12.

Sosman R.B., 1965, The Phases of Silica. Rutgers University Press, New Brunswick, New Jersey. pp388.

Turner G. and Bannon M.P., (1992) Argon isotope geochemistry of inclusion fluids from granite-associated mineral veins in southwest and northeast England. *Geochim. Cosmochim. Acta* **56**, 227-243.

Turner G., Burnard P., Ford J.L., Gilmour J.D., Lyon I.C., and Stuart F.M. (1993) Tracing fluid sources and interactions. *Phil. trans. Roy. Soc. Lon. A* **344**, 127-140.

Tuttle, O.F. and Bowen N.L., 1958, Experimental studies in the system NaAlSi$_3$O$_8$-KAlSi$_3$O$_8$-SiO$_2$-H$_2$O. *Memoir of the Geological Society of America* **74**, 153 pp.

Watson E.B., and Cherniak D.J., 2003, Lattice diffusion of Ar in quartz, with constraints on Ar solubility and evidence of nanopores. *Geochim et Cosmochim. Acta* **67**, 2043-2062.

Williams P.J., 1998, Metalliferous economic geology of the Mt Isa Eastern Succession, Queensland. *Australian Journal of Earth Sciences* **45**, p329-341.

Worden R.H. (1996) Controls on halogen concentrations in sedimentary formation waters. *Min. Mag.* **60**, 259-274.

Zherebtsova I.K. and Volkova N.N., (1966) Experimental study of behaviour of trace elements in the process of natural solar evaporation of Black Sea water and Lake Sasky-Sivash brine. *Geochem. Int.* **3**, 656-670

Chapter 5: Evaluation of ^{40}Ar-^{39}Ar quartz ages: Implications for fluid inclusion retentivity and determination of initial ^{40}Ar/^{36}Ar values in Proterozoic samples.

M.A. Kendrick, J.McL. Miller and D. Phillips

Summary

The argon isotope systematics of quartz vein samples related to the Mt Isa copper mineralization of the western succession, and the Osborne plus Eloise iron-oxide-copper-gold (IOCG) deposits of the eastern succession have been investigated in detail.

We demonstrate that, as in previous studies when fluid inclusions contain captive-mica impurities, excess ^{40}Ar$_E$ is strongly correlated with fluid inclusion Cl while radiogenic ^{40}Ar$_R$ is strongly correlated with K. The data define a plane in 3D ^{40}Ar-K-Cl-^{36}Ar space, which enables the determination of a robust 3D isochron. However, we conclude that in this case the ~1027 Ma age obtained for Mt Isa is related to thermal cooling and in these circumstances quartz ages do not always represent the age of quartz formation.

In contrast, fluid inclusions from Osborne and Eloise are K-rich but do not contain captive-mica. In these cases multiple stepped heating experiments constrained the maximum formation ages to a precision of 5% for Osborne and 15% for Eloise. The data support models in which the Osborne deposit formed during an early syn-D$_2$ 1595 Ma event and are compatible with the Eloise deposit forming during a later 1514-1530 Ma mineralisation event. Where captive mica impurities are absent, the correction for post mineralization radiogenic ^{40}Ar production is small and, the measured ^{40}Ar/^{36}Ar value is close to the initial value.

The data indicate that quartz is retentive to Ar over billions of years. However, where captive mica is present ^{40}Ar-loss can occur from within the sub-reservoir into the surrounding fluid inclusion. As most previous studies have determined ages for rapidly cooled Phanerozoic magmatic-hydrothermal systems, cooling ages have been indistinguishable from formation ages. The presence of mica impurities can be identified from sample degassing profiles and mean K/Cl values of >1. It is then essential to determine the siting of the impurity within the sample. Backscattered electron microscopy has been used to confirm the presence, and determine the size range, of captive-mica within the fluid inclusions of the Mt Isa sample. In light of these findings, some unexpectedly young quartz ages determined in other studies may need to be reassessed.

5.1   Introduction

Age constraints on many classes of ore deposit have traditionally been limited by the low abundance of radioactive parent elements in most ore minerals. However, direct dating of hydrothermal phases via solid or fluid inclusions has enabled several previously problematic classes of ore deposit to be dated. Variably successful methods include; Ar-Ar quartz (Kelley et al., 1986; Turner and Bannon, 1992; McKee et al., 1993; Qui 1996; Kendrick et al., 2001a) and Ar-Ar pyrite (York et al., 1982; Smith et al., 2001; Miller et al., 2004); aswell as; Rb-Sr sphalerite (Brannon et al., 1992; Nakai et al., 1990, 1993), Rb-Sr quartz (Sheppard and Darbyshire, 1981; Darbyshire and Sheppard, 1985; Pettke and Diamond, 1995) and U/Th-Pb Calcite (Coveney et al., 2000).

Additionally, the Ar-isotope composition of fluid inclusions in quartz provides understanding of fluid origins and is in many cases of equal interest to the samples age (Kelley et al., 1986; Turner and Bannon, 1992; Kendrick et al., 2001ab). For example, initial $^{40}Ar/^{36}Ar$ values vary by orders of magnitude and can easily distinguish meteoric water with values of ~295 from deep crust or mantle fluids with values of up to or even greater than 40,000 (Burnard et al., 1999).

Successful determination of either an Ar-Ar quartz age or the initial $^{40}Ar/^{36}Ar$ value depends upon deconvolution of post-entrapment radiogenic $^{40}Ar_R$ formed *in situ* by the radioactive decay of ^{40}K, from atmospheric $^{40}Ar_A$ ($295 \times {}^{36}Ar_A$) plus excess $^{40}Ar_E$ that determine the initial $^{40}Ar/^{36}Ar$ value. If the samples age is known, the measured $^{40}Ar/^{36}Ar$ value can be easily corrected to the fluid inclusions initial $^{40}Ar/^{36}Ar$ value, because K is measured as $^{39}Ar_K$. However, the prevalence of excess $^{40}Ar_E$ in fluid inclusions, provides a significant challenge to Ar-Ar age determination (Rama et al., 1964). The problem has previously been overcome through the use of isochron diagrams, and where they fail 3D multi-component correlation diagrams. In the present study, we constrain when such diagrams can be used, and identify why different noble gas extraction techniques have been variably successful; with reference to six samples collected in the Mt Isa Inlier, northeast Australia (Fig 5-1).

Fluid inclusions from the Eloise (1530 Ma; Baker et al., 2001) and Osborne (1595 Ma; Gauthier et al., 2001) Iron Oxide Copper Gold (IOCG) deposits of the Eastern succession are dominated by excess $^{40}Ar_E$ Despite a K-rich composition and Proterozoic age they have measured $^{40}Ar/^{36}Ar$ values close to their initial values and ^{40}Ar is poorly correlated with K or Cl in 3D ^{40}Ar-^{36}Ar-K-Cl space.

In contrast, a sample selected from the Railway Fault, 13 km south of the Mt Isa copper mine, with accidentally trapped mica present in its fluid inclusions exhibits a strong correlation between ^{40}Ar, K and Cl. The isochron obtained proves that the fluid inclusions have not leaked for more than a billion years. However, the apparent age is younger than expected and provides insight of intra-sample $^{40}Ar_R$ remobilization processes.

Fig 5-1 (Kendrick et al., 2005)
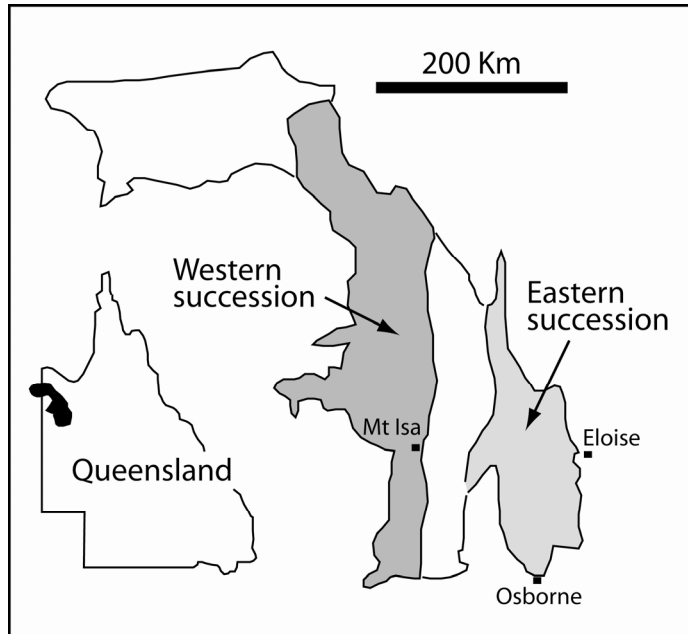
Fig 5-1. Locality map indicating the position of the Mt Isa Inlier within western Queensland, northeast Australia, and the location of Eloise and Osborne plus Mt Isa, 13km north of the Railway Fault.

5.2   Methodology and samples

5.2.1 Fluid inclusions

The origin of the samples is summarized in Table 5-1. The fluid inclusions have been analysed by microthermometry and are described in detail in Part I (Kendrick et al., 2005). The IOCG samples from Eloise and Osborne include predominantly primary ultra-high-salinity multi-solid (MS), liquid-vapour-daughter (LVD) and lower-salinity, predominantly secondary, liquid-vapour (LV), monophase (M) and carbon-dioxide (CO_2) fluid inclusions. Pottassium is present in solution, and in sylvite daughter minerals.

Sample AW02-002 from the Railway Fault includes primary liquid-vapour fluid inclusions that define growth zones and include accidentally trapped mica (Fig 5-2). The accidentally trapped mica was not optically visible but has been imaged by electrom microscopy (Figs 5-1b versus 5-1def). The sample Ar, K and Cl abundances are summarized in Table 5-2 and allow it to be inferred that the accidentally trapped mica (Fig. 5-2def) fills an average of 50% of the fluid inclusions volume. This and the sample K/Cl values of >1 indicate that the accidentally trapped mica is the major reservoir for K in this sample.

Table 5-1: Sample material

Sample	description	location
Eloise		
EL 48179	Quartz vein samples with populations of multiple fluid	Drill holes –
EL 48177	inclusion types. Described in detail by Baker (1998).	END39, 311.1m
		145B/END35C/290m
Osborne		
OS 37A	Quartz veins with (37A) po-py-cpy-mag-bio (dominantly	Drill hole –
OS 37B	infill) and (37B) mag-py-cpy (dominantly magnetite	TTNQ260/220-
	with less abundant infill texture).	220.19m/3E ore body
Railway Fault		
AW02-002a	Two separates from one quartz vein hand specimen.	GR 344770 7694060
AW02-002b	Quartz zoning is defined by Cu-rich primary two-phase	13 km south of the Mt
OS37B	liquid-vapour fluid inclusions.	Isa Cu mine.

The Eloise, Osborne and Railway Fault samples where provided by T. Baker, R. Mustard and A. Wilde, respectively. The fluid inclusion assemblages are described in detail in Part I (Kendrick et al., 2005).

Fig 5-2 (Kendrick et al., 2005)
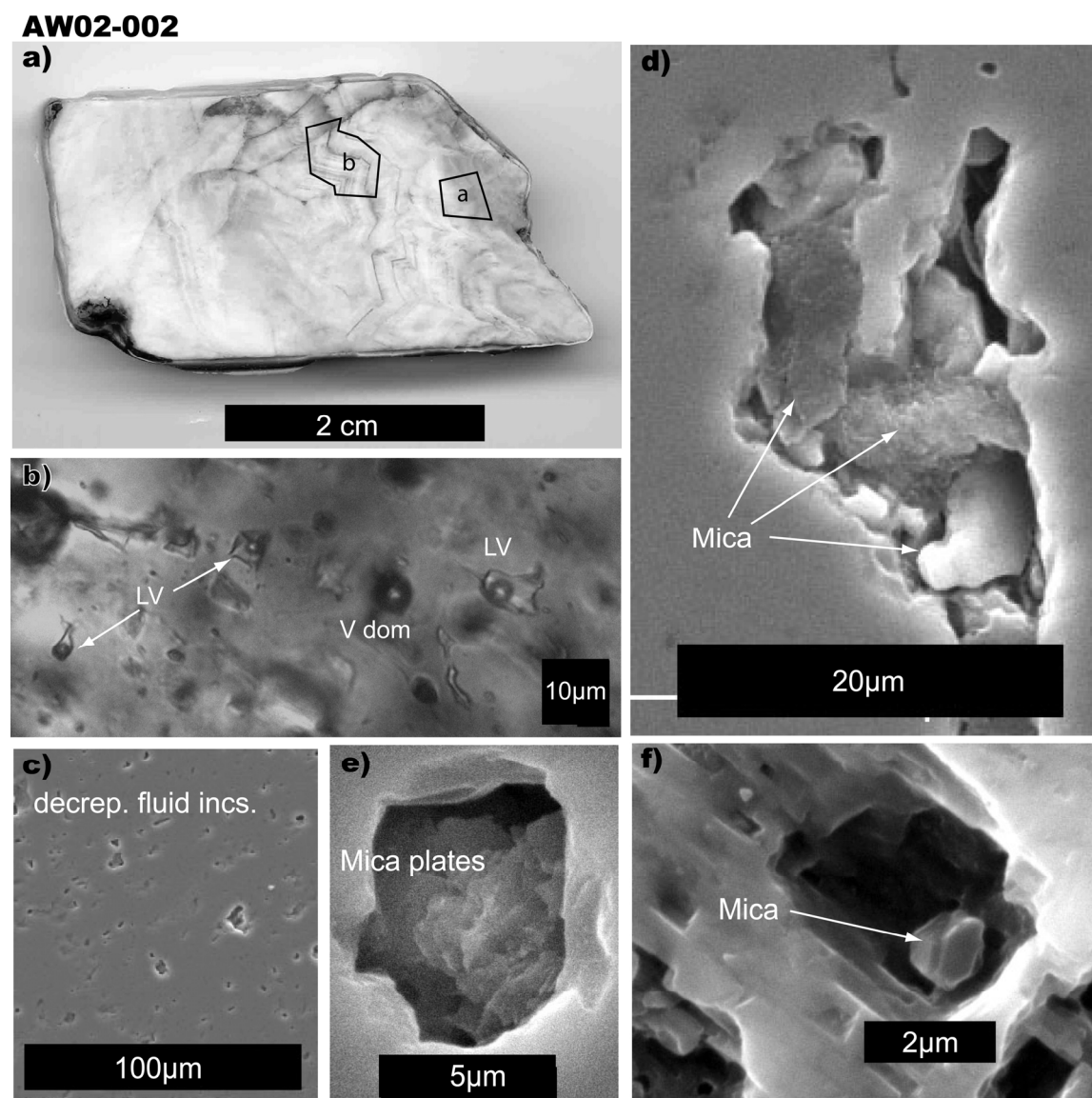
AW02-002

Fig. 5-2. Sample AW02-002 from the Railway Fault. a) Photograph of the hand specimen indicating the positions of the splits AW02-002a and AW02-002b. Note zoning defined by primary fluid inclusions. b) Optical microscopic image of two-phase liquid-vapour fluid inclusions. Solid daughter or captured phases were not observed in any of the fluid inclusions (see also Kendrick et al., 2005, Part I). c-f) Back scattered electron micrograph. Fluid inclusions are observed as craters/pits in the gold coated polished surface of the sample. Platey mica crystals are clearly observed in d and e, and possibly in f. These crystals were confirmed as K-Al-silicates by electron dispersive analysis.

Table 5-2: Determination of impurity characteristics from argon K-Cl data[1] and fluid inclusion characteristics

| Quartz sample | | | | | | Fluid inclusions (FI) | | | | Impurities | | Max. fill of |
| | Mass | Vol. [2] | K/Cl | K | Cl | Ar | NaCl eq. [3] | % V | FI [4] | Vol % | Musc. [5] | Vol % | musc in FI |
Name	(mg)	(mm^3)	molar	ppm	ppm	ppb	Wt %	Fill [3]	(mm^3)	FI	(mm^3)	musc	%[6]
Eloise													
EL 48177	22.5	8.5	0.06	40	655	10	30 ± 10	15 ± 10	0.09 ± 0.02	1.0 ± 0.2			
EL 48177	26.0	9.8	0.05	31	549	7	30 ± 10	15 ± 10	0.08 ± 0.02	0.8 ± 0.2			
EL 48179	92.0	34.7	0.05	9	154	3	25 ± 15	15 ± 10	0.10 ± 0.03	0.3 ± 0.1			
Osborne													
OS37A	41.9	15.8	0.28	12	39	2	25 ± 10	15 ± 10	0.012 ± 0.003	0.07 ± 0.02	minor ?		
OS37B	43.2	16.3	0.12	27	200	1	45 ± 15	15 ± 10	0.04 ± 0.01	0.3 ± 0.1			
Railway Fault													
AW02-002a	126	47.5	8.63	819	86	41	12 ± 5	50 ± 30	0.32 ± 0.14	0.7 ± 0.3	0.37	0.77	53 ± 24
AW02-002b	22.9	8.6	7.00	726	94	34	12 ± 5	50 ± 30	0.06 ± 0.03	0.7 ± 0.3	0.06	0.68	48 ± 23
AW02-002b	23.3	8.8	7.00	591	77	27	12 ± 5	50 ± 30	0.05 ± 0.02	0.6 ± 0.3	0.05	0.56	48 ± 23

1. *Full data set available in Appendix B.*
2. *Sample volume calculated assuming the density of quartz 2.65 g cm^{-3}*
3. *A large uncertainty is assigned to reflect the range of fluid inclusion types.*
4. *The total fluid inclusion volume is calculated from the sample Cl abundance, the fluid inclusion salinity, degree of fill and by assuming all Cl is present within the fluid inclusions and the liquid phase has a density of 1 g cm^{-3}..*
5. *Where present the volume of accidentally trapped mica has been calculated based on the sample K abundance, the chemical formula and density (2.88 g cm^{-3}) of muscovite and the assumption that all K is hosted by the mica impurity.*
6. *The % fill of accidentally trapped mica in the fluid inclusions = (musc vol.)/(musc + FI vol.). The uncertainty is due to the variable fluid inclusion characteristics. The figure represents an upper limit because the volume of mica will have been slightly over estimated if significant K is present as a solute within the fluid inclusions.*

5.2.2 Irradiation and mass spectrometry

The analytical protocol has been described in detail in Part I (Kendrick et al., 2005). Sample gas was extracted from fluid inclusions in quartz vein samples by stepped heating. In addition, duplicate analyses of samples AW02-002b and EL 48177 were obtained by combined *in vacuo* crushing and stepped heating of the crushed residue.

The Ar isotopic composition of purified noble gas was measured utilizing the MAP 215-50 (Mass Analyser Products) noble gas mass spectrometer at the University of Melbourne. The samples were irradiated for 150 MWH in position 5c of the McMaster reactor and received a total neutron fluence of $\sim10^{19}$ neutrons cm^{-2}. The irradiation parameters determined from Hb3Gr and GA1550 monitors are given in Chapter 4. Standard corrections have been made for Ar-interference reactions, mass discrimination and decay of ^{37}Ar and ^{36}Cl since the time of irradiation. The molar abundances of K, Cl and Ca are calculated from the irradiation parameters J, β and α (Kelley et al., 1986) using the noble gas proxies ^{39}Ar$_K$, ^{38}Ar$_{Cl}$ and ^{37}Ar$_{Ca}$.

5.3   Age determinations

5.3.1 Osborne

The Osborne samples exhibit a weak correlation that is close to defining a plain in 3D ^{40}Ar-K-Cl-^{36}Ar space with one outlier (Fig 5-3a). The weak correlation between $^{40}Ar/^{36}Ar$ and K/^{36}Ar is also apparent in a conventional 2D isochron (Fig 5-3b). Although a regression can be forced through selected data points the uncertainty is actually improved by assuming an atmospheric intercept and calculating apparent ages for individual heating steps (fig 5-3b). The slope defined by the data point with the youngest apparent age is shown in Figure 5-3b. The proportion of heating steps that have within error apparent ages are indicated by the proximity of most data points to the reference line and by an age spectrum plot (Figs. 5-3bc).

The youngest apparent age of 1630 ± 89 Ma determined for Osborne has a low precision of 5%, but is close to the Re-Os molybdenite, U-Pb titanite and Ar-Ar metamorphic biotite ages of 1595-1600 Ma that are considered to constrain the syn-D$_2$ mineralisation event (Perkins and Wyborn, 1998; Gauthier et al., 2001; Rubenach et al., 2001; Giles and Nutman, 2002). Despite the 5% precision it is slightly older than previous Ar-Ar hydrothermal biotite ages of <1540 Ma (Perkins and Wyborn, 1998) that may constrain a later retrograde-hydrothermal-event (Gauthier et al., 2001; Rubenach et al., 2001) or be explained as cooling ages.

5.3.2 Eloise

Data from the Eloise samples are very weakly correlated in 3D ^{40}Ar-K-Cl-^{36}Ar space and the weak correlation there is, is due to mixing of different fluid inclusion types and has no age significance (Fig 5-3d).   It is clearly seen on the 2D isochron regression that the majority of data points lie close to the $^{40}Ar/^{36}Ar$ axis (Fig 5-3d) indicating that they are dominated by excess $^{40}Ar_E$. This is despite the mean fluid inclusion salinity of 25-30 wt % NaCl eq. and K/Cl values of 0.05-0.35 (Table 5-2) that indicate fluid inclusion K concentrations of several weight percent.

As for the Osborne samples, the youngest apparent age is within error of the deposits true age of 1514-1530 Ma (Fig 5-3e; Baker et al., 2001). However, this time the age of 1790 ± 270 Ma is so imprecise that it does not represent a useful constraint. Furthermore, the age is based on a small proportion of the sample gas (9% of EL 48177), with the majority of steps have apparent ages of older than the Earth (Appendix B).

5.3.2.1 In vacuo crushing

In contrast, heating steps obtained from the crushed residue of sample EL 48177 are strongly correlated in K/^{36}Ar versus $^{40}Ar/^{36}Ar$ space (Fig 5-3f).   Although the analytical uncertainty on individual steps is large, due to the small volume of gas released in these steps, a regression forced through selected data points yields an age of 1542 ± 266 Ma (Fig 5-5f). This age remains imprecise but is almost identical to the preferred mineralization age of 1514-1530 Ma determined from hydrothermal

biotite (Baker et al., 2001) and has a non-atmospheric initial $^{40}Ar/^{36}Ar$ value of ~735 that is realistic for the sample (Fig 5-3f).

It is well documented that *in vacuo* crushing preferentially samples fluid inclusions and can allow an improved age determination from K-mineral impurities within quartz samples (Turner and Bannon, 1992; Kendrick et al., 2001). However, even the most K-rich heating steps in Figure 5-3f have K/Cl values of <0.35. This value is realistic for K-rich primary fluid inclusions and indicates that a significant mineral impurity is not present. Instead, the improved isochron, obtained from the crushed sample can be explained if *in vacuo* crushing has preferentially decrepitated secondary fluid inclusions that lie along plains of weakness. The crushed residue would then be enriched in primary fluid inclusions that were trapped over a much shorter period of time, relative to secondary fluid inclusions, and have a more uniform initial $^{40}Ar/^{36}Ar$ composition (Fig 5-3f).

Fig 5-3 (Kendrick et al., 2005)
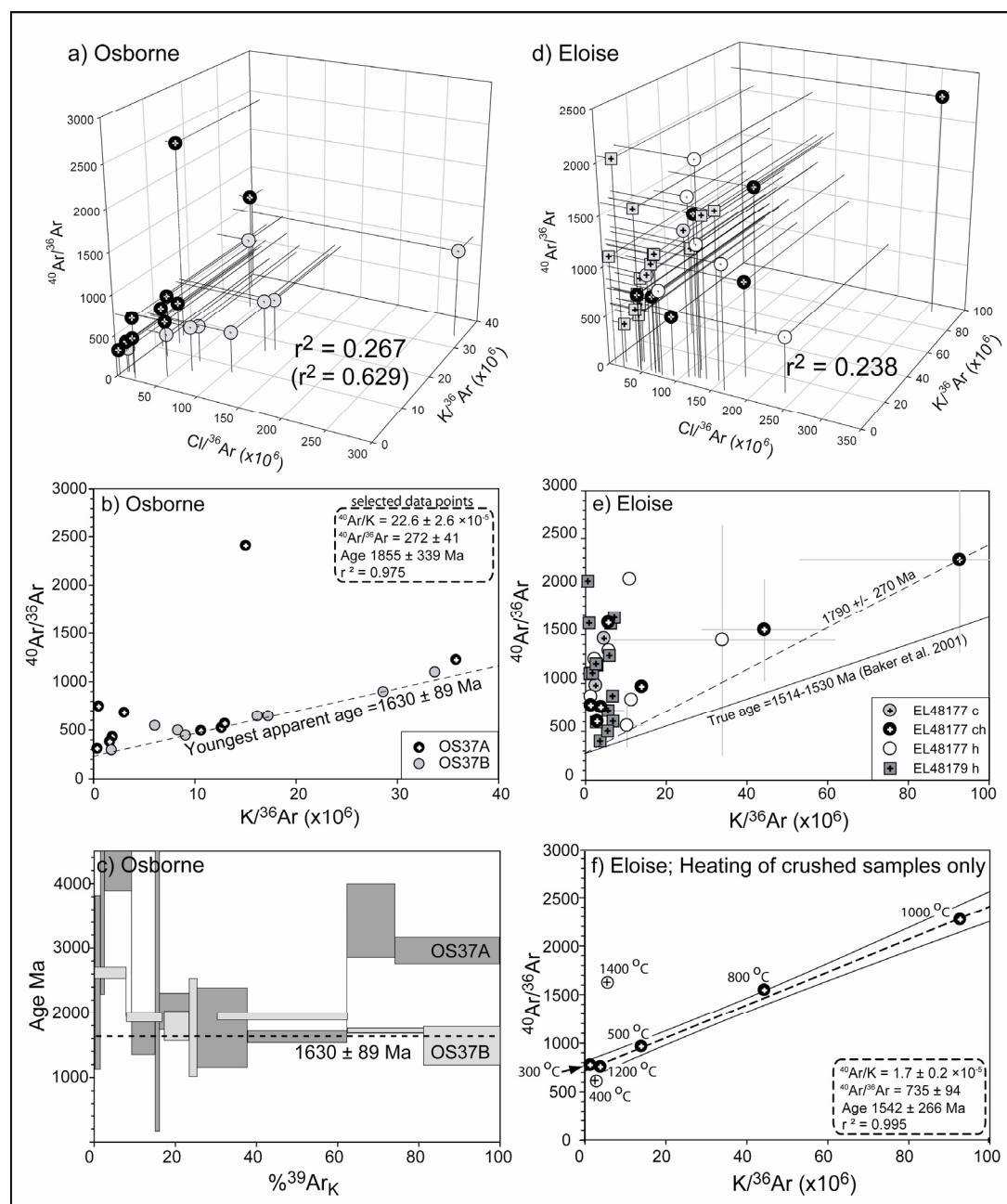
Fig 5-3. Age constraints on the Osborne and Eloise IOCG deposits of the Eastern Succession.
a) 3D ^{40}Ar-K-Cl-^{36}Ar multi-component correlation diagram for Osborne. The correlation
coefficient is shown for all the data points and in brackets with the outlier omitted. b) 2D
isochron plot for Osborne showing the youngest apparent age of an individual step and the
statistics for the best regression that can be obtained for selected datapoints. c) Age spectrum
plot for the Osborne. d) 3D ^{40}Ar-K-Cl-^{36}Ar multi-component correlation diagram for Eloise.
e) 2D isochron plot for Eloise, showing the youngest apparent age obtained for an individual
heating step. f) Isochron regression for the crushed residue of sample EL 48177. nb –
Regressions in b and f have been obtained by weighting each data pointed equally and
disregarding analytical uncertainty (model 2) so MSWD values are not given.

5.3.3 The Railway Fault

Sample AW02-002 exhibits a strong correlation between ^{40}Ar, K and Cl in 3D ^{40}Ar-^{36}Ar-K-Cl space (Fig 5-4ab). As in previous studies (Kelley et al., 1986; Turner and Bannon, 1992; Kendrick et al., 2001a) the mixing-planes are defined by three components; 1) atmospheric ^{40}Ar$_A$ and ^{36}Ar with ^{40}Ar/^{36}Ar intercept of 295.5; 2) Cl-correlated fluid inclusion ^{40}Ar; and 3) K-correlated radiogenic ^{40}Ar$_R$ produced *in situ* within captured mica-crystals (Fig 5-3)[1].

The 3D isochron regressions are compared with 2D isochron regressions in Figure 5-4 (both at the 95% confidence level). The ^{40}Ar/^{36}Ar intercept values obtained from the 2D isochrons are 1900 for AW02-002a and 660 for AW02-002b, indicating there was interzonal variation in the Ar-isotope composition of sample AW02-002 at t = 0 (Fig 5-2a).

The 3D isochron regressions represent much improved data fits with MSWD values of <30 compared to >1000 in the 2D isochrons (Fig 5-4). The ^{40}Ar$_R$/K slopes define fairly imprecise (~10%) ages that are within error for both splits of the sample. The ^{40}Ar/Cl values of 3.3×10^{-4} and 1.8×10^{-4} defined by the intersections of the planes with the ^{40}Ar/^{36}Ar versus Cl/^{36}Ar axes (Fig 5-4ab), represent the fluid inclusion values at t=0 and are different in different zones of the sample.

The best fit to the data is obtained by plotting K/Cl versus ^{40}Ar/Cl (Turner and Bannon, 1992). This is advantageous because both components are free of atmospheric ^{40}Ar$_A$ and so the three component mixture can be presented in 2D (Fig 5-3ef). These regressions have ^{40}Ar/Cl intercepts within error of the values determined from the 3D isochron slopes (compare figures 5-4ab with 5-4ef) and give the lowest MSWD's of just 11 and 21. The quality of fit is limited by the variable Ar-isotope composition at t = 0 of fluid inclusions in different zones within each sample. Nonetheless, the apparent ages of AW02-002a and AW02-002b are indistinguishable at 1049 ± 56 Ma and 1027 ± 41 Ma (Fig 5-4ef). The most precise age of 1027 ± 41 Ma has uncertainty at the 4% level.

The above apparent ages are 100's of Ma younger than the preferred ~1523 Ma age of Cu-mineralization at the Mt Isa mine, that has been constrained by textural relationships, Ar-Ar biotite ages and Pb-isotope data (Swager, 1985; Perkins et al., 1999; Carr et al., 2004). It is possible that the Railway Fault is unrelated to mineralization at Mt Isa, and that the ~1030 Ma age represents the time of movement on this fault. However, an alternative explanation for the discrepancy is examined below.

---

[1] ^{40}Ar* = ^{40}Ar$_E$ + ^{40}Ar$_R$ = ^{40}Ar$_{total}$ − (295.5 × ^{36}Ar)

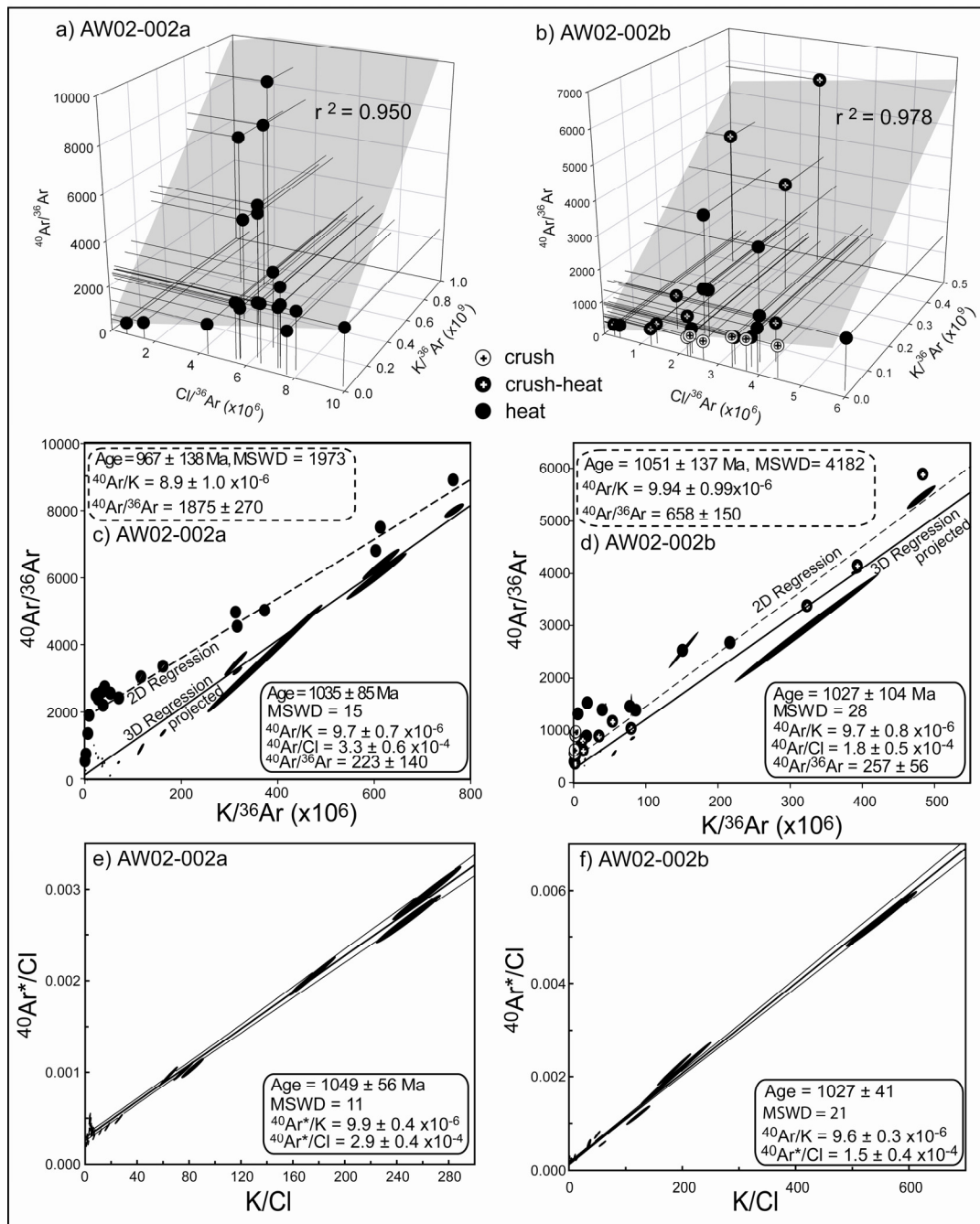**Fig 5-4 (Kendrick et al., 2005)**

Fig 5-5. Age constraints on samples AW02-002a and AW02-002b from the Railway Fault. a and b) Stepped heating only and combined in vacuo crushing plus stepped heating data define a planes in 3D ^{40}Ar-K-Cl-^{36}Ar space. c and d) The data are shown as circles on standard 2D isochron diagrams a regression through this data and the corresponding statistics are identified by dashed lines. In addition, error ellipses are shown for the data projected down the slope of the 3D planes (in a and b), the 3D regression and statistics are identified by solid lines. e and f) The atmospheric component is absent in ^{40}Ar/Cl-K/Cl diagrams and the regression line represents mixing between the Cl-dominated fluid inclusions and K-rich captive-mica component. ^{40}Ar* = ^{40}Ar$_{total}$ − (^{36}Ar×295.5) = ^{40}Ar$_R$ + ^{40}Ar$_E$*

5.4   Significance of Ages

5.4.1 Quartz fluid inclusion ages

The samples from Eloise and Osborne have mean K/Cl values of < 0.3 (Table 5-2), suggesting that significant mica impurities are absent and K is sited directly in the fluid inclusions of these samples. The youngest apparent ages determined, are within error of the ages preferred for the two deposits. Therefore, the data confirm that the fluid inclusions have not leaked since the time of trapping 1.5-1.6 Ga ago.

However, robust isochron regressions were not obtained and the apparent ages are calculated assuming an initial $^{40}Ar/^{36}Ar$ value of atmospheric composition. If excess $^{40}Ar_E$ was present the age will have been overestimated and the age is therefore interpreted as representing the maximum age of mineralisation. The assumption of an atmospheric intercept appears to have been reasonable for the Osborne samples, where an intercept within error of the atmospheric value is obtained by regression of selected data points (Fig 5-3b), but the apparent age obtained for Eloise is elevated by the presence of excess $^{40}Ar_E$ (Fig 5-3e).

5.4.1.2 Secondary fluid inclusions and mixing

The IOCG samples contain multiple types of fluid inclusion and secondary LV fluid inclusions dominate in some of the samples (Part I; Kendrick et al., 2005). The proximity of most datapoints to the 1630 ± 89 Ma a ge obtained for Osborne (Fig 5-3b), suggests that the secondary fluid inclusions must had been trapped during or soon after mineralization. The isochron obtained for the crushed residue of sample EL 48177 (Fig 5-3f) was explained by suggesting that *in vacuo* crushing removes secondary fluid inclusions preferentially.

We now examine the possibility of producing mixing lines with apparent ages older or younger than the deposit age by mixing of different types of contemporaneous fluid inclusion. Mixing lines that are younger than the sample will have elevated $^{40}Ar/^{36}Ar$ intercepts and mixing lines that are older than the sample will have low $^{40}Ar/^{36}Ar$ intercepts (Fig 5-5). However, the minimum intercept value that is possible, is the atmospheric $^{40}Ar/^{36}Ar$ value of 295, this places some restriction on the range of compositions and apparent ages that can be obtained by mixing scenarios.

Interpretation of the maximumn mineralisation age for Osborne of 1630 ± 89 Ma is not affected by possible mixing scenarios because it was calculated by assuming an atmospheric intercept. It was demonstrated in part I that different fluid inclusion types decrepitate at different temperatures (Kendrick et al., 2005), compatible with the variation in $K/^{36}Ar$ values seen in the isochron diagram (Fig 5-3b). Therefore the proximity of most data points to the 1630 Ma reference line determined for Osborne (Fig 5-3b) suggests that mixing has occurred between different fluid inclusions with similar initial $^{40}Ar/^{36}Ar$ values of close to 295 (Fig 5-5c). The few outlying points seen in the 3D plot and the 2D isochron represent fluid inclusion populations with higher initial $^{40}Ar/^{36}Ar$ values.

The Eloise samples exhibit greater spread in $^{40}Ar/^{36}Ar$ and the data is not correlated in $^{40}Ar/^{36}Ar$ versus $K/^{36}Ar$ space (Fig 5-3de). This is compatible with the decrepitation and mixing of different fluid inclusions types with different initial $^{40}Ar/^{36}Ar$ values, but it has not resulted in a mixing line that could be mistaken for the age of mineralization (Fig 5-3de). The isochron regression obtained for the crushed residue of sample EL 48177 has a non-atmospheric intercept (Fig 5-3f) that yields

an imprecise age almost identical to the preferred age of mineralization. Therefore it must also represent mixing of fluid inclusions with similar initial $^{40}Ar/^{36}Ar$ values (Fig 5-5c).

In conclusion, although mixing lines are theoretically possible in complex samples containing multiple types of fluid inclusion. The samples analysed here that have fluid inclusions with variable $^{40}Ar/^{36}Ar$ do not produce mixing lines. The only mixing lines produced are between fluid inclusions with similar initial $^{40}Ar/^{36}Ar$ values (Fig 5-5c) that therefore produce ages close to the deposit age. Mixing does not appear to have been significant for the fluid inclusion ages determined here with precision of only 4-5%. Furthermore, the quality of an isochron regression is likely to decrease as increasingly dissimilar fluid types are mixed and it is therefore likely that the precision will decrease to such a level that all mixing ages will remain within error of true age.

Fig 5-5 (Kendrick et al., 2005)
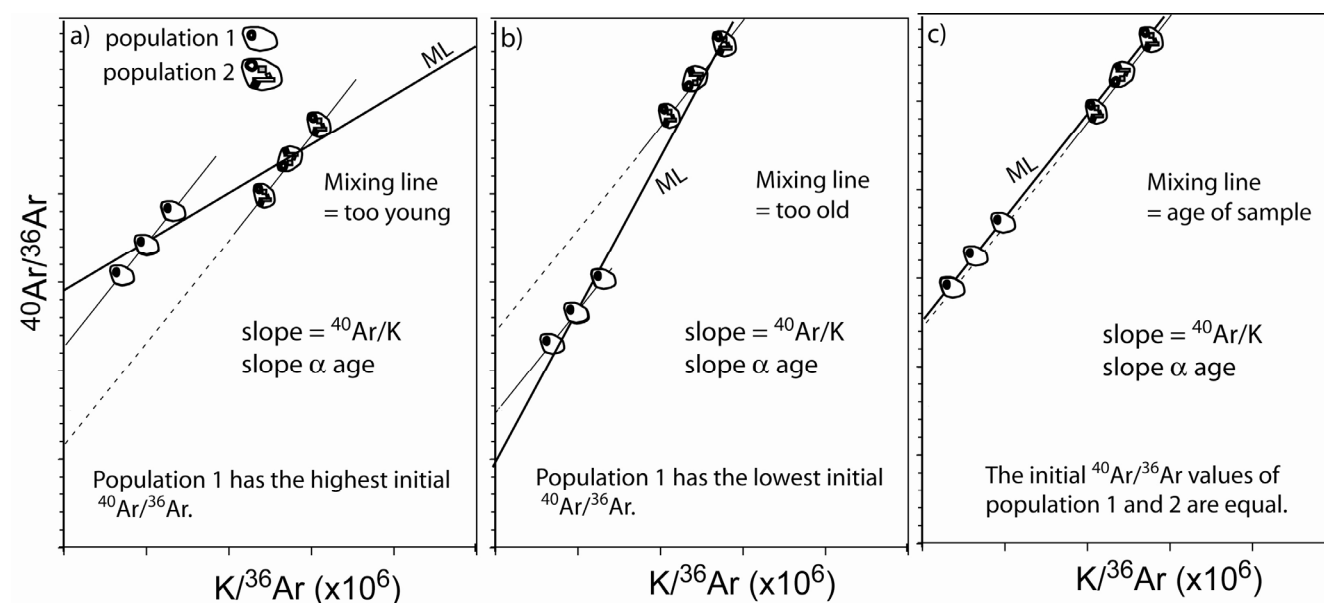
Fig 5-5. Possible fluid inclusion mixing scenarios in samples with complex fluid inclusion assemblages. a) Mixing resulting in a young age. b) Mixing resulting in an old age. c) mixing does not influence the age if the different fluid inclusion types have similar initial $^{40}Ar/^{36}Ar$ values. ML = mixing line.

5.4.2 Quartz mineral impurity ages

Sample AW02-002 includes accidentally trapped mica as the major reservoir of K (Fig. 5-2; Table 5-1; and Part I Kendrick et al., 2005). Most previous quartz ages, determined on samples that include a mineral impurity, have been close to independently determined ages for the associated mineralization, or where the mineralization age was unconstrained have been compatible with existing mineralisation models (Kelley et al., 1986; Turner and Bannon, 1992; Kendrick et al., 2001a). Furthermore, the deposits selected have been rapidly cooled Phanerozoic magmatic-hydrothermal-systems.

In contrast, sample AW02-002, was collected from close to the Proterozoic Mt Isa copper mineralizing system and the area had a protracted thermal history (Spikings et al., 2002). The age is much younger than expected and does not constrain the time of mineralization at Mt Isa. The ~1030 Ma mineral impurity age demonstrates that, like the fluid inclusion ages above, the fluid inclusions have not leaked and are retentive to ^{40}Ar over the billion year timescale. However, we now examine the possibility of Ar-remobilisation between the accidentally trapped mica crystals and the surrounding fluid inclusions.

5.4.2.1 Intra sample ^{39}Ar-recoil

The production of $^{39}Ar_K$ by the neutron reaction $^{39}K(n,p)^{39}Ar$ has a mean recoil energy of 177 keV and results in recoil of ^{39}Ar over several hundred nm leaving a mean ^{39}Ar depletion depth of 0.082 μm in silicate minerals (Turner and Cadogan, 1974; Onstott et al., 1995). Recoil of $^{39}Ar_K$ does not appear to be significant for fluid inclusion ages, because K and Cl are released from the sample simultaneously, indicating that the fluid inclusions remain the major reservoir of recoiled $^{39}Ar_K$ (see Part I; Kendrick et al., 2005).

The accidentally trapped mica in sample AW02-002 has maximum dimensions of a few μm and includes many sub-5 μm grains (Fig 5-2). However, the minimum dimension of these platy crystals are substantially less than 5 μm. Therefore recoil of $^{39}Ar_K$, that would result in an increased apparent age for the accidentally trapped mica, could be significant. Nonetheless, the release systematics of K from sample AW02-002 indicate that the accidentally trapped mica remains the predominant host of K (see Part I; Kendrick et al., 2005), implying once again that recoil effects are not very large. Furthermore, the apparent age of the accidentally trapped mica is younger than expected, suggesting that loss of $^{40}Ar_R$ from the mica crystals is more significant than $^{39}Ar_K$ recoil.

5.4.2.2 Intra sample ^{40}Ar-loss

The fluid inclusion homogenization temperatures for sample AW02-002 lie in the range 120-300 °C (Part I; Kendrick et al., 2005) which defines the minimum temperature of this sample at the time of fluid trapping. The actual temperature of the fluids at the time of trapping depend on the samples depth at the time of trapping. As the sample is favoured to be genetically related to Mt Isa copper mineralization (quartz-chalcopyrite; A. Wilde pers. Comm., 2005) the maximum temperature of the fluids is inferred to be close to 270-350 °C, obtained for associated dolomitic alteration at Mt Isa (Heinrich et al., 1989).

Electron dispersive analysis confirmed the platey crystals observed in Figure 5-2 as K-Al-silicates, no Fe or Mg was detected. The mineral is therefore probably muscovite mica, but biotite cannot be ruled out if Fe and Mg were undetected. Muscovite and biotite are commonly assigned nominal closure temperatures of 350 ºC and 300 ºC respectively (McDougal and Harrison, 1999). The

closure temperature of >10μm captive white mica in rapidly cooled Sn-W related mineralization was estimated as 350 °C (Kelley et al., 1986). These values are all similar to the fluid trapping temperature in sample AW02-002.

However, closure temperature is a function of not only composition, but also the grain-size plus cooling rate, and the calculated value depends upon the geometry of the diffusion domain (McDougall and Harrison, 1999). The effective closure temperature of the accidentally trapped mica in this study, could have been as low as 160-200 ºC and was probably not higher than 250 ºC (Fig 5-6): 1) The regional cooling rate may have been as low as 0.2 ºC Ma^{-1}. Ar-Ar mica and feldspar cooling ages indicate cooling from approximately 350 ºC at ~1400 Ma to 250 ºC at ~800 Ma (Fig 5-7; Spikings et al., 2002). 2) The mica crystals have variable size, some are as large at 10 μm but the majority are sub-5 μm (Fig 5-2). 3) For muscovite, an infinite cylinder is a better description of the diffusion domain than a plane sheet. A plane sheet does not adequately describe ^{40}Ar* loss parrellel to the c-axis (Hames and Bowring, 1994). The effect these parameters have on closure temperature is illustrated in Figure 5-6.

The quartz vein age is plotted against the maximum estimated closure temperature on the regional cooling T-t path of Spikings et al. (2002), see Figure 5-7. The apparent age and estimated mica closure temperature plot close to the interpreted regional cooling trajectory and are compatible with an interpretation of sample AW02-002 were it formed during regional fluid flow and mineralization at Mt Isa (~1523 Ma; Perkins et al., 1999) and cooled through the effective closure temperature of variably sized accidentally trapped mica at ~1030 Ma.
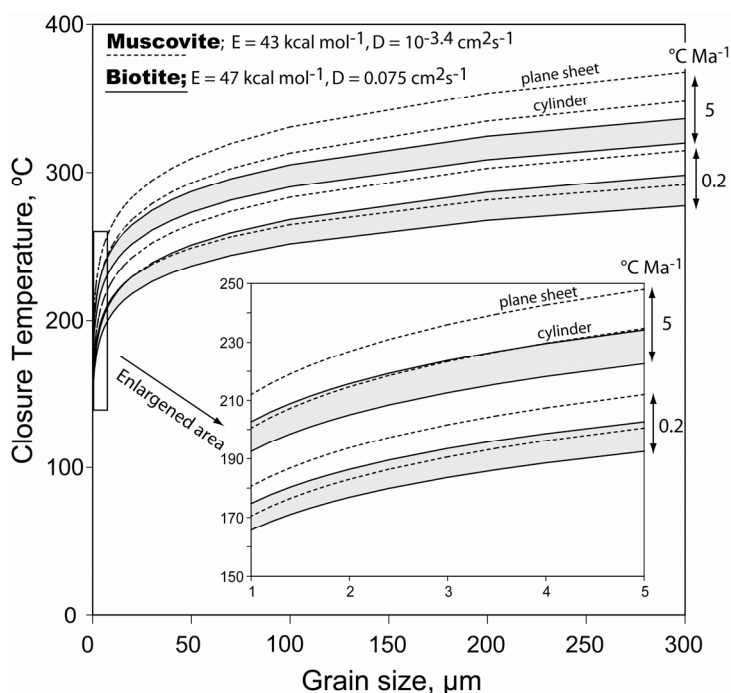
Fig 5-6. Closure temperature versus grain size for muscovite and biotite. The closure temperatures have been calculated for different cooling rates and different diffusion domain geometries. The top four curves have cooling rates of 5 ℃ Ma^{-1} and represent; 1) muscovite, plane sheet, 2) muscovite, cylinder, 3) biotite, plane sheet, 4) biotite, cylinder. The bottom four curves represent the same grains cooled at a slower rate of 0.2 ℃ Ma^{-1}. The curves have been calculated using the closure equation of Dodson (1973) and activation energies (Ea) plus diffusion coefficients (Do) that are considered representative for the Cooma biotite and muscovite (see McDougall and Harrison, 1999).
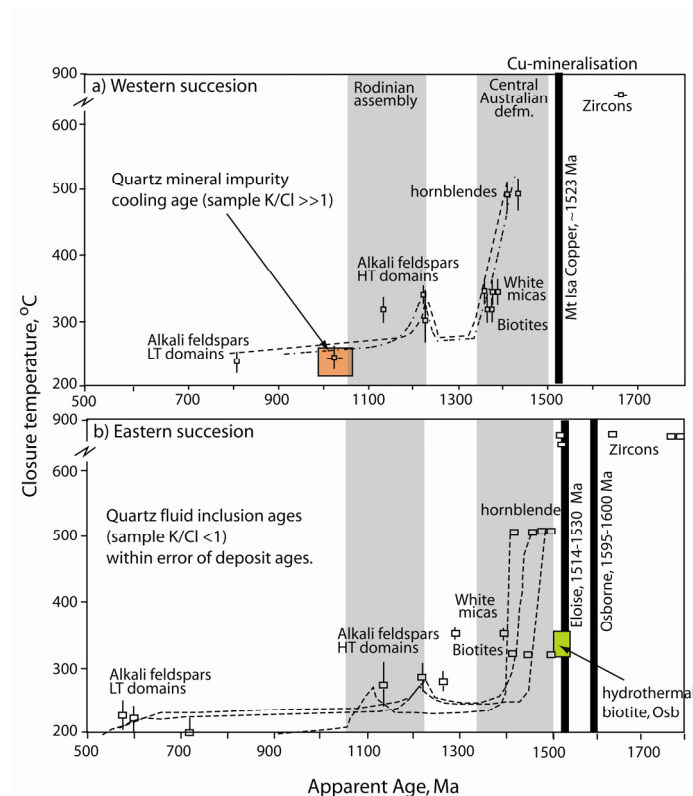
Fig 5-7 (Kendrick et al., 2005)

Fig 5-7. Interpreted Ar-Ar cooling trajectories for the western (a) and eastern (b) successions of Mt Isa (modified after Spikings et al. 2001, 2002; HT – high temperature; LT – low temperature). (a) The preferred ~1523 Ma hydrothermal biotite age for Mt Isa Cu mineralization (Perkins et al., 1999) and the isochron age of sample AW02-002 together with the maximum closure temperature of sub-5µm mica crystals are shown. (b) The preferred 1595 Ma and 1514-1530 Ma mineralization ages are shown for Osborne and Eloise, respectively (Rubenach et al., 2001; Gauthier et al., 2001; Baker et al., 2001).   The younger <1540 Ma hydrothermal biotite age is also shown for Osborne (Perkins and Wyborn, 1998) and may be related to either retrograde hydrothermal overprinting (Rubenach et al., 2001; Gauthier et al., 2001) or biotite closure temperature.

Fig 5-8 (Kendrick et al., 2005)
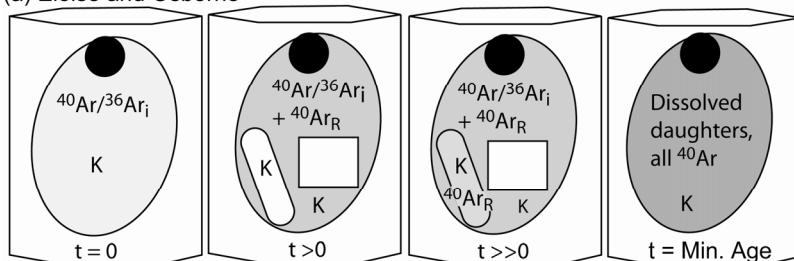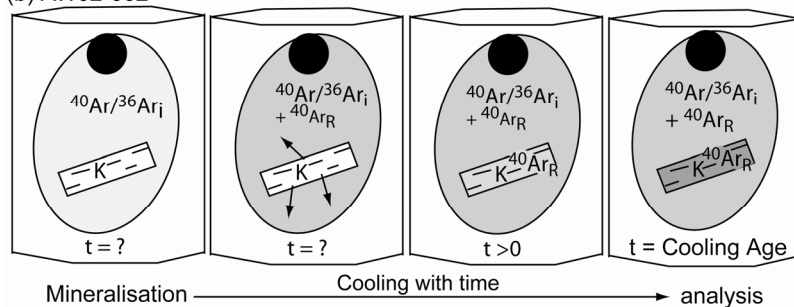
Fig 5-8. Ar-Ar sytematics of (a) quartz fluid inclusion ages and (b) quartz mineral impurity ages. The initial $^{40}Ar/^{36}Ar_i$ value at the time of mineralization is increased by insitu production of radiogenic $^{40}Ar_R$. The shading of the fluid inclusions and mineral impurities reflects the increasing concentration of $^{40}Ar_R$.

5.5 Implications for noble gas studies

The fluid inclusion ages presented above have demonstrated that quartz is retentive to ^{40}Ar over the billion's of years time scale and have suggested that the secondary fluid inclusions present in the Osborne samples have a similar timing to the primary fluid inclusions formed at the time of mineralization.

As mentioned, when the age of the deposit is known, it is straight forward to correct the measured ^{40}Ar/^{36}Ar value to that of the initial value because K is measured as ^{39}Ar$_K$. However, many noble gas studies are undertaken on samples that are not irradiated, meaning that K cannot be measured. The size of the correction for radiogenic ^{40}Ar$_R$ for each of the Proterozoic samples studied here is evaluated in Figure 5-9.

The correction for radiogenic ^{40}Ar$_R$ is much smaller than the intra-sample variation in the IOCG samples from Eloise and Osborne. In many cases the uncorrected measured ^{40}Ar/^{36}Ar value is within error of the corrected, initial ^{40}Ar/^{36}Ar value (Figs 5-9a-d). This surprising result demonstrates that in samples that do not contain K-mineral impurities (K/Cl values < 1) uncertainties in the deposit age of 100's of Ma will be of little consequence in terms of determining and interpreting the initial ^{40}Ar/^{36}Ar value. Furthermore, in most cases it will not be critical if a correction for ^{40}Ar$_R$ cannot be made because the K concentration is unknown.

In contrast, sample AW02-002 from the Railway Fault includes accidentally trapped mica (Fig 5-2; K/Cl values > 1). In this case the correction for post entrapment *in situ* production of radiogenic ^{40}Ar$_R$ is large and the value determined is sensitive to the mineralization age used in the correction (Figs 5-9ef). A further implication of this is that intra-sample variation in the initial ^{40}Ar/^{36}Ar value cannot be reliably determined.

It was demonstrated in part I (Kendrick et al., 2005) that extraction of K from sample AW02-002 is unrelated to the extraction of Cl or ^{40}Ar* from the fluid inclusions. As a result the correction for ^{40}Ar$_R$ will be too small where 40Ar* is extracted from fluid inclusions and ^{39}Ar$_K$ is retained in the accidentally trapped mica, and the correction will be too large when ^{39}Ar$_K$ is preferentially outgassed from mica (Part I; Kendrick et al., 2005). The only way to overcome this problem is to calculate sample mean values that are presented in Figure 5-9ef. The mean corrected values of samples AW02-002a and AW02-002b of 1921 and 728 are 22-24% lower than the uncorrected values. The significant difference in the sample values confirms the interzonal variation in sample AW02-002 suggested above.

Chapter 5

Fig 5-9 (Kendrick et al., 2005)
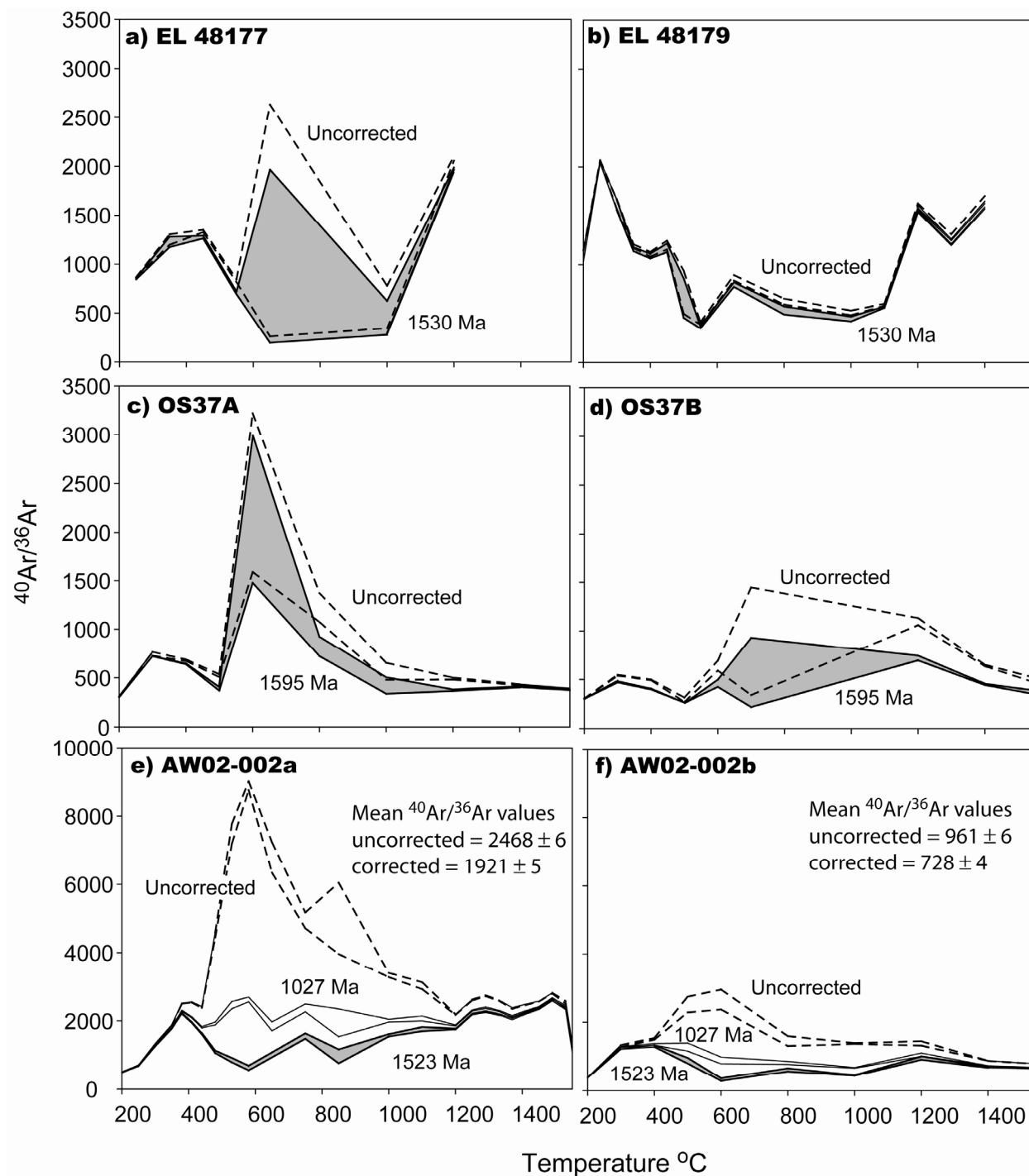
Fig 5-9. $^{40}Ar/^{36}Ar$ values as a function of temperature. The large uncertainty for $^{40}Ar/^{36}Ar$ in the temperature range 600-800 °C is due to the low volume of gas released at these temperatures (Fig 5-5). a and b) Eloise samples; c and d) Osborne samples; e and f) The Railway Fault samples have been corrected using the preferred 1523 Ma age of mineralization at Mt Isa, and the mineral impurity cooling age determined in Figure 5-3.

5.6   *Perspective*

5.6.1 Technique Comparison

Ar-Ar age constraints on fluid inclusions that do not contain accidentally trapped mica, where fluid inclusions are the dominant reservoir of K (Osborne and Eloise), represent the maximum age of formation because fluid inclusions are retentive to ^{40}Ar over billions of years. Age constraints were difficult to obtain for the samples in this study, that include multiple types of fluid inclusion, using either isochron diagrams or 3D ^{40}Ar-^{36}Ar -K-Cl plots. However, if mixing occurred it occurred between fluid inclusions with similar ^{40}Ar/^{36}Ar$_i$ and reduced the precision (not accuracy) of the isochron regressions that remained within error of the deposit ages.

In samples that contain accidentally trapped mica, *in vacuo* crushing preferentially extracts inclusion fluids (Turner and Bannon, 1992; Kendrick et al., 2001). Therefore, *in vacuo* crushing should yield fluid inclusion ages, similar to those described above, that represent the maximum age of formation. Where a homogenous population of fluid inclusion with uniform ^{40}Ar/^{36}Ar$_i$ is present robust isochrons can be obtained (Qui, 1996; Qui et al., 2002). The Tin-Tungsten and Gold related quartz samples dominated by fluid inclusions with atmospheric ^{40}Ar/^{36}Ar$_i$ values (Qui, 1996) and the Dongchuan copper quartz samples (Qui et al., 2002) appear to represent examples of this phenomenon. However, ^{40}Ar$_R$ loss from a mineral impurity into the surrounding fluid inclusion could elevate the apparent age of the fluid inclusion. Furthermore, the impurity would remain undetected because ^{39}Ar$_K$ and ^{40}Ar$_R$ are not extracted from it by crushing.

Subsequent stepped heating of the crushed residue has previously been applied to obtain gas from the solid-phase impurities (Turner and Bannon, 1992; Kendrick et al., 2001a; Qui et al., 2002). Resultant isochrons based primarily on the stepped heating data are therefore attributed to accidentally trapped mica and/or other impurity and not the fluid inclusions themselves (Kelley et al., 1986; Kendrick et al., 2001; Qui et al., 2002). In many cases the mineral impurity ages may represent a cooling age rather than the formation age but in most rapidly cooled Phanerozoic magmatic-hydrothermal systems studied to date the cooling ages have been indistinguishable from the formation ages (Kelley et al., 1986; Kendrick et al., 2001a). However, apparent quartz ages that are up to 80 Ma younger than the age of associated granite intrusion in Cornwall (Turner and Bannon, 1992) could be re-interpreted as cooling ages, and may not indicate that mineralization proceeded for ~80 Ma after granite intrusion.

Laser ablation quantitatively removes Ar from daughter minerals (Kendrick et al., 2001), but it is untested how efficiently ^{39}Ar$_K$ or ^{40}Ar$_R$ are removed from mineral impurities. Its effect could be one of micro-crushing and where isochrons are not obtained it has provided only a maximum age of formation (Irwin and Roedder, 1995).

Laser heating samples with a single generation of fluid inclusions has resulted in some good isochrons (McKee et al., 1993). However, laser heating could easily extract ^{39}Ar$_K$ and ^{40}Ar$_R$ from mineral impurities as well as the fluid inclusions. If unrecognized, an age obtained from a K-mineral sub-reservoir within fluid inclusions could provide an alternative explanation for younger than expected quartz ages in samples previously interpreted to contain only much-later secondary fluid inclusions (McKee et al., 1993).

5.6.2 Recommendations and future directions

We have demonstrated that for a meaningful interpretation of quartz ages it is essential to understand the citing of K within the sample: if K is cited in fluid inclusions resultant ages represent the maximum age of formation, if K is cited in a mineral impurity cooling ages can result.

Samples that require detailed investigation can be identified from mean K/Cl values of greater than one (Table 5-1), and the degassing behaviour of K-derived $^{39}Ar_K$ relative to fluid inclusion hosted $^{38}Ar_{Cl}$ (Part I; Kendrick et al., 2005). Because the calculation of K and Cl from the noble gas proxies $^{38}Ar_{Cl}$ and $^{39}Ar_K$ provides a transparent method by which the nature of impurities in quartz can be assessed (e.g. Table 5-1) it should be considered an essential part of obtaining a 'quartz' age. The presence of optically invisible but abundant accidentally trapped-mica can then be confirmed by backscattered electron microscopy (Fig 5-2).

We have demonstrated that precision is obtainable at the 5% level even in samples with K-hosted in several different types of fluid inclusion (Kendrick et al., 2005), that do not contain K-mineral impurities, and for which true isochron regressions are difficult to obtain (Fig 5-5). The Ar-Ar fluid inclusion ages currently support models with early ~1595 Ma syn-D_2 mineralisation at Osborne and are compatible with later 1514-1530 Ma D_3 mineralisation at Eloise. However, a major finding of this study is that the measured $^{40}Ar/^{36}Ar$ values of Proterozoic fluid inclusion are close to their initial values and provided K-mineral impurities are absent can in most cases be interpreted with out any need for post-entrapment $^{40}Ar_R$ correction.

Acknowledgements

Appendix A – Argon data

Eloise

Temp °C	⁴⁰Ar mols (×10⁻¹⁵)	³⁶Ar mols (×10⁻¹⁵)	Cl mols (×10⁻⁹)	K mols (×10⁻⁹)	%³⁹Ar	Apparent Age Ma
EL 48177 Combined crushing and stepped heating data						**22.5 mg**
Cr 1	28.0 ± 0.1	0.17 ± 0.01	1.29 ± 0.08			
Cr 2	2403.6 ± 2.4	2.46 ± 0.01	142.16 ± 9.23	6.19 ± 0.04	26.7	5620 ± 244
Cr 3	1065.3 ± 0.5	0.73 ± 0.01	78.92 ± 5.12	3.34 ± 0.02	41.1	5511 ± 278
200	140.31 ± 0.01	0.35 ± 0.01	18.0 ± 1.2			
300	240.3 ± 0.1	0.31 ± 0.01	14.0 ± 0.9	0.41 ± 0.01	42.9	6127 ± 1281
400	239.1 ± 0.2	0.39 ± 0.01	35.4 ± 2.3	1.14 ± 0.03	47.8	4063 ± 467
500	130.4 ± 0.2	0.135 ± 0.003	23.1 ± 1.5	1.88 ± 0.02	55.9	2840 ± 104
600	39.0 ± 0.4	0.224 ± 0.002	3.9 ± 0.3	1.75 ± 0.02	63.4	--- --
800	51.5 ± 0.1	0.02 ± 0.01	7.0 ± 0.5	2.1 ± 0.2	72.4	1793 ± 274
1000	67.08 ± 0.04	0.04 ± 0.01	5.5 ± 0.4	1.9 ± 0.2	80.7	2128 ± 428
1200	316.7 ± 0.7	0.42 ± 0.01	25.5 ± 1.7	1.6 ± 0.1	87.6	4252 ± 657
1400	823.7 ± 0.8	0.51 ± 0.01	60.9 ± 4.0	2.9 ± 0.1	100	5370 ± 1218
Total	5545 ± 3	5.76 ± 0.04	416 ± 12	23.2 ± 0.3	Fusion	4804 ± 282
EL 48177 Stepped heating data						**26.0 mg**
150	27.6 ± 0.1	0.14 ± 0.01	0.06 ± 0.01	0.17 ± 0.02	0.8	--- ---
250	687.2 ± 0.5	0.79 ± 0.01	16.8 ± 1.1	1.04 ± 0.08	5.9	6442 ± 2273
350	884.0 ± 0.6	0.71 ± 0.03	54.2 ± 3.5	1.60 ± 0.04	13.7	6393 ± 1251
450	964.6 ± 0.6	0.72 ± 0.01	118.1 ± 7.7	4.15 ± 0.03	34.0	4931 ± 174
550	116.8 ± 0.1	0.141 ± 0.003	17.2 ± 1.1	1.60 ± 0.05	41.9	2808 ± 192
650	29.8 ± 0.1	0.02 ± 0.02	5.3 ± 0.3	0.70 ± 0.03	45.3	2360 ± 826
800	38.60 ± 0.02	0.14 ± 0.01	7.0 ± 0.5	1.52 ± 0.07	52.7	--- ---
1000	72.7 ± 1.1	0.13 ± 0.05	6.0 ± 0.4	1.33 ± 0.07	59.2	2016 ± 1152
1200	1587.8 ± 1.1	0.76 ± 0.01	177.7 ± 11.5	8.34 ± 0.07	100	4760 ± 199
Total	4409 ± 2	3.56 ± 0.06	402 ± 14	20.4 ± 0.2	Fusion	4777 ± 218
EL 48179 Stepped heating data						**92.0 mg**
200	330.2 ± 0.1	0.30 ± 0.02	2.1 ± 0.1	0.32 ± 0.09	1.5	7412 ± 5164
250	1249.3 ± 0.8	0.606 ± 0.004	12.9 ± 0.8	0.34 ± 0.07	3.2	9969 ± 7149
300	696.3 ± 0.3	0.43 ± 0.01	20.1 ± 1.3	0.38 ± 0.00	5.0	8655 ± 1416
350	385.60 ± 0.04	0.32 ± 0.01	22.0 ± 1.4	0.93 ± 0.06	9.4	5871 ± 1674
400	406.8 ± 0.3	0.37 ± 0.01	24.4 ± 1.6	0.64 ± 0.03	12.5	6568 ± 1973
450	496.6 ± 0.4	0.41 ± 0.02	29.0 ± 1.9	1.07 ± 0.06	17.7	6060 ± 1659
500	75.18 ± 0.01	0.10 ± 0.03	3.6 ± 0.2	0.58 ± 0.36	20.5	3523 ± 2892
550	39.2 ± 0.1	0.098 ± 0.003	1.8 ± 0.1	0.35 ± 0.07	22.2	2176 ± 762
650	55.7 ± 0.1	0.064 ± 0.002	2.4 ± 0.2	0.43 ± 0.03	24.2	3713 ± 803
800	84.89 ± 0.04	0.14 ± 0.01	4.9 ± 0.3	0.95 ± 0.05	28.8	2775 ± 502
1000	128.9 ± 0.1	0.26 ± 0.01	9.1 ± 0.6	1.39 ± 0.01	35.5	2530 ± 386
1100	208.5 ± 0.7	0.349 ± 0.004	13.2 ± 0.9	0.94 ± 0.01	40.0	4144 ± 212
1200	1400.0 ± 1.0	0.86 ± 0.01	112.7 ± 7.3	5.40 ± 0.05	65.9	5201 ± 247
1300	716.1 ± 0.4	0.56 ± 0.01	63.9 ± 4.1	3.29 ± 0.02	81.7	4805 ± 200
1400	894.8 ± 0.6	0.53 ± 0.01	78.0 ± 5.1	3.80 ± 0.05	100	5049 ± 353
Total	7182 ± 2	5.47 ± 0.05	400 ± 10	20.8 ± 0.4	Fusion	5601 ± 632

Osborne

Temp °C	⁴⁰Ar mols (×10⁻¹⁵)	³⁶Ar mols (×10⁻¹⁵)	Cl mols (×10⁻⁹)	K mols (×10⁻⁹)	%³⁹Ar	Apparent Age Ma
OS 37A Stepped heating data						**41.9 mg**
200	161.0 ± 0.2	0.52 ± 0.01	0.81 ± 0.05	0.19 ± 0.01	1.4	2475 ± 1340
300	188.2 ± 0.4	0.25 ± 0.01	5.2 ± 0.3	0.13 ± 0.03	2.4	7715 ± 5425
400	200.96 ± 0.02	0.296 ± 0.004	14.5 ± 0.9	0.89 ± 0.02	9.2	4343 ± 459
200	31.4 ± 0.1	0.060 ± 0.002	1.15 ± 0.08	0.76 ± 0.07	15.0	1595 ± 250
600	27.9 ± 0.1	0.012 ± 0.004	0.15 ± 0.02	0.17 ± 0.16	16.3	4506 ± 4339
800	36.9 ± 0.1	0.030 ± 0.004	0.45 ± 0.03	1.08 ± 0.08	24.5	2018 ± 284
1000	76.3 ± 7.6	0.13 ± 0.02	0.38 ± 0.03	1.75 ± 0.05	37.7	1764 ± 617
1200	149.6 ± 0.2	0.30 ± 0.01	1.92 ± 0.13	3.23 ± 0.04	62.3	1630 ± 89
1400	358.4 ± 0.2	0.84 ± 0.01	10.4 ± 0.7	1.56 ± 0.09	74.1	3422 ± 571
1600	804.7 ± 0.7	2.12 ± 0.01	11.7 ± 0.8	3.41 ± 0.06	100	2955 ± 198
Total	2035 ± 8	4.57 ± 0.03	47 ± 1	13.2 ± 0.2	Fusion	2952 ± 171
OS 37B Stepped heating data						**43.2 mg**
200	218.5 ± 0.8	0.718 ± 0.005	4.5 ± 0.3		0.0	--- ---
300	212.2 ± 0.0	0.391 ± 0.005	25.8 ± 1.7	2.37 ± 0.01	7.9	2610 ± 89
400	154.6 ± 0.6	0.312 ± 0.003	33.0 ± 2.1	2.60 ± 0.04	16.6	1926 ± 72
500	36.5 ± 1.2	0.12 ± 0.01	0.8 ± 0.1	0.22 ± 0.04	17.3	--- ---
600	72.5 ± 0.4	0.11 ± 0.01	12.9 ± 0.8	1.8 ± 0.1	23.4	1793 ± 235
700	17.1 ± 0.2	0.02 ± 0.01	0.8 ± 0.1	0.55 ± 0.03	25.2	1768 ± 752
800	18.6 ± 0.1		0.7 ± 0.0	0.67 ± 0.01	27.5	--- ---
1000	20.1 ± 0.1	0.07 ± 0.01	1.7 ± 0.1	0.60 ± 0.11	29.5	--- ---
1200	321.6 ± 0.0	0.29 ± 0.01	84.8 ± 5.5	9.9 ± 0.1	62.4	1914 ± 50
1400	209.5 ± 0.3	0.326 ± 0.004	40.0 ± 2.6	5.62 ± 0.03	81.2	1724 ± 35
1600	275.4 ± 0.3	0.62 ± 0.04	38.5 ± 2.5	5.7 ± 0.1	100	1496 ± 294
Total	1557 ± 2	2.99 ± 0.05	243.6 ± 7.2	30.0 ± 0.2	Fusion	1818 ± 68

Railway Fault

Temp °C	^{40}Ar mols (×10^{-15})	^{36}Ar mols (×10^{-15})	Cl mols (×10^{-9})	K mols (×10^{-9})	%^{39}Ar	Apparent Age Ma
AW02-002a Stepped heating data						**126 mg**
150	27.7 ± 0.1	0.10 ± 0.003			---	--- ---
200	456.5 ± 0.4	0.91 ± 0.01	0.64 ± 0.04	0.90 ± 0.04	0.0	5176 ± 1091
250	1427.6 ± 1.3	2.01 ± 0.02	3.0 ± 0.2	5.94 ± 0.05	0.3	4508 ± 190
300	2967.3 ± 2.9	2.23 ± 0.02	9.6 ± 0.6	15.6 ± 0.1	0.9	4594 ± 132
350	7352.7 ± 7.0	3.91 ± 0.03	29.9 ± 1.9	37.9 ± 0.3	2.3	4759 ± 155
380	3909.5 ± 3.0	1.56 ± 0.01	15.3 ± 1.0	40.7 ± 0.2	3.8	3692 ± 72
410	3716.9 ± 2.8	1.46 ± 0.01	11.4 ± 0.7	78.7 ± 0.5	6.8	2639 ± 36
440	3907.2 ± 3.1	1.63 ± 0.02	9.9 ± 0.6	116.0 ± 0.7	11.2	2180 ± 27
480	2305.7 ± 1.5	0.51 ± 0.01	2.1 ± 0.1	161.6 ± 1.0	17.3	1304 ± 12
530	2290.6 ± 1.7	0.31 ± 0.01	1.1 ± 0.1	187.7 ± 1.2	24.4	1188 ± 11
580	2022.6 ± 1.2	0.23 ± 0.00	0.66 ± 0.04	174.0 ± 1.1	31.0	1152 ± 10
650	1896.2 ± 1.2	0.28 ± 0.02	0.68 ± 0.04	168.7 ± 1.0	37.4	1115 ± 11
750	2746.2 ± 2.2	0.56 ± 0.03	2.7 ± 0.2	174.0 ± 1.0	44.0	1406 ± 14
850	1380.4 ± 0.2	0.28 ± 0.06	1.2 ± 0.1	103.0 ± 0.6	47.9	1252 ± 26
1000	2948.2 ± 2.4	0.88 ± 0.02	5.5 ± 0.4	143.7 ± 0.9	53.4	1644 ± 17
1100	3545.9 ± 3.2	1.17 ± 0.04	8.0 ± 0.5	137.2 ± 0.9	58.6	1892 ± 25
1200	11238.7 ± 9.5	5.15 ± 0.04	28.6 ± 1.9	198.7 ± 1.2	66.1	2863 ± 43
1250	14282.0 ± 9.8	5.47 ± 0.04	39.1 ± 2.5	206.1 ± 1.2	73.9	3198 ± 53
1290	12847.1 ± 8.7	4.70 ± 0.04	34.0 ± 2.2	197.9 ± 1.2	81.4	3109 ± 51
1330	10912.9 ± 7.2	4.20 ± 0.03	27.0 ± 1.8	158.4 ± 1.0	87.4	3188 ± 53
1370	9613.4 ± 6.8	4.06 ± 0.04	22.7 ± 1.5	116.6 ± 0.7	91.8	3442 ± 62
1410	9143.2 ± 6.2	3.70 ± 0.03	20.1 ± 1.3	88.8 ± 0.5	95.2	3799 ± 79
1450	9020.0 ± 6.2	3.51 ± 0.02	17.5 ± 1.1	72.0 ± 0.4	97.9	4120 ± 97
1490	6065.7 ± 3.6	2.16 ± 0.01	10.9 ± 0.7	40.6 ± 0.3	99.4	4425 ± 117
1530	1960.0 ± 0.4	0.77 ± 0.01	3.6 ± 0.2	12.28 ± 0.08	99.9	4515 ± 133
1550	333.3 ± 0.2	0.27 ± 0.02	0.73 ± 0.05	2.29 ± 0.02	100	4128 ± 315
Total	128318 ± 24	52.0 ± 0.1	306 ± 5	2639 ± 4	Fusion	2674 ± 9

Railway Fault

Temp °C	^{40}Ar mols ($\times 10^{-15}$)	^{36}Ar mols ($\times 10^{-15}$)	Cl mols ($\times 10^{-9}$)	K mols ($\times 10^{-9}$)	%^{39}Ar	Apparent Age Ma
AW02-002b Combined crushing and stepped heating data						**22.9 mg**
Cr 1	132.5 ± 0.2	0.24 ± 0.03	0.53 ± 0.04	0.35 ± 0.03	0.1	4844 ± 2039
Cr 2	283.1 ± 0.1	0.51 ± 0.02	1.34 ± 0.10	0.94 ± 0.05	0.3	4499 ± 980
Cr 3	1163.8 ± 0.5	1.89 ± 0.01	4.3 ± 0.3	3.44 ± 0.05	1.1	4883 ± 343
Cr 4	2717.3 ± 1.9	2.93 ± 0.02	10.7 ± 0.7	7.69 ± 0.05	2.9	5418 ± 236
Cr 5	2767.4 ± 1.3	3.11 ± 0.02	10.3 ± 0.7	8.52 ± 0.05	4.9	5238 ± 203
Cr 6	1739.0 ± 0.5	1.81 ± 0.02	8.0 ± 0.5	6.46 ± 0.06	6.4	4983 ± 266
200	359.8 ± 0.3	1.01 ± 0.01	0.26 ± 0.03	2.69 ± 0.04	7.1	1853 ± 162
300	395.83 ± 0.03	0.65 ± 0.01	0.86 ± 0.06	8.91 ± 0.06	9.2	1866 ± 68
400	749.7 ± 0.3	0.64 ± 0.02	2.6 ± 0.2	34.9 ± 0.2	17.4	1482 ± 29
500	1587.4 ± 0.3	0.27 ± 0.01	0.71 ± 0.07	130.7 ± 1.0	48.1	1174 ± 12
600	784.3 ± 0.3	0.189 ± 0.002	0.14 ± 0.01	74.5 ± 0.5	65.6	1038 ± 9
800	451.20 ± 0.01	0.13 ± 0.03	0.36 ± 0.04	43.4 ± 0.3	75.8	1014 ± 28
1000	201.1 ± 0.2	0.196 ± 0.004	0.27 ± 0.02	15.7 ± 0.1	79.5	985 ± 14
1200	589.5 ± 0.6	0.67 ± 0.01	1.32 ± 0.09	23.8 ± 0.1	85.1	1511 ± 26
1400	2871.3 ± 3.6	3.57 ± 0.02	11.9 ± 0.8	45.4 ± 0.3	95.7	2581 ± 41
1600	2926.4 ± 2.1	5.78 ± 0.09	7.2 ± 0.5	18.2 ± 0.1	100	3329 ± 216
Total	19719 ± 5	23.6 ± 0.1	61 ± 1	425 ± 1	Fusion	2197 ± 17
AW02-002b Stepped heating data						**23.3 mg**
200	168.7 ± 0.1	0.44 ± 0.01	0.18 ± 0.01	0.67 ± 0.03	0.2	3136 ± 480
300	1206.6 ± 1.0	0.92 ± 0.02	3.6 ± 0.2	5.9 ± 0.1	1.9	4714 ± 277
400	1318.0 ± 0.7	0.87 ± 0.02	5.1 ± 0.3	16.9 ± 0.1	6.7	3227 ± 82
500	661.0 ± 0.2	0.26 ± 0.02	0.8 ± 0.1	39.8 ± 0.2	18.0	1394 ± 28
600	418.7 ± 0.3	0.16 ± 0.02	0.18 ± 0.04	34.1 ± 0.2	27.7	1127 ± 23
800	639 ± 64	0.439 ± 0.003	1.0 ± 0.1	34.4 ± 0.2	37.4	1402 ± 249
1000	161.8 ± 0.4	0.117 ± 0.001	0.24 ± 0.02	10.2 ± 0.1	40.3	1246 ± 15
1200	935.9 ± 1.0	0.68 ± 0.03	2.5 ± 0.2	27.1 ± 0.2	48.0	2076 ± 53
1400	5391.3 ± 6.0	6.13 ± 0.04	22.6 ± 1.5	113.7 ± 0.7	80.3	2261 ± 32
1600	4710.4 ± 3.8	6.24 ± 0.04	14.0 ± 0.9	69.2 ± 0.4	100	2628 ± 43
Total	15611 ± 64	16.2 ± 0.1	50 ± 2	352 ± 1	Fusion	2230 ± 30

References

Baker, T., 1998, Alteration, Mineralisation, and Fluid Evolution at the Eloise Cu-Au Deposit, Cloncurry District, Northwest Queensland, Australia. Econ. Geol. 93, p1213-1236.

Baker, T., Perkins C., Blake K.L., and Williams P.J., 2001, Radiogenic and Stable Isotope Constraints on the Genesis of the Eloise Cu-Au Deposit, Cloncurry District, Northwest Queensland. Econ. Geol. 96, p723-742.

Brannon J. C., Podosek F. A., and McLimans R. K., 1992, Alleghenian age of the Upper Mississippi Valley zinc-lead deposit determined by Rb-Sr dating of sphalerite. Nature 356, p509-511.

Böhlke J.K. and Irwin J.J. (1992) Brine history indicated by argon, krypton, chlorine, bromine, and iodine analyses of fluid inclusions from the Mississippi Valley type lead-fluorite-barite deposits at Hansonburg, New Mexico. Earth Planet. Sci. Lett. 110, 51-66 p.

Carr G.R., Denton G.J., Parr J., Sun S., Korsch M.J., and Bodon S.B., 2004, Lightning does strike twice: multiple ore events in major mineralised systems in northern Australia. SEG 2004: Predictive Mineral Discovery Under Cover, 27th Sept-1st Oct 2004, (eds; Muhling J., Goldfarb R., Vielreicher N., Bierlein F., Stumpfl E., Groves D.I., Kenworthy S.) Centre for Global Metallogeny, The University of Western Australia, Publication no., 33.

Coveney R.M. Jr., Ragan V.M., Brannon J.C., 2000, Temporal benchmarks for modeling Phanerozoic flow of basinal brines and hydrocarbons in the southern Midcontinent based on radiometrically dated calcite. Geology 28, p795-798.

Darbyshire D. P. F. and Shepherd T. J. (1985) Chronology of granite magmatism and associated mineralization, S. W. England. J. Geol. Soc. London 142, 1159-1177.

Dodson, M.H., 1973, Closure temperature in cooling geochronological and petrological systems. Contrib. Mineral. Petrol. 40, 259-274.

Gauthier L., Hall G., Stein H., Schaltegger U., 2001, The Osborne Deposit, Cloncurry District: A 1595 Ma Cu-Au Skarn Deposit. In A Hydrothermal Odyssey, Extended conference Abstracts, Ed. Williams P.J., James Cook University, Townesville, pp 58-59.

Giles D., and Nutman A.P., 2002, SHRIMP U-Pb monazite dating of 1600-1580 Ma amphibolite facies metamorphism in the southeastern Mt Isa block, Australia. Australian Journal of Earth Sciences 49, p455-465.

Heinrich C.A., Bain J.H.C, Mernagh T.P., Wyborn L.A.I., 1995, Fluid and Mass Transfer during Metabasalt Ateration and Copper Mineralisation at Mount Isa, Australia. Economic Geology 90, p705-730.

Irwin J.J., and Roedder E., (1995) Diverse origins of fluid inclusions at Bingham (Utah, USA), Butte (Montana, USA), St. Austell (Cornwall, UK) and Ascension Island (mid-Atlantic, UK), indicated by laser microprobe analysis of Cl, K, Br, I, Ba + Te, U, Ar, Kr, and Xe. Geochim. Cosmochim. Acta 59(2), 295-312.

Kelley S., Turner G., Butterfield A.W., and Shepherd T.J. (1986) The source and significance of argon isotopes in fluid inclusions from areas of mineralization. Earth Plan. Sci. Lett. 79, 303-318.

Kendrick M.A., Burgess R., Pattrick R.A.D., and Turner G., 2001a, Halogen and Ar-Ar age determinations of inclusions within quartz veins from porphyry copper deposits using complementary noble gas extraction techniques. Chem. Geol. 177, p351-370.

Kendrick M.A., Burgess R., Pattrick R.A.D., and Turner G., 2001b, Noble gas and halogen evidence on the origin of Cu-Porphyry mineralising fluids. Geochim. Cosmochim. Acta 65, p2651-2668.

Kendrick M.A., Burgess R., Pattrick R.A.D., and Turner G. (2002a) Hydrothermal fluid origins in a fluorite-rich Mississippi valley-type deposit: combined noble gas (He, Ar, Kr) and halogen (Cl, Br, I) analysis of fluid inclusions from the South Pennine Orefield, United Kingdom, Econ. Geol. 97 (3), p435-451.

Kendrick M.A., Burgess R., Leach D. and Pattrick R.A.D. (2002b) Hydrothermal fluid origins in Mississippi valley-type ore deposits: combined noble gas (He, Ar, Kr) and halogen (Cl, Br, I) analysis of fluid inclusions from the Illinois-Kentucky Fluorspar district, Viburnum Trend, and Tri-State districts, mid-continent United States. *Econ. Geol.* **97** (3), p452-479

Kendrick M.A., Miller J.McL, Phillips D., 2005, Part I. Stepwise heating of quartz: Implications for fluid inclusion analysis and the solubility of noble gases and halogens in quartz. Submitted to GCA.

Kendrick M.A., Burgess R., Harrison D., and Bjørlykke A., 2005b, Noble gas and halogen evidence on the origin of Scandinavian sandstone-hosted Pb-Zn deposits. Geochimica et Cosmochimica Acta, In Press.

McDougall I., and Harrison T.M., 1999, Geochronology and Thermochronology by the ^{40}Ar/^{39}Ar Method. Oxford University Press, Oxford, New York. p269.

McGoldrick P.J., and Keays R.R., 1990, Mount Isa copper and lead-zinc-silver ores: coincident or cogenesis? Economic Geology 85, 641-650.

McKee E.H., Conrad J.E., Turrin B.D., and Theodore T.G., 1993, 40Ar/39Ar studies of fluid inclusions in vein quartz from battle mountain, Nevada. USGS Bulletin 2039, p155-165.

Miller J.McL, Kendrick M.A., Phillips D., 2004, Testing the 'Fools Clock' and tales from fluid inclusions. Extended abstracts of Predictive Mineral Discovery Cooperative Research Centre June 2004 Barrossa Valley Conference (Eds. Barnicoat A.C. and Korsch R.J.). Geoscience Australia Record 2004/9, p 133-137.

Nakai S., Halliday A. N.. Kesler S. E., and Jones H. D. (1990) Rb-Sr dating of sphalerites from Tennessee and the genesis of Mississippi Valley type ore deposits. Nature 346, 354-357.

Nakai S., Halliday A. N., Kesler S. E., Jones H. D., Kyle J. R., and Lane T. E. (1993) Rb-Sr Dating of Sphalerites from Mississippi Valley-Type (MVT) Ore Deposits. *Geochim. Cosmochim. Acta 57, 417-427.*

Page R.W., Jackson M.J., and Krassay A.A., 2000, Constraining sequence Stratigraphy in north Australian basins: SHRIMP U–Pb zircon geochronology between Mt Isa and McArthur River. Australian Journal of Earth Sciences (2000) 47, 431–459

Pettke T., and Diamond L.W., 1995, Rb-Sr isotopic analysis of fluid inclusions in quartz: Evaluation of bulk extraction procedures and geochronometer systematics using synthetic fluid inclusions. Geochimica et Cosmochimica Acta 59, p4009-4027.

Perkins C., and Wyborn L.A.I., 1998, Age of Cu-Au mineralization, Cloncurry district, eastern Mt Isa Inlier, Queensland, as determined by 40Ar/39Ar dating. Australian Journal of Earth Sciences 45, p233-246.

Perkins C., Heinrich C.A. and Wyborn L.A.I., 1999, $^{40}Ar/^{39}Ar$ Geochronology of Copper Mineralisation and Regional Alteration, Mount Isa, Australia. Econ. Geol. 94, p23-36.

Qui H-N., 1996, $^{40}Ar-^{39}Ar$ dating of the quartz samples from two mineral deposits in western Yunnan (SW China) by crushing in vacuum. Chemical Geology 127, p211-222.

Qui H-N., Zhu BQ., Sun DZ., 2002, Age significance interpreted from Ar-40-Ar-39 dating of quartz samples from the Dongchuan Copper Deposits, Yunnan, SW China, by crushing and heating. Geochemical Journal 36, p475-491.

Rubenach M.J., Adshead N., Oliver N., Tullemans F., Esser D., and Stein H., 2001, The Osborne Cu-Au Deposit: geochronology and genesis of mineralization in relation to host albitites and irostones. In A Hydrothermal Odyssey, Extended conference Abstracts, Ed. Williams P.J., James Cook University, Townesville, pp 172-173.

Shepherd T. J. and Darbyshire D. P. F. (1981) Fluid inclusion Rb-Sr isochrons for dating mineral deposits. Nature 290, 578-579.

Smith P.E., Evensen N.M., York D., Szatmari P., Oliveira D.C. de, 2001, Single crystal 40Ar-39Ar dating of pyrite: No fool's clock. Geology 29, p403-406.

Spikings R.A., Foster D.A., Kohn B.P., Lister G.S., 2002, Post-orogenic (<1500 Ma) thermal history of the Palaeo-Mesoproterozoic, Mt. Isa province, NE Australia. Tectonophysics 349, p327-365.

Swager C.P., 1985, Syndeformational Carbonate-Replacement Model for the Copper Mineralisation at Mount Isa, Northwest Queensland: A Microstructural Study. Economic Geology, 80, p107-125.

Turner G., 1988, Hydrothermal fluids and argon isotopes in quartz veins and cherts. Geochimica et Cosmochimica Acta 52, p1443-1448.

Turner G. and Bannon M.P., (1992) Argon isotope geochemistry of inclusion fluids from granite-associated mineral veins in southwest and northeast England. Geochim. Cosmochim. Acta, 56, 227-243.

Turner G., Burnard P., Ford J.L., Gilmour J.D., Lyon I.C., and Stuart F.M. (1993) Tracing fluid sources and interactions. Phil. trans. Roy. Soc. Lon. A 344, 127-140.

York D., Masiliwec A., Kuybida P., Hanes J.A., Hall C.M., Kenyon W.J., Spooner E.T.C. and Scott S.D., 1982, 40Ar/39Ar dating of pyrite. Nature 300, p52-53.